Volume 37
No. 1

JNSChE
Mar/April 2022

ISSN
0794-6759

DOI: 10.51975/EFSD2591

JOURNAL OF THE NIGERIAN SOCIETY OF CHEMICAL ENGINEERS

MODELLING, SIMULATION AND OPTIMIZATION OF BIOETHANOL PRODUCTION FROM LIGNOCELLULOSE MATERIALS USING OPEN-SOURCE SOFTWARE- SCILAB, R AND AP MONITOR
Olowookere, F. V. and Williams, A. O.F. 1

HEAT AND MASS TRANSFER CONSIDERATIONS IN THE DESIGN OF A COILED ABSORBER FOR AMMONIA-WATER REFRIGERATION SYSTEM
Mumah, S.N, Akande, H.F., Oyawoye, M. R., Ibrahim, T.G., Mudi, K.Y., Olaniyan, O. and Samuel, F. 18

WEB APPLICATIONS AND ONLINE RESOURCES FOR 21ST CENTURY CHEMICAL ENGINEERING EDUCATION: A REVIEW
Irivwegu, M. and Amadi, E. E 40

ASSESSMENT OF SOLAR ENERGY POTENTIAL OF NIGERIA FOR SOLAR POWER GENERATION THROUGH NUMERICAL SOLAR IRRADIANCE MAPPING
Mumah, S.N., Akande, H.F., Oyawoye, M. R., Mudi, K.Y., Samuel, F. and Olaniyan, I.O. 47

MODELING AND OPTIMIZATION OF PARTICLEBOARDS PRODUCED FROM RICE HUSK WASTE USING R7AD2 ADHESIVE
Hamidu, L. A. J., Aroke, U. O., Osha, O. A., Muhammad, I. M. 66

ECONOMIC STUDY OF CONVENTIONAL AND IMPROVED EXTRACTIVE DISTILLATION SYSTEM USING ASPEN ECONOMIC ANALYSER
Zubairu, A. A. and Eletta, O. A. A. 75

EVALUATION OF THE SUGAR CONTENT OF SELECTED COKE DRINKS
Offurum, J. C.; Ibeto, T. M. and Nwakaudu, A. A. 84

JUSTIFICATION OF ORDER OF CORROSION INHIBITION KINETICS FOR ESTERS OF CASTOR AND RUBBER SEED OILS
Offurum, J. C., Chukwu, M.M., Mbadike, C. A., Nwaneri, T. U. and Nwakaudu, A. A. 88

PERFORMANCE EVALUATION OF TETRABUTYLAMMONIUM BROMIDE-BASED DEEP EUTECTIC SOLVENTS IN ENHANCED OIL RECOVERY OF NIGERIAN HEAVY OIL
Abdurrahman, A. , Shuwa, S.M., Dabai, F. N., Orodu, O. D., Ogunkunle, F. T., Adamu, S.Y., and El-Yakubu, B.J. 94

EFFICIENCY OF ACTIVATED PERIWINKLE CHAR IN THE RECOVERY OF LEAD (II) ION FROM INDUSTRIAL WASTEWATER USING FIXED BED ADSORPTION PROCESS
*Babalola, R. and Aniediong, U. 103

INSTRUCTION TO AUTHORS 112

Published by,
THE NIGERIAN SOCIETY OF CHEMICAL ENGINEERS
National Secretariat: Infinite Grace House, Plot 4, Oyetubo Street,
Off Obafemi Awolowo Way, Ikeja, Lagos State, Nigeria.
E-mail: nationalhqtrs@nsche.org, nsche_headquarters@yahoo.com
Website: https://www.nsche.org.ng; Journal URL: https://journal.nsche.org.ng
Submission of Manuscripts: nschejournal@yahoo.com and copy: stevmomoh@yahoo.com

JOURNAL OF THE NIGERIAN SOCIETY OF CHEMICAL ENGINEERS
A Publication on the Science and Technology of Chemical Engineering

EDITORIAL BOARD

Engr. Dr. S. O. Momoh, *FNSE*, *FNSChE*, Chairman/Editor-in-Chief
The Presidency
National Agency for Science and Engineering Infrastructure (NASENI). Abuja
stevmomoh@yahoo.com
Engr. Prof. O. Taiwo, *FAEng*, *FNSE*, *FIChemE*, *FNSChE*, Deputy Chairman/Editor-in-Chief
Department of Chemical Engineering, Obafemi Awolowo University, Ile-Ife
femtaiwo@yahoo.com
Engr. Prof. E. A. Taiwo, ***FNSChE, MNSE*, *MCSN*** Associate Editor
Department of Chemical Engineering, Obafemi Awolowo University, Ile Ife
eataiwo@yahoo.com
Engr. Prof. O. F. Joel, *FNSChE*, Associate Editor
Department of Petroleum & Gas Engineering, University of Port Harcourt
ogbonna.joel@uniport.edu.ng
Engr. Prof. E. O. Aluyor, *FNSChE*, *FNIBE*, *MNSE*, Associate Editor
Department of Chemical Engineering, University of Benin, Benin City
aluyoreo@gmail.com
Engr. Prof. G. O. Mbah, *FNSChE*, *MNSE*, Associate Editor
Department of Chemical Engineering, Enugu State University of Science & Technology, Enugu
mbagordian@yahoo.com
Engr. Prof. O. A. Ajayi, *MNSE*, *MNSChE*, Associate Editor
Department of Chemical Engineering, Ahmadu Bello University, Zaria
segeaj@gmail.com
Engr. Prof. A. S. Kovo, *MNSE*, *MNSChE*, Associate Editor/Secretary
Department of Chemical Engineering, Federal University of Technology, Minna
kovoabdulsalami@gmail.com
Engr. Dr. M. Alhassan, *MNSE, MNSChE,* Associate Editor
Department of Chemical Engineering, Federal University of Technology, Minna
moh.alhass@futminna.edu.ng

2022 BOARD OF DIRECTORS AND OFFICIALS

Engr. S. A. Mohammed, *FNSChE*	National President
Engr. A. U. Ogbuigwe, FNSChE	Deputy National President
Engr. O. A. Anyaoku, *FNSChE*	Immediate Past President
Engr. D. Uweh, *MNSChE*	Publicity Secretary
Engr. Ben Akaakar, *FNSChE*	Asst. Publicity Secretary
Engr. Anthony Ogheneovo, *MNSChE*	National Treasurer
Engr. Dr (Mrs.) Edith A. Alagbe, *MNSChE*	Asst. National Treasurer
S. O. Bosoro, *MNSChE*	Executive Secretary

INTERNAL AUDITORS

Engr. Dr. Mrs. G. Akujobi-Emetuche, *FNSChE*	Internal Auditor I
Engr. Prof. Edwin N.Ikezue, *FNSChE*	Internal Auditor II

CHAPTER CHAIRMEN

Engr. G. H. Abubakar, *MNSChE*	Kogi
ENgr. Oghenenovo Ememerurai *MNSChE*	Edo/Delta
Dr,. Idris Mohammed, *MNSChE*	ABBYGOT
Engr. G. T. Muhammad, F*NSChE*	Kaduna
Prof. M. S. Nwakaudu, *FNSChE*	Imo/Abia
Dr. P. C. N. Ejikeme, *MNSChE*	Anambra/Enugu/Ebonyi
Dr. Innocent Akuvue, *FNSChE*	RIVBAY
Prof. Abudulfatai Jimoh, MN*SChE*	Niger
Engr. O. O. Onugu, *FNSChE*	FCT/Nasarawa
Prof. E. A. Taiwo, *FNSChE*	Oyo/Osun/Kwara
Dr. K. F. K. Oyedeko, *FNSChE*	Lagos/Ogun
Engr. T. S. Soom, *MNSChE*	Benue Industrial
Engr. Benedict Edenseting, *MNSChE*	Akwa Ibom/Cross River
Prof. E. I. Dada, *FNSChE*	USA

SUBSCRIPTION

a.	**Individual Member**	₦3,000.00
b.	**Overseas Subscribers**	US$100.00
c.	**Institution, Libraries, etc**	₦5,000.00

DOI:10.51975/22370101.som
Journal of the Nigerian Society of Chemical Engineers, 37(1), 2022

MODELLING, SIMULATION AND OPTIMIZATION OF BIOETHANOL PRODUCTION FROM LIGNOCELLULOSE MATERIALS USING OPEN-SOURCE SOFTWARE- SCILAB, R AND AP MONITOR

Olowookere, F. V.[1] **and *Williams, A. O.F.** [2]
[1,2]*Department of Chemical and Petroluem*
Engineering, University of Lagos, Lagos, Nigeria
*Email of the Corresponding author: afwillaims@unilag.edu.ng

ABSTRACT

Bioethanol production from lignocellulose biomass has gained a lot of traction over the last two decades because it is a viable alternative energy source to fossil fuel and does not compete with the food supply like first-generation bioethanol does. In this study, previously reported research is used to generate mathematical models for enzymatic hydrolysis, and co-fermentation operations, which are then improved to include the decomposition of hemicellulose to xylose sugars. Two case studies were investigated and modelled in the Scilab and R software which are free and open-source software for numerical and statistical computing, respectively. The first case study examined the impact of alkaline loading and temperature (represented by A & B respectively) on delignification. Results show that A and A² are significant model terms and the optimum process parameters for delignification of 61% are 0.8% alkaline loading and 121℃. The second case investigated how the simultaneous saccharification and co-fermentation (SSCF) operation responds to the key control variables namely cellulose loading(A), hemicellulose loading(B), enzyme loading (C), yeast loading (D), temperature (E) and time (F). From the analysis of variance, the variables found to be significant model terms are: cellulose loading (A), enzyme loading (C), time (F), and then AF, A², C², F². Major parameters of the SSCF unit are then optimized using the APMonitor modeling package in Python to give 0.1263kg/kg minimum enzyme adsorbed per substrate loading, maximum cellulose conversion as 26.26% and a 47.9% maximum ethanol yield.

Keywords: *bioethanol; optimize; simultaneous saccharification and co-fermentation; dynamic modelling*

1. INTRODUCTION

The need for energy accessibility and sustainability in Nigeria cannot be overemphasized. The U.S. National Intelligence Council Report (2012) projects that by 2030, the global energy demand would have increased by 50%. A factor worthy of note is the Human Development Index (HDI). It is an essential means of ascertaining the state of sustainable energy development and dimensions of human well-being. A correlation of HDI value with energy production over the last three decades for Nigeria shows a negative slope as opposed to other developing/developed countries (Adesina, 2019). As reflected in the Sustainable Development Goal 7 (affordable and clean energy) set by the UN towards 2030, there is a need for increase in accessibility to alternative energy sources which are renewable and sustainable as they play a major role in green technology. One of these is the production of bioethanol from biomass.

The production of bioethanol essentially consists of three phases – pretreatment, saccharification and fermentation. This is illustrated with the block diagram shown in Figure 1. Biomass is pretreated to structurally modify its accessibility so that the polysaccharides can be broken down into fermentable sugars. These sugars are further converted to bioethanol and carbon dioxide by the action of a fermenting microorganism (such as Saccharomyces cerevisiae strain 1400 (pLNH33)).

The major classes of biomass used in bioethanol production are starch/food crops and lignocellulose materials. The former, considered as a 1st generation biofuel, has shown a low degree of sustainability due to its competition with world food supply (Byadgi, 2016). Recently, lignocellulose materials have attracted increased interest for research in 2nd generation biofuel production. They are moderately inexpensive and do not contend with the world's food supply. However, the cost of setting up a bioethanol production facility is still commercially unattractive as shown in Table 1. This is largely due to the amount of resources used (e.g. biomass, enzymes, etc.) and the operating conditions it is operated (Duque-escobar, 2011; Anwar et al., 2014). It is therefore essential to investigate recent methods and examine process conditions to maximize bioethanol yield.

Kadam et al. (2004) developed a model to describe the enzymatic hydrolysis of lignocellulose biomass materials... For this study, the model is consolidated to three sugars: glucose (representing the hexoses), xylose (representing the pentoses) and cellobiose (intermediate product). The model was verified (Morales-Rodriguez, 2011), validated with experimental results using acid pretreated corn stover (Kadam, 2004) and modified to include the decomposition of hemicellulose to xylose sugars (Camara, 2015). Cellobiose and β-glucosidase activities are treated as a unit activity that occurred in the reaction (Camara, 2015). Intrinsic and extrinsic parameters are also defined in this model i.e., substrate reactivity, end-product inhibition, enzyme adsorption. Krishnan et al. (1999) also proposed a model for the simultaneous fermentation of the C5 (xylose) and C6 (glucose) sugars to give ethanol, using recombinant Saccharomyces cerevisiae strain 140.0 (pLNH33). It describes the effects of inoculum size, product and substrate inhibition rates. The model is further modified to account for the inhibitory effects on the ethanol production rate. (Morales-Rodriguez, 2011).

This study aims to examine the influence of operating parameters (such as alkaline loading, temperature, enzyme loading, etc.) on lignocellulose biomass and to determine the best set of conditions that can work for a defined process route. This is achieved by utilizing the mathematical models for the production of bioethanol from lignocellulose materials reported in the literature. Simulation studies are carried out using Scilab; while constrained optimization is done using the APMonitor modelling package in Python to determine the best conditions for maximizing ethanol production. The influence of the operating parameters is investigated using a design of experiment (DoE) based on the Box-Behnken method and analysis of variance (ANOVA) implemented using the R software. Scilab (Mittal and Singh, 2013) is a free and open-source software for numerical computation, and simulation with capabilities much like Matlab. The R software is also a free and open-source software for statistical computing and graphics. Similarly, Python is a free an open-source programming software which supports dynamic optimization using the direct APMonitor modeling structure.

Apart from the foregoing stated objectives, this paper is also aimed at promoting the use of free and open-source software for the solution of chemical engineering modeling, simulation and optimization problems that does not involve the usual high cost associated with the well-known commercial computing software. Even with discounted academic licenses for such expensive software, they are often out of reach for routine use in research and teaching in many of our universities. It is therefore hoped that this paper would inspire other researchers and students in our universities to consider adopting and using free and open-source software in their research/teaching since no costs are involved.

Table 1 costs of bioethanol production (Zhao et al., 2015)

Amount of feedstock (per day)	2,000 tons
Annual bioethanol production rate	35,150,000 gallons
Total capital investment (TCI)	$ 255,306,332
Total variable operating cost (per year)	$127,690,000
Total fixed operating cost (per year)	$ 25,209,580
Current bioethanol selling price (2013)	$3.45/gal

2. MATERIALS AND METHODS

2.1 Mathematical Models for the SSCF unit operation

Figure 1 shows the block flow diagram for the production of bioethanol based on biomass hydrolysis and fermentation. The process route consists mainly of Alkaline Pretreatment, SHF (Separate Hydrolysis and Fermentation), Stripping Column and Distillation Column.

Based on the works of Camara et al (2015), Tables 2 and 3 show a listing of the reactions that take place in enzymatic hydrolysis of polysaccharides (cellulose, hemicellulose and lignin), the rate equations, and the applicable mass balances. Table 4 shows the rate equations for the co-fermentation process based on the work of and Krishnan (1999), These models form the basis of the simulation and optimization studies carried out in this work.

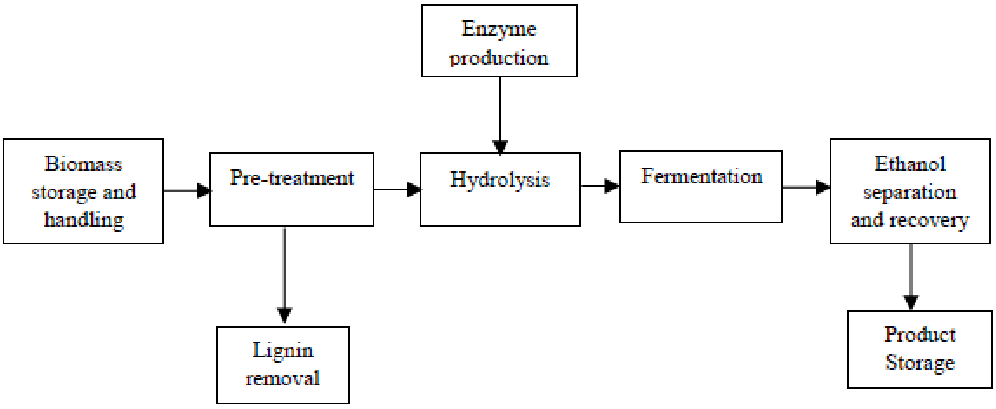

Figure 1 Block flow diagram for the production of bioethanol based on biomass hydrolysis and fermentation

Table 2 Mathematical model for enzymatic hydrolysis (Camara, 2015)

S/N	Reaction	Equation
1	Cellulose-glucose reaction with glucose, cellobiose and x inhibition	$r_1 = \frac{k_1[CE]R_S C_c}{1+\frac{C_{cb}}{K_{1IC_{cb}}}+\frac{C_g}{K_{1IC_g}}+\frac{C_X}{K_{1IC_X}}}$
2	Cellulose-cellobiose reaction with glucose, cellobiose and x inhibition	$r_2 = \frac{k_2[CE]R_S C_c}{1+\frac{C_{cb}}{K_{2IC_{cb}}}+\frac{C_g}{K_{2IC_g}}+\frac{C_X}{K_{2IC_X}}}$
3	Cellobiose-Glucose reaction with glucose and xylose inhibitio	$r_3 = \frac{k_3 C_E C_{Cb}}{K_{3C}\left(1+\frac{C_g}{K_{3IC_g}}+\frac{C_X}{K_{1IC_X}}\right)+C_{cb}}$
4	Hemicellulose-xylose reaction with glucose, cellobiose and x inhibition	$r_4 = \frac{k_4[CH]R_S C_H}{1+\frac{C_{cb}}{K_{4IC_{cb}}}+\frac{C_g}{K_{4IC_g}}+\frac{C_X}{K_{4IC_X}}}$
5	Enzyme Adsorption – Langmuir isotherm	$E_{ad} = \frac{E_{imax}K_{ia}C_E C_s}{1+K_{ia}C_E}$
6	Amount of enzyme adsorbed on cellulose and hemicell surfaces	$[CE] = \frac{E_{ad}}{C_s}C_c$, $[CH] = \frac{E_{ad}}{C_s}C_H$
7	Temperature dependence (Arrhenius Equation)	$k_{i\,(T2)} = k_{i\,(T1)}e^{-\frac{E_{ia}}{R}\left(\frac{1}{T_1}-\frac{1}{T_2}\right)}$ $30°C \leq T \leq 50°C$
8	Substrate reactivity	$R_S = \gamma\frac{c_s}{s_0}$

Table 3: Mass Balance equations for enzymatic hydrolysis (Camara, 2015)

Solids	$C_S = C_C + C_H + C_L$
Cellulose	$\frac{dC_c}{dt} = -r_2 - r_1$
Cellobiose	$\frac{dC_{cb}}{dt} = 1.056r_2 - r_3$
Glucose	$\frac{dC_g}{dt} = 1.111r_1 + 1.053r_3$
Hemicellulose	$\frac{dC_H}{dt} = -r_4$
Xylose	$\frac{dC_X}{dt} = 1.136r_4$
Enzymes	$E_T = C_E + E_{ad}$

Table 4: Kinetic models for co-fermentation process (Krishnan, 1999)

S/N	Reaction	Equation
1	Rate of consumption of glucose	$-r_5 = \frac{1}{Y_{E_{g/G}}}\frac{dC_{E_g}}{dt} = \frac{1}{Y_{X_{g/G}}}\frac{dC_{X_g}}{dt} + M_g C_{X_g}$
2	Rate of consumption of xylose	$-r_6 = \frac{1}{Y_{E_{x/X}}}\frac{dC_{E_x}}{dt} = \frac{1}{Y_{X_{x/X}}}\frac{dC_{X_x}}{dt} + M_x C_{X_x}$
3	Cell growth rate on glucose	$r_8 = \frac{dC_{X_g}}{dt} = \frac{\mu_{M,g} C_g}{K_{8g} + C_g + \frac{C^2{}_g}{K_{8Igg}}}\left[1 - \left(\frac{C_{E_g}}{E_{Mg}}\right)^{\alpha_g}\right]$
4	Cell growth rate on xylose	$r_9 = \frac{dC_{X_x}}{dt} = \frac{\mu_{M,x} C_X}{K_{9x} + C_X + \frac{C^2{}_X}{K_{9Igx}}}\left[1 - \left(\frac{C_{E_x}}{E_{Mx}}\right)^{\alpha_x}\right]$
5	Rate of formation of ethanol from glucose	$r_{10} = \frac{1}{C_{xg}}\frac{dC_{E_g}}{dt} = \frac{v_{M,g} C_g}{k_{10g} + C_g + \frac{C^2{}_g}{k_{10Igg}}}\left[1 - \left(\frac{C_{E_g}}{E'_{Mg}}\right)^{\beta_g}\right]$
6	Rate of formation of ethanol from xylose	$r_{11} = \frac{1}{C_{xx}}\frac{dC_{E_x}}{dt} = \frac{v_{M,x} C_X}{k_{11x} + C_X + \frac{C^2{}_X}{k_{11Igx}}}\left[1 - \left(\frac{C_{E_x}}{E'_{Mx}}\right)^{\beta_x}\right]$
7	Total ethanol production rate	$r_{12} = \frac{dC_{Et}}{dt} = r_{10} + r_{11}$

2.2 Method

Two case studies were considered in this study:

1. Investigation of the effects of alkaline loading and temperature on delignification
2. Determination of the optimal process conditions for the SSCF unit.

The choice of feedstock has a major impact on the final product because it is the amount of sugars extracted that will be converted to ethanol. Consequently, three feedstocks (bamboo, wheat straw and sorghum) are investigated using the alkaline pretreatment process in the first case study. This will be based on the maximum amount of lignin that can be removed from the feedstock by varying alkaline loading ranging from 0% to 1.5% (w/v) and temperatures of 121°C, 125°C, and 131°C. The literature indicates that lignin is an undesirable compound in the hydrolysis/fermentation process (Alvira et al., 2010). Hence, the best feedstock can be established by the least amount of lignin and maximum amount of sugars after pretreatment.

It should be noted that no bamboo plantation has yet been established in Nigeria (Ladapo et al, 2017). As a result, its production volume remains relatively low. Wheat straw and sorghum, both of which are relatively abundant in Nigeria, are potential feedstocks for the bio-based economy (Ben-Iwo et al., 2016).

It has also been reported in literature (Byadgi, 2016) that alkali pretreatment has a major impact on the final composition of lignin, cellulose and hemicellulose. It is identified as causing less sugar degradation than acid pre-treatment and is more effective on agricultural residues than wood materials. Thus, owing to the improbability of designing models for alkaline pretreatment, a preliminary model (Prathyusha et al., 2016) is used to determine the extent of lignification under a range of process conditions (alkaline loading and temperature). This is given by the following equation (Prathyusha et al., 2016):(

$$X_d = X_d^{max}\,(1 - \exp(-(k_{d1}A + k_{d2}))) \qquad (1)$$

or

$$\frac{X_d}{X_d^{max}} = (1 - \exp(-(k_{d1}A + k_{d2}))) \qquad (2)$$

The equation structure was chosen such that X_d approaches a limiting value at higher alkaline loading and the nonlinear dependency of X_d on alkaline concentration can be captured. The other two parameters were then linearly correlated in terms of the temperature as:

$$k_{d1} = \beta_{11} + \beta_{12}T \qquad (3)$$

$$k_{d2} = \beta_{21} + \beta_{22}T \qquad (4)$$

Experiments were carried by Prathyusha et al. (2016) to obtain the regression model parameters (β_{11}, β_{12}, β_{21}, β_{22}) shown in Table 5.

Table 5 Kinetic parameters for the delignification model (Prathyusha et al., 2016)

Feedstock	**β_{11}**	**β_{12}**	**β_{21}**	**β_{22}**
Bamboo	-6.67411	0.06074	-3.018595	0.0215143
Wheat Straw	-24.4093	11.01869	0.21921	-0.097147
Sorghum	-4.63015	0.05156	2.05135	-0.214534

For the second scenario, The SSCF unit is simulated under high and low ranges of variables that influence the hydrolysis and fermentation. These variables include temperature, time, enzyme loading, yeast loading and substrate loading.

Kadam et al. (2004) estimated model parameters in Matlab using the "Isqnonlin" function. Parameters from other works are also presented for comparison. Camara et al. (2015) modified the model to include the conversion of hemicellulose to xylose sugars as well as the cellobiase and -glucosidase activities as a single activity. The extents of inhibition by the major product in each reaction are stated to be greater than the extents of inhibition by the other products from that same reaction. On the other hand, Khodaverdi et al. (2011) did not include xylose inhibition or enzyme adsorption on lignin (because cotton was used as a substrate). The extension of the original model by Zheng et al. (2009) accounted for the adsorption of enzymes onto lignin. But none of these research works – (Zheng et al., 2009; Khodaverdi et al., 2012) – included conversion of hemicellulose to xylose sugars and as such, it can be expected that the parameters might have a bit of difference from the original model. If model structures are different, it is possible for the reaction schemes to be divergent and this results in difference in parameter values. Experimental conditions also have an impact in determining parameter values so the difference is expected.

Optimization is carried out to determine best process conditions for the SSCF unit. The general form of single-objective optimization obtained in literature is given as:

Objective (to be minimized/ maximized):

$$f(x_i);\ i=1, 2\ldots, j \tag{5}$$

Constraints (to confine the results):

$$g_m(\mathbf{x}) \geq 0;\ m=1, 2\ldots, m \tag{6}$$

$$h_k(\mathbf{x}) = 0;\ k=1, 2\ldots, k \tag{7}$$

Decision variables:

$$\text{Lower bound} \leq x_i \leq \text{Upper bound};\ i=1, 2\ldots, j \tag{8}$$

To achieve optimum operation of the SSCF process, the hydrolysis and fermentation operation must be balanced; this means that finding the conditions under which both processes would occur simultaneously is a top priority. From a model assessment, it can be seen that cellulose conversion, hemicellulose conversion, bioethanol yield and enzyme consumption are main parameters of the SSCF unit (Duque-escobar, 2011; Shadbahr, 2017).

$$\text{Cellulose Conversion: } A = \frac{[C_c]_o - [C_c]_f}{[C_c]_o} \times 100\% \tag{9}$$

Ethanol yield:

$$B = \frac{C_{Et}}{0.511\ (C_{g0} + C_{x0} + (1.111 \times C_{c0}))} \times 100\% \tag{10}$$

Enzyme consumption per 1g/L ethanol produced:

$$C = \frac{C_E}{C_{Et}} \tag{11}$$

where $[C_c]_o$ indicates initial cellulose concentration (g/kg), $[C_c]_f$ the final cellulose concentration (g/kg), C_{Et} the ethanol concentration (g/kg), C_{g0} the initial glucose concentration (g/kg), C_{x0} the initial xylose concentration (g/kg) and C_E the enzyme concentration (g/kg).

To further understand how major parameters influence the SSCF process, six factors are defined in the analysis of variance: *cellulose loading (A), hemicellulose loading (B), Enzyme loading (C), yeast loading (D), temperature (E) and time(F),* The response is bioethanol concentration. The Box-Behnken experimental design method is employed to avoid extreme treatment combinations, and it produced a total of 54 experimental simulation runs. Numerical optimization is also used to determine the optimal conditions for producing maximum ethanol yield.

2.3 Analysis, Simulation and Optimization Platforms

2.3.1.Design of Experiment platform

The design of experiment simulation runs for the SSCF and the pretreatment processes are carried out in the free and open-source R software (Ferreira et al, 2014). It is the only open-source software (together with Python) that combines the full range of DoE and optimization with the flexibility of a sophisticated script language that enables any type of data pre-processing and post-processing within a single software environment. That makes R better to many commercial GUI-based applications, which frequently sacrifice flexibility for user-friendliness.

2.3.2. Simulation platform
The SSCF unit operation is simulated using the object-oriented Scilab platform. Scilab is a free open-source software written in a set of high level numerically aligned programming languages (C, C++, Java, Fortran). Scilab is one of the two major open-source software alternatives to MATLAB, the other being GNU Octave. They are quite similar; the only difference is the syntactic compatibility with MATLAB and Scilab appears to be preferable (Mittal and Singh, 2013).

2.3.3. Optimization platform
Following the analysis of the bioethanol process's behavior, the optimal conditions are determined using a single objective optimization on key operation parameters. A batch reactor is used to run the process under different conditions/variables (time, substrate loading, enzyme adsorption, temperature and cell dry mass) which are reported in the open literature (Morales-Rodriguez, 2011). It is a dynamic optimization problem because the major factors change over time. In this run, the differential equations established in the mathematical model that depicts hydrolysis and fermentation are applied. The APMonitor modelling language is the modelling structure adapted for the ODEs and built in the open-source Python software because it is suited for optimizing differential algebraic equations. The IPOPT (interior point optimizer) and APOPT (advanced process optimizer) solvers are used to solve the problems of minimizing enzyme adsorption per substrate loading, optimizing cellulose conversion, and maximizing ethanol yield.

2.4 Data
The parameters of the models were obtained from pilot studies that developed and validated them. The preliminary model for Case study I is tested and validated by Prathyusha et al. (2016). Since the pre-treatment unit is the major focus of Case study I, the range of process conditions for simulation are collected from the preliminary study by Prathyusha et al (2016).

The parameters in the hydrolysis for Case study II are based on those reported by Camara et. al (2015). The process conditions (Morales-Rodriguez, 2011) are presented in Table 6. Under these conditions, the density of the mixture is taken to be 1kg/L, so that both saccharification and co-fermentation models can be integrated. This is because the concentration of sugars in the model is measured in g/g and ethanol concentration in g/L. Hence, the concentration of sugars has to be converted to g/L to ensure dimensional consistency. It was noted earlier that the improbability of the pretreatment model for Case study II makes it difficult to simulate the pretreatment process in relation to the subsequent steps i.e., hydrolysis and fermentation. Therefore, experimental results from previous studies will be used to determine the input conditions in the SSCF unit (cellulose loading, hemicellulose loading, amount of solids, etc.).

Table 6 Process conditions for the SSCF unit (Morales-Rodriguez, 2011)

Process parameters	**Value**
Initial substrate concentration (g/kg)	100
Initial cellulose loading (g/kg)	44.5
Initial hemicellulose loading (g/kg)	9.9
Enzyme loading (g/kg)	0.005 – 0.021
Yeast loading (g/kg)	0.016
Density of mixture (kg/L)	1.0
Microorganism	*Saccharomyces cerevisiae*
Temperature (K)	310 – 328
Reactor type	Batch
Feedstock	Corn stover
Operating time (h)	120

2.5 Flowcharts and Codes

Appendix A presents the flowcharts and sample codes for the simulation, analysis and optimization studies reported in this paper.

3. RESULTS AND DISCUSSION

3.1 Simulation results for the Pretreatment unit

The results for the effects of parameters on delignification for all three feedstocks are illustrated in Figure 2. The plots show that the extent of delignification increases with alkaline loading (%). This is consistent with the literature, which specifies that disrupting lignin-cellulose-hemicellulose interactions necessitates the use of more pre-treatment agents (sodium hydroxide in this case). Furthermore, the extent of delignification is greatest in sorghum and least in bamboo. This is most likely because of the physical structure of these feedstocks. A maximum of 99.1% sorghum delignification for 1.5% alkaline loading at 130°C is achieved. Figure 2 indicates that some of the measurements (e.g., sorghum at 130°C and 0.2% alkaline loading, and wheat straw at 121°C and 0.2% alkaline loading). does not follow the trend shown in other measurements, and this is due to the insignificant effect of low alkaline loading cases at the selected temperatures. It is critical to use minimal alkaline loading while also maximizing delignification when calculating the best conditions. Wheat straw generally exhibited a better trend because its minimum alkaline loading is 0.4%, resulting in higher output as temperature rises. Temperature has also been found to have a similar effect on increasing alkaline loading. These results show that delignification is at its peak when alkaline loading and temperature are at their highest, and these values must be carefully chosen to strike a balance between economics and performance.

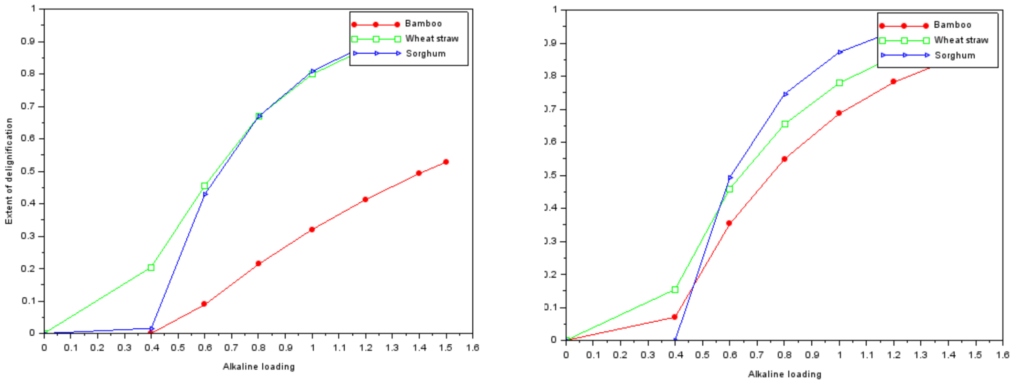

(a) 121°C (b) 125°C

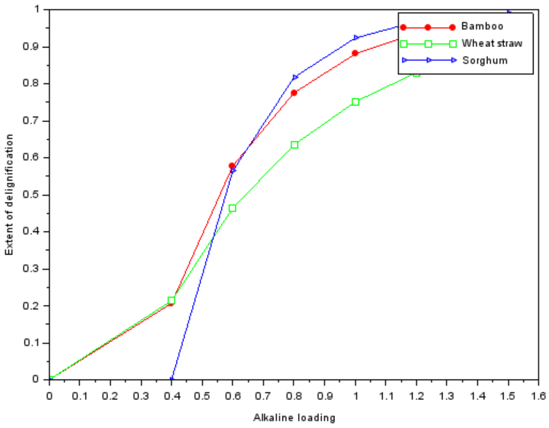

(c) 130°C

Figure 2 Effects of alkaline loading and temperature on extent of delignification for bamboo, wheat straw and sorghum

3.2 Simulation results for the SSCF unit operation

The simulation is run to determine the response of the hydrolysis and co-fermentation models to various modified input factors and to draw out observations about the SSCF process. Input factors that can be changed include enzyme loading, temperature, yeast loading, substrate loading and time. Camara et al. (2015) reported the model parameters used for the hydrolysis phase, while Krishnan et al. (1999) reported the model parameters for the co-fermentation part, which are listed in the nomenclature section.

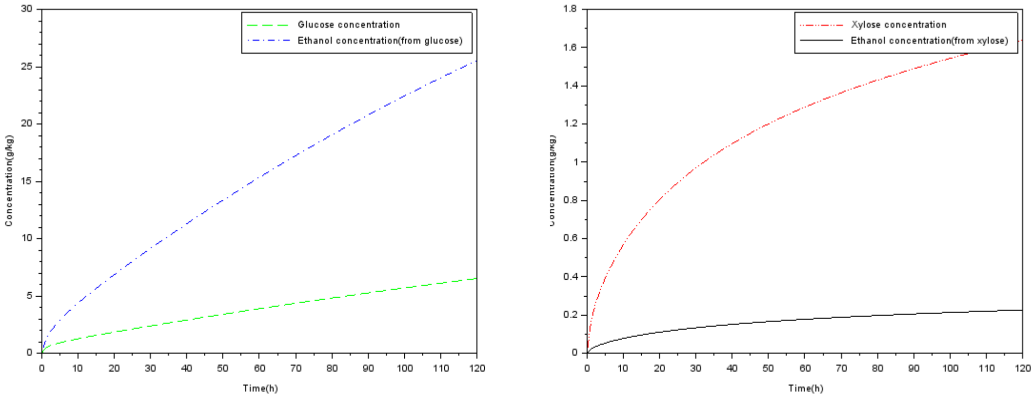

(a) Glucose and bioethanol at low enzyme loading

(b) Xylose and bioethanol at low enzyme loading

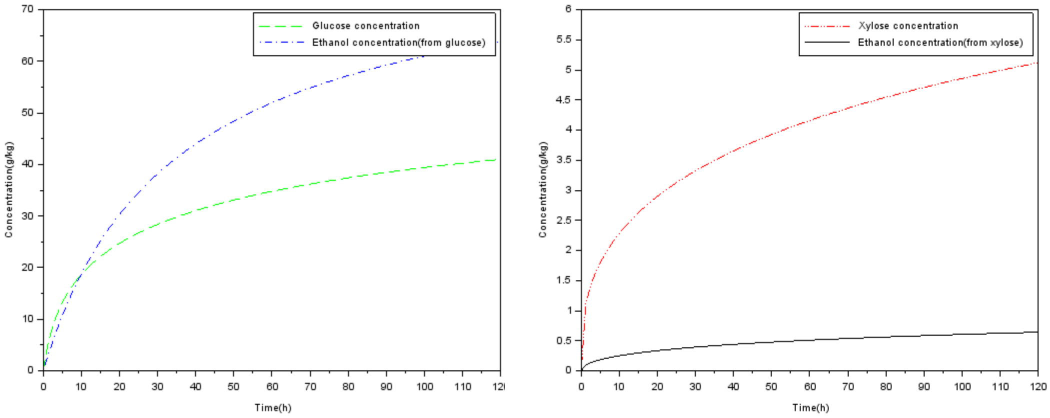

(c) Glucose and bioethanol at high enzyme loading

(d) Xylose and bioethanol at high enzyme loading

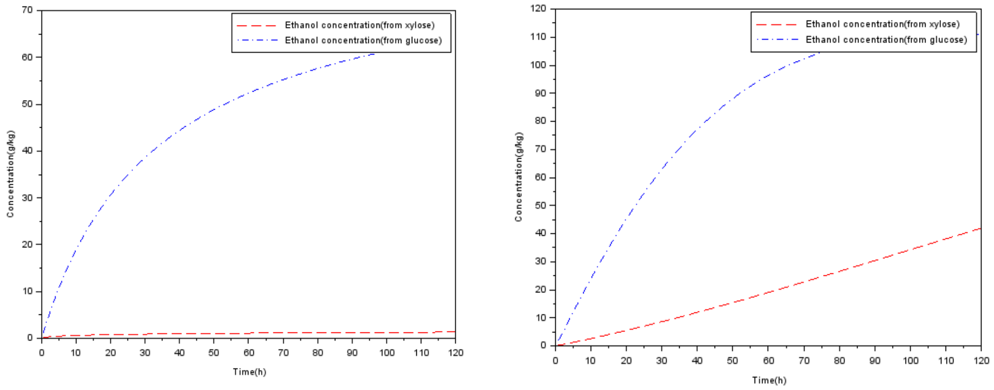

(e) Bioethanol at low yeast loading

(f) Bioethanol at high yeast loading

Figure 3 Concentration profiles in the SSCF unit for glucose, xylose, bioethanol at high and low range of manipulated variables

Figures 3 and 4 show the simulated bioethanol concentration patterns from glucose and xylose at low and high ranges of control variables. Generally, the results show a good agreement with earlier reported experimental research results for ethanol from glucose and xylose (Morales-Rodriguez, 2011; Shadbahr, 2017; Kadam et al., 2004; Krishnan, 1999). An increase in enzyme loading, yeast loading, substrate loading, and temperature, results in a rise in bioethanol concentration. In each case, glucose and xylose were swiftly converted to ethanol, resulting in a significant reduction in glucose and xylose concentrations. Cellobiose, an intermediate product, surged rapidly in the first two hours and then steadily fell.

Higher enzyme loading generally improves cellulose conversion. Higher glucose and cellobiose concentrations, on the other hand, may cause osmotic stress in the yeast (due to a sudden change in solute concentration causing a rapid change in the movement of water across its cell membrane) and affect its fermentation performance, resulting in a reduction in the amount of bioethanol produced. As a result, the amount of enzyme to be used should be selected strategically.

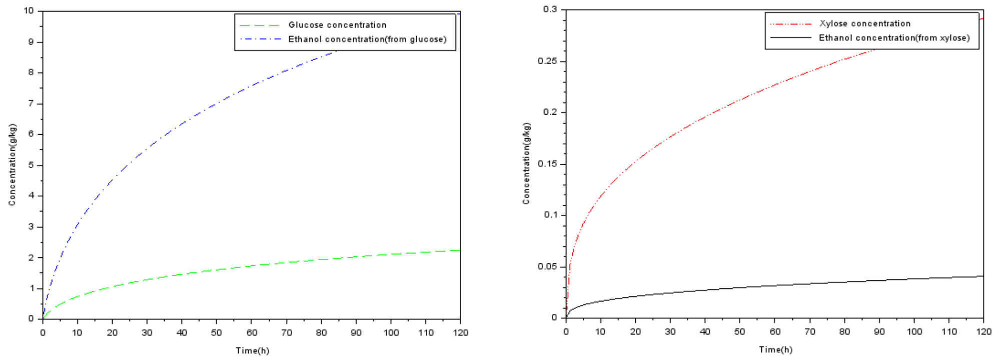

(g) Glucose and bioethanol at low substrate loading

(h) Xylose and bioethanol at low substrate loading

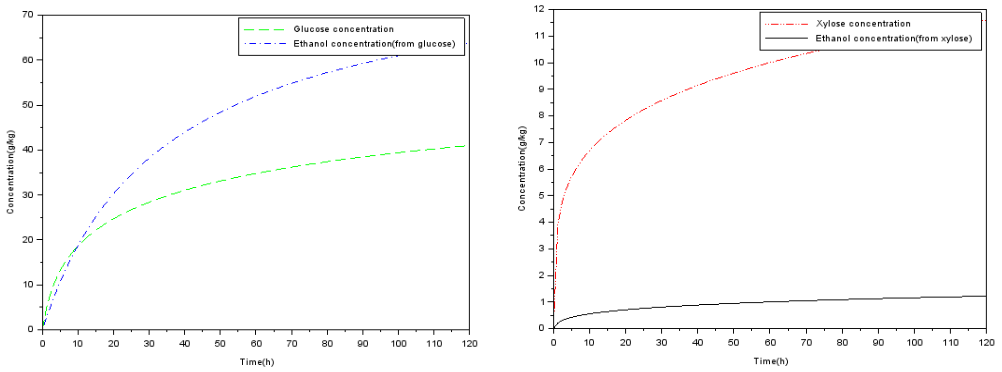

(i) Glucose and bioethanol at high substrate loading

(j) Xylose and bioethanol at high substrate loading

Figure 4 Concentration profiles in the SSCF unit for glucose, xylose, bioethanol and enzyme at high and low range of manipulated variables

To further understand how the major parameters influence the SSCF process an analysis of variance was carried out with the results presented in Table 7. These show that A (cellulose loading), C (enzyme loading), F (time), AF, A^2, C^2, F^2 are significant model terms ($p < 0.01$). It is also clear that the FO (first order) and PQ (pure quadratic) terms contribute significantly to the model. The 3D response surface plots are shown in Figures 5 and 6. The Predicted R^2 of 0.9128 is in reasonable agreement with the Adjusted R^2 of 0.9660.

Table 7 Analysis of variance of the SSCF model

	Estimate	Std. Error	t value	p value
Intercept	4.088e+01	1.3644e+00	29.9613	< 2.2e-16
A (cellulose loading)	2.0167e+01	6.8221e-01	29.5619	<2.2e-16
B (hemicellulose loading)	3.7917e-01	6.8221e-01	0.5558	0.58311
C (enzyme loading)	4.5529e+00	6.8221e-01	6.6737	4.431e-07
D (yeast loading)	-3.9708e-01	6.8221e-01	-0.5821	0.56555
E (temperature)	1.3521e+00	6.8221e-01	1.9819	0.05815
F (time)	1.4114e+01	6.8221e-01	20.6882	< 2.2e-16
AB	-1.750e+01	1.1816e+00	-0.1481	0.88341
AC	9.8705e-02	1.1816e+00	0.0836	0.93404
AF	-1.0250e-01	1.1816e+00	7.6896	3.685e-08
BE	-3.625e-02	8.3554e-01	0.1058	0.96572
BF	5.0000e-02	1.1816e+00	-0.0423	0.96657
CE	-1.2725e+00	1.1816e+00	-1.0769	0.29141
CF	3.7188e-01	8.3554e-01	0.4451	0.65995
DE	-1.0663e+00	1.1816e+00	-0.9024	0.37515
DF	-1.2891e-15	1.1816e+00	0.0000	1.00000
EF	-8.2500e-02	1.1816e+00	-0.0698	0.94487
A^2	-6.7282e+00	1.0421e+00	-6.4564	7.666e-07
B^2	-6.7282e+00	1.0421e+00	-1.101	0.28098
C^2	-4.8690e+00	1.0421e+00	-4.6723	7.982e-05
D^2	-1.1494e+00	1.0421e+00	-1.1030	0.28013
E^2	-2.1611e-01	1.0421e+00	-0.2074	0.83733
F^2	-6.5240e+00	1.0421e+00	-6.2605	1.262e-06

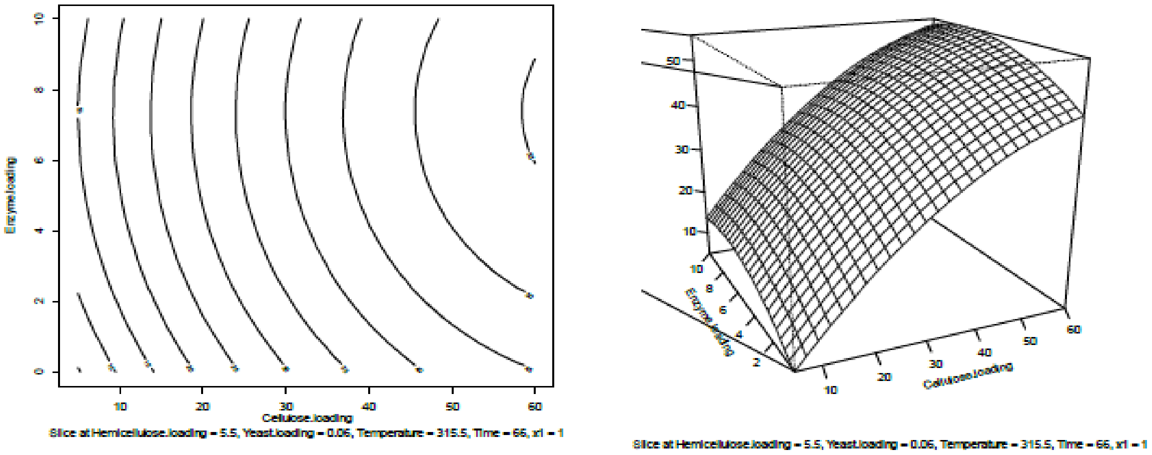

Figure 5: 3D surface plot of cellulose loading and enzyme loading with bioethanol concentration

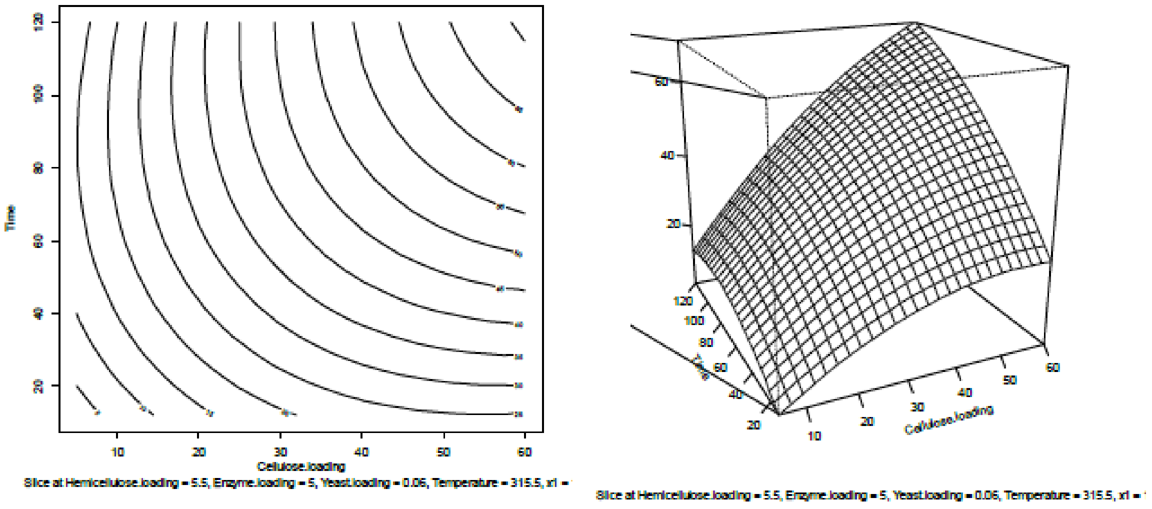

Figure 6: **3D surface plot of cellulose loading and time with bioethanol concentration**

The final product (bioethanol) also has an inhibitory effect on the synthesis of sugars (i.e., xylose and glucose). The inhibition coefficient determined by Philippidis et al. (1993) is incorporated into the model, revealing that the inhibition coefficient of ethanol on cellulose is approximately ten times greater than that of cellobiose on cellulose conversion. So, in the model developed by Kadam et al. (2004), the inhibition coefficient of cellobiose is multiplied by 10 to obtain the inhibition coefficient of ethanol on cellulose. Figure 7 depicts the model's performance with and without the inhibitory impact of ethanol on polysaccharides and sugars.

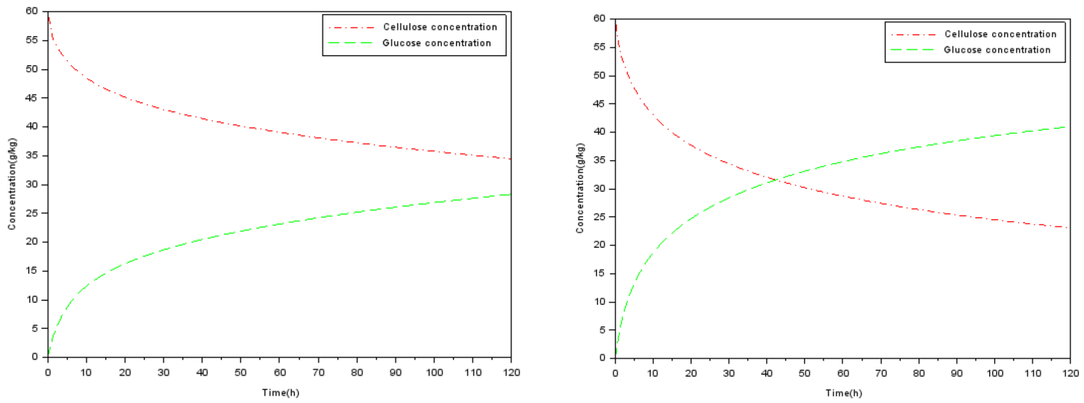

(a) With end product inhibition on glucose formation

(b) Without end product inhibition on glucose formation

Figure 7 **End product (bioethanol) inhibition effect on glucose formation**

3.3 Optimization results

Figure 8 presents the solutions to the aforementioned optimization problems. The minimal amount of enzyme adsorbed per substrate loading is determined to be 0.1263kg/kg. The largest cellulose conversion achievable is 26.26%. The largest total ethanol yield achieved is 47.9%, which is approximately 94% of the theoretical value. This gives better results than Krishnan et al. (1999) (47% yield) and Morales-Rodriguez (1999) (43% yield).

Numerical optimization of the delignification model parameters determined that the best parameters for a 61% delignification are 0.799% alkaline loading and 121°C.

Numerical optimization of the SSCF parameters also reveals that for a minimal cellulose loading of 28.13g/kg, a minimal hemicellulose loading of 1.0g/kg, a minimal enzyme loading of 0.4g/kg, a minimal yeast loading of 0.01g/kg, 327.99K temperature, and 46.29 hrs., a maximum ethanol concentration of 24.79g/L is achieved (assuming the density of the mixture is 1g/L).

3.4. Discussion

Two case studies were considered in this study to get a thorough understanding of the bioethanol production process, with a particular emphasis on pretreatment and simultaneous saccharification and co-fermentation (SSCF) activities. The first case study looked at how alkaline loading and temperature affected the delignification of three different feedstocks: bamboo, wheat straw, and sorghum. The other case study used input factors such as temperature, enzyme loading, substrate loading, and yeast loading to study the response of the SSCF operation.

On the report of the first case study's findings, increasing alkaline loading and temperature causes an increase in delignification in the pretreatment unit. At 1.5% alkaline loading and 130°C, maximum delignification is achieved. However, when deciding on these parameters, economics and performance must be considered.

In simulating the SSCF operation, hemicellulose decomposition to xylose is integrated in the mathematical models by Camara et al. (2015) and Krishnan et al. (1999). When using 0.1g/kg enzyme loading, increasing the substrate concentration from 5g/kg cellulose and 1g/kg hemicellulose to 60g/kg cellulose and 20g/kg hemicellulose resulted in a greater ethanol concentration. Furthermore, higher enzyme loading (10g protein/kg solids) enhanced ethanol concentration, but not as much as high yeast loading (0.1g protein/kg solids). As the temperature rose, so did the amount of enzyme adsorbed. However, it is important to note that saccharomyces cerevisiae is only efficient between 30°C and 50°C. Extreme heat can kill the microorganisms and ultimately destroy the bio-reactor. As a result, an appropriate operating temperature must be chosen.

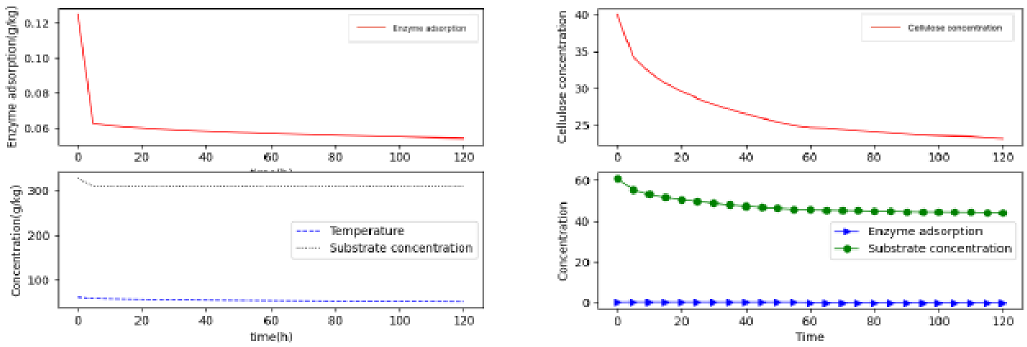

(a) minimizing enzyme adsorption per substrate loading

(b) Maximizing cellulose conversion

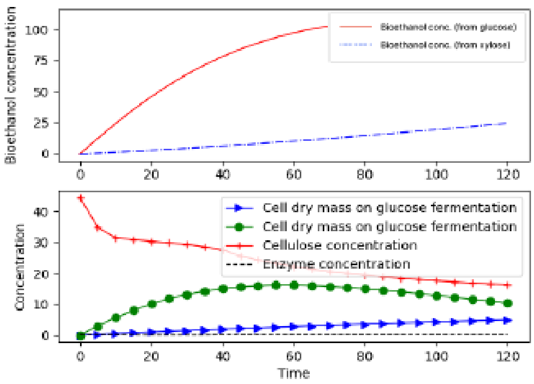

(a) Maximizing ethanol yield

Figure 8 Single objective optimization of major parameters in the SSCF unit

The solutions for minimizing enzyme adsorption per substrate loading, maximizing cellulose conversion, and maximizing ethanol output are shown in Figure 8. As predicted, the decision variables have a large impact on the objective functions. Only by deliberately optimizing the enzyme loading can ethanol yield be optimized in the case of increased cellulose conversion. The results also show that a high substrate loading is useful to achieving a high ethanol yield while using a tolerable enzyme loading. Finally, the maximum ethanol production obtained is almost 94% of the theoretical value, outperforming prior reported results e.g. (Krishnan, 1999; Morales-Rodriguez, 2011).

5. CONCLUSION

The modified SSCF model is simulated using the data from Morales-Rodriguez (2011) in a batch reactor. Results show that increase in enzyme loading, substrate loading, yeast loading and temperature results in an increase in ethanol concentration. It is also seen that cellulose loading, enzyme loading and time have the most significant influence on the simultaneous saccharification and co-fermentation process and alkaline loading has the greatest influence on the delignification process (based on the DoE results). Finally, the SSCF unit parameters are optimized to provide a minimum enzyme amount adsorbed of 0.1263 kg/kg substrate loading, a maximum cellulose conversion of 26.26%, and a maximum ethanol yield of 47.9%. The ideal conditions for an optimum delignification of 61% are 0.799% alkaline loading and 121℃ and the ideal conditions for the optimum bioethanol yield of 24.79g/L are 28.13g/kg, 1.0g/kg, 0.4g/kg, 0.01g/kg, 327.99K and 46.29hrs for cellulose loading(A), hemicellulose loading(B), enzyme loading (C), yeast loading (D), temperature (E) and time (F), respectively. These findings show that these models can appropriately explain a wide range of simultaneous saccharification and co-fermentation systems and so they will be powerful tools for process design, optimization and scale-up of bioethanol production, including the identification of the parameters that have a significant impact on the performance of the SSCF process.

6. NOMENCLATURE

A	Alkaline loading, %
[CE]	bound concentration of enzymes unto glucose, g/kg
[CH]	bound concentration of enzymes unto hemicellulose, g/kg
C_c	substrate (cellulose) concentration, g/kg
C_{cb}	concentration of cellobiose, g/kg
C_E	concentration of enzymes, g/kg
C_{E_g}	ethanol concentration from glucose fermentation, g/L
C_{Et}	concentration of ethanol, g/L
C_{E_x}	ethanol concentration from xylose fermentation, g/L
C_g	concentration of glucose, g/kg
C_H	hemicellulose concentration, g/kg
C_s	concentration of solids, g/kg
C_X	concentration of xylose, g/kg
C_{X_g}	cell dry mass in glucose fermentation, g/L
C_{X_x}	cell dry mass in xylose fermentation, g/L
E_{ad}	bound concentration of enzymes onto solids, g/kg
E_{ia}	activation energy, -5540 cal/mol
E_{imax}	maximum mass of enzyme that can adsorb onto a unit mass of substrate (g protein/g cellulose), 0.026g/g
E_{Mg}	ethanol concentration above which cells do not produce ethanol in glucose fermentation, (103 for $C_{Et} \leq 103$ g/L; 136.40 for $103 < C_{Et} \leq 136.4$ g/L)
E_{Mx}	ethanol concentration above which cells do not produce ethanol in xylose fermentation, 60.2g/L
E_T	total concentration of enzymes (g/kg)
K_{3C}	cellobiose saturation constant, 24.5 g/kg
K_{8g}	Monod constant for growth on glucose in reaction 8, 1.342 g/L
K_{8Igg}	inhibition constant for growth of glucose in reaction 8, 283.7 g/L
K_{9x}	Monod constant for growth on xylose in reaction 9, 3.4g/L
K_{9Igx}	inhibition constant for growth of xylose in reaction 9, 18.1 g/L
K_{ia}	dissociation constant for adsorption/desorption reaction with solids (g/g-protein), 8.577g/g
$K_{1IC_{cb}}$	inhibition constant for cellobiose 1, 0.015 g/kg
$K_{2IC_{cb}}$	inhibition constant for cellobiose 2, 9.83 g/kg
K_{1IC_g}	inhibition constant for glucose 1, 0.15 g/kg
K_{2IC_g}	inhibition constant for glucose 2, 0.176 g/kg
K_{3IC_g}	inhibition constant for glucose 3, 41.75 g/kg
K_{4IC_g}	inhibition constant for glucose 4, 0.023 g/kg
K_{1IC_X}	inhibition constant for xylose 1, 8.79 g/kg

K_{2IC_X}	inhibition constant for xylose 2, 9.54 g/kg
K_{4IC_X}	inhibition constant for xylose 4, 9.81 g/kg
K_{1IC_X}	inhibition constant for xylose 1, 8.79 g/kg
k_1	reaction rate constant for reaction 1, 3.17 g/mg.h
k_2	reaction rate constant for reaction 2, 0.265 g/mg.h
k_3	reaction rate constant for reaction 3, 254.5 h^{-1}
k_4	reaction rate constant for reaction 4, 57.79 g/mg.h
k_{10g}	Monod constant for product formation from glucose in reaction 10, 0.565 g/L
k_{10Igg}	Inhibition constant for product formation from glucose in reaction 10, 4890 g/L
k_{11x}	Monod constant for product formation from xylose in reaction 11, 3.4 g/L
k_{11Igx}	Inhibition constant for product formation from xylose in reaction 11, 81.3 g/L
M_g	maintenance constant in glucose fermentation, 0.097 h^{-1}
M_x	maintenance constant in xylose fermentation, 0.067 h^{-1}
R	Universal gas constant, 1.9872 cal/mol.K
R_s	substrate reactivity parameter, 1
r_i	reaction rate for reaction i (i = 1,2,3,4…), g/kg.h
S_0	initial substrate concentration, g/kg
T	temperature, K
t	time, h
X_d	extent of delignification
X_d^{max}	maximum extent of delignification
$Y_{E_g/G}$	product yield constant (ethanol/glucose), 0.47 g/g
$Y_{E_x/X}$	product yield constant (ethanol/xylose), 0.4 g/g
$Y_{X_g/G}$	cell yield constant from glucose (cells/substrate), 0.115 g/g
$Y_{X_x/X}$	cell yield constant from xylose (cells/substrate), 0.162 g/g
α_g	constant in product inhibition model in glucose fermentation, 1.29 for Et ≤ 95.4 g/L, 0.25 for 95.4 < Et ≤ 129.9 g/L
α_x	constant in product inhibition model in xylose fermentation, 1.036 g/L
β_g	maximum specific rate of glucose formation, 1.42 for Et ≤ 95.4 g/L
β_x	maximum specific rate of xylose formation, 0.608 g/L
$\mu_{M,g}$	maximum specific growth rate in glucose fermentation, 0.662 h^{-1}
$\mu_{M,x}$	maximum specific growth rate in xylose fermentation, 0.190 h^{-1}
$v_{M,g}$	maximum specific rate of glucose formation, 2.005 h^{-1}
$v_{M,x}$	maximum specific rate of glucose formation, 0.250 h^{-1}

7. REFERENCES

Adesina A.A. (2019). Making the Case for Agro-Based Energy Development: A National Priority for Sustainable Energy. Lagos, s.n., p. 7.

Alvira, P., Tomás-Pejó, E., Ballesteros, M., & Negro, M. J. (2010). Pretreatment technologies for an efficient bioethanol production process based on enzymatic hydrolysis: A review., s.l.: Bioresource Technology, 101(13), 4851–4861.

Anwar Z., Gulfraz, M., & Irshad, M. (2014). Agro-industrial lignocellulosic biomass a key to unlock the future bio-energy: A brief review, s.l.: Journal of Radiation Research and Applied Sciences, 7(2), 163– 173.

Ben-Iwo, J., Manovic, V., & Longhurst, P. (2016). Biomass resources and biofuels potential for the production of transportation fuels in Nigeria. Renewable and Sustainable Energy Reviews, 63, 172–192.

Byadgi, S. A., & Kalburgi, P. B. (2016). Production of Bioethanol from Waste Newspaper. Procedia Environmental Sciences, 35, 555–562.

Camara, M. (2015). Kinetic Modeling and Simulation for the Enzymatic Hydrolysis of Sugarcane Bagasse Pretreated by Alkaline Hydrogen Peroxide,

Duque-escobar, P. G. (2011). Modeling and Optimization of a Bioethanol Production Facility. Master's thesis, Texas A&M University.

Ferreira, Eric & Cavalcanti, Pórtya & Nogueira, Denismar. (2014). ExpDes: an R package for ANOVA and experimental designs. Applied Mathematics. 5. 2952-2958. 10.4236/am.2014.519280.

Kadam, K. L., Rydholm, E. C., & McMillan, J. D. (2004). Development and validation of a kinetic model for enzymatic saccharification of lignocellulosic biomass. Biotechnology Progress, 20(3), 698–705.

Khodaverdi, M., Karimi, K., Jeihanipour, A., & Taherzadeh, M. J. (2012). Kinetic modeling of rapid enzymatic hydrolysis of crystalline cellulose after pretreatment by NMMO. Journal of Industrial Microbiology and Biotechnology, 39(3), 429-438.

Krishnan, M. S., Ho, N. W. Y., & Tsao, G. T. (1999). Fermentation kinetics of ethanol production from glucose and xylose by recombinant Saccharomyces 1400(pLNH33). Applied Biochemistry and Biotechnology - Part A Enzyme Engineering and Biotechnology, 77–79, 373–388.

Mittal, P., & Singh, J. 2013. Use of open source software in engineering. International Journal of Advanced Research in Computer Engineering & Technology, 2(3), 1114–1117.

Morales-Rodriguez, R., Gernaey, K. V., Meyer, A. S., & Sin, G. (2011). A Mathematical model for simultaneous saccharification and co-fermentation (SSCF) of C6 and C5 sugars. Chinese Journal of Chemical Engineering, 19(2), 185–191.

National Intelligence Council (US) (Ed.). (2012). Global Trends 2030: Alternative Worlds: a Publication of the National Intelligence Council. US Government Printing Office.

Philippidis, G. P., Smith, T. K., & Wyman, C. E. (1993). Study of the enzymatic hydrolysis of cellulose for production of fuel ethanol by the simultaneous saccharification and fermentation process. Biotechnology and bioengineering, 41(9), 846-853.

Prathyusha, N., Kamesh, R., Rani, K. Y., Sumana, C., Sridhar, S., Prakasham, R. S., Yashwanth, V. V. N., Sheelu, G., & Kumar, M. P. (2016). Modelling of pretreatment and saccharification with different feedstocks and kinetic modeling of sorghum saccharification, s.l.: Bioresource Technology, 221, 550–559.

Shadbahr, J. (2017). Modeling, optimization, and life cycle assessment of bioethanol production (Doctoral dissertation, Memorial University of Newfoundland).

Ladapo, H. L., Oyegoke, O. O., & Bello, R. O. (2017). Utilization of vast Nigeria’s bamboo resources for economic growth: A review. Journal of Research in Forestry, Wildlife and Environment, 9(2), 29-35.

Zhao, L., Zhang, X., Xu, J., Ou, X., Chang, S., & Wu, M. (2015). Techno-economic analysis of bioethanol production from lignocellulosic biomass in China: Dilute-acid pretreatment and enzymatic hydrolysis of corn stover., s.l.: Energies, 8(5), 4096–4117.

Zheng, Y., Pan, Z., Zhang, R., & Jenkins, B. M. (2009). Kinetic modeling for enzymatic hydrolysis of pretreated creeping wild ryegrass. Biotechnology and Bioengineering, 102(6), 1558–1569.

APPENDIX A

A.1 Simulation Flowchart

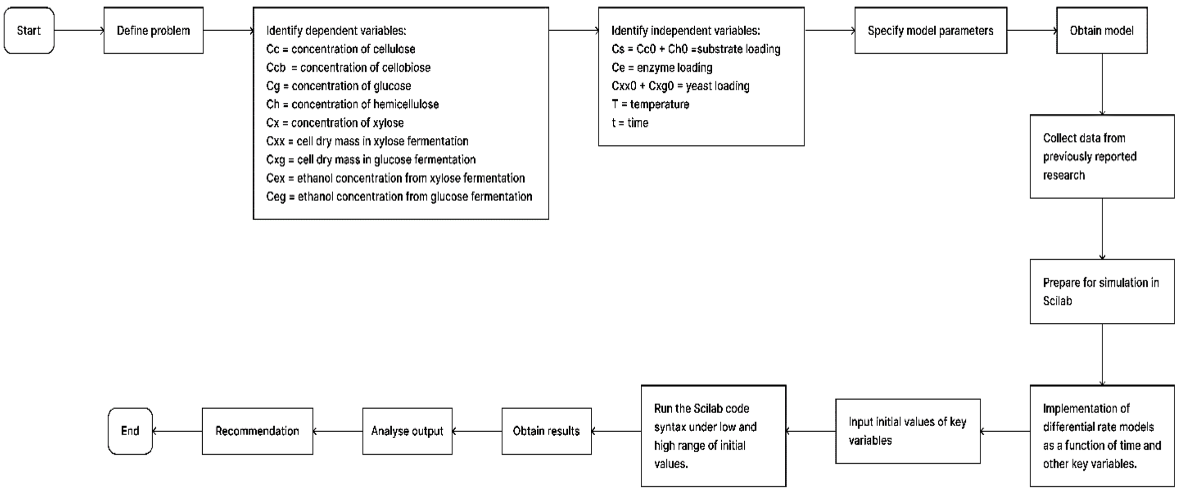

A.2 Design of Experiment Flowchart

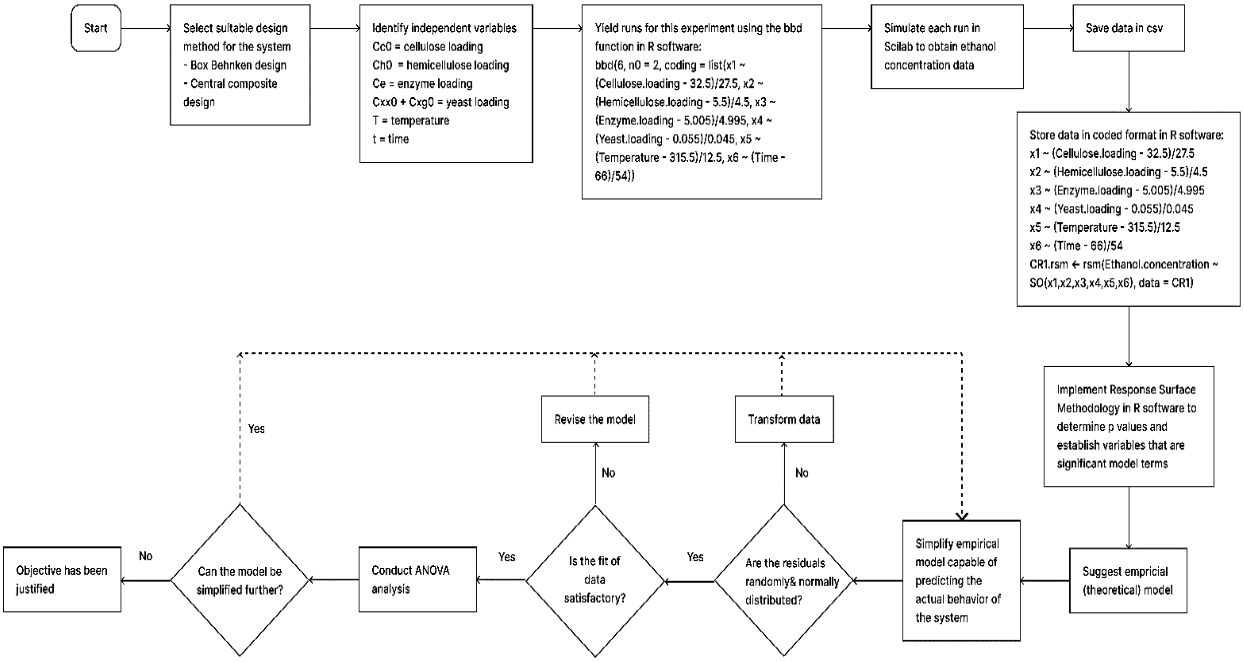

A.3 Optimization Flowchart

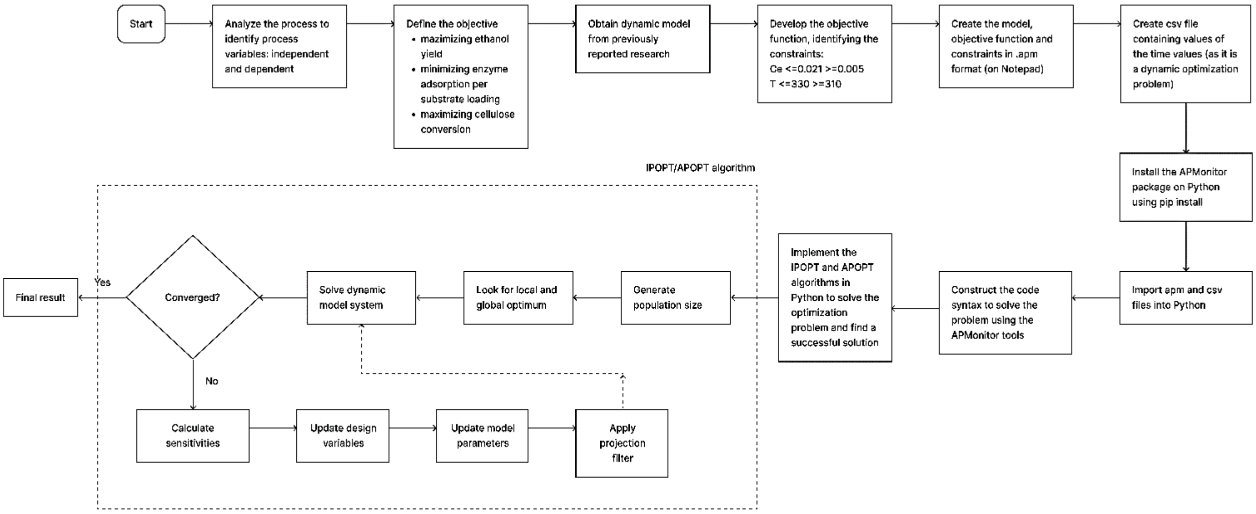

A.4 Sample Scilab Simulation Code

```
// Combined the rate equations into a specific function f = bioet(t,A)
function f=bioet(t, A)
      Cc = A(1); Ccb = A(2); Cg = A(3); Ch = A(4); Cx = A(5); Cxx = A(6); Cxg = A(7); Cex = A(8); Ceg = A(9);
   // Defined supporting equations for the ODEs
   k1 = ki1*exp((-Eia/R)*(1/T1 - 1/T2)); k2 = ki2*exp((-Eia/R)*(1/T1 - 1/T2));     k3 = ki3*exp((-Eia/R)*(1/T1 - 1/T2)); k4 = ki4*exp((-Eia/R)*(1/T1 - 1/T2))
   Cs = Cc + Ch + Cl
   Ead = (Emax*Kia*Ce*Cs)/(1 + Kia*Ce); Et = Ce + Ead; CE = (Ead*Cc)/Cs; CH = (Ead*Ch)/Cs; Rs = (r*Cs)/S0;
   r1 = (k1*CE*Rs*Cc)/(1 +(Ccb/K1Ccb) + (Cg/K1Cg) + (Cx/K1Cx));
   r2 = (k2*CE*Rs*Cc)/(1 +(Ccb/K2Ccb) + (Cg/K2Cg) + (Cx/K2Cx));
   r3 = (k3*Ce*Ccb)/((K3C*(1 + (Cg/K3Cg) + (Cx/K1Cx))) + Ccb );
   r4 = (k4*CH*Rs*Ch)/(1 +(Ccb/K4Ccb) + (Cg/K4Cg) + (Cx/K4Cx));
   // ODEs for the dependent variables
   dCcdt = -r2 - r1;
   dCcbdt = 1.056*r2 - r3;
   dCgdt = 1.111*r1 + 1.053*r3;
   dChdt = -r4;
   dCxdt = 1.136*r4;
   dCxgdt = ((ug*Cgdt)/(K4G + Cgdt + (Cgdt^2/K4IG)))*(1-(Ceg/Eg)^bg);
   dCxxdt = ((ux*Cxdt)/(K5X + Cxdt + (Cxdt^2/K5IX)))*(1-(Cex/Ex)^bx);
   dCegdt = ((vg*Cgdt*Cxgdt)/(K8G + Cgdt + (dCgdt^2/K8IG)))*(1-(Ceg/Eg1)^rg);
   dCexdt = ((vx*Cxdt*Cxxdt)/(K9X + Cxdt + (dCxdt^2/K9IX)))*(1-(Cex/Ex1)^rx);
   dCegdt = Yeg*((dCxgdt/Yxg) + (mg*Cxgdt));
   dCexdt = Yex*((dCxxdt/Yxx) + (mg*Cxxdt));
   f = [dCcdt;dCcbdt;dCgdt;dChdt;dCxdt;dCxxdt;dCxgdt;dCexdt;dCegdt]
endfunction
// All necessary constants of the function
T1 = 298; T2 = 310; Eia = -5540; R = 1.9872; r = 1; ki1 = 3.71; ki2 = 0.65; ki3 = 254.5; ki4 = 57.79; K1Ccb = 119.26; K2Ccb = 9.83; K3C = 24.5; K1Cg = 0.15; K2Cg = 0.176; K3Cg = 41.75; K4Cg = 0.023; K1Cx = 8.79; K2Cx = 9.54; K4Cx = 9.81; K4Ccb = 16.25; Emax = 0.026; Kia = 8.577; Ce = 0.1; K4G = 0.565; K4IG = 283.7; K5X = 3.4; K5IX = 18.1; K8G = 1.342; K8IG = 4890; K9X = 3.4; K9IX = 81.3; mg = 0.097; mx = 0.067; Eg = 95.4; Ex = 59.040; Eg1 = 103; Ex1 = 60.2; Yeg = 0.47; Yex = 0.4; Yxg = 0.115; Yxx = 0.162; bg = 1.29; bx = 1.036; rg = 1.42; rx = 0.608; ug = 0.662; ux = 0.19; vg = 2.005; vx = 0.25; K1Et = 0.15; Cl = 8.1; S0 = 100
//Time range for simulation
t = linspace(0,120); t0 = t(1);
//Initial values of dependent variables
sol0 = [44.5;0;0;9.9;0;0.016;0.016;0;0];
//Solution of the combined ODEs
sol = ode(sol0,t0,t,bioet); disp(sol)
plot( t, sol)
```

A.5 Sample Optimization Code in Python using APMonitor

```
from apm import*
s  = 'http://byu.apmonitor.com'
a = 'dynopt'
apm(s,a,'clear all')
apm_load(s,a,'celluloseconversion.apm')
csv_load(s,a,'data.csv')
apm_option(s,a,'nlc.nodes',4)
apm_option(s,a,'nlc.solver',1)
apm_option(s,a,'nlc.imode',6)
apm_option(s,a,'nlc.mv_type',1)
output = apm(s,a,'solve')
print (output)
y = apm_sol(s,a)
import matplotlib.pyplot as plt
plt.figure(1)
plt.subplot(2,1,1)
plt.plot(y['time'],y['cc'],'r-', linewidth =1)
plt.ylabel('Cellulose concentration')
plt.subplot(2,1,2)
plt.plot(y['time'],y['ead'],'b->', linewidth=1)
plt.plot(y['time'],y['cs'],'g-o',linewidth=1)
plt.legend(['Enzyme adsorption','Substrate concentration'])
plt.ylabel('Concentration')
plt.xlabel('Time')
plt.show()
```

DOI:10.51975/22370102.som
Journal of the Nigerian Society of Chemical Engineers, 37(1), 2022

HEAT AND MASS TRANSFER CONSIDERATIONS IN THE DESIGN OF A COILED ABSORBER FOR AMMONIA-WATER REFRIGERATION SYSTEM

***Mumah, S.N.[1], Akande, H.F.[1], Oyawoye, M. R.[1], Ibrahim, T.G.[2], Mudi, K.Y.[1], Olaniyan, O.[3] and Samuel, F.[1]**

[1] Department of Chemical Engineering, Kaduna Polytechnic, Kaduna, Nigeria
[2] Department of Mechanical Engineering, Kaduna Polytechnic, Kaduna, Nigeria
[3] Department of Civil Engineering, Kaduna Polytechnic, Kaduna, Nigeria
*Corresponding Author: mumahsdoyi@kadunapolytechnic.edu.ng

ABSTRACT

The performance of the absorber significantly affect the overall efficiency of any absorption refrigeration system. One of the major reasons for the poor design of the absorber for ammonia-water refrigeration systems is the neglect of mass transfer resistances in the vapour or liquid phase in favour of only heat transfer considerations. Heat removal is critical to the absorption process, however, the ammonia gas is constantly absorbed by the liquid ammonia-water solution. This means that two-phase mass and heat transfer operations take place during the absorption process. Therefore, this implies that, for any proper absorber design, both heat and mass transfer considerations are paramount. Accurate absorber design is further predicated on accurate properties correlations. The correlations required for the absorber design include liquid and vapour enthalpies, saturated vapour pressure, specific heat capacity of water and ammonia vapour, liquid solution dynamic viscosity, liquid solution density, surface tension, liquid solution thermal conductivity, liquid-liquid diffusivity and vapour-liquid diffusivity. Procedures for calculating these parameters have been presented in this paper and their accuracy with previous studies compared. Results showed relatively low percentage deviations and so can be applied for the design and simulation of the absorber. Designs of the absorber for various cooling capacities have been carried in this paper. The variation of ammonia vapour temperatures, liquid ammonia-water solution temperatures, cooling water temperatures, and flow rates of ammonia-water solution and ammonia vapour across the absorber is investigated for the four cooling capacities. For refrigeration systems with cooling capacities of 1 kW, 2 kW, 3 kW and 4 kW, the calculated lengths for a water-cooled coiled absorber are 4.484 m, 8.1467 m, 12.50459 m and 14.78329 m respectively. The calculated overall heat transfer coefficients for the absorption process for the four cooling capacities (1 kW, 2 kW, 3 kW and 4 kW) were 0.4427, 0.4376, 0.4208 and 0.4309 kWm^{-2}K^{-1} while the mass transfer coefficients were 3.721 x10^{-9}, 4.206 x10^{-9}, 4.556 x10^{-9}and 4.856 x10^{-9} m^{2}s^{-1} respectively. Concurrent flow is considered in this study, but the procedure can also be applied to countercurrent flow.

KEYWORDS: *Absorption Refrigeration, Ammonia Water Heat and Mass Transfer, Design*

1.0 INTRODUCTION

The effective distribution of vaccines requires cold chains or refrigerators which are maintained at temperatures between 2°C and 8°C (36°F and 46°F). Freezers should maintain temperatures between -50°C and -15°C (*https://www.cdc.gov/vaccines/pubs/pinkbook/vac-*).

Most refrigeration systems that run with regular electric power are of the vapour-compression mode. Using this type of refrigeration system is only possible if there is a steady electric power supply. That is where the problem lies for many African countries. Taking Nigeria and Brazil as case studies, it is easily visible why vaccine distribution is much smoother in Brazil than in Nigeria. Brazil, with a population of 211 million (2019) estimates (World Bank) has an installed power generation capacity of 174.0 GW compared to Nigeria, considered the largest economy in Africa and has an estimated population of 201million (2019 World Bank estimates), has an estimated generation capacity of 13.0 GW. Compounding this low energy supply is that less than 60% of the population has access to electricity, even those who have suffered from the intermittent supply. It can be argued that Brazil level of industrialization is higher than that of Nigeria, but even at peak energy demand of about 9.0GW, supply hovers at most time below 4.0GW (https://www.worldbank.org/en/news/press-release/2021/02/05)

The scenario painted above is not different from many African countries. There is, therefore, the need to explore other refrigerating systems that can be used in these locations and that is now always electric power dependent.

Solar-powered systems have found increasing use in urban areas in Nigeria, but their application to cold storage has been limited. The reasons for this are not farfetched. Solar power is intermittent, and to use it efficiently, solar power storage systems must be incorporated to operate 24 hours. The additional challenge of low solar intensity at some periods of the year must be solved. Furthermore, the rural electrification situation in the country is very pathetic. With the never-ending threat of an increase in the cost of electricity from electric power distribution companies, stakeholders cannot afford to pay for cold storage facilities unless there is intervention from governments, private or public organisations.

The use of solar energy as an alternative energy source to power refrigerating systems is well documented (Mumah, 1994; Ioan and Sebarchievici, 2015; Siddiqui and Saad, 2015). The limitation is obvious; operating alone, they can only provide cooling during periods of peak sunshine. To ensure that such systems have all day use, augmentation systems must be incorporated.

Two types of absorption refrigerating systems are commonly used, the Ammonia-Water (NH_3/H_2O) and the Lithium Bromide-Water ($LiBr_2/H_2O$) absorption systems (Mumah, 1991; Mumah, 2008; Chung *et al.*, 2014). Since the storage of most agricultural produce can be achieved at 5^oC or less, ammonia-water absorption system will be the system best suited for this purpose.

2.0 WHY AMMONIA WATER SYSTEM?

Today, ammonia remains the refrigerant of choice for large industrial applications. For large refrigeration systems, ammonia has many advantages. Ammonia(R-717) costs less. Not only is ammonia significantly cheaper than the least expensive halocarbons fluorocarbons, but because the density of ammonia is half of all halocarbons, only half as much material is required in the system (https://www.goodway.com/hvac-blog/2009/08/ammonia-as-a-refrigerant-pros-and-cons/). Ammonia is more efficient since the mass flow rate of a given capacity is one-seventh than that of HCFC-22. This means that only one-seventh of the liquid needs to be pumped for a given refrigeration capacity. The heat transfer and thermodynamic properties are highly advantageous and provide cost savings. Ammonia requires smaller vapour line pipe sizes for large systems spread over a large area due to less drop in saturation temperatures than Freon. Ammonia systems are more tolerant of water contamination than Freon systems. Water concentrations of less than 100 ppm cause no adverse effects to ammonia system operation (https://axaxl.com*› pdfs › prc7212ammoniahazardsv1)*.

2.1. Ammonia /Water Absorption Refrigerating System

The use of solar energy as an energy source for ammonia-water refrigerating systems is well documented (Mumah, 1991; 1994). Figure 1 shows the schematic diagram of a simple ammonia-water absorption refrigeration system. An absorption system like the ammonia-water system usually consists of an evaporator, condenser, generator with a rectifying section, an absorber, and an economizer to optimize the generator and absorber for heat exchange optimization. Water is the absorbent, and ammonia is the refrigerant in this system. Since the absorption process lowers the pressure in the absorber, more ammonia is drawn into the equipment. However, this process is accompanied by the evolution of heat. For the process to operate efficiently, there must be a process in place to remove the heat.

Most absorbers are forced-convection air-cooled or water-cooled heat exchangers. Both vapour and liquid phases are involved and should be considered in the design. The two pressure regimes are maintained by the pump (usually between the absorber and generator) and the expansion valve (between the condenser and evaporator). The heating sources for the generator are usually electric heat coils, gas-fired, or solar power (concentric systems are usually used) or a combination of any of these sources. Heat storage materials can be introduced into the mix, especially when solar energy is considered. In the generator, the heating process generates the ammonia which is usually rectified before the condensation process in the condenser. The sudden expansion of the ammonia liquid from the condenser causes the cooling effect in the evaporator. Heat is extracted from the evaporator environment, which leads to an increase in the refrigerant vapour temperature. This vapour is then absorbed by the ammonia-water solution in the absorber.

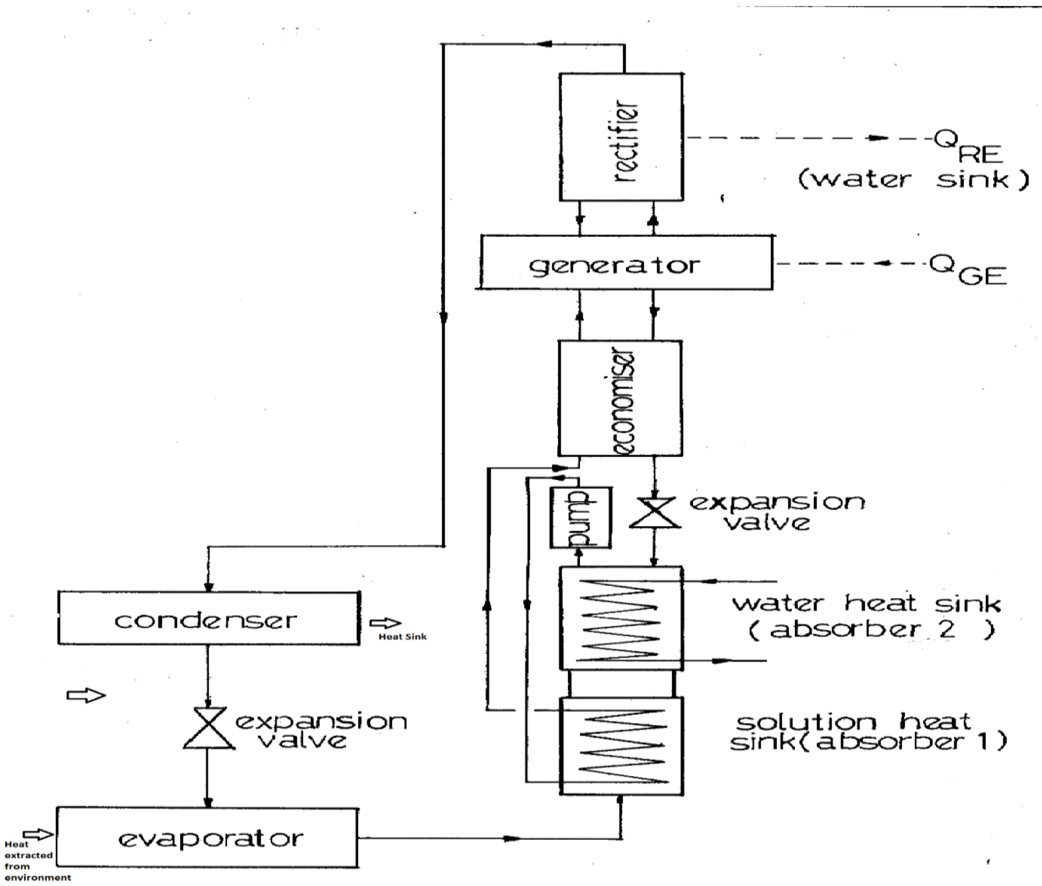

Figure 1. Schematic Diagram of Simple Vapour Absorption Refrigeration System

Of all the components shown in Figure 1, the design of the absorber is the major challenge. This is because, in the absorber, there is the absorption of ammonia vapour by ammonia-water liquid solution which makes it a two-phase mass transfer operation. Furthermore, there is the evolution of heat which brings in the heat transfer dimension. For the absorber to operate efficiently, this heat must continuously be removed until all the ammonia is absorbed. Without the removal of the heat, the absorption process becomes inefficient (Issa *et al.* (2002).

2.2. Ammonia Water Refrigeration System Absorber Design

It has been established that a proper design of the absorber drastically affects the overall performance of the refrigeration system. This is because the rate of heat removal is critical to the absorption process (Mittermaier and Ziegler, 2015). Many analytical and experimental attempts have been made to characterize the absorption process properly (Issa *et al.* (2002). Predicting heat and mass transfer characteristics is important to any absorber's proper design that requires the removal of heat. Many approaches have been used in the design of the absorber. Cerezo *et al.*(2009) studied a bubble absorber using a one-dimensional model to estimate absorption fluxes and absorption coefficients, while Goel and Goswami (2005) studied a counter current absorber using a finite difference method empirical correlations for transfer coefficients to understand coupled transfers.

Killion and Garimella (2001) identified that one of the major reasons for the poor design of the absorber for ammonia-water refrigeration systems is the neglect of mass transfer resistances in the vapour or the liquid phase. Therefore for any proper design, mass transfer resistances must be considered. Triché *et al.* (2015) carried out a numerical and experimental study where heat and mass transfers resistances that take place in a plate heat exchanger was considered. The method used was one dimension model, which allowed the iterative resolution of non-linear equations in each differential control volume of the absorber. Gommed *et al.* (2001) used the finite volume method to quantify the absorption process

The absorption of ammonia into ammonia-water solution is accompanied by the liberation of a great quantity of heat Kumar and Das (2015). This results in the elevation of the temperature of the liquid. The absorbent (strictly water) is not as volatile as ammonia at the absorber temperature. Thus, there is no vaporisation of part of the absorbent. Heat is also transferred to or from the gas resulting in a change in the temperature of the gas. Thus, the absorption process, in this case, cannot be analysed on the basis of mass transfer alone but by simultaneous heat and mass transfers.

The transfer of heat through a fluid near a phase boundary will be expedited or retarded by the superimposed parallel or counter diffusion of compounds in the fluid mixture. The conduction of heat in a gas where there is molecular transfer (diffusion) of the gas in the direction of heat flow is greater if the gas is stagnant. This effect appears to be negligible in most practical cases (Issa *et al.*, 2002). Thus, ordinary diffusion and heat transfer equations are applied as if each of the processes is occurring independently of the other. The liberation of heat during absorption leads to the following effects:

a. The position of the equilibrium line is changed since the equilibrium concentration of the gaseous phase is a function, not only of the liquid concentration but also of the liquid temperature. With an increase in temperature, the equilibrium line shifts upward, thereby decreasing the driving force.
b. As already mentioned, a temperature gradient is created between the liquid and the gas, leading to heat-exchange processes in addition to mass-exchange ones (simultaneous heat and mass transfer)

To eliminate or decrease the adverse effects listed above, absorption with heat evolution is usually carried out with heat removal. This can be done by – introducing a cooling element inside the absorber (internal heat removal), recirculation of the liquid through outside coolers (circulation heat removal) or placing coolers between the stages in multistage absorption (intermediate heat removal).

The Ammonia water absorber is a non-isothermal equipment. For the non-isothermal case, the cooling process will be by internal heat removal. It is important to note that the statics of absorption, that is, the equilibrium between the liquid and gaseous phases, determines the state established after long contact between the phases. The equilibrium between the phases is determined by the thermodynamic properties of the component and absorbent and it depends on the composition of one of the phases, the temperature and its pressure. The kinetics of absorption, that is, the rate of mass transfer is determined by the driving force of the process (the degree of deviation of the process from the equilibrium state), the properties of the absorbent, component, and inert gas where applicable. It is also determined by the way in which the phases are brought in contact (design of absorption apparatus and hydrodynamic operating conditions).

2.3 Non-isothermal Case

In absorption with the evolution of heat, the differential equation are non-linear because y* and the liquid temperature are not proportional. The equation system can be solved by a reduction of the equation methods. For parallel flow, initial conditions (values when the area is zero) are given and the problem can be solved by using Cauchy Method (Chapra and Canale, 2020). For countercurrent flow, the boundary conditions are given partly for A = 0 (gas entering), and A = A (liquid entering), and the case becomes a boundary problem. This boundary problem can be solved numerically by iteration (successive approximation)._The successive approximation method will be applied. The absorption of ammonia into water will be looked into as a case study.

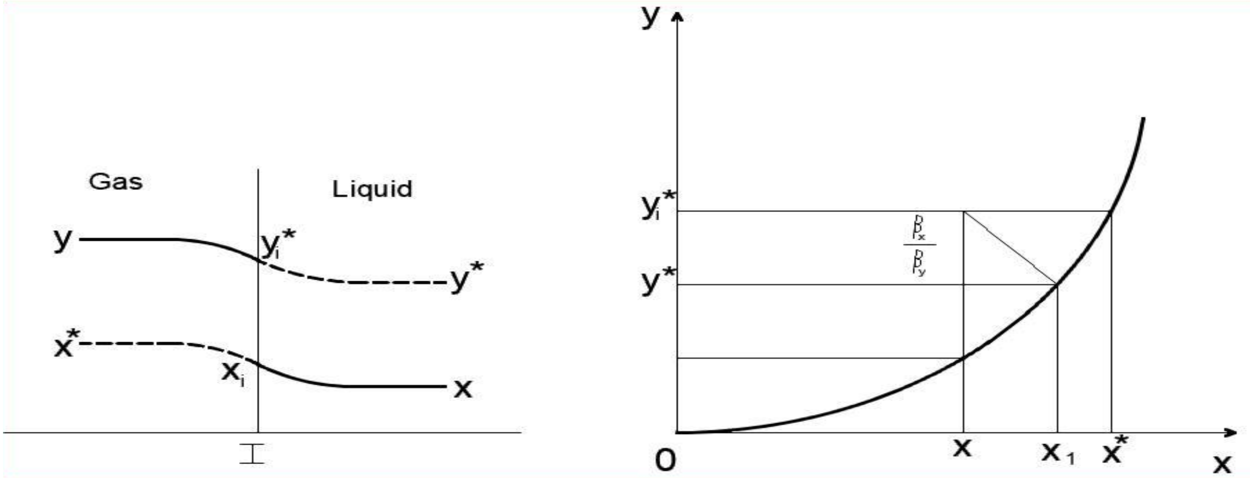

Figure 2: Mass transfer in an absorption process

2.4 Mass Transfer Coefficient for the absorption process

A gas can be said to be readily, moderately or sparingly soluble in a liquid depending upon the criteria one bases his comparison. An easy method of comparison is by comparing their mass transfer coefficients. If a material be transferred from the gaseous phase into the liquid phase (Figure (2)), the mass transfer equations for the gaseous and liquid phases can be expressed as

$$\mathrm{W_A} = \beta_y \mathrm{A}(\mathrm{y} - \mathrm{y_i}) \qquad (1)$$

and

$$\mathrm{W_A} = \beta_x \mathrm{A}(\mathrm{x_i} - \mathrm{x}) \qquad (2)$$

respectively. Since there is no accumulation at the interface, $\mathrm{W_A}$ in both equations are same. Equations (1) and (2) can be combined assuming that the phases are in equilibrium at their interface to give

$$\mathrm{W_A} = \kappa_y \mathrm{A}(\mathrm{y} - y^*) \qquad (3)$$

where

$$1/\kappa_y = \frac{1}{\beta \mathrm{y}} + \frac{\mathrm{m}}{\beta \mathrm{x}} \qquad (4)$$

where W_A is the mass flow rate of cooling liquid ($\mathrm{kgs^{-1}}$), A is the total surface area of the tube, y^* is the gas concentration in equilibrium with the liquid concentration *x*, *m* is the mean value of the phase equilibrium constant given by (Ramm, 1968), κ_y is the heat Transfer coefficient ($\mathrm{Wm^{-2}K^{-1}}$) of the vapour phase, βy is the mass transfer coefficient ($\mathrm{m^2s^{-1}}$) of the vapour phase and βx is the mass transfer coefficient ($\mathrm{m^2s^{-1}}$) of the liquid phase.

$$m = \frac{y_i - y^*}{x_i - x^*} \qquad (5)$$

where $y_i - y^*$ is the driving force. Equation (5) can also be written in terms of the liquid concentration as

$$W_A = \kappa_x A(x^* - x) \qquad (6)$$

Where

$$\frac{1}{\kappa_x} - \frac{1}{m\beta_y} + \frac{1}{\beta_x} \qquad (7)$$

m is given by

$$m = \frac{y - y_i}{x - x_i} \qquad (8)$$

In Equations (4) and (7), $1/\beta_y$ represents the resistance to mass transfer shown by the gaseous phase, while the term $m\beta_x$ is the resistance of the liquid phase. The sum of these values, $1/\kappa_x$ is the overall resistance to heat transfer (Mumah, 1991).

2.5 Absorption with Internal Heat Removal

The rates of heat and mass transfer equations for the absorption of the component can be represented by (Mumah, 1991)

$$dW_A = -G_o dY_A = \kappa_y (y_A - y_A^*) dA \qquad (9)$$

$$= \pm L_o dX_A = \kappa_x (x_A^* - x_A) dA \qquad (10)$$

where *x* is the mole fraction of the liquid phase, *y* is the mole fraction of the vapour phase, W_A is the mass flow rate of cooling liquid ($\mathrm{kgs^{-1}}$), G_o is the gas flow rate (kg/s) and L_o is the liquid flow rate (kg/s).

For vaporization of the absorbent

$$dW_B = -G_o dy_B = \kappa_B (y_B^* - y_B) dA \qquad (11)$$

The interphasal heat-exchange equation is represented by

$$L_o C_p d\theta = (t - \theta) dA \qquad (12)$$

where C_p is the Specific Heat capacity ($\mathrm{Jkg^{-1}K^{-1}}$) of the ammonia vapour, θ is the temperature of gas (K) and *t* is the temperature of the cooling medium (K).
or

$$G_o C_p dt = (\theta - t) dA \qquad (13)$$

and the heat transferred from the medium of the absorber to the cooling agent

$$dQ_o = \kappa_x (\theta - t) dA = \pm W_w C_w d\delta \qquad (14)$$

The plus sign on the right-hand side of Equation (14) refers to concurrent flow and the minus sign to countercurrent flow. This equation assumes that the heat transferred is from the gaseous (and not from the liquid) phase to the cooling wall. This assumption apparently corresponds to the actual operation of the absorber with internal heat removal.

3.0 SIMULATION PROCEDURE

Equations (9) to (14) form a system of differential equations that can be solved in several ways. The accurate method of successive approximation is applied to solve the equations with the aim of designing an absorber for an ammonia-water heat pump system for cooling. A computer algorithm was developed and a programme was written using Visual FORTRAN to solve Equations (9) to (14) for the absorber of an ammonia-water absorption refrigeration system. The design of the concurrent coiled tube heat exchanger follows the procedure presented by Bonafoni and Capata (2015) and to take care of heat and mass transfer during the absorption process Equations (9) to (14) were applied. All thermodynamic properties were calculated using the procedures presented in this paper.

. In the computation, a coil length and thickness are assumed, and the simulation is carried. If the calculated length is equal to the assumed length ± maximum 20 %, the coil length and diameter are accepted. If the deviation is more than 20%, the coil length and/or diameter are changed until the maximum ±20% is achieved. Deviation of lower than ±20 deviation of coil length does not significantly affect the calculated coil length. The simulation carried out in this study is for the concurrent flow of vapour and solution. The cooling water flows in the same direction as the ammonia vapour. 4 capacities (1.0 kW to 4.0 kW) are considered in this study. The simulation is completed when the ammonia vapour flow rate is zero. Zero flow rates mean absorption of ammonia vapour is complete. The variation of the following properties and parameters are investigated; ammonia vapour temperature, ammonia-water solution temperature, cooling water temperature, and flow rates of ammonia-water solution and ammonia vapour.

4.0 CALCULATIONS OF VARIOUS PROPERTIES

4.1 Calculation of Liquid Enthalpy

The double Chebychev series for the calculation of liquid enthalpies can be represented as shown in Equation (15).

$$H_l = \sum_{i-0}^{K}\sum_{j=0}^{L} A_{ij} P_i\,(T_1\,) P_j(X_2\,) \qquad (15)$$

where H_l is the liquid enthalpy in kJ/kg, A_{ij} is the Chebychev coefficient, X is the ammonia concentration in the solution in weight percent and T is the solution temperature in K.

The steps to be followed while applying the Chebychev polynomial for the calculation of liquid enthalpies for temperature ranges usually encountered in absorbers of ammonia-water refrigeration systems are presented in Table 1. Mumah *et al.* (2021) has presented correlations for other temperature ranges. The ranges of the temperature and concentration are selected based on the experimental data for enthalpy provided by Macriss *et al.* (1964).

Table 1. Steps to follow when applying Chebychev polynomial to calculate liquid enthalpies (kJ/kg)

Section (1)				
Start by selecting *T*, the temperature and *PC*, the percentage concentration within these ranges: $233.15K \leq T < 272.03449K;\;\; 10.0wt\% \leq PC \leq 100.0Wt\%$ The constants after expanding Equation (15) are				
A(1) $-9.1303\text{x}10^{+02}$	A(2) $1.6526\text{x}10^{+02}$	A(3) $2.3290\text{x}10^{+00}$	A(4) $-7.1415\text{x}10^{-01}$	A(5) $8.6908\text{x}10^{-01}$
A(6) $8.1098\text{x}10^{+01}$	A(7) $8.4783\text{x}10^{+00}$	A(8) $-1.5322\text{x}10^{+00}$	A(9) $3.9225\text{x}10^{-01}$	A(10) $-5.1072\text{x}10^{-01}$
A(11) $2.1503\text{x}10^{+02}$	A(12) $-4.1738\text{x}10^{+00}$	A(13) $1.3162\text{x}10^{+00}$	A(14) $-2.2661\text{x}10^{-01}$	A(15) $3.2467\text{x}10^{-01}$
A(16) $-2.5040\text{x}10^{+01}$	A(17) $3.9042\text{x}10^{+00}$	A(18) $-1.3482\text{x}10^{+00}$	A(19) $4.2061\text{x}10^{-01}$	A(20) $-4.0873\text{x}10^{-01}$
A(21) $-4.2814\text{x}10^{+00}$	A(22) $-3.2019\text{x}10^{+00}$	A(23) $1.0509\text{x}10^{+00}$	A(24) $-4.7134\text{x}10^{-01}$	A(25) $4.4445\text{x}10^{-01}$
A(26) $1.5513\text{x}10^{+00}$	A(27) $2.0490\text{x}10^{+00}$	A(28) $-5.6347\text{x}10^{-01}$	A(29) $2.5490\text{x}10^{-01}$	A(30) $-4.3315\text{x}10^{-01}$
Other parameters are calculated as follows: $U = (2.0T - (272.038888 + 233.15))/(272.038888 - 233.15)$ $V = (2.0PC - 110.0)/90.0$ $X_1 = cos(arccosU)$ $X_2 = cos(2.0arccosU)$ $X_3 = cos(3.0arccosU)$ $X_4 = cos(4.0arccosU)$ $Y_1 = cos(arccosV)$ $Y_2 = cos(2.0arccosV)$ $Y_3 = cos(3.0arccosV)$ $Y_4 = cos(4.0arccosV)$ $Y_5 = cos(5.0arccosV)$ $Z = 1.0$				

$A = 0.25(Z)A\ (1) + 0.5A(2)X_1 + 0.5A(3)X_2 + 0.5A(4)X_3 + 0.5A(5)X_4$
$B = Y_1(0.5(Z)A(6) + A(7)X_1 + A(8)X_2 + A(9)X_3 + A(10)X_4)$
$C = Y_2(0.5(Z)A(11) + A(12)X_1 + A(13)X_2 + A(14)X_3 + A(15)X_4)$
$D = Y_3(0.5(Z)A(16) + A(17)X_1 + A(18)X_2 + A(19)X_3 + A(20)X_4)$
$E = Y_4(0.5(Z)A(21) + A(22)X_1 + A(23)X_2 + A(24)X_3 + A(25)X_4)$
$F = Y_5(0.5(Z)A(26) + A(27)X_1 + A(28)X_2 + A(29)X_3 + A(30)X_4)$
$H_l = A + B + C + D + E + F$

Section (2)

Follow the same procedure as in Section (1.1)
$272.03449K \leq T < 360.92778K$
$0.0wt\% \leq PC \leq 100.0wt\%$

A(1)	A(2)	A(3)	A(4)	A(5)	A(6)
$3.2796\text{x}10^{+02}$	$4.1765\text{x}10^{+02}$	$7.2486\text{x}10^{+00}$	$1.4096\text{x}10^{+00}$	$1.3842\text{x}10^{+00}$	$8.0727\text{x}10^{-01}$
A(7)	A(8)	A(9)	A(10)	A(11)	A(12)
$3.6984\text{x}10^{+01}$	$1.8083\text{x}10^{+01}$	$3.7172\text{x}10^{+00}$	$1.3878\text{x}10^{+00}$	$5.7801\text{x}10^{-01}$	$2.6093\text{x}10^{-01}$
A(13)	A(14)	A(15)	A(16)	A(17)	A(18)
$2.5064\text{x}10^{+02}$	$-1.4995\text{x}10^{+00}$	$1.4144\text{x}10^{+00}$	$1.2629\text{x}10^{+00}$	$4.5639\text{x}10^{-01}$	$1.2939\text{x}10^{-01}$
A(19)	A(20)	A(21)	A(22)	A(23)	A(24)
$-6.7469\text{x}10^{+00}$	$3.2120\text{x}10^{+00}$	$1.3634\text{x}10^{+00}$	$4.7048\text{x}10^{-01}$	$4.8789\text{x}10^{-01}$	$3.9950\text{x}10^{-01}$
A(25)	A(26)	A(27)	A(28)	A(29)	A(30)
$-1.7843\text{x}10^{+01}$	$-2.8775\text{x}10^{-01}$	$2.9878\text{x}10^{-01}$	$2.9766\text{x}10^{-01}$	$2.1430\text{x}10^{-01}$	$2.3201\text{x}10^{-01}$
A(31)	A(32)	A(33)	A(34)	A(35)	A(36)
$6.2351\text{x}10^{+00}$	$9.4842\text{x}10^{-01}$	$4.9746\text{x}10^{-01}$	$5.2922\text{x}10^{-01}$	$5.8257\text{x}10^{-01}$	$3.2683\text{x}10^{-01}$
A(37)	A(38)	A(39)	A(40)	A(41)	A(42)
$2.4057\text{x}10^{+00}$	$1.4490\text{x}10^{+00}$	$6.9218\text{x}10^{-01}$	$4.1905\text{x}10^{-01}$	$4.7021\text{x}10^{-01}$	$2.9575\text{x}10^{-01}$

$U = (2.0T - (360.927778 + 272.038888))/(360.927778 - 272.038888)$
$V = (2.0PC - 100.0)/100.0$

$X_1 = cos(arccosU)$
$X_2 = cos(2.0arccosU)$
$X_3 = cos(3.0arccosU)$
$X_4 = cos(4.0arccosU)$
$Y_1 = cos(arccosV)$
$Y_2 = cos(2.0arccosV)$
$Y_3 = cos(3.0arccosV)$
$Y_4 = cos(4.0arccosV)$
$Y_5 = cos(5.0arccosV)$
$Z = 1.0$

$A = 0.25(Z)A\ (1) + 0.5A(2)X_1 + 0.5A(3)X_2 + 0.5A(4)X_3 + 0.5A(5)X4 + 0.5A(6)X_5$
$B = Y_1(0.5(Z)A(7) + A(8) * X_1 + A(9)X_2 + A(10)X_3 + A(11)X_4 + A(12)X_5)$
$C = Y_2(0.5(Z)A(13) + A(14)X_1 + A(15)X_2 + A(16)X_3 + A(17)X_4 + A(18)X_5)$
$D = Y_3(0.5(Z)A(19) + A(20)X_1 + A(21)X_2 + A(22)X_3 + A(23)X_4 + A(24)X_5)$
$E = Y_4(0.5(Z)A(25) + A(26)X_1 + A(27)X_2 + A(28)X_3 + A(29)X_4 + A(30)X_5)$
$F = Y_5(0.5(Z)A(31) + A(32)X_1 + A(33)X_2 + A(34)X_3 + A(35)X_4 + A(36)X_5)$
$G = Y_6(0.5(Z)A(37) + A(38)X_1 + A(39)X_2 + A(40)X_3 + A(41)X_4 + A(42)X_5)$
$H_l = A + B + C + D + E + F + G$ (% deviation=±0.978)

4.2. Calculation of Vapour Enthalpy

This can be represented by the double Chebychev series

$$H_v(T,Y) = \sum_{i-0}^{K}\sum_{j=0}^{L} A_{ij}P_i\,(T_1\,)P_j(Y_2\,) \qquad (16)$$

where H_v is the vapour enthalpy in kJ/kg, A_{ij} is the Chebychev coefficient, Y of the concentration of the ammonia in the vapour in weight percent and T is the vapour temperature in K. Table 2 shows the various steps to follow when applying the double Chebychev series approach in calculating saturated vapour enthalpies.

Table 2. Steps to follow when applying Chebychev polynomial to calculate saturated vapour enthalpies (kJ/kg)

Section(1)				
Start by selecting T, the temperature and PC, the percentage concentration within these ranges: $233.15K \le T < 272.03449K;\ \ 10.0wt\% \le PC \le 100.0wt\%$				
A(1) $5.0722\text{x}10^{+03}$	A(2) $8.6271\text{x}10^{+01}$	A(3) $2.0373\text{x}10^{+00}$	A(4) $-2.1750\text{x}10^{+00}$	A(5) $1.9510\text{x}10^{-01}$
A(6) $-8.6667\text{x}10^{+01}$	A(7) $-2.3583\text{x}10^{+01}$	A(8) $-2.2498\text{x}10^{+00}$	A(9) $9.7238\text{x}10^{-01}$	A(10) $6.9894\text{x}10^{-01}$
A(11) $4.2873\text{x}10^{+01}$	A(12) $1.3137\text{x}10^{+01}$	A(13) $1.5338\text{x}10^{+00}$	A(14) $-9.4574\text{x}10^{-01}$	A(15) $-2.9239\text{x}10^{-01}$
A(16) $-2.5459\text{x}10^{+01}$	A(17) $-8.3678\text{x}10^{+00}$	A(18) $-1.0347\text{x}10^{+00}$	A(19) $1.2421\text{x}10^{+00}$	A(20) $-1.0012\text{x}10^{-01}$
A(21) $1.4819\text{x}10^{+01}$	A(22) $5.8819\text{x}10^{+00}$	A(23) $8.0059\text{x}10^{-01}$	A(24) $-8.9299\text{x}10^{-01}$	A(25) $-8.9632\text{x}10^{-02}$
A(26) $-6.1504\text{x}10^{+00}$	A(27) $-3.0295\text{x}10^{+00}$	A(28) $-7.6234\text{x}10^{-01}$	A(29) $3.6674\text{x}10^{-01}$	A(30) $-1.6957\text{x}10^{-01}$
Other parameters are calculated as follows: $U = (2.0T - (272.038888 + 233.15))/(272.038888 - 233.15)$ $V = (2.0PC - 110.0)/90.0$ $X_1 = cos(arccosU)$ $X_2 = cos(2.0arccosU)$ $X_3 = cos(3.0arccosU)$ $X_4 = cos(4.0arccosU)$ $Y_1 = cos(arccosV)$ $Y_2 = cos(2.0arccosV)$ $Y_3 = cos(3.0arccosV)$ $Y_4 = cos(4.0arccosV)$ $Y_5 = cos(5.0arccosV)$ $Z = 1.0$ $A = 0.25(Z)A\,(1) + 0.5A(2)X_1 + 0.5A(3)X_2 + 0.5A(4)X_3 + 0.5A(5)X_4$ $B = Y_1(0.5(Z)A(6) + A(7)X_1 + A(8)X_2 + A(9)X_3 + A(10)X_4)$ $C = Y_2(0.5(Z)A(11) + A(12)X_1 + A(13)X_2 + A(14)X_3 + A(15)X_4)$ $D = Y_3(0.5(Z)A(16) + A(17)X_1 + A(18)X_2 + A(19)X_3 + A(20)X_4)$ $E = Y_4(0.5(Z)A(21) + A(22)X_1 + A(23)X_2 + A(24)X_3 + A(25)X_4)$ $F = Y_5(0.5(Z)A(26) + A(27)X_1 + A(28)X_2 + A(29)X_3 + A(30)X_4)$ $H_v = A + B + C + D + E + F$				

Section (2)
Follow the same procedure as in Section (3.1) $272.03449K \le T < 360.92778K$ $0.0wt\% \le PC \le 100.0wt\%$

A(1) $6.1550\text{x}10^{+03}$	A(2) $2.0995\text{x}10^{+02}$	A(3) $3.4432\text{x}10^{+00}$	A(4) $3.2670\text{x}10^{+01}$	A(5) $5.3165\text{x}10^{+00}$	A(6) $1.6198\text{x}10^{+01}$
A(7) $-7.8540\text{x}10^{+02}$	A(8) $-8.0272\text{x}10^{+01}$	A(9) $-1.2773\text{x}10^{+00}$	A(10) $-6.7427\text{x}10^{+00}$	A(11) $4.7341\text{x}10^{+00}$	A(12) $-5.3236\text{x}10^{+00}$
A(13) $5.0954\text{x}10^{+02}$	A(14) $2.2547\text{x}10^{+01}$	A(15) $4.6424\text{x}10^{+00}$	A(16) $2.1336\text{x}10^{+01}$	A(17) $2.7418\text{x}10^{+00}$	A(18) $1.0491\text{x}10^{+01}$
A(19) $-3.5716\text{x}10^{+02}$	A(20) $1.0388\text{x}10^{+01}$	A(21) $6.8376\text{x}10^{+00}$	A(22) $-6.7143\text{x}10^{+00}$	A(23) $2.8077\text{x}10^{+00}$	A(24) $-3.9867\text{x}10^{+00}$
A(25) $2.3151\text{x}10^{+02}$	A(26) $8.6627\text{x}10^{-01}$	A(27) $7.2526\text{x}10^{+00}$	A(28) $1.7469\text{x}10^{+01}$	A(29) $2.4523\text{x}10^{+00}$	A(30) $9.7139\text{x}10^{+00}$
A(31) $-1.2528\text{x}10^{+02}$	A(32) $1.3289\text{x}10^{+01}$	A(33) $9.1136\text{x}10^{+00}$	A(34) $-4.4525\text{x}10^{+00}$	A(35) $5.8272\text{x}10^{+00}$	A(36) $-3.0551\text{x}10^{+00}$
A(37) $7.2356\text{x}10^{+01}$	A(38) $3.8791\text{x}10^{+00}$	A(39) $1.8614\text{x}10^{+00}$	A(40) $1.2283\text{x}10^{+01}$	A(41) $3.3641\text{x}10^{-01}$	A(42) $6.8522\text{x}10^{+00}$
$U = (2.0T - (360.927778 + 272.038888))/(360.927778 - 272.038888)$ $V = (2.0PC - 100.0)/100.0$					
$X_1 = cos(arccosU)$ $X_2 = cos(2.0arccosU)$ $X_3 = cos(3.0arccosU)$ $X_4 = cos(4.0arccosU)$ $X_5 = cos(5.0arccosU)$ $Y_1 = cos(arccosV)$ $Y_2 = cos(2.0arccosV)$ $Y_3 = cos(3.0arccosV)$ $Y_4 = cos(4.0arccosV)$ $Y_5 = cos(5.0arccosV)$ $Z = 1.0$					
$A = 0.25(Z)A\ (1) + 0.5A(2)X_1 + 0.5A(3)X_2 + 0.5A(4)X_3 + 0.5A(5)X4 + 0.5A(6)X_5$ $B = Y_1(0.5(Z)A(7) + A(8) * X_1 + A(9)X_2 + A(10)X_3 + A(11)X_4 + A(12)X_5)$ $C = Y_2(0.5(Z)A(13) + A(14)X_1 + A(15)X_2 + A(16)X_3 + A(17)X_4 + A(18)X_5)$ $D = Y_3(0.5(Z)A(19) + A(20)X_1 + A(21)X_2 + A(22)X_3 + A(23)X_4 + A(24)X_5)$ $E = Y_4(0.5(Z)A(25) + A(26)X_1 + A(27)X_2 + A(28)X_3 + A(29)X_4 + A(30)X_5)$ $F = Y_5(0.5(Z)A(31) + A(32)X_1 + A(33)X_2 + A(34)X_3 + A(35)X_4 + A(36)X_5)$ $G = Y_6(0.5(Z)A(37) + A(38)X_1 + A(39)X_2 + A(40)X_3 + A(41)X_4 + A(42)X_5)$ $H_v = A + B + C + D + E + F + G$					

4.3. Calculation of Vapour Pressure

The saturated vapour pressure can be represented by the double Chebychev series shown in Equation (17).

$$P_v(T, X) = \sum_{i-0}^{K} \sum_{j=0}^{L} A_{ij} P_i\ (T_1\ ) P_j(xX_2\ ) \qquad (17)$$

where P_v is the vapour pressure in Bar, A_{ij} is the Chebychev coefficient, X of the weight percent of the ammonia in the liquid solution and T is the solution temperature in K. Table 3 shows the various steps to follow when applying the double Chebychev series approach in calculating saturated vapour pressure.

Table 3: Steps to follow when applying Chebychev Polynomial to calculate the saturated vapour pressure (Bar)

Section(1)
Start by selecting T, the temperature and PC, the percentage concentration within these ranges: $233.15K \leq T < 272.03449K;\ \ 10.0wt\% \leq PC \leq 100.0wt\%$

A(1) $3.6808\text{x}10^{+00}$	A(2) $1.4653\text{x}10^{+00}$	A(3) $2.6908\text{x}10^{-01}$	A(4) $6.1717\text{x}10^{-03}$	A(5) $3.7519\text{x}10^{-03}$
A(6) $2.2835\text{x}10^{+00}$	A(7) $8.8163\text{x}10^{-01}$	A(8) $1.2951\text{x}10^{-01}$	A(9) $2.4266\text{x}10^{-02}$	A(10) $-2.6143\text{x}10^{-03}$
A(11) $2.7893\text{x}10^{-01}$	A(12) $9.9338\text{x}10^{-02}$	A(13) $2.6932\text{x}10^{-02}$	A(14) $-1.3214\text{x}10^{-02}$	A(15) $3.8809\text{x}10^{-03}$
A(16) $-2.5774\text{x}10^{-01}$	A(17) $-9.5328\text{x}10^{-02}$	A(18) $-2.3879\text{x}10^{-02}$	A(19) $1.1666\text{x}10^{-02}$	A(20) $-3.6895\text{x}10^{-03}$
A(21) $-4.3672\text{x}10^{-02}$	A(22) $-4.3636\text{x}10^{-03}$	A(23) $8.7169\text{x}10^{-03}$	A(24) $9.2548\text{x}10^{-03}$	A(25) $3.4843\text{x}10^{-03}$
A(26) $6.5733\text{x}10^{-02}$	A(27) $1.9132\text{x}10^{-02}$	A(28) $-1.2631\text{x}10^{-03}$	A(29) $5.1231\text{x}10^{-03}$	A(30) $-1.1155\text{x}10^{-03}$

Other parameters are calculated as follows:

$U = (2.0T - (272.038888 + 233.15))/(272.038888 - 233.15)$
$V = (2.0PC - 110.0)/90.0$
$X_1 = cos(arccos U)$
$X_2 = cos(2.0 arccos U)$
$X_3 = cos(3.0 arccos U)$
$X_4 = cos(4.0 arccos U)$

$Y_1 = cos(arccos V)$
$Y_2 = cos(2.0 arccos V)$
$Y_3 = cos(3.0 arccos V)$
$Y_4 = cos(4.0 arccos V)$
$Y_5 = cos(5.0 arccos V)$
$Z = 1.0$
$A = 0.25(Z)A\,(1) + 0.5A(2)X_1 + 0.5A(3)X_2 + 0.5A(4)X_3 + 0.5A(5)X_4$
$B = Y_1(0.5(Z)A(6) + A(7)X_1 + A(8)X_2 + A(9)X_3 + A(10)X_4)$
$C = Y_2(0.5(Z)A(11) + A(12)X_1 + A(13)X_2 + A(14)X_3 + A(15)X_4)$
$D = Y_3(0.5(Z)A(16) + A(17)X_1 + A(18)X_2 + A(19)X_3 + A(20)X_4)$
$E = Y_4(0.5(Z)A(21) + A(22)X_1 + A(23)X_2 + A(24)X_3 + A(25)X_4)$
$F = Y_5(0.5(Z)A(26) + A(27)X_1 + A(28)X_2 + A(29)X_3 + A(30)X_4)$
$P_v = A + B + C + D + E + F$

Section (2)

Follow the same procedure as in Section (2.1)
$272.03449K \leq T < 360.92778K$
$0.0wt\% \leq PC \leq 100.0wt\%$

A(1) $3.7173\text{x}10^{+01}$	A(2) $1.9211\text{x}10^{+01}$	A(3) $4.3453\text{x}10^{+00}$	A(4) $5.7224\text{x}10^{-01}$	A(5) $7.0691\text{x}10^{-02}$	A(6) $9.0808\text{x}10^{-02}$
A(7) $2.2473\text{x}10^{+01}$	A(8) $1.1212\text{x}10^{+01}$	A(9) $2.3399\text{x}10^{+00}$	A(10) $2.4366\text{x}10^{-01}$	A(11) $2.0406\text{x}10^{-02}$	A(12) $4.4588\text{x}10^{-02}$
A(13) $3.1567\text{x}10^{+00}$	A(14) $1.4732\text{x}10^{+00}$	A(15) $2.7733\text{x}10^{-01}$	A(16) $1.1513\text{x}10^{-01}$	A(17) $4.8693\text{x}10^{-02}$	A(18) $6.7805\text{x}10^{-02}$
A(19) $-1.7614\text{x}10^{+00}$	A(20) $-6.3199\text{x}10^{-01}$	A(21) $3.2855\text{x}10^{-02}$	A(22) $1.6148\text{x}10^{-01}$	A(23) $8.6963\text{x}10^{-02}$	A(24) $7.5052\text{x}10^{-02}$
A(25) $-7.4369\text{x}10^{-03}$	A(26) $2.5397\text{x}10^{-01}$	A(27) $2.3136\text{x}10^{-01}$	A(28) $2.1380\text{x}10^{-01}$	A(29) $1.0714\text{x}10^{-01}$	A(30) $8.7518\text{x}10^{-02}$
A(31) $7.0209\text{x}10^{-01}$	A(32) $4.4647\text{x}10^{-01}$	A(33) $2.1997\text{x}10^{-01}$	A(34) $1.6861\text{x}10^{-01}$	A(35) $9.9284\text{x}10^{-02}$	A(36) $6.3939\text{x}10^{-02}$

A(37)	A(38)	A(39)	A(40)	A(41)	A(42)
$1.9149\text{x}10^{-01}$	$1.5159\text{x}10^{-01}$	$1.2422\text{x}10^{-01}$	$1.1215\text{x}10^{-01}$	$6.3871\text{x}10^{-02}$	$3.8718\text{x}10^{-02}$

$$U = (2.0T - (360.927778 + 272.038888))/(360.927778 - 272.038888)$$
$$V = (2.0PC - 100.0)/100.0$$

$$X_1 = cos(arccosU)$$
$$X_2 = cos(2.0arccosU)$$
$$X_3 = cos(3.0arccosU)$$
$$X_4 = cos(4.0arccosU)$$
$$X_5 = cos(5.0arccosU)$$

$$Y_1 = cos(arccosV)$$
$$Y_2 = cos(2.0arccosV)$$
$$Y_3 = cos(3.0arccosV)$$
$$Y_4 = cos(4.0arccosV)$$
$$Y_5 = cos(5.0arccosV)$$
$$Z = 1.0$$

$$A = 0.25(Z)A\ (1) + 0.5A(2)X_1 + 0.5A(3)X_2 + 0.5A(4)X_3 + 0.5A(5)X4 + 0.5A(6)X_5$$
$$B = Y_1(0.5(Z)A(7) + A(8) * X_1 + A(9)X_2 + A(10)X_3 + A(11)X_4 + A(12)X_5)$$
$$C = Y_2(0.5(Z)A(13) + A(14)X_1 + A(15)X_2 + A(16)X_3 + A(17)X_4 + A(18)X_5)$$
$$D = Y_3(0.5(Z)A(19) + A(20)X_1 + A(21)X_2 + A(22)X_3 + A(23)X_4 + A(24)X_5)$$
$$E = Y_4(0.5(Z)A(25) + A(26)X_1 + A(27)X_2 + A(28)X_3 + A(29)X_4 + A(30)X_5)$$
$$F = Y_5(0.5(Z)A(31) + A(32)X_1 + A(33)X_2 + A(34)X_3 + A(35)X_4 + A(36)X_5)$$
$$G = Y_6(0.5(Z)A(37) + A(38)X_1 + A(39)X_2 + A(40)X_3 + A(41)X_4 + A(42)X_5)$$
$$P_v = A + B + C + D + E + F + G$$

4.4. Liquid Thermal Conductivity

Conde-Petit (2006) proposed a quasi-ideal correlation to calculate thermal conductivity as shown in Equation (18)

$$\lambda_m = x\lambda_{NH_3}(\rho^{+}_{NH_3}) + (1-x)\lambda_{H_2O}(T^{*}_{H_2O}) \qquad (18)$$

Where T*, the liquid temperature when quasi-ideal state is assumed, is calculated from the procedure presented in Conde-Petit (2006) and the density parameter is calculated from Equation (19) (Conde-Petit (2006).

$$\rho^{+}_{NH_3} = \rho_{NH_3}(T^{*}_{NH_3})x^{0.425} \qquad (19)$$

The method presented here to calculate the thermal conductivity of the mixture requires the values of the property at the pure state.

The liquid thermal conductivity can be expressed for pure ammonia and water as follows:

$$\lambda_{NH_3} = 2551.30 - 376.62\,\text{x}10^{-02}\text{T} - 29.35x\ 10^{-04}T^2 \qquad (20)$$

$$\lambda_{H_2O} = -916.62 + 1254.73\,\text{x}10^{-02}T - 152.12x\ 10^{-04}T^2 \qquad (21)$$

If $\lambda_{NH_3} > \lambda_{H_2O}$ $A = \lambda_{NH_3}$

If $\lambda_{NH_3} > \lambda_{H_2O}$ $B = \lambda_{H_2O}$

If $\lambda_{NH_3} \geq \lambda_{H_2O}$ $X = x_m$

where x_m is mass fraction of ammonia in ammonia-water solution.

If $\lambda_{NH_3} \leq \lambda_{H_2O}$ $A = \lambda_{H_2O}$

If $\lambda_{NH_3} \leq \lambda_{H_2O}$ $B = \lambda_{NH_3}$

If ($\lambda_{NH_3} \leq \lambda_{H_2O}$ X=1.0-x_m

$$\lambda_m = ((1.0-X)^{1.5}(A-B)+B)4.187x10^{-07} \qquad (22)$$

4.5. Liquid density of ammonia-water solution

To calculate the density of the mixture, it is regarded as a quasi-ideal solution the procedure presented by Conde-Petit (2006) is used. This is represented by Equation (23)

$$\rho_{sol} = \text{x}\rho_{NH_3\,T^{*}_{NH_3}} + (1-x)\rho_{H_2O\,T^{*}_{H_2O}} + \Delta\rho_{T^{\updownarrow}_{m,x}} \qquad (23)$$

To correct for non-ideality, the excess density value $\Delta\rho_{T^{\updownarrow}_{m,x}}$ value is added. This is calculated from Equation (24)

$$\Delta\rho_{T^{\updownarrow}_{m,x}} = x(1-x) - Ax^2(1-x)\rho^{0.5}_{NH_3 T^{*}_{NH_3}}\rho^{0.5}_{H_2O\,T^{*}_{H_2O}} \qquad (24)$$

where

$$T^{\updownarrow}_{m,x} = \frac{T_m}{T_{c,H_2O}} \qquad (25)$$

The parameter A is calculated from the expression (Conde-Petit, 2006)

$$A = \sum_{i=0}^{2} A_{1,i}\, T_m^{\updownarrow i} + 1/x(\sum_{i=0}^{2} A_{2,i}\, T_m^{\updownarrow i} \qquad (26)$$

where A_1 and A_2 are defined as follows (Conde-Petit, 2006)

	i=0	*i=1*	*i=2*
A_1	-2.410	8.310	-6.924
A_2	2.118	-4.050	4.443

The $T^*$are calculated as follows (Conde-Petit, 2006).

T_{c,H_2O}= 647.15 (27)

T_{c,NH_3}= 405.15 (28)

The critical temperature of the mixture is represented by Equation (29) (Conde-Petit, 2006).

$T_{c,m}=a_0+a_1x+a_2x^2+a_3x^3+a_4x^4$ (29)

Where

a_0	647.14
a_1	-199.822371
a_2	109.035522
a_3	-239.626217
a_4	88.689691

$\tau = 1.0 - T_m / T_{c,m}$ (30)

$\theta = T_m / T_{c,m}$ (31)

$T^*_{NH_3} = \theta T_{c,NH_3}$ (32)

$T^*_{H_2O} = \theta T_{H_2O}$ (33)

The density of pure water is calculated from Equation (34) using $T^*_{H_2O}$.

$\rho_{H_2O} = a_1T^6+a_2T^5 + a_3T^4+a_4T^3 + a_5T^2 + a_6T + a_7$ (34)

where

$a_1 = -9.031x10^{-12}$, a_2 = 2.3572302x10^{-08},

a_3 =-2.5271885494x10^{-05},$a_4 = 0.014237361079319$,

a_5 =-4.446432939499160, a_6 = 729.744030889966,

a_7 = -48149.866657815

To calculate density of pure ammonia liquid, the equation presented by Cragoe and Harper (1923) is used. Also $T^*_{NH_3}$ is used.

V=Absolute value of (*133.0-(T-273.15)*) (35)

D=(4.2830+0.813055V$^{0.5}$-0.0082861V)/(1.0+0.424805V$^{0.5}$+0.015938V) (36)

$\rho_{NH_3} = (1.0/D)1.0x10^{+03}$ (37)

4.6. Dynamic Viscosity for the Liquid Ammonia-Water Solution

Conde-Petit (2006) presented an equation that is considered to represent accurately experimental data. The model proposed used pure ammonia and water viscosity values at reduced temperature.

$$ln(\eta_m) = xln\eta_{NH_3,T^*_{NH_3}} + (1-x)ln\eta_{H_2O,T^*_{H_2O}} + \Delta\eta_{T_m,x} \qquad (38)$$

$$\Delta\eta_{T_m,x} = \left(0.534 - 0.815\frac{T_m}{T_{c,H_2O}}\right)F(x) \qquad (39)$$

$$F(x) = 6.38(1-x)^{1,125x}\left(1 - e^{-0.585x(1-x)^{0.18}}\right)ln\left(\eta^{0.5}_{NH_3,T^*_{NH_3}}\eta^{0.5}_{H_2O,T^*_{H_2O}}\right) \qquad (40)$$

The reduced temperature are calculated from the critical temperatures as follows (Conde-Petit, 2006)

$T_{c,H_2O} = 374.0 + 273.15$ (41)

$T_{c,NH_3} = 132.0 + 273.15$ (42)

The critical temperature of the mixture is represented by Equation (43) (Conde-Petit, 2006).

$T_{cm} = a_0 + a_1x + a_2x^2 + a_3x^3 + a_4x^4$ (43)

where

a_0	647.14
a_1	-199.822371
a_2	109.035522
a_3	-239.626217
a_4	88.689691

$T = 1 - T_{sol}/T_{c,m}$ (44)

$\theta = T_{sol}/T_{c,m}$ (45)

$T^*_{NH_3} = \theta\, T_{c,NH_3}$ (46)

$T^*_{H_2O} = \theta\, T_{c,H_2O}$ (47)

The viscosity of water is ammonia and water are calculated as follows.

$$\eta_{NH_3} = 1.0x10^{+03}\left(10^{(-8.591+867.4/T+2.681T^{-02}-36.12T^{-06}T^2)}\right) \quad (48)$$

$$\eta_{H_2O} = aT^6 + bT^5 + cT^4 + dT^3 + eT^2 + fT + g \quad (49)$$

where

a	4.524x10^{-17}
b	- 1.2692894x10^{-13}
c	1.4709554085x10^{-10}
d	-9.014393368784x10^{-8}
e	3.082715014561580X10^{-5}
f	-0.00558379692056264
g	0.419428700262259

4.7. Calculation of liquid-liquid diffusivity

The correlation proposed by Wilke and Chang (1955) is used to calculate the liquid-liquid diffusivity. This is represented as shown in Equation (50).

$$D_{12}^{o} = 7.4x10^{-8}\left(\frac{\Psi_2 M_2)^{\frac{1}{2}}T}{(V_{21}^{0.6}\eta}\right) \quad (50)$$

where D_{12}^{o} is the diffusivity of solute 1 into solvent 2 in cm^2s^{-1}. M_2 is the molecular weight of the solvent (water =18.015), T is the temperature in K, η is the viscosity of of the solvent in cP and V_{21} is the solute molar volume at its normal boiling point in cm^3/mol and Ψ_2 is the association factor of solvent 2 (water). For water the association factor for water is 2.26.The solute molar volume (ammonia) can be established once the density and molecular mass is known. The density of the solvent(water) and dynamic viscosity of solute (ammonia) are calculated following the procedures in Sections (4.5) and (4.6) respectively.

4.8. Mass Transfer Coefficient (Diffusivity - Ammonia Vapour into Ammonia-Water Solution)

To calculate the diffusivity of ammonia vapour into ammonia-water solution, an adaptation of the Wilke-Chang Equation is used (Conde-Petit, 2006). This is represented by

$$D_{12}^{o} = 117.282x10^{-18}\left(\frac{\Psi_{12} M_{12})^{\frac{1}{2}}T}{(V_{21}^{0.6}\eta_{12}}\right) \quad (51)$$

where D_{12}^{o} is the diffusivity of ammonia gas (1)into Ammonia water solution (2) in m^2s^{-1}.

$$\Psi_{12} = x\Psi_{NH_3} + (1-x)\Psi_{H_2O} \quad (52)$$

$$M_{12} = xM_{NH_3} + (1-x)M_{H_2O} \quad (53)$$

$$V_{21} = \frac{M_{NH_3}}{\rho_{H_2O,T_m}} \quad (54)$$

The parameters are defined as follows

$\Psi_{NH_3} = 1.7$, $\Psi_{H_2O} = 2.6$

$M_{NH_3} = 17.03$ $M_{H_2O} = 18.0152$

η_{12} is the dynamic viscosity in Pa s.

4.9. Surface Tension of Mixture

The model proposed by King and Hall and Ware has been applied in the calculation of surface tension (Conde-Petit, 2006).

$$\sigma_m = x\sigma_{NH_{3},T_{NH_3}^{*}} + (1-x)\sigma_{H_2O,T_{H_2O}^{*}} + \Delta\sigma_{T_{m,x}} \quad (55)$$

$$\Delta\sigma_{T_{m,x}} = -\left(\sigma_{H_2O,T_{H_2O}^{*}} - \sigma_{NH_{3},T_{NH_3}^{*}}\right)F(x) \quad (56)$$

$$F(x) = 1.442(1-x)[1 - e^{-2.5x^4}] = 1.106x[1 - e^{-2.5(1-x)^6}] \quad (57)$$

The values of the surface tension of the pure components are represented by:

$$\sigma_{NH_{3,}} = [\left(\frac{405.55 - T}{405.55 - 228.15}\right)]^{1.1548x36.67} \quad (58)$$

$$\sigma_{H_2O} = [\left(\frac{647.35 - T}{647.35 - 298.15}\right)]^{0.8105x71.97} \quad (59)$$

$T_{H_2O}^{*}$ and $T_{NH_3}^{*}$ are calculated as presented in the Section (4.5).

The specific heat capacity of water (kJkg^{-1}K^{-1}) can be expressed as:

$$C_{p_{H_2O,l}} = 4.187(0.6741 + 2.825x10^{-03}T - 8.371x10^{-06}T^2 + 8.601x10^{-09}T^3) \quad (60)$$

The specific heat capacity of ammonia vapour (kJkg^{-1}K^{-1}) can be expressed as;

$$C_{p_{NH_{3,,v}}} = 4.187(6.07 + 8.23x10^{-03}T - 0.16x10^{-06}T^2 - 0.66x10^{-09}T^3)/17.031 \quad (61)$$

5.0 ANALYSIS OF RESULTS

Table 4 shows values of properties calculated for 2 conditions from the correlations outlined in this paper. Generally absorbers for ammonia-water refrigeration systems operate at conditions within this range (Mumah, 1991). As can be seen from Table (5), there are low deviations between calculated properties and experimental values from literature. The low deviation is significant as wide deviations affect the accuracy of the design of the absorber significantly.

Figures (3) to (14) show the variations of various properties and absorber dimensions for various capacities (1kW to 4 kW) of the ammonia-water absorption refrigeration system. The major properties investigated include the variation of the following properties across the absorber; ammonia vapour temperature, ammonia-water solution temperature, cooling water temperature, and flow rates of ammonia water solution and ammonia vapour. In the procedure presented in this study, the final coil lengths are reached once there is total absorption of the ammonia vapour. The absorption process is exothermic and the increase in temperature decreases the rate of absorption. The cooling water ensures that the ammonia-water solution temperature does not vary significantly during the absorption process thereby maintaining the rate of absorption of the ammonia by the ammonia-water solution. Heat removal also ensures that absorption is completed at shorter coil lengths. From an economic perspective, shorter coil length means lower absorber cost.

Table 4: Values of properties for 2 conditions usually encountered in absorbers of ammonia water refrigeration system

Property	**30wT% of Ammonia and 303.15k**	**50WT% of Ammonia and 323.15k**	**Reference data**	**Maximum % Deviations**
Liquid Enthalpy (kJ/kg)	$-0.79522\,x10^{+02}$	$-0.23477\,x10^{+02}$	Macriss *et al.* (1964), Mumah *et al.* (1991) Mumah *et al.* (2021)	±0.554
Vapour Heat Enthalpy (kJ/kg)	$0.13938\,x10^{+04}$	$0.13750\,x10^{+04}$	Macriss *et al.* (1964), Mumah *et al.* (1991) Mumah *et al.* (2021)	±1.24
Saturated Vapour Pressure (Bar)	$0.10377x10^{+01}$	$0.6862x10^{+01}$	Macriss *et al.* (1964), Mumah *et al.* (1991) Mumah *et al.* (2021)	±0.452
Liquid Density(kg/m^3)	$0.86436\,x10^{+03}$	$0.77000\,x10^{+03}$	(Conde-Petit, 2006)	±0.655
Liquid Dynamic Viscosity (Pa s)	$0.96225\,x10^{-03}$	$0.51183\,x10^{-03}$	(Conde-Petit, 2006)	±1.22
Vapour-Solution Diffusivity (m^2/s)	$0.24983\,x10^{-08}$	$0.44592\,x10^{-08}$	(Conde-Petit, 2006)	± 1.54
Liquid Conductivity(Wm^{-1} K^{-1})	$0.56290\,x10^{+00}$	$0.50756\,x10^{+00}$	(Conde-Petit, 2006)	± 1.62
Surface Tension(N/m)	$0.51408\,x10^{-01}$	$0.36372\,x10^{-01}$	(Conde-Petit, 2006)	±0.95
Ammonia Liquid-Water Diffusivity (m^2/s)	$0.23905\,x10^{-08}$	$0.37350\,x10^{-08}$	(Conde-Petit, 2006)	± 1.32
Water Specific Heat Capacity (kJkg^{-1}K^{-1})	$0.41904\,x10^{+01}$	$0.41999\,x10^{+01}$	Mumah *et al.*(1991) Mumah *et al.* (2021)	±0.44
Ammonia Vapour Specific Heat Capacity (kJkg^{-1}K^{-1})	$0.20975\,x10^{+01}$	$0.21365\,x10^{+01}$	Mumah *et al.* (1991) Mumah *et al.* (2021)	±3.23

Figures (3) to (6) show the variations of the temperature of the various fluids across the length of the coil. As can be seen from these plots, there are convergences of the temperatures of the ammonia vapour and ammonia water solution along the coil. Furthermore, there is a decrease of the temperature gradient between the cooling water and the ammonia-water solution along the length of the coil. This is expected since the simulation was done for concurrent flow.

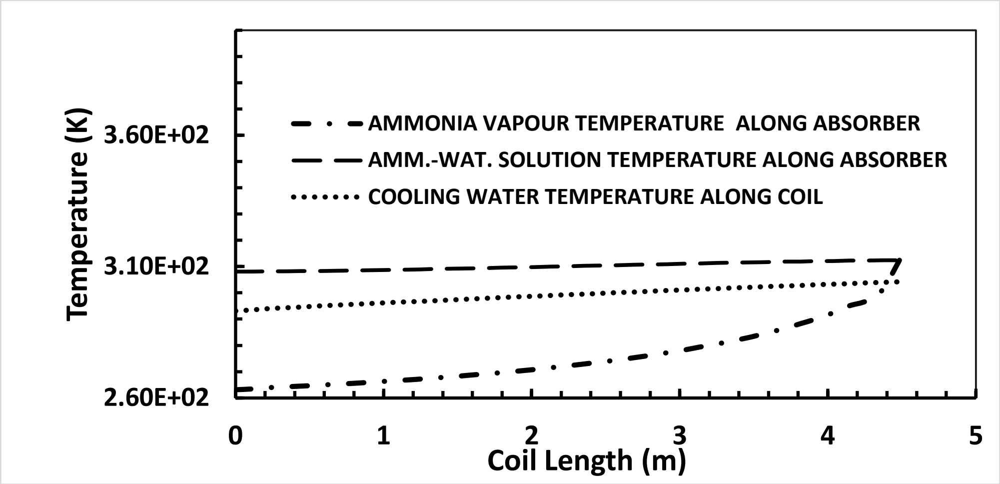

Figure 3. Change of ammonia vapour and ammonia-water solution temperatures along the coil length for 1.0 kW cooling capacity for ammonia-water absorption refrigeration system

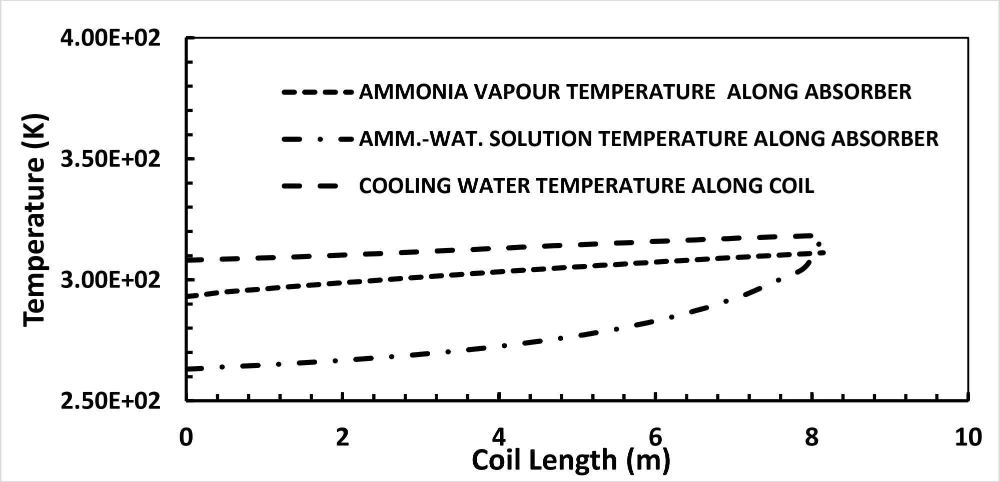

Figure 4. Change of ammonia vapour and ammonia-water solution temperatures along coil length for 2.0 kW cooling capacity for ammonia-water absorption refrigeration system

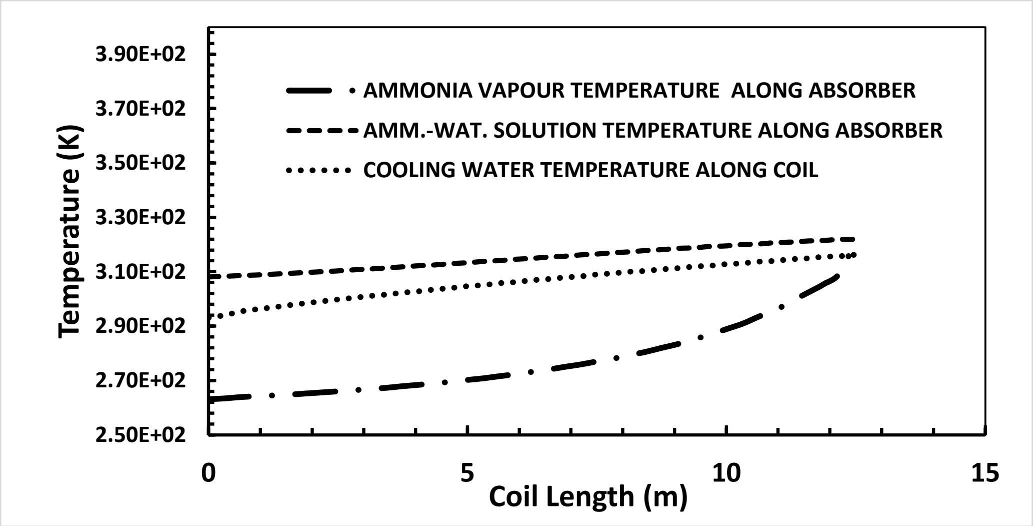

Figure 5. Change of ammonia vapour and ammonia water solution temperatures along coil length for 3.0 kW cooling capacity for ammonia-water absorption refrigeration system

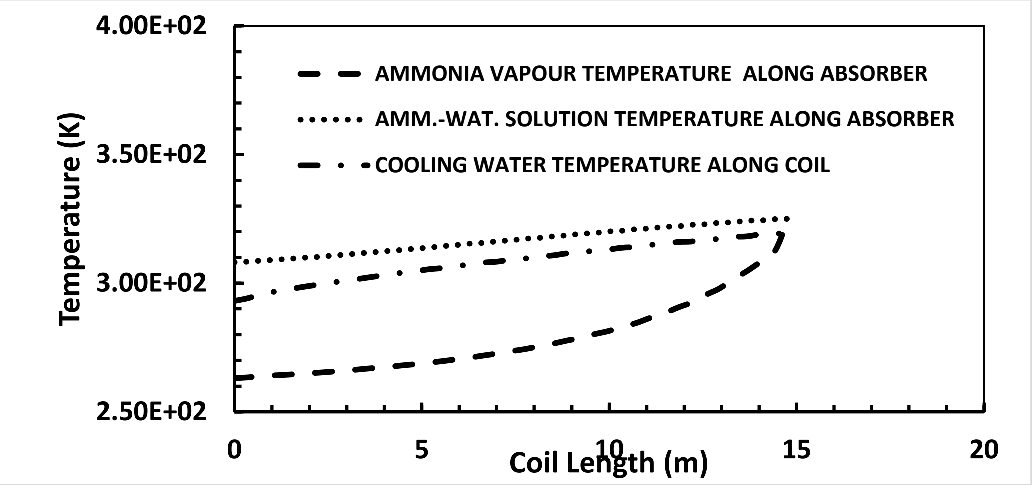

Figure 6. Change of ammonia vapour and ammonia-water solution temperatures along coil length for 4.0 kW cooling capacity for ammonia-water absorption refrigeration system

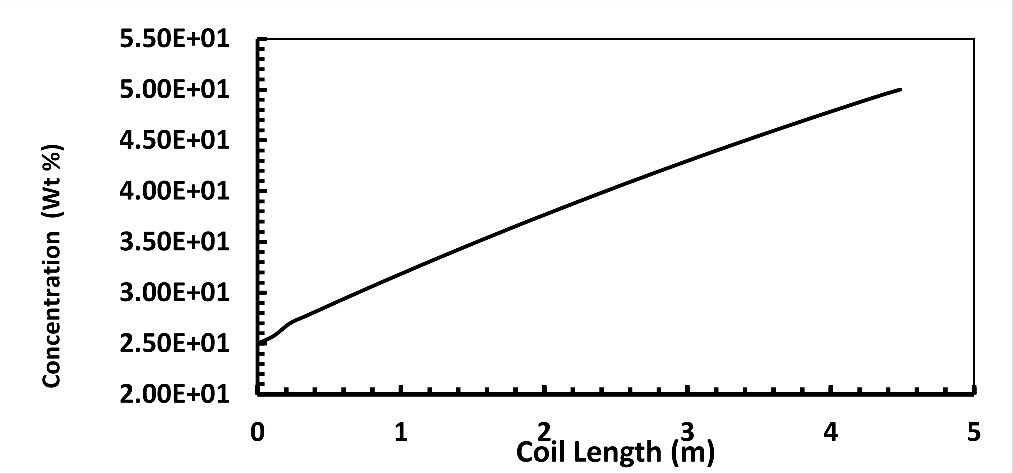

Figure 7: Change of ammonia-water solution concentration along coil length for 1.0 kW cooling capacity for ammonia-water absorption refrigeration system

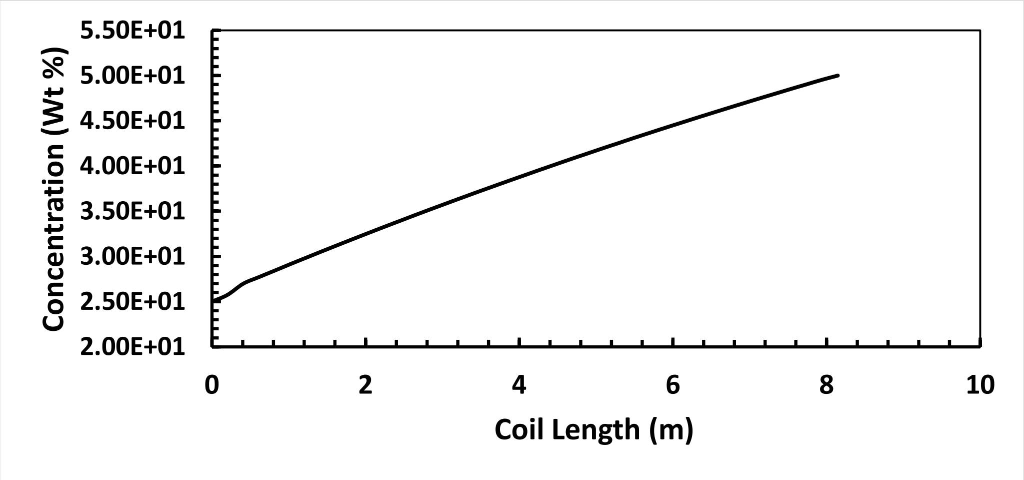

Figure 8: Change of ammonia-water solution concentration along coil length for 2.0 kW cooling capacity for ammonia-water absorption refrigeration system

DOI:10.51975/22370102.som
Journal of the Nigerian Society of Chemical Engineers, 37(1), 2022

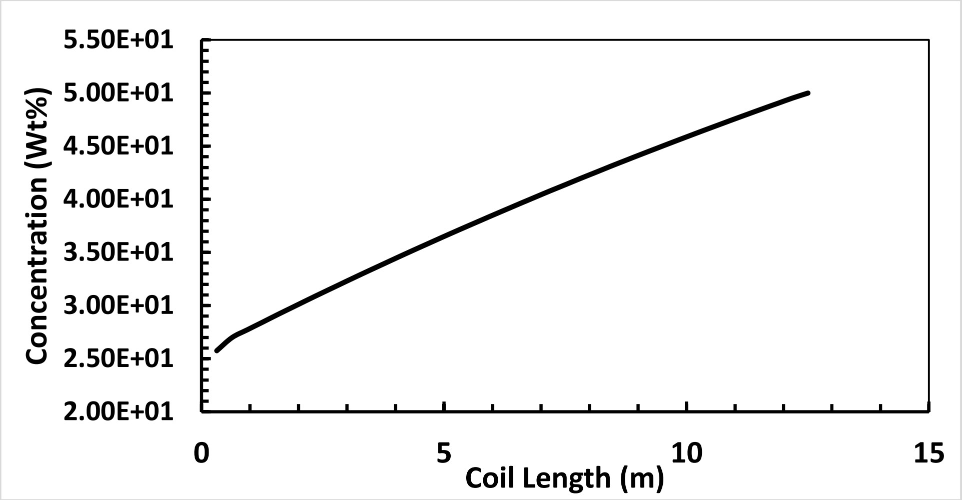

Figure 9: Change of ammonia-water solution concentration along coil length for 3.0 kW cooling capacity for ammonia-water absorption refrigeration system

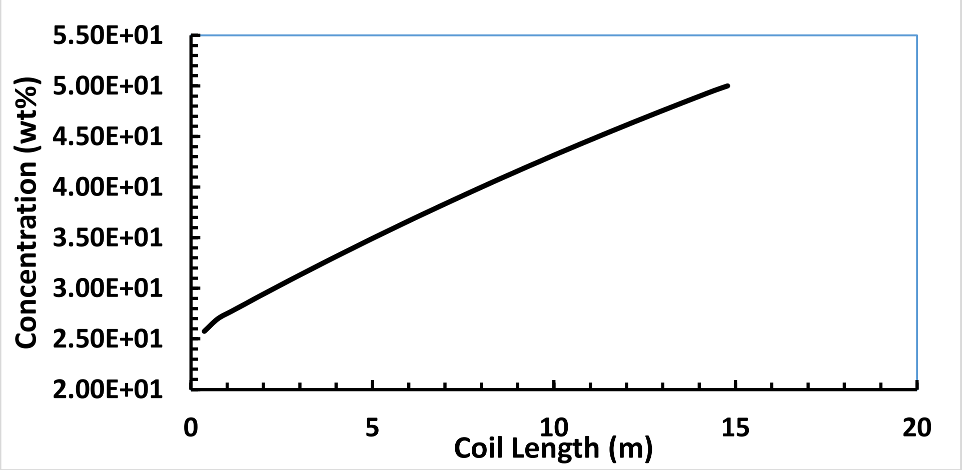

Figure 10: Change of ammonia-water solution concentration along coil length for 4.0 kW cooling capacity for ammonia-water absorption refrigeration system

Figures (7) to (10) show the changes of concentration along the length of the coil as the ammonia vapour from the evaporator is absorbed. The simulation was performed for an inlet concentration of 20 wt%. As the coiling capacity of the system increases, the length of the coil also increases.

Figures (11) to (14) show the variation of the flow rate of ammonia water solution and ammonia vapour respectively. As the ammonia is being absorbed, the ammonia vapour flow rate decreases and the flow rate of the ammonia-water solution increases. The final length of the coil is determined after the ammonia vapour flow rate is zero, that is, when there is complete absorption of the ammonia vapour by the ammonia-water solution in the absorber.

Table 5 shows the dimensions and values of various parameters for the coiled absorber calculated from the design procedure outlined in this paper. Table 5 can be used to predict coil lengths for other capacities within the range and for predicting the lengths for other capacities, not above 8 kW. Table (5) also presents the heat transfer coefficients and the mass transfer coefficients for the 4 capacities simulated in this study. From Table 5, values of the coefficients are within the ranges obtained from literature (Narváez-Romo *et al*., 2017; Conde-Petit, 2006). As can be seen from Table (5), as the cooling capacity increases, there is an increase in the ammonia vapour flow rate. However, there are corresponding decreases in the heat and mass transfer coefficients. As noted by Sabharwall *et al.* (2009), considering the ammonia-water solution as an incompressible fluid , the heat transfer coefficient decreases by up to 10% with a threefold increase in the mass flow rate if turbulent flow regime is considered. Sabharwall *et al.* (2009) however noted there is an increase in the heat transfer coefficient if the area is maintained constant but this will result in an increase in the pressure drop which is usually a critical consideration in any heat exchanger design. An elevation in pressure drop can lead to an elevation of boiling point and therefore any benefit derived from the higher heat transfer coefficient may be lost Sabharwall *et al.* (2009).

Figure (15) shows a schematic of the absorber for 1.0 kW cooling capacity. For other capacities (2 kW, 3 kW and 4 kW), Table 5 can be used to produce similar schematics.

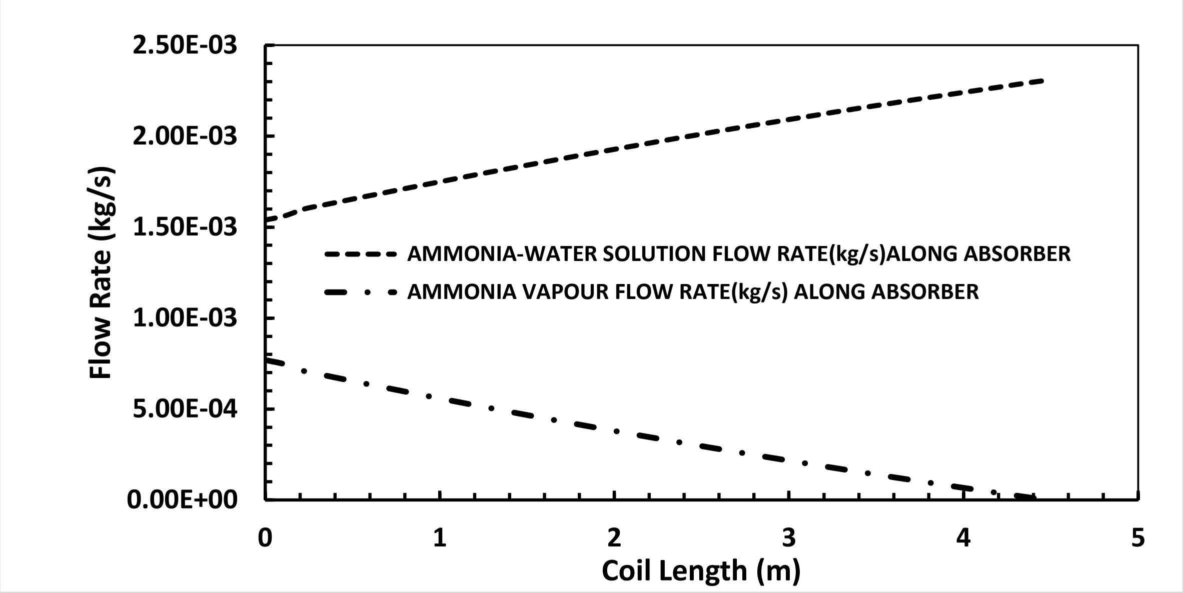

Figure 11. Change of ammonia vapour and ammonia-water solution flow rates along Coil length for 1.0 kW cooling capacity for ammonia-water absorption refrigeration system

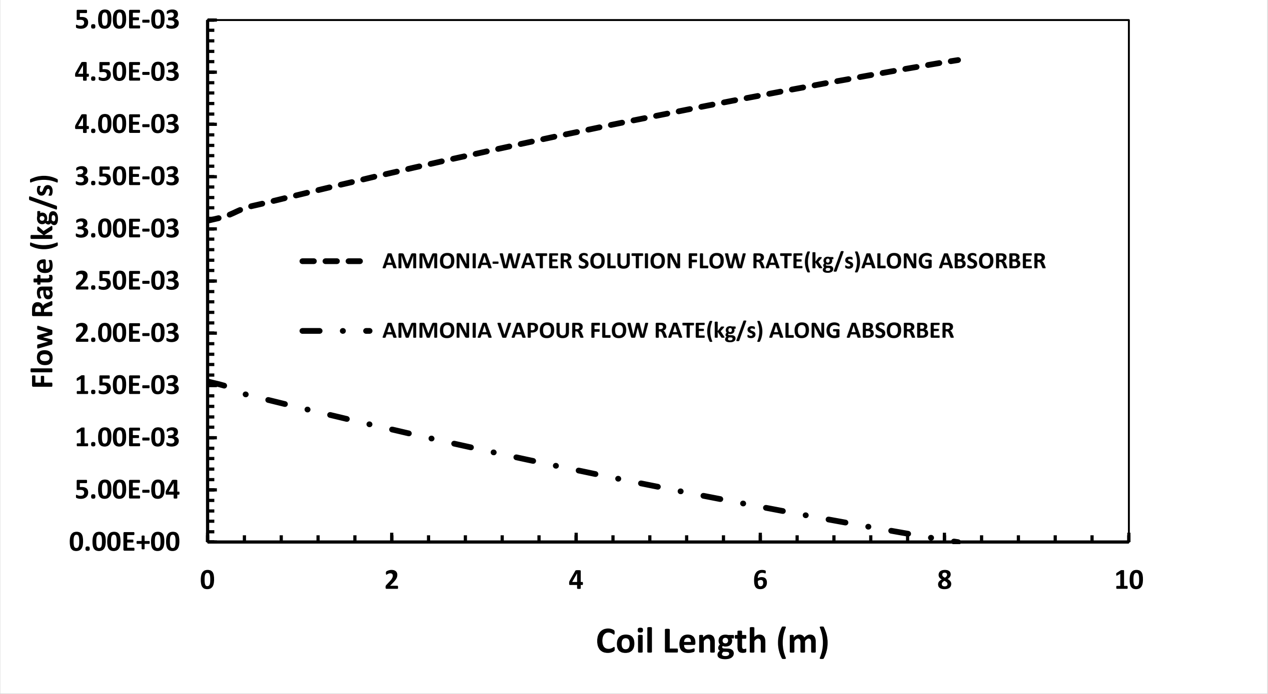

Figure 12. Change of ammonia vapour and ammonia-water solution flow rates along coil length for 2.0 kW cooling capacity for ammonia-water absorption refrigeration system

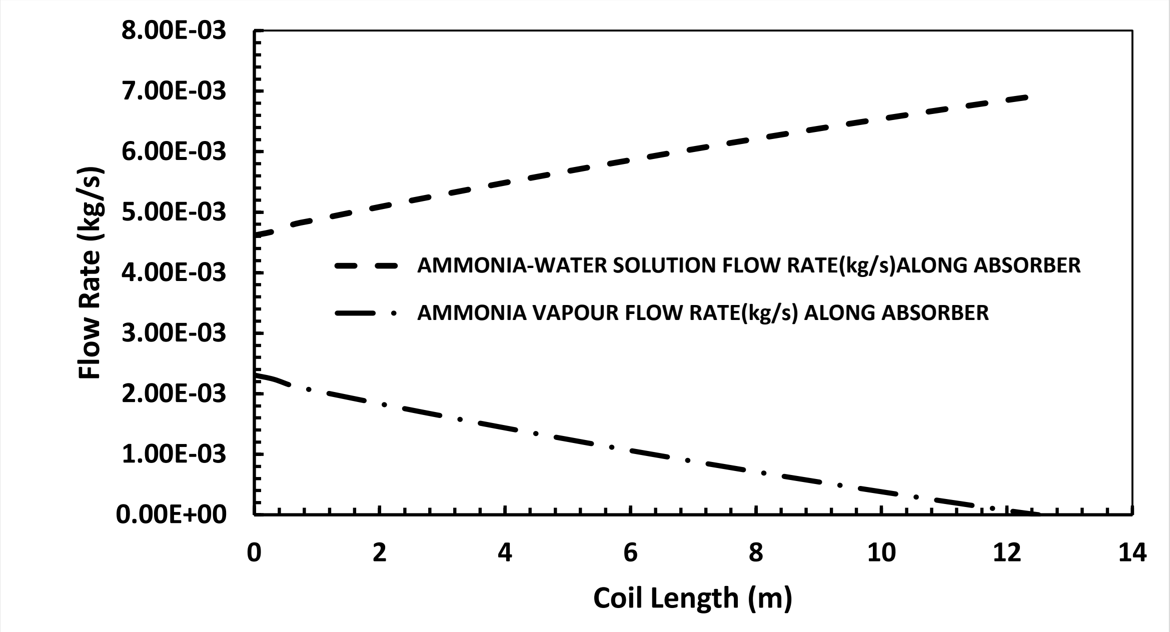

Figure 13. Change of ammonia vapour and ammonia-water solution flow rates along coil length for 3.0 kW cooling capacity for ammonia-water absorption refrigeration system

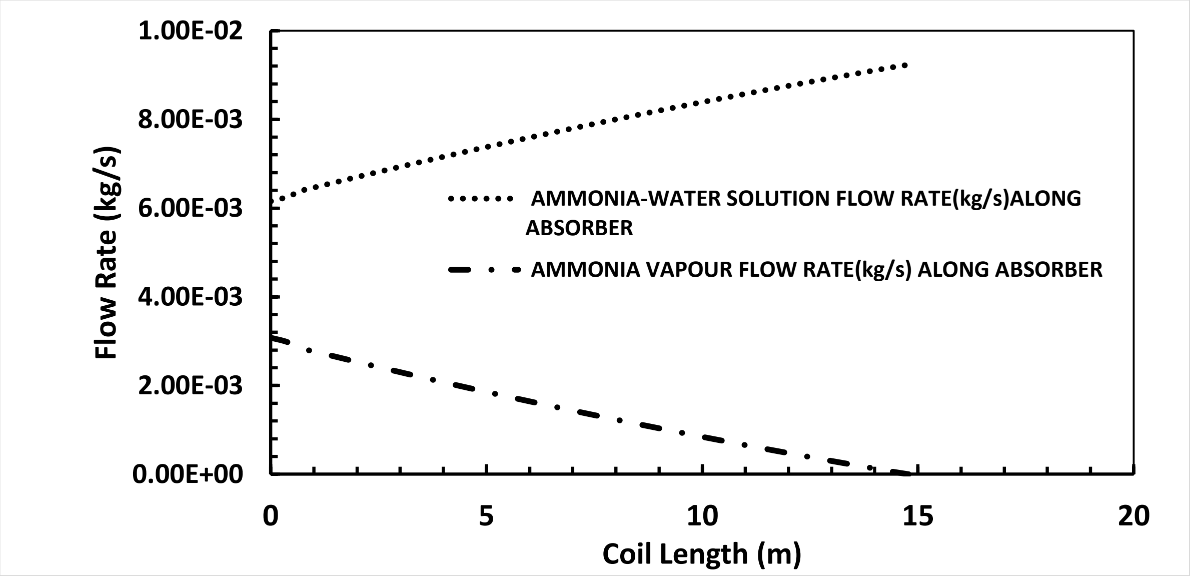

Figure 14. Change of ammonia vapour and ammonia-water solution flow rates along coil length for 4.0 kW cooling capacity for ammonia-water absorption refrigeration system

6.0 CONCLUSION

Predicting heat and mass transfer characteristics is vital to the proper design of any absorber that requires heat removal. The performance of the absorber significantly affected the overall efficiency of any absorption refrigeration system. Simultaneous heat and mass transfer operations occur in the absorber of an ammonia-water refrigeration system and, therefore, the design procedure takes the two transfer operations into effect.

Table 5: Dimensions and values of various parameters for the cooling coiled absorber

Parameters	1 kW	2kW	3kW	4kW
Tube Total Area (m^2)	$0.8945130x10^{-01}$	$0.1625200x10^{+00}$	$0.2494555x10^{+00}$	$0.2949135x10^{+00}$
Coil Length (m)	$0.4483973x10^{+01}$	$0.8146726x10^{+01}$	$0.1250459x10^{+02}$	$0.1478329x10^{+02}$
Coil Height (m)	$0.3873500x10^{+00}$	$0.7175500x10^{+00}$	$0.1073150x10^{+01}$	$0.1276350x10^{+01}$
Tube Internal Diameter (m)	$0.4572x10^{-02}$	$0.4572x10^{-02}$	$0.4572x10^{-02}$	$0.4572x10^{-02}$
Tube Thickness (m)	$0.889x10^{-03}$	$0.889x10^{-03}$	$0.889x10^{-03}$	$0.889x10^{-03}$
Shell Height (m)	$0.48735x10^{+00}$	$0.81755x10^{+00}$	$0.117315x10^{+01}$	$0.137635x10^{+01}$
Diameter of Shell (m)	$0.1270000x10^{+00}$	$0.127x10^{+00}$	$0.127x10^{+00}$	$0.127x10^{+00}$
Number of Coils (-)	$0.1500000x10^{+02}$	$0.28x10^{+02}$	$0.42x10^{+02}$	$0.50x10^{+02}$
Flow Rate of Weak Solution at Inlet (kg/s)	$0.1538571x10^{-02}$	$0.3077142x10^{-02}$	$0.4615713x10^{-02}$	$0.6154284x10^{-02}$
Temperature of Weak Solution at Inlet (K)	$0.30815x10^{+03}$	$0.30815x10^{+03}$	$0.30815x10^{+03}$	$0.30815x10^{+03}$
Concentration of Weak Solution at Inlet (wt %)	$0.250x10^{+02}$	$0.250x10^{+02}$	$0.250x10^{+02}$	$0.250x10^{+02}$
Outlet Concentration of Absorber (wt %)	$0.50x10^{+02}$	$0.50x10^{+02}$	$0.50x10^{+02}$	$0.50x10^{+02}$
Flow Rate, of Ammonia Vapour (Inlet) (kg/s)	$0.7692855x10^{-03}$	$0.1538571x10^{-02}$	$0.2307857x10^{-02}$	$0.3077142x10^{-02}$
Temperature of Ammonia Vapour at Inlet (K)	$0.26315x10^{+03}$	$0.26315x10^{+03}$	$0.26315x10^{+03}$	$0.26315x10^{+03}$
Concentration of Ammonia Vapour (wt %)	$0.100x10^{+03}$	$0.10x10^{+03}$	$0.10x10^{+03}$	$0.10x10^{+03}$
Pitch of Coil (m)	$0.254x10^{-01}$	$0.254x10^{-01}$	$0.254x10^{-01}$	$0.254x10^{-01}$
Overall Heat Transfer Coefficient $kWm^{-2}K^{-1}$)	0.4427	0.4376	0.4208	0.4309
Mass Transfer Coefficient (m^2s^{-1})	$3.721 \text{ x}10^{-9}$	$4.206 \text{ x}10^{-9}$	$4.556 \text{ x}10^{-9}$	$4.856 \text{ x}10^{-9}$

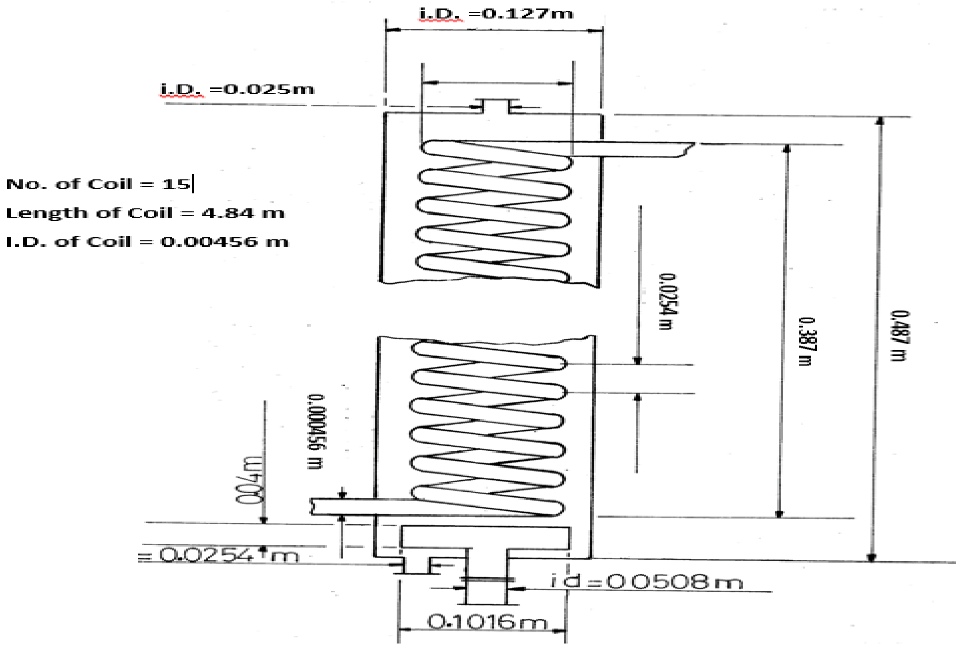

Figure 15: Schematic of the Absorber for 1kW capacity of cooling

Procedures for calculating the various thermodynamic properties required for the design of the absorber of an ammonia-water refrigeration system parameters have been presented in this paper, and their percentage deviations from experimental values presented in literature calculated. Results show relatively low percentage deviations and so are applied for the design and simulation of the absorber. Designs of the absorber for various cooling capacities have been carried out in this paper. The variation of ammonia vapour temperature, ammonia-water solution temperature, cooling water temperature, and flow rates of ammonia-water solution and ammonia vapour across the absorber is investigated for four capacities. The calculated overall heat transfer coefficients for the absorption process for the four cooling capacities (1kW, 2kW, 3kW and 4kW) were 0.4427, 0.4376, 0.4208 and 0.4309 $kWm^{-2}K^{-1}$ while the mass transfer coefficients were 3.721 $x10^{-9}$, 4.206 $x10^{-9}$, 4.556 $x10^{-9}$and 4.856 $x10^{-9}$ m^2s^{-1} respectively. The design produced coiled lengths of 4.484 m, 8.1467 m, 12.50459 m, 14.78329 m for 1 kW, 2 kW, 3 kW and 4 kW, respectively. Co-current flow was considered in this study, but the procedure can also be applied to countercurrent flow.

Acknowledgement:
The authors wish to acknowledge the funding provided for this research work by Tertiary Education Trust Fund (TETFund) under the National Research Fund (NRF) Grants. REF: TETF/R&D/CE/NRF/POLY/KADUNA/VOL. 1/B5).

7.0 REFERENCES

Bonafoni, G., Capata, R. (2015). Proposed Design Procedure of a Helical Coil Heat Exchanger for an Orc Energy Recovery System for Vehicular Application. Mechanics, Materials Science & Engineering Journal, Magnolithe, 2015, 10.13140 /RG.2.1.2503.5282 (https://hal.archives-ouvertes.fr/hal-01302036)

Cerezo, J., Bourouis M, Vallès M, Coronas A, Best R. (2009) Experimental study of an ammonia-water bubble absorber using a plate heat exchanger for absorption refrigeration machines. *Applied Thermal Engineering*; 29: pp. 1005-1011.

Chapra, S.C. and R.P. Canale (2020), Numerical Methods for Engineers McGraw-Hill

Chung, W. J., Seung Sun An, Yong Tae Kang. (2014) Thermal performance estimation of ammonia-water plate bubble absorbers for compression/absorption hybrid heat pump application. *Energy*. Online publication date: 1-Aug-2014.

Conde-Petit, M. (2006) Thermophysical Properties of NH_3/H_2O Mixtures for the Industrial Design of Absorption Refrigeration Equipment. Formulation for Industrial Use. M. Conde Engineering, Zurich, Switzerland

Cragoe, C. S., E.C. McKelvey, and G.F. O'Connor, Specific Volume of Saturated Ammonia Vapor, Sci. Pap. Bureau of Standards. 18, 655 (1923)

Goel, N., Goswami DY. (2005) Analysis of a countercurrent vapour flow absorber. International *Journal of Heat and Mass Transfer*; 48(12) pp 83-92

https://www.worldbank.org/en/news/press-release/2021/02/05/nigeria-to-improve-electricity-access-and-services-to-citizens

https://axaxl.com › pdfs › prc7212ammoniahazardsv1: Property Risk Consulting: Ammonia Hazards/

Ioan, S., Calin Sebarchievici. (2015) General review of solar-powered closed sorption refrigeration systems. *Energy Conversion and Management, t*105, 403-422. Online publication date: 1-Nov-2015.

Issa, M, Ishida, K. and M. Monde (2002). Mass and heat transfers during absorption of ammonia into ammonia water mixture. *International Communications in Heat and Mass Transfer* 29(6):773-786

Killion, J.D., Garimella S. (2001) A critical review of models of coupled heat and mass transfer in falling-film absorption. *International Journal of refrigeration*;24(7), pp. 55-97

Kumar, M. and R. K. Das (2015) Thermodynamic study of diffusion absorption refrigeration system with organic fluid, *International Journal of Mechanical Engineering and Robotics Research,* 4(1), pp. 474-484

Macriss, R. A., Eakin, B. E., Ellington, R. T., Huebler, J. (1964) Physical and thermodynamic properties of ammonia-water mixtures; Research Bulletin - Institute of Gas Technology; No. 34.

Mittermaier M, Ziegler F. (2015) Theoretical evaluation of absorption and desorption processes under typical conditions for chillers and heat transformers. International Journal of Refrigeration.

Mumah, S.N. (1991). Simulation and Optimisation of Solar-powered and Hybrid Heat Pump System for cooling. (PhD Thesis, Department of Chemical Engineering, Ahmadu Bello University, Zaria, Nigeria)

Mumah, S.N., Adefila S.S. and Arinze E.A.;1994; Properties generation procedures for First and Second law analyses of Ammonia-water heat pump system; *Energy Conversion and Management*, Vol. 35, No.8, pp 727-736; published by Pergamon Press Exeter, England.

Mumah, S. N. (2008) 'Selection of heat storage materials for ammonia-water and lithium bromide solar-powered absorption heat pump systems', *International Journal of Sustainable Energy*, 27:2, pp. 81-93

Mumah, S.N., H.F. Akande, K.Y. Mudi O. Olaniyan and Francis Samuel (2021) Development and Validation of Correlations for Liquid and Vapour Enthalpies and Procedures for generating Saturated Vapour Pressure for Ammonia-Water Solution, submitted for publication to the *Nigerian Journal of Technological Research*, Federal University of Technology, Minna, Nigeria.

Narváez-Romo, B., Marx Chhay, Elí Zavaleta-Aguilar, José Simões-Moreira (2017) A Critical Review of Heat and Mass Transfer Correlations for LiBr-H_2O and NH_3-H_2O Absorption Refrigeration Machines Using Falling Liquid Film Technology. Applied Thermal Engineering, Elsevier, 2017, 10.1016/j.applthermaleng.2017.05.092 hal-01527189

Ramm, V.M. (1968) Absorption of gases, Israel Program for Scientific Translation, Jerusalem

Sabharwall, P., V. Utgikar and F. Gunnerson (2009) Effect of Mass Flow Rate on the Convective Heat Transfer Coefficient: Analysis for Constant Velocity and Constant Area Case, *Nuclear Technology*, 166, 2, pp 197-200

Sherwood, T.K. and R.L. Pigford (1952) Absorption and extraction; 2nd Edition, McGraw-Hill Books Co. New York

Siddiqui, M.U., S.A.M. Said. (2015) A review of solar-powered absorption systems. *Renewable and Sustainable Energy Reviews* 42, 93-115. Online publication date: 1-Feb-2015.

Triché, D., Sylvain Bonnot, Maxime Perier-Muzet, François Boudéhenn, Hélène Demasles, Nadia Caney (2015), International Conference on Solar Heating and Cooling for Buildings and Industry

Wilke, C. R., and P. Chang, (1955) Correlation for diffusion coefficient in dilute solutions, *AIChE*, 1 (2), pp. 264-270.

DOI:10.51975/22370103.som
Journal of the Nigerian Society of Chemical Engineers, 37(1), 2022

WEB APPLICATIONS AND ONLINE RESOURCES FOR 21ST CENTURY CHEMICAL ENGINEERING EDUCATION: A REVIEW

***Irivwegu, M. and Amadi, E. E**
Department of Chemical Engineering, University of Port Harcourt, Choba, Nigeria
*Email of the Corresponding author: mudiagairivwegu@gmail.com

ABSTRACT
The chemical engineering profession has evolved over the years. The areas in which chemical engineering finds application has gone beyond the boundaries of the traditional chemical industry. The demands of the industry on new chemical engineering graduates have changed over the years and the Covid-19 pandemic brought an urgency on institutions of higher learning to move learning online. The use of web applications and online resources are not new and can be blended with in-class lectures to deliver some of the deliverables expected from chemical engineering programs including ability to handle experiments remotely. This paper explores the trend in teaching chemical engineering in a more digitized world, highlight some of these digital tools and how they can be used effectively in chemical engineering education.

Keywords: *Covid-19; flipped classroom; chemical engineering education; virtual lab; digital tools.*

1. INTRODUCTION

The aftermath of lockdowns as a result of the Covid-19 pandemic that disrupted traditional in-class learning in 2020, has brought to the fore the need to incorporate virtual classrooms and effectively use online and/or web resources for teaching and learning (Dhawan, 2020). Online resources are web pages, documents and other resources including support software that are accessible via the internet (IGI Global). Web applications are application software that are stored on a remote server and delivered over the internet through a browser interface. Since they can be accessed across the web they do not need to be downloaded. The use of online resources as part of the instructional materials in engineering education is not a recent phenomenon. The increased access to internet, internet-based services and internet-enabled devices has revolutionized how we connect and how easily information can be shared.

The educational industry in recent years has been adjusting to the impact of these rapid advances in digital technologies on traditional teaching and lecture delivery style. This adjustment is evident from the inclusion of online learning resources and the use of digital products for lecture delivering, resource sharing, collaboration and assessment of student's performance. Educational and research materials are relatively much easier to assess. The chemical engineering departments of higher institutions are not left out of this shift from traditional classroom learning to flipped classrooms.

While the use of these e-resources is not new and several universities especially those in more advanced countries have well developed online or virtual learning platforms and technologies for delivering online lectures, the pandemic brought a new urgency and challenged the way engineering education is delivered (Ventura-Medina, 2020). It is safe to say that Covid-19 brought the future of learning faster than we envisaged. Engineering education is based on science and mathematics and this makes delivery across virtual platforms relatively difficult compared to other disciplines. This is so because of the need for laboratory work and complex mathematical equations (Ventura-Medina, 2020). However, advances in technology over years has permitted representation of complex structures and objects by computers. E-learning resources are also now available in different forms and can be easily accessed and downloaded by students.

Banday *et al.* (2014) x-rayed current practices of Information, Communication and Technology (ICT) and e-learning in engineering education. They reported that adoption of ICT tools is still at the early stages in developing countries due to lack of sufficient Information Technology (IT) infrastructure. For some universities in developing countries like Nigeria, the lockdowns as a response to slow the spread of Covid-19, gravely affected learning since most institutions were not equipped with the needed technology to completely move lectures online. This was also made difficult with the cost of internet services for those who decided to use the Zoom video conferencing platform to deliver lectures.

This paper reviews the trend of teaching chemical engineering and examines how web resources and online tools are becoming indispensable instructional materials in today's educational institutions especially post Covid. Examples of how these resources are being used in several institutions of higher learning are highlighted and some simple digital tools that can be useful for instructional and assessment purposes are introduced.

2. THE TREND: FLIPPED CLASSROOM

Flipped classroom is a type of blended learning where the primary educational materials are studied by students at home and then worked on in the classroom. Flipped classrooms apply active learning and digital methods to present lecture content. The online resources used in these classes will typically include videos, quizzes, reading or some form of group activity before the actual classes. The aim is to increase students' engagement and learning. For this model to work effectively, the instructional materials are made available before the class in form of screencast, lecture videos and e-notes.

Nogales-Delgado *et al.* (2020) shared experiences on how the chemical engineering laboratory at the University of Extremadura, managed the university teaching and final year degree follow-up during the Covid-19 lockdowns. The tools used included a virtual learning site, an online library and guides to help teachers and students. They mentioned that the transition was almost seamless because the school had a robust and active virtual platform prior to the pandemic but noted that in-class learning still presents many advantages and suggested a blend with online classes. This is where Flipped Classrooms come in since it is a blend of in-person and online learning. It shifts the attention from the lecturer to a more student-centred approach.

Several universities like the University of Cambridge, University of Michigan, University of Colorado and the Massachusetts Institute of Technology (MIT) have lecture materials and videos for several of their chemical engineering courses on their website. These online resources are available to students to study before the course is taken. Falconer *et al.* (2018) in their paper introduced an e-learning site (www.learncheme.com) from the Chemical Engineering department of the University of Colorado. This chemical engineering resource website provides screencasts of lectures, simulations of chemical engineering processes, ConcepTest (a resource provided by Course instructors to test student's knowledge of the key concepts taught in a topic) and several online resources for the students such as access to POLYMATH. With these resources that can be easily accessed over the web, the students are introduced to the lecture content at home to practice and test their understanding before they come to class. Students can also follow the videos and screencasts made by the Lecturers and catch up on areas missed during the class.

Chen *et al.* (2019) investigated several research issues of applying flipped learning in science education and mentioned that the flipped classroom experience can be divided into three stages (before-class stage, in-the class stage and after-class stage). From reviewing several literatures, they found that most flipped classroom studies in science education used instructional videos as the major learning material in the before-class stage, problem-based learning as the major learning strategy in class and administered examinations in the after-class stage to explore the learning outcomes. They concluded that flipped learning "generally meets the expectation of scholars and is still developing in the science education domain."

3. VIRTUAL LABORATORIES – WEBLAB

One of the biggest challenges of delivering engineering lectures and taking courses online is the lack of access to Laboratory infrastructure (Ventura-Medina, 2020). Acquiring hands-on laboratory practical skills is an important part of the teaching and learning outcome for any chemical engineering degree (Glassey and Magalhaes, 2020; Bhute *et al.*, 2021). Remote and virtual laboratories (commonly called Weblabs) are becoming popular as tools to develop important practical skills. These virtual laboratory experiments involve the use of technology to simulate and/or replicate actual laboratory experiments (Byrne *et al.*, 2012). They are not entirely new as several universities have developed virtual laboratories operated across the web for some popular chemical engineering processes.

For teaching laboratory skills, Bhute *et al*. (2021) classified the nature of experiments and their learning outcomes into three broad categories – experiential learning activities where the hands-on-skill is the objective, experiential learning activities where equipment is used but not the main objective of the experiment (the focus is to develop data collection, analysis and interpretation skills) and experiential learning that use simulations as the primary mode of experimentation. The first two categories are usually difficult to operate virtually due to their reliance on physical equipment, while learning outcomes for the third category can be achieved using virtual laboratories. Experiments and their learning objectives in chemical engineering usually cover aspects from the three categories. However, efforts have been made over the years to deliver experiments from the first two categories remotely and using virtual platforms especially with recent advances in technologies such as augmented reality, AR (Bhute *et al.*, 2021). These efforts became intensified with the outbreak of Covid-19.

For example, the Department of Chemical Engineering at the Imperial College London, is working on a project called CREATE Lab. The aim as reported on their website (www.imperial.ac.uk) is to transform traditional teaching laboratory facilities to a modular lab approach where experiments can be done remotely and students can participate in lab projects in real time using multiple controllable cameras, remote access over the lab computers and HoloLens Augmented Reality (AR) headset provided by Microsoft. This means that equipment can be controlled remotely and students can participate and perform experiments even though they are not physically present in the lab.

The idea of performing experiments remotely, is not a new one as Selmer *et al.* (2007) described the technology involved in making educational experiments available on the internet and how they are used for teaching at MIT, the University of Cambridge and the University of Leipzig. These weblabs provide access to experiments from any location through the internet and brings lab experience to the lecture hall. MIT used these remotely controlled experiments to teach Transport Phenomena to year three students. One of the heat exchangers used in that experiment, have also been used by the University of Texas and University of Cambridge (Selmer *et al.*, 2007). The heat exchanger was operated and controlled remotely by the students. This is one of the advantages of web applications and online resources, since resources can be shared easily. They concluded from the review of existing weblabs and students' experiences that it is a very useful tool in chemical engineering education but cannot replace hands-on experiments.

Bansagi and Rodgers (2017) describes a HTML/JS/CSS-based interactive graphic web application developed for teaching and learning of Liquid-Liquid Extraction (LLE) using ternary diagrams. This web application was tested by chemical engineering students at the University of Manchester. They mentioned that from a survey of students who used the application, many of the respondents liked using the application and felt that it aided their understanding. Domingues et al. (2010) also described the design and implementation of two virtual laboratories for biochemical engineering education at the University of Minho Vlabs project. Students can access the virtual lab, animations and videos via the web on https://vlabs.uminho.pt. A virtual integrated platform to teach chemical processes developed by the Universities of Coimbra and Porto, in Portugal is reported by Rasteiro *et al.* (2012). Virtual experiments and videos of experiments conducted in the laboratory on areas such as separation, reaction and process systems engineering and also biological processes are available on the university's website. They also investigated efforts to teach chemical processes through this online platform to secondary school students to expose them to basics needed for a career in chemical engineering.

It is also interesting to note that some real-life industrial processes are operated remotely. Therefore, exposing students early, on how to operate and handle equipment remotely, apply theoretical knowledge to collect, analyze and interpret data can come in handy when they are in the industry (Selmer *et al.*, 2007). This learning outcome can be achieved via virtual learning environment. The ability to use chemical engineering tools and software (e.g., ASPEN HYSYS and Design Expert) for generating data, designing of experiments and analysis of process variables and outcomes are learning outcomes that can be delivered effectively using web and online resources.

4. MASSIVE OPEN ONLINE COURSES (MOOCS)

The internet has also made it possible for formal learning to go beyond the walls of a classroom. The advent of Massive Open Online Courses (MOOCs) has challenged how lectures are delivered. MOOCs offer educational resources in a distant and virtual mode. There are several online or web platforms offering chemical engineering and a host of other courses online. Students can sign up and take the classes at any time or place. Massive Open Online Courses (MOOCs) offer specialize courses on how to use technological tools relevant to chemical engineers. Some of the popular courses offered include: MATLAB, Python programming, Machine learning for engineering production as well as courses on core chemical engineering topics like thermodynamics, chemical reaction engineering, chemical kinetics, transport processes and numerical analysis. A few of these MOOCs that offer a range of courses online both free and paid include:

- Khan Academy
- Udemy
- edX
- MIT OpenCourseWare
- Alison
- Coursera
- LinkedIn Learning

Several universities have courses on some of these platforms already. Activities can also be planned by course instructors to encourage students to enrol in these programs and take some prerequisite courses online. Educators can also adapt laboratory experiments and integrate them into MOOCs to improve the learning experience (Bhute *et al.*, 2021). Lecturers can also take advantage of these platforms to give lectures on specialty areas and probably make extra income from there.

5. SIMPLE DIGITAL TOOLS FOR INSTRUCTION, CLASS MANAGEMENT AND ASSESSMENT

Assessing students' performances and maintaining the integrity of assessments can prove quite difficult with online learning. However, there are some quite handy digital tools that course instructors and lecturers can explore to help them manage their class, follow student's progress, receive and mark assignments as well as give continuous assessments especially as quiz. Google classroom and Piazza are popular examples of digital tools that can be used for class management. Students can interact amongst themselves, submit assignments and get feedbacks from Lecturers. Lecture materials can be uploaded and accessed by learners at any time. For class assessment and quizzes; google forms, Jotform, Quizstar, ProProf are some popular tools that can be used. FormsApp is a good mobile application available on Google play store for creating quizzes and questionnaires. It can be used to create timed quiz or assessments. Gradescope (www.gradescope.com) is another online digital tool that has the potential to revolutionize the grading of handwritten scripts in an easier and efficient way online.

While some of these tools may not totally eliminate cheating on quizzes or assignments, they can serve as great tools to help manage online learning. For example, many undergraduate chemical engineering classes in Nigerian Universities are usually quite large. This makes it difficult for course lecturers who are overwhelmed with the teaching of several classes in a semester to give test or assignments to assess students' understanding of the subject and/or topic been taught. Using digital tools like Google Forms, lecturers can give quizzes that are graded automatically, with the learners seeing the correct answers to questions given, when they submit. Since this process is automated, it makes the job of the course lecturer easy and allows for several test and quizzes to be administered during the duration of the lectures. This way, students can tell early enough if they understand the concepts been taught and can ask better questions in class. Lecturers can also quickly identify areas or concept that are not properly understood by the students.

Video recordings and screencasts form part of the instructional materials in a flipped classroom. They are becoming popular as instructional material in digitized classrooms. In fact, several individuals and schools are exploring video recordings and screencasts as the major mode of instruction especially for online courses. Faculties and departments can develop or make budgets for tools that can help course instructors make videos easily. They can subscribe to using video recording software like Camtasia or explore the recording capabilities of common video conferencing apps like Zoom or Google Meet with a premium account. Where these budgets are not readily available, lecturers and instructors looking to explore these digital options can make lecture presentations or lecture videos using free screen recording tools like Loom. Loom offers an easy and free way to record videos and screen recordings with the click of a button. It can be used to record the content on your computer screen along with a footage of yourself narrating and/or explaining concepts. Loom can be used on both Windows and Mac devices, can be downloaded as a desktop app or used from the Chrome internet browser (TT College of Human Sciences, 2020).

6. MOBILE LEARNING AND SOCIAL MEDIA AS A TOOL FOR CHEMICAL ENGINEERING EDUCATION

Many students own mobile and/or portable devices that can be used to access the internet (Diaz-Sainz *et al.*, 2021). Mobile learning is an important part of electronic learning. It takes advantage of the opportunities offered by mobile devices since they are portable and enable students to learn even outside the class (Diaz-Sainz *et al.,* 2021). Lecturers can easily use them in developing lessons and several of the digital tools discussed in the previous session, can be used on mobile devices or have a mobile version. Diaz-Sainz *et al.* (2021) did an extensive review with case studies of several digital tools available on mobile devices and common amongst chemical engineering lecturers. They reported that the feedback from majority of the case studies were satisfactory and had positive effects on the learning process.

A lot of people especially young students are on social media. While they may not be on social media to learn chemical engineering, it can be explored to drive home some chemical engineering principles or showcase popular chemical engineering processes. Klvunja (2015) investigated the use of social media technologies (Google Circles Learning Communities – GCLCs) in the education of teachers at a teacher training university in Australia. The results obtained suggested that learners in this age spend most of their time on social media and use it effectively for communication. The paper suggests that it makes sense therefore to communicate with these learners through this media.

There are pages on Facebook (Process Engineering World and Core Chemical Engineering) that give chemical engineering content and interactions. These pages feature animations showing and explaining the working principles of several reactors and their applications. These animated videos bring to life the principles taught in class and help the students identify popular equipment mentioned in class. There are also lots of videos on YouTube explaining chemical engineering concepts, processes and principles. These videos also come in handy for teaching and learning how to use tools such as MATLAB, Python Programming and ASPEN HYSYS. They can also form part of the lecture materials used in class.

The chemical engineering department of the Imperial College London has an Instagram page and a YouTube channel that is been used to explain recent advances on the use of their CREATE Lab. The University of Colorado also use YouTube videos to explain concepts and teach how screencasts can be made and used for instructional purposes. Diaz-Sainz *et al.* (2021) reviewed some works on the use of social networks such as Instagram and Snapchat to teach chemistry, biochemistry and natural sciences. It was reported that the interest of students in the subject areas increased significantly, when images and videos of laboratory set-up were shared using these platforms. Lecturers in Nigerian Universities can also take advantage of these social media platforms to put their work out.

7. BEST PRACTICES AND FUTURE TRENDS

Given the extent to which the work environment of the chemical engineer is changing, the teaching and learning methods in chemical and process engineering must attempt to capture the spectacular progress of information technology and sciences and equip graduates with skills to work successfully in a broad range of job environments (Molzahn and Wittstock, 2002; Cristea *et al.,* 2005). The teaching of Chemical Engineering students using online resources involve the use of ICT for delivery of classroom lectures, demonstration and conducting of laboratory experiments, class management and administration. One of the biggest challenges of online delivery of lectures for chemical engineering programs as stated earlier, is hands-on laboratory exposure. Though, computer and web-based resources have proved to be useful tools in providing virtual laboratory and project learning experiences as well as delivering course content (Drury and O’Connell, 2006), the practical exposure of students to laboratory procedures are still very important. However, the latest trend is to include delivering of laboratory work using remote and virtual platforms.

The development of weblabs is an interesting and very viable concept to transfer much needed industrial exposure to students (Agrawal and Srivastava, 2007). Several institutions like the University of Cambridge are partnering with Automation companies to set up weblabs using an industrial operating system that essentially features all the important elements of an industrial plant (Selmer *et al.*, 2007). A deliberate effort needs to be made by institutions to partner with technological companies and industry practitioners to create course content that delivers on the core chemical engineering curriculum and is relevant to the expanding role of chemical engineers in the industry.

The future of using online resources for teaching chemical engineering do not only involve accessing information but also involves the use of same resources for teaching and collaborative purposes over a network of connections. Chemical Engineering departments especially in African Universities as a matter of urgency should begin to seek collaborations amongst themselves and counterpart abroad on how to include these resources for teaching and learning.

8. CONCLUSION

Online resources provide a veritable avenue to share resources, research findings and be up-to-date with trends in a fast-evolving and more digitalized world. While in-class teaching, hands-on laboratory work and contact time between lecturers and students are still very necessary, they should be blended with web and online resources for more wholesome learning. This also speeds up the process of getting feedbacks for projects done and helps student's understanding of basic chemical engineering concepts. Web applications and online resources enables meaningful collaboration amongst universities and engineering faculties since resources and research findings can easily be shared, accessed quickly and course materials can be updated easily.

9. RECOMMENDATIONS

The following are recommendations based on the review done in this paper:

- IT platforms should be created to facilitate sharing of experiments and resources between institutions and industry.
- Web based frameworks that allow for seamless and quick incorporation of new experiments and learning materials should be developed.
- For institutions in developing countries, classroom designs should include gadgets and equipment to aid the use of online resources.
- Video simulations of industrial processes should be developed and promoted on social media platforms to expose learners to real life industrial processes early on. Professional bodies and Industry practitioners can contribute by offering training videos and simulation of popular industrial processes.

10. REFERENCES

Agrawal, A. and Srivastava, S. (2007), *Weblab: A Generic Architecture for Remote Laboratories,* [Paper Presentation]. 15th International Conference on Advanced Computing and Communications (ADCOM 2007). DOI: 10.1109/ADCOM.2007.140

Banday, M.T., Ahmed, M. and Jan, T.R. (2014), Applications of E-learning in Engineering Education: A Case Study, *Procedia – Social and Behavioral Sciences 123, 406-413.*

Bansagi, T. and Rodgers, T.L. (2017), Graphic Web-Apps for Teaching Ternary Diagrams and Liquid-Liquid Extraction, *Education for Chemical Engineers*. https://doi.org/10.1016/j.ece

Bhute, V.J., Inguva, P., Shah, U. and Brechtelsbauer, C. (2021), Transforming traditional teaching laboratories for effective remote delivery – A review, *Education for Chemical Engineers, 35(2021), 96-104.*

Byrne, E., Barett, J., Jiricek, T., Kelly, A. and Sullivan, C.O. (2012), *Experiences of Using a Web-based Virtual Shell and Tube Heat Exchanger Experiment by Adult Continuing Learners,* [Paper Presentation]. 4th International Symposium for Engineering Education, The University of Sheffield, July 2012, UK.

Chen, C., Huang, N.N and Hwang, G. (2019). Findings and Implications of Flipped Science learning Research: A review of journal publications, *Interactive Learning Environments,* DOI:10.1080/10494820.2019.1690528

Cristea, V.M., Imre-Lucaci, A., Nagy, Z.K. and Agachi, S.P. (2005), E-tools for Education and Research in Chemical Engineering. *Chem. Bull. "POLITEHNICA" 50(64)1-2*

Dhawan, S. (2020), Online learning: A Panacea in the Time of COVID-19 Crisis, *Journal of Educational Technology, 49(1), 5-22*

Diaz-Sainz, G., Perez, G., Gomez-Coma, L., Ortiz-Martinez, V.M., Dominguez-Ramos, A., Ibanez, R. and Rivero, M.J. (2021). Mobile learning in Chemical Engineering: An outlook based on case studies, *Education for Chemical Engineers, 35(2021), 132-145*

Domingues, L., Rocha, I., Dourado, F., Alves, M. and Ferreira, E.C. (2010), Virtual Laboratories in (bio)Chemical Engineering Education, *Education for Chemical Engineers, 5(2010), e22-e27*

Drury, H., Langrish, T. and O'Carroll, P. (2006), Online Approach to teaching Report Writing in

Chemical Engineering: Implementation and Evaluation, *Int. J. Engrg Ed. 22(4), 858-867*

Falconer, J.I, DeGrazia, J., Medlin, J.W. and McDaniel K. (2018), LearnChemE.com: Teaching/Learning Resources for Chemical Engineering, *Chemical Engineering Education 52(3), 176-180*

Feise, H.J. and Schaer, E. (2021), Mastering Digitized Chemical Engineering, *Education for Chemical Engineers, 34(2021), 78-86.* https://doi.org/10.1016/j.ece.2020.11.011

Gauss, B., Jimenez, L., Urbas, L. Hausmanns, C. and Wozny, G. (2004), E-learning in Process and Chemical Engineering – Trends and Challenges, Proceedings at the IEEE International Conference on Advanced Learning Technologies (ICALT'04)

IGI Global (n.d.). What is Online Resource? Retrieved on March 25th from https://www.igi-global.com/dictionary/use-of-e-resources-through-consortia-with-special-reference-to-college-libraries/21050

Imperial College London (n.d.), Remote Learning and Teaching – Remote Lab, retrieved on September 12, 2021 from https://www.imperial.ac.uk/chemical-engineering/courses/undergraduate/remote-learning-and-teaching/

Klvunla, C. (2015), The use of social media Technologies in Collaborative Learning in Higher Education, *International Journal of Conceptions on Management and Social Sciences 3(4), 74-80*

Molzahn, M. and Wittstock, K. (2002), Chemical Engineers for the 21st Century – Challenges for University Education, *Chem Eng. Technol. 25 (2002)3. 231-235*

Nogales-Delgado, S., Suero, S.R. and Martin, J.M.E (2020), Covid-19 Outbreak: Insights about Teaching Tasks in a Chemical Engineering Laboratory, *Educ. Sci. 10, 226*

Rasteiro, M.G., Carvalho, M.G., Ferreira, A., Gaudencio, C.B. and Granjo, J. (2012), Using a Web Platform Developed for Teaching of Chemical Processes to reach Secondary School Students, *iJOE, Special Issue 2(8), 42-48.*

Selmer, A., Kraft, M., Moros, R. and Colton, C.K. (2007), Weblabs in Chemical Engineering Education, *Trans IChemE, Part D, Education for Chemical Engineers, 2, 38-45*

TT College of Human Sciences (2020). How to use Loom for Video and Screen Recording? Retrieved from https://www.depts.ttu.edu/hs/news/posts/2020/blog/how-to-record-videos-with-loom.php

Ventura-Medina, E. (2020). Chemical Engineering Education in the Age of Disruption. Retrieved from https://ichemblog.org/2020/08/26/chemical-engineering-educatin-in-the-in on March 6th, 2021.

DOI:10.51975/22370104.som

Journal of the Nigerian Society of Chemical Engineers, 37(1), 2022

ASSESSMENT OF SOLAR ENERGY POTENTIAL OF NIGERIA FOR SOLAR POWER GENERATION THROUGH NUMERICAL SOLAR IRRADIANCE MAPPING

***Mumah, S.N.[1], Akande, H.F.[1], Oyawoye, M. R.[1], Mudi, K.Y.[1], Samuel, F.[1] and Olaniyan, I.O.[2]**

[1] Department of Chemical Engineering, Kaduna Polytechnic, Kaduna, Nigeria
[2] Department of Civil Engineering, Kaduna Polytechnic, Kaduna, Nigeria
E-mail addresses: mumahsdoyi@kadunapolytechnic.edu.ng (S. N. Mumah)
hassan.akande@kadunapolytechnic.edu.ng (H. F. Akande)
m_r_oyawoye@kadunapolytechnic.edu.ng (M. R. Oyawoye)
m.kehinde@kadunapolytechnic.edu.ng (K. Y. Mudi)
francissamuel@kadunapolytechnic.edu.ng (F. Samuel)
dejoolaniyan@kadunapolytechnic.edu.ng (I. O. Olaniyan)
* Corresponding author

ABSTRACT

Any thorough analysis of solar energy applications in the country requires a solar resources map. Many maps have been developed, but they only show distributions presented in colour intensities. Solar irradiance can only be estimated from such maps. Using on the spot experimental data for solar map production does not provide accurate maps because various climatic and environmental conditions such as dust haze and cloud cover affect the amount of solar energy that reaches the ground in various locations in Nigeria. This is particularly true during the harmattan period. Therefore data generated from such methods cannot be used to develop accurate numerical solar maps. Data for such applications should be collected from outer space and over a long time for various locations. The National Aeronautics and Space Administration (NASA) provides a resources base for such data. The data used in this study covered 25 years (1994-2018). The average daily global solar irradiance for various longitude-latitude nodes is calculated from such data. With these data available, it is possible to estimate the average daily global solar irradiance for any location provided the longitude and latitude is known. Irradiance values for 300 locations in the country are evaluated from details presented by the maps. To validate the map, experimental irradiance values for selected locations are compared with values extracted from the solar irradiance map. Calculated irradiance values are found to agree satisfactorily with experimental values. The maximum percentage difference between calculated and experimental values is 6.8%. This proved that the solar map developed is a satisfactory provides a satisfactory representation of solar data for the various locations and can be used for other locations where such data does not exist.

KEYWORDS: *Solar Energy, Solar Maps, Irradiance, Energy Patterns,*

1.0 INTRODUCTION

The high availability of solar energy in Nigeria is established. Abdullahi *et al.* (2021) reported that Nigeria receives adequate solar radiation to generate sustainable electricity for household and industrial needs. The radiation is distributed relatively well distributed over its entire land area (Charles, 2014). Figure 1 shows the normal irradiation map of Nigeria (average daily/yearly sums) for the period of 25 years (1994-2018) (Global Solar Atlas, 2019).

Annually, Nigeria receives average solar energy of 6.5 million petajoules. The solar thermal power potential in Nigeria is estimated at over 427,000MW (Newson, 2012). per year (PJ/yr) (Charles, 2014). This amount of solar energy is about 120,000 times the total electrical energy generated by the National Electric Power Authority (NEPA) for the whole country in 2002 (Federal Ministry of Power and Steel, 2006).

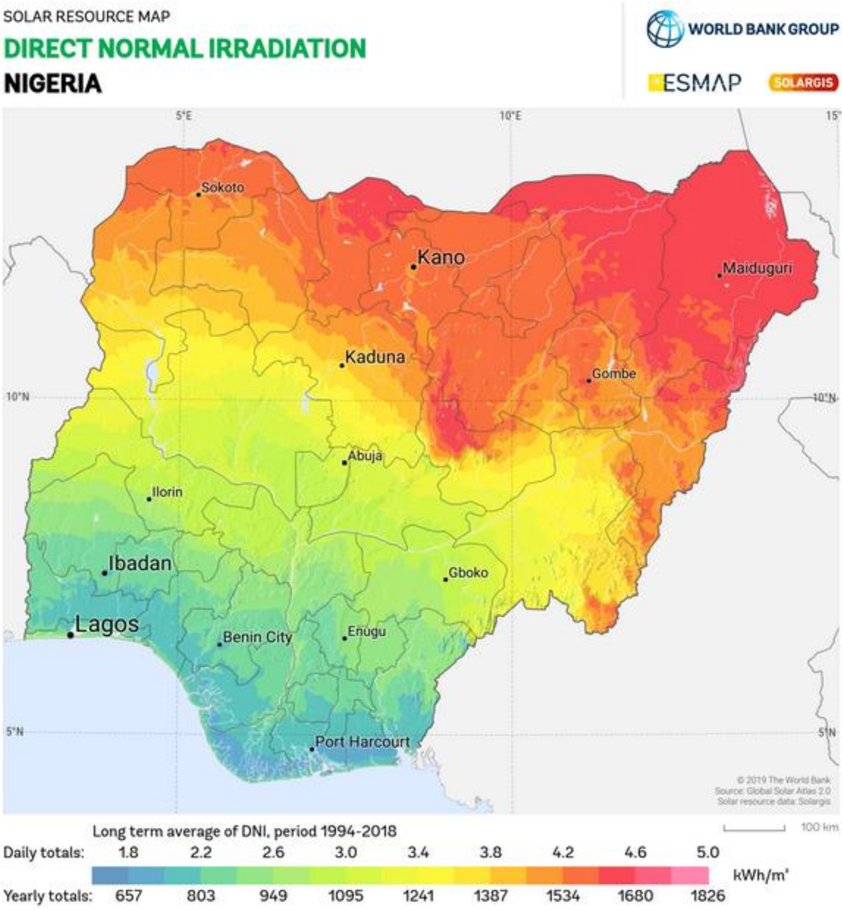

Figure 1: The direct normal irradiation (DNI) map of Nigeria (Global Solar Atlas, 2019).

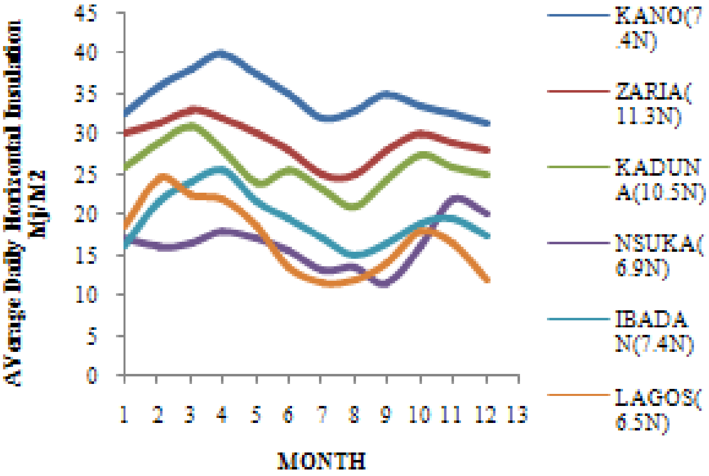

Figure 2: Average daily Horizontal Radiation of some sites in Nigeria (Charles, 2014)

Figure 2 shows the average daily horizontal irradiation of some sites in Nigeria (Charles, 2014). The Figure indicates that all the sites receive peak solar energy in March and April and a low solar energy variability in July through September.

An analysis of Nigeria's electric power production, distribution, and consumption patterns leave much to be desired. With most of the energy supply coming from gas-powered turbine and hydro-power systems, the inadequacies of quantity and quality of energy by these modes have been quite visible over the years. Power supply inadequacies have adversely affected the economy's growth, and there is a need to explore other alternatives to reposition the economy and thus the livelihood of the citizenry. To tackle this power supply, distribution and consumption dilemma in the country, there is the need for a thorough analysis of the situation and patterns to identify energy gaps present in the country.

Using on the spot experimental data for solar map production does not provide accurate maps because various climatic conditions such as dust haze and cloud cover affect the amount of solar energy that reaches the ground in various locations in Nigeria. This is particularly true during the harmattan period. It has been revealed that the effect of the harmattan is high during November and January but is highest in December. The high level of dust haze leads to clearness indexes alow as 0.36 (Awachie and Okeke, 1985). Therefore data from such sources cannot be used for the accurate design and optimization of solar systems. Data for such applications should be those collected from outer space and over a period of time for various locations.

Solar Irradiance data for Nigeria has been developed based on the National Aeronautics and Space Administration (NASA) data. The data covers a period of 25 years (1994-2018). The average daily global solar irradiance for various longitude-latitude nodes was projected from such data. With these data available, it is possible to estimate the average daily global solar irradiance for any location provided the longitude and latitude is known. Irradiance values for 300 locations in the country are evaluated from details presented by the maps. To validate the map, experimental irradiance values for selected locations were compared with values extracted from the solar irradiance map. These values were found to agree closely with a maximum deviation of 6.8% from values on the map. This proved that the solar map developed is a satisfactory representation of solar data for the various locations and can be used for other locations where such data does not exist. The procedure presented can be applied to countries and regions.

2.0 DEVELOPING SOLAR ENERGY MAP FOR NIGERIA

Solar energy systems analysis data is usually required to arrive at the correct conclusions for long periods. Taking solar irradiances or insolation readings for various locations in the country over long periods is very expensive and tedious. This challenge, however, has been solved by NASA by providing solar irradiance data in the form of figures for various locations in the world over a long period. Numerical values can be extracted from these figures for the period under consideration. The challenge now is to locate the region, isolate the data for that region and analyze them to produce a solar map for the country or region. Geographic Information System (GIS) and Global Positioning System (GPS) are critical to solar mapping since site locations are needed. Other applications extend to meteorological forecasting, spatial/network analysis, geospatial modeling, facilities management and economic analysis-forecasting (Gao, 2002).

2.1 Method for Assessing Irradiance Values for Different Localities in Nigeria

The development of a solar resources map for Nigeria is dependent on the data provided by the National Aeronautics and Space Administration (Surface meteorology and Solar Energy *(SSE-release 6.0).* This is a renewable energy resource website sponsored by NASA's Applied Sciences Program in the Science Mission Directorate (NASA Prediction of Worldwide Energy Resources (POWER), 2021). The SSE data set has over 200 primary and derived solar, meteorology, and associated cloud parameters framed for evaluating and designing renewable energy systems. SSE data have been obtained through mutual partnerships with industries and governments interested in renewable energy applications. This is a user-friendly data portal that provides industry-friendly parameters for renewable energy study and advancement (NASA Prediction of Worldwide Energy Resources, 2021).

Solar irradiance is defined as power per unit area received from the Sun in the form of electromagnetic radiation reported in the measuring instrument's wavelength range. Solar irradiance is often integrated over a given period in order to report the radiant energy emitted into the immediate environment during that time. This integrated solar irradiance is called solar irradiation, solar isolation or exposure (Boxwell, 2012).

2.2 Procedures for Analysis of Data

The data used for this study were obtained from the database provided by NASA (NASA Prediction of Worldwide Energy Resources, 2021). Figures 3 to 5 show Irradiance values for three selected locations in Nigeria (Lat 7°N: Long 3°E, Lat 9°N: Long 8°E, Lat13°N: Long 13°E) for a period of 25 years (1994 – 2018) are examples of the data. Collection and analysis of the irradiance values extracted from monthly mean values of the data provided by NASA were done using the Microsoft Excel software package. The Data obtained from the NASA database were averaged for 25 years (1994-2018) for the latitude-longitude nodes applicable to Nigeria to provide the average daily global irradiance (MJ/m^2/day). With the values known, it was possible to determine the irradiance for any position in Nigeria by interpolation.

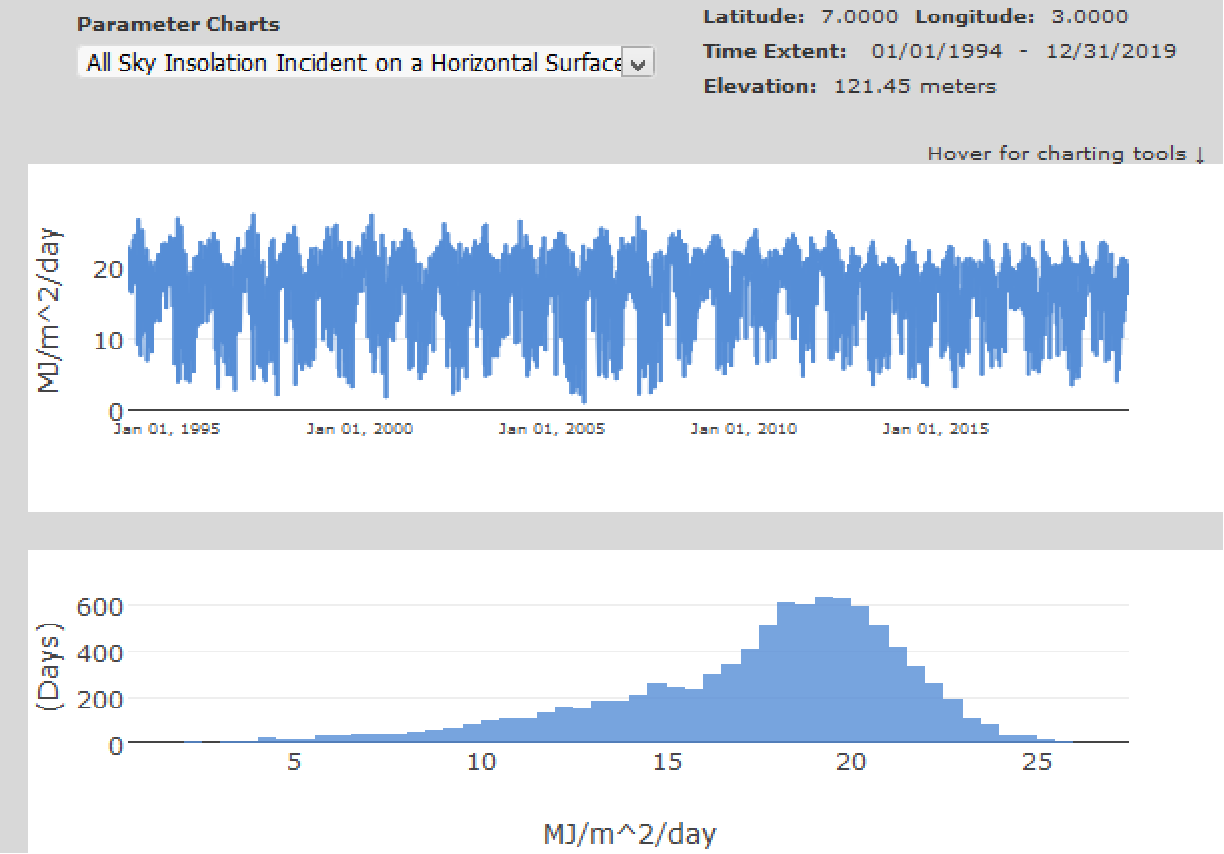

Parameter Charts
All Sky Insolation Incident on a Horizontal Surface

Latitude: 7.0000 Longitude: 3.0000
Time Extent: 01/01/1994 - 12/31/2019
Elevation: 121.45 meters

Figure 3: Irradiance values for a specific location (Lat 7/Long 3) for the period Jan. 1995 to Dec. 2018

Figures 3 to 5 show average daily irradiance values for 25 years for three locations in Nigeria. Documented values of total irradiance lie within 20.01–25.01 MJ/m^2/day (Osinowo *et al.*, 2015). As can be seen from these figures, the irradiance values cannot be extracted because of the long period. Global Solar Atlas (GSA) used such data provided in Figures 3 to 5 to develop solar maps for Nigeria and other countries. Figures 6 shows a map for normal irradiation and global horizontal irradiation (average daily/yearly sums) for 25 years (1994-2018). It can be seen from Figure 6 that daily irradiance averaged between 1.5 kWh/m^2 /day in the coastal areas to 5.0 5.25 kWh/m^2 /day in the northern area of the country. Abam *et al.* (2014) presented mean values daily solar radiation is about 5.25 kWh/m^2 /day, ranging from 3.5 kW/m^2 /day at coastal zones to 7.0 kWh/m^2 /day in the north of the country. It is easy to appreciate the values for various periods if we drastically reduce the length of the periods. The database provided by GSA is calculated by the Solargis Model from atmospheric and satellite data with 15-minute and 30-minute time steps. This information can then be used to produce solar maps like the one shown in Figure 6. As shown in Figure 6, numerical values of irradiance cannot be easily extracted. Only estimates can be obtained for various locations. This makes it difficult to design and optimize solar systems using the map shown in Figure 6.

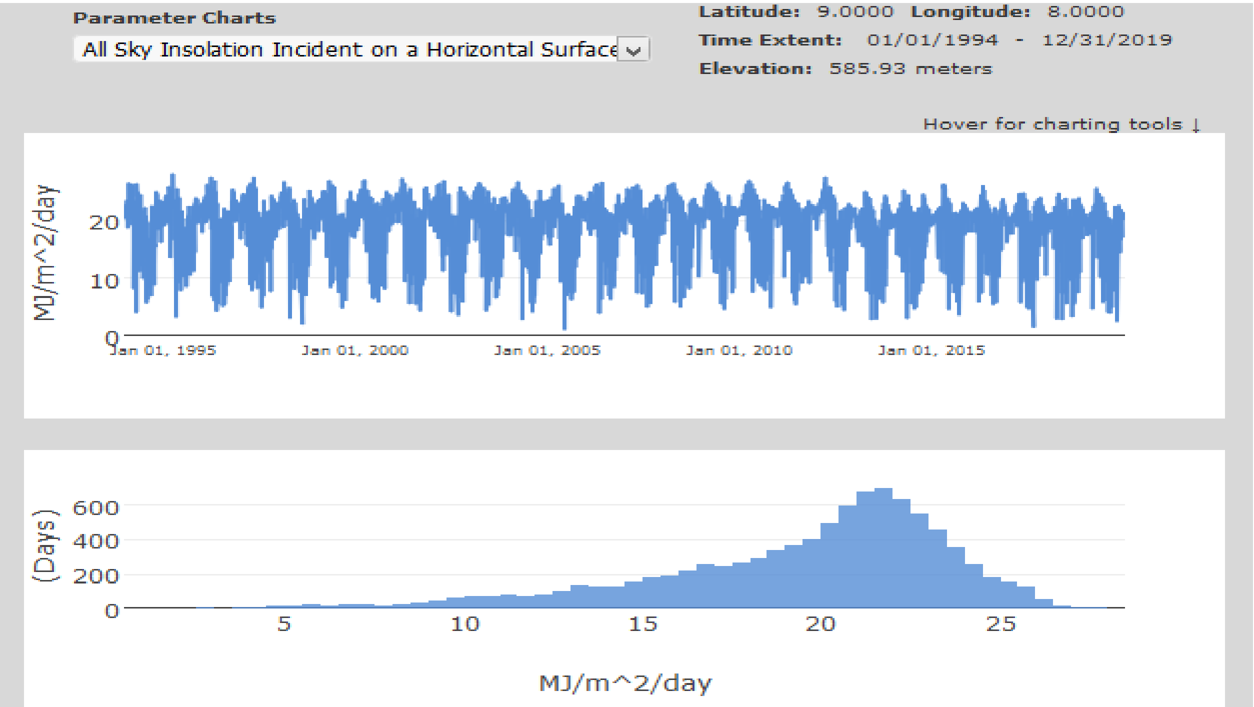

Parameter Charts
All Sky Insolation Incident on a Horizontal Surface
Latitude: 9.0000 Longitude: 8.0000
Time Extent: 01/01/1994 - 12/31/2019
Elevation: 585.93 meters

Figure 4: Irradiance values for a specific location (Lat 9/Long 8) for the period Jan.1995 to Dec. 2018

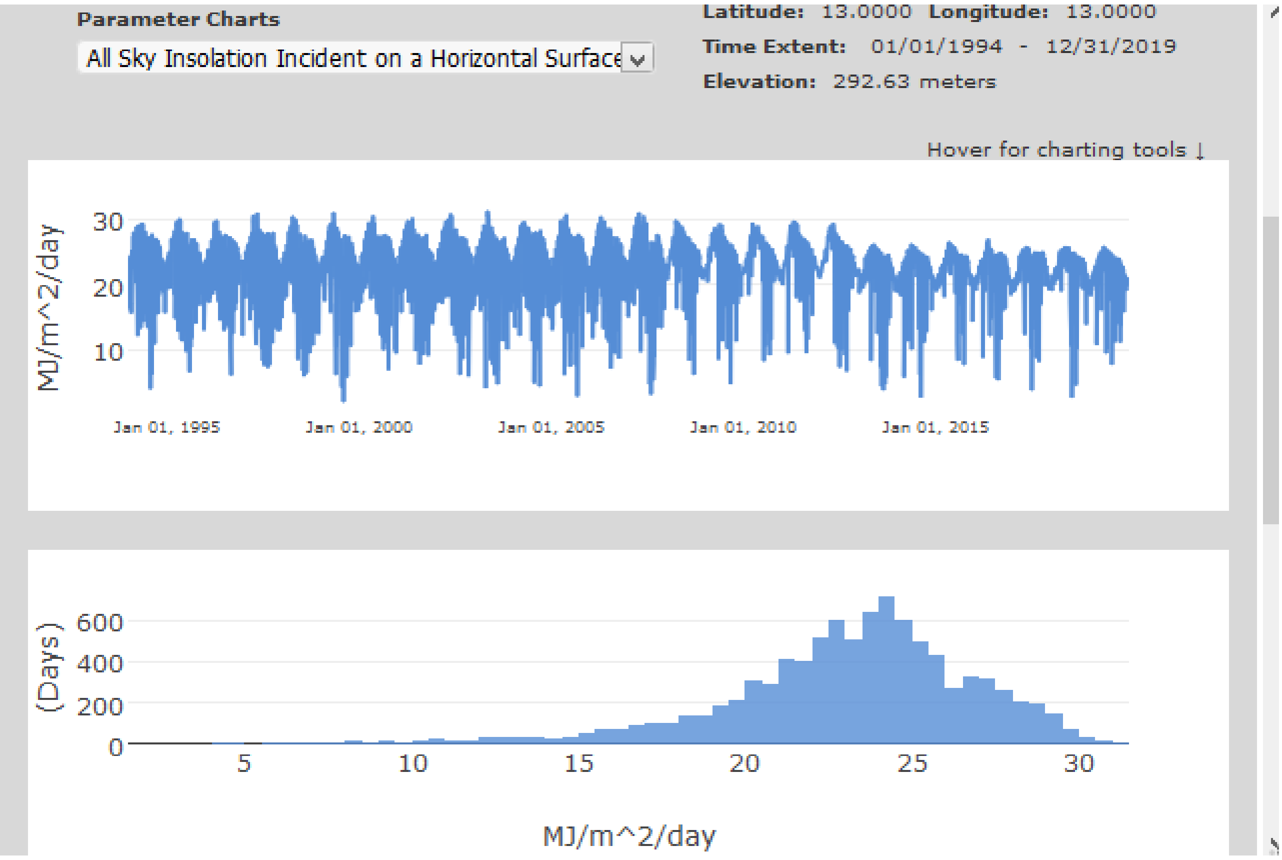

Parameter Charts
All Sky Insolation Incident on a Horizontal Surface
Latitude: 13.0000 Longitude: 13.0000
Time Extent: 01/01/1994 - 12/31/2019
Elevation: 292.63 meters

Figure 5: Irradiance values for a specific location (Lat 13/Long 13) for the period Jan.1995 to Dec. 2018

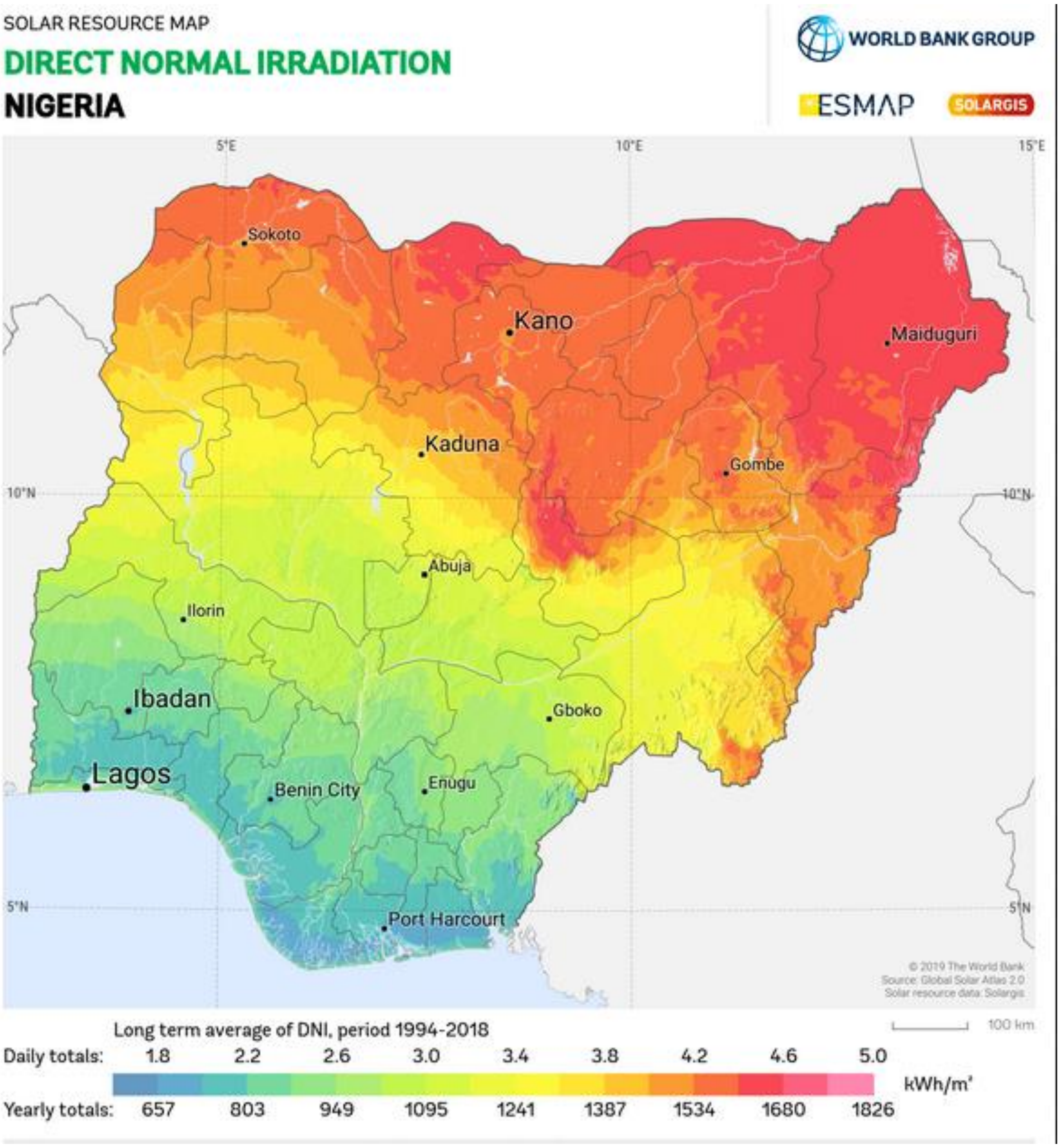

Figure 6: Direct Normal Irradiation Map for Nigeria (Global Solar Atlas (GSA): The World Bank Group (The World Bank Group, 2021)

3.0 RESULTS AND DISCUSSIONS

3.1 Results

Figures 7 to 9 show the isolation (average daily global solar irradiance (MJ/m^2/day) for the three selected locations in Nigeria for the period from 1st January 2018 to 31st March, 2018 while Figures (10) to (12) show values from 1st January to 5th January 2018. Values for such period can easily be seen. Figures (6) to (8) show results for 25 years and values are not visible because of the long period).

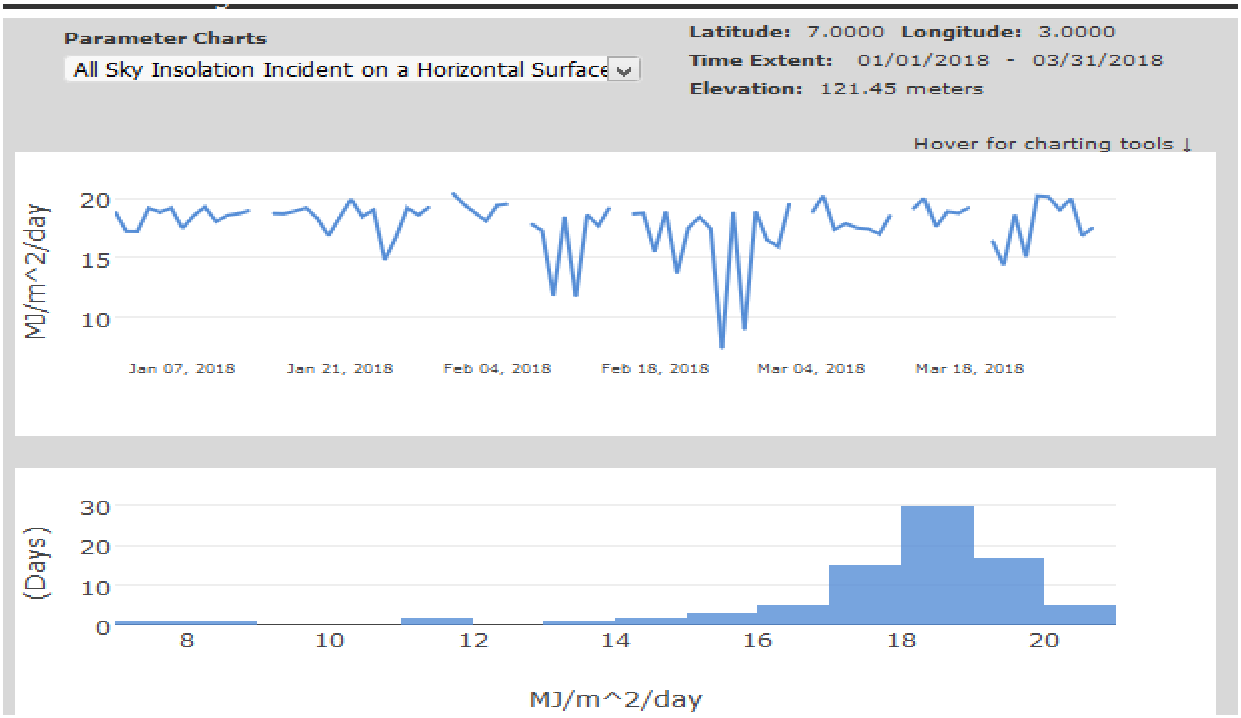

Parameter Charts
All Sky Insolation Incident on a Horizontal Surface
Latitude: 7.0000 Longitude: 3.0000
Time Extent: 01/01/2018 - 03/31/2018
Elevation: 121.45 meters

Figure 7. Irradiance values for a specific location (Lat 7/Long 3) for Jan. 2018 to Mar. 2018

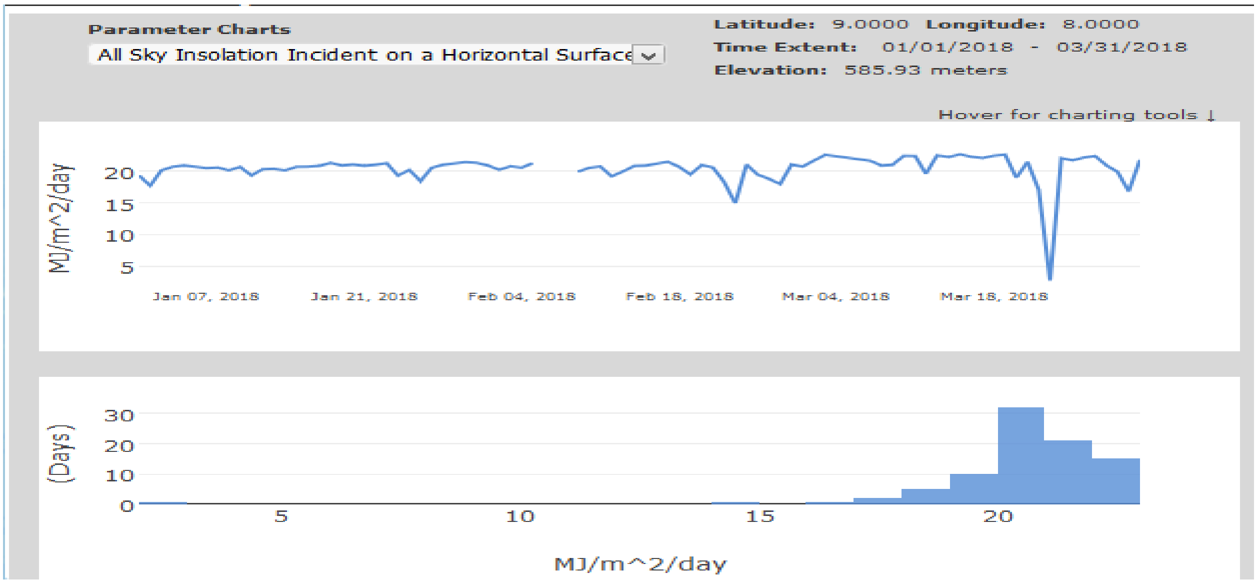

Parameter Charts
All Sky Insolation Incident on a Horizontal Surface
Latitude: 9.0000 Longitude: 8.0000
Time Extent: 01/01/2018 - 03/31/2018
Elevation: 585.93 meters

Figure 8. Irradiance values for Lat. 9/Long. 8 for the period Jan.1998 to Mar. 2018

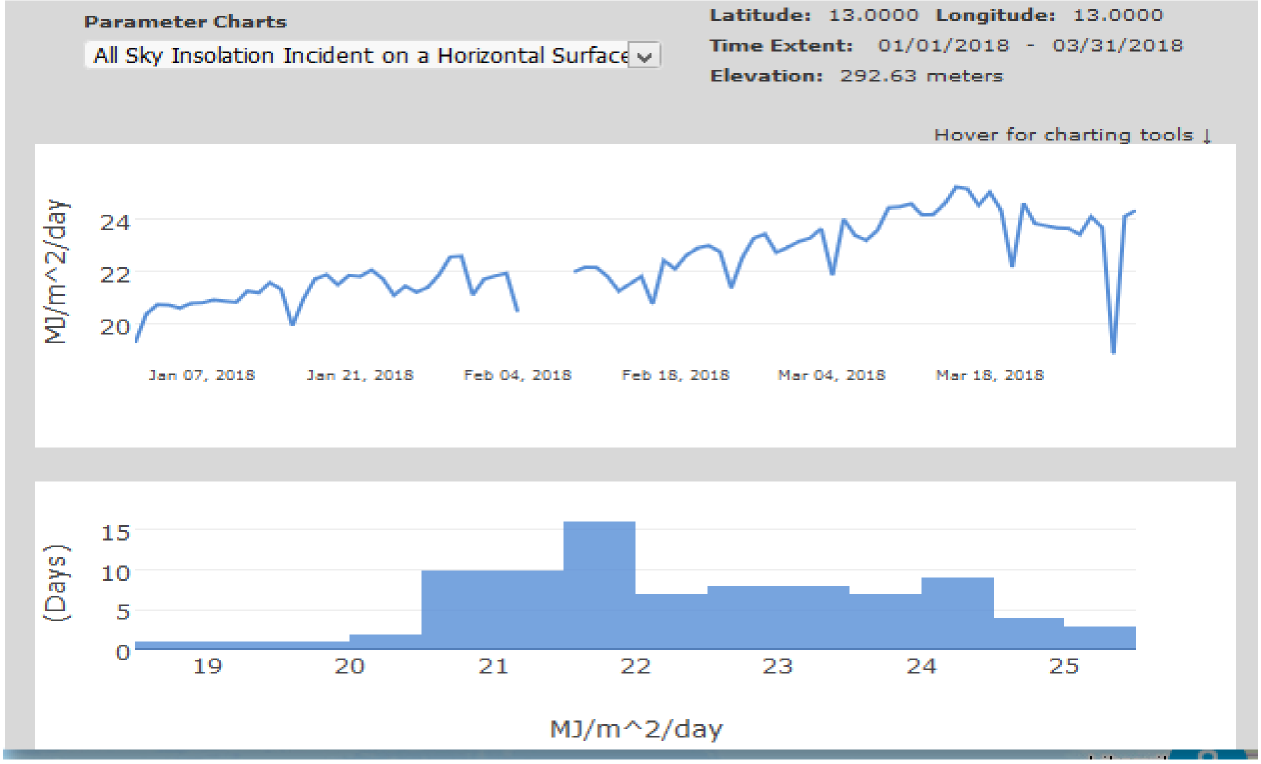

Parameter Charts
All Sky Insolation Incident on a Horizontal Surface

Latitude: 13.0000 Longitude: 13.0000
Time Extent: 01/01/2018 - 03/31/2018
Elevation: 292.63 meters

Figure 9. Irradiance values for Lat. 13/Long. 13 for Jan.1998 to Mar. 2018

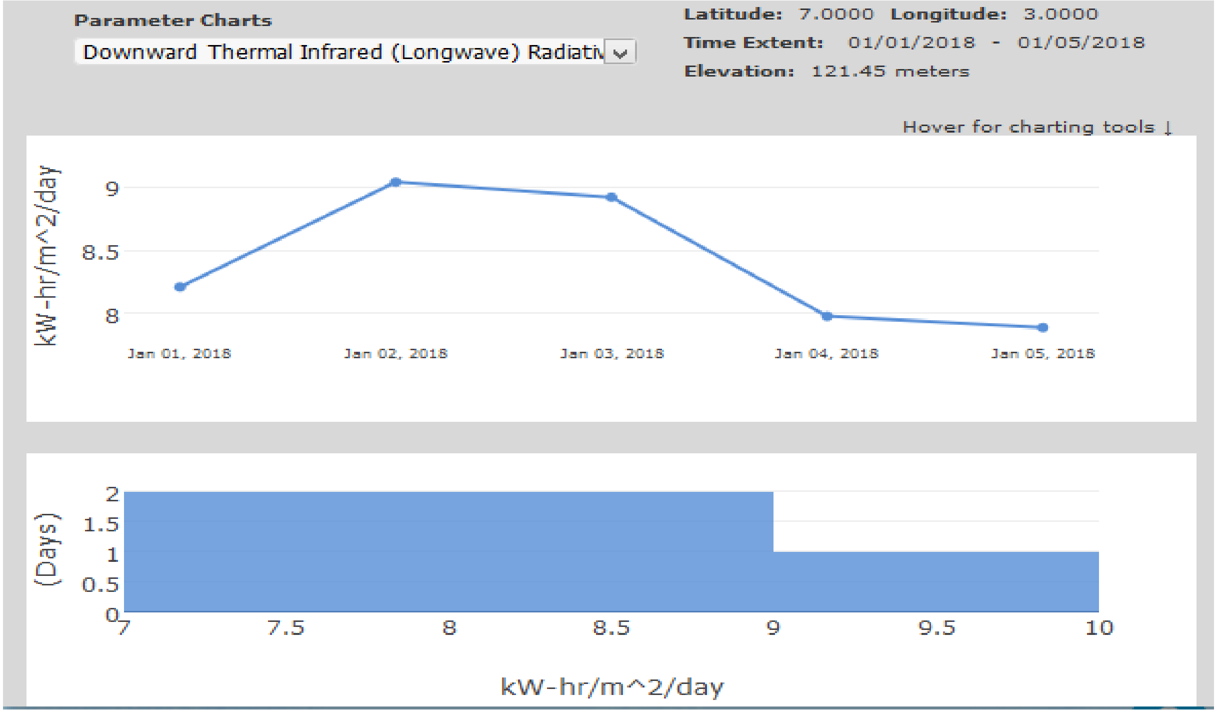

Parameter Charts
Downward Thermal Infrared (Longwave) Radiati

Latitude: 7.0000 Longitude: 3.0000
Time Extent: 01/01/2018 - 01/05/2018
Elevation: 121.45 meters

Figure 10. Irradiance values for Lat. 7/Long. 3 for 1st Jan. 2018 to 5th Jan. 2018

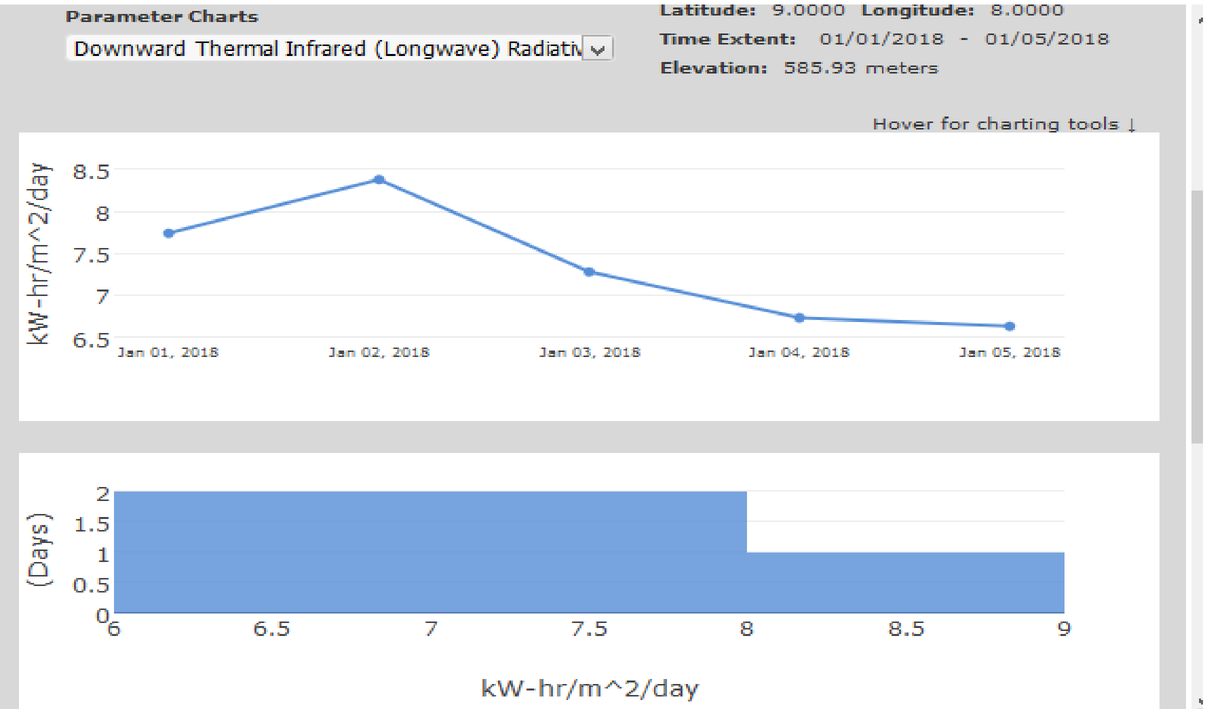

Parameter Charts
Downward Thermal Infrared (Longwave) Radiati
Latitude: 9.0000 Longitude: 8.0000
Time Extent: 01/01/2018 - 01/05/2018
Elevation: 585.93 meters

Figure 11. Irradiance values for Lat. 9/Long. 8 for 1st Jan. 2018 to 5th Jan. 2018

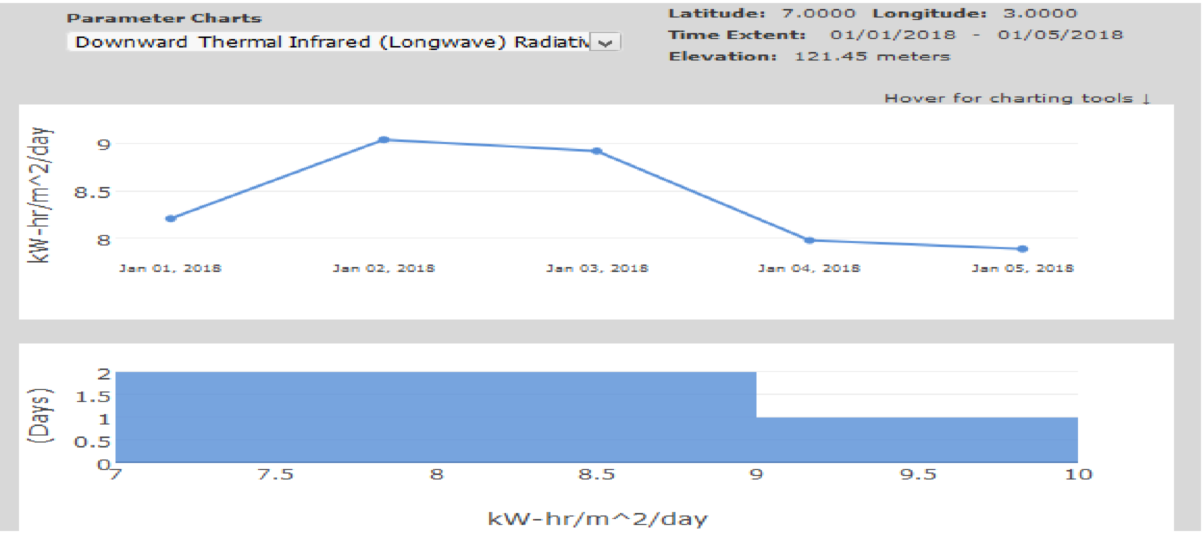

Parameter Charts
Downward Thermal Infrared (Longwave) Radiati
Latitude: 7.0000 Longitude: 3.0000
Time Extent: 01/01/2018 - 01/05/2018
Elevation: 121.45 meters

Figure 12. Irradiance values for Lat. 7/Long. 3 for 1st Jan. 2018 to 5th Jan. 2018

3.2 Discussion

The world have become inhospitable without the natural greenhouse effect. Human activities are increasingly influencing the climate and the earth's temperature. These activities include farming and production of livestock that drastically increase the amount of **Methane (CH_4) in the atmosphere.** The burning of fossil fuels increases CO_2 production. These processes add enormous amounts of greenhouse gases to those naturally occurring in the atmosphere. Increasing the greenhouse effect and global warming and the amount of solar radiation that reaches the surface of the earth. While CO_2 has a long lifetime, **Methane (CH_4)** is 30 times stronger than carbon dioxide as an absorber of infrared radiation. However methane is present in smaller concentrations than carbon dioxide and also has relatively short-lived (lasting approximately 8 years) in the atmosphere. Ozone O_3 exist in the stratosphere and absorbs solar ultra-violet radiation and therefore determines the quantity of the Sun's heat that is radiated back into space (Foster *et al.*, 2007)

The values of average daily global solar irradiance for the various latitude-longitude nodes in Nigeria are presented in Figure 13.

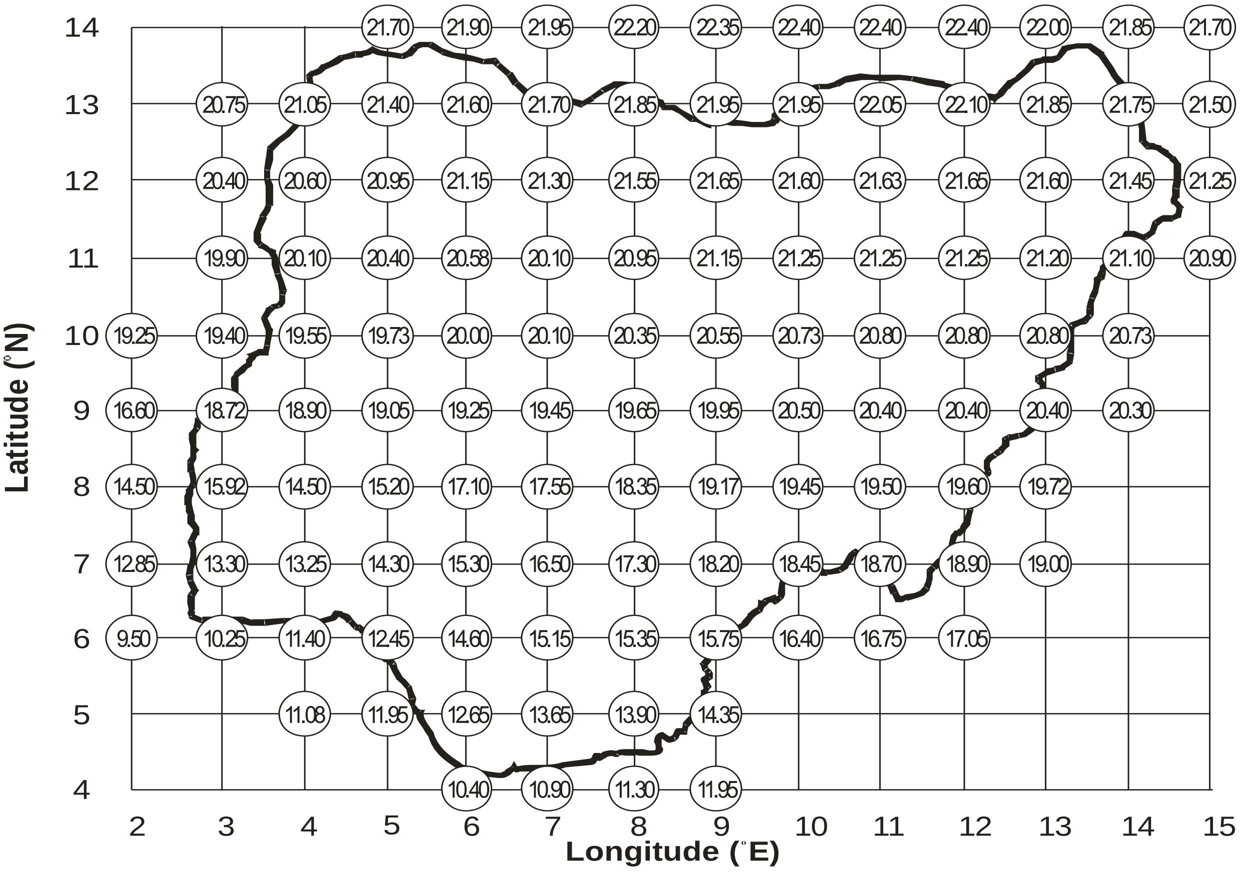

Figure 13: Average Daily Global Solar Irradiance (MJ/m^2/day) for various Latitude and Longitude points in Nigeria

Table 2 shows the values of global horizontal irradiance for 300 different locations in Nigeria. The global horizontal irradiance is the total solar radiation falling on a horizontal surface, and it is the sum of Direct Normal Irradiance (DNI), Diffuse Horizontal Irradiance (DHI), and ground-reflected radiation (Solar Resources Glossary, 2021). Normally, ground-reflected radiation is usually insignificant compared to direct and diffuse. Therefore, for all practical purposes, global radiation is said to be the sum of direct and diffuse radiation only. For locations not available in Table 3, the values can be estimated by simple interpolation from known nearest values.

Table 2: Irradiance values for various locations in Nigeria

S/No	City	Latitude ^{0}N	Longitude ^{0}E	Average global solar irradiance calculated from Solar Map (MJ/m^2/day)
1	Lagos	6.450	3.470	12.05
2	Kano	12.000	8.520	21.60
3	Ibadan	7.380	3.930	14.24
4	Kaduna	10.520	7.440	20.25
5	Port Harcourt	4.780	7.000	12.44
6	Benin	6.340	5.620	14.16

S/No	City	Latitude ^{o}N	Longitude ^{o}E	Average global solar irradiance calculated from Solar Map (MJ/m^{2}/day)
7	Maiduguri	11.850	13.160	21.43
8	Zaria	11.080	7.710	20.50
9	Aba	5.100	7.350	14.51
10	Ilorin	8.500	4.530	16.91
11	Jos	9.930	8.890	20.12
12	Ogbomosho	8.080	4.180	16.91
13	Oyo	7.830	3.920	14.24
14	Enugu	6.330	7.500	16.07
15	Abeokuta	7.160	3.350	14.24
16	Onitsha	6.160	6.780	15.39
17	Warri	5.510	5.750	12.91
18	Sokoto	13.070	5.240	21.50
19	Okene	7.560	6.230	16.61
20	Calabar	4.960	8.310	12.87
21	Oshogbo	7.830	4.580	14.31
22	Katsina	13.000	7.600	21.92
23	Akure	7.250	5.200	15.47
24	Ife	7.550	4.570	14.31
25	Ikorodu	6.610	3.510	12.05
26	Bauchi	10.310	9.840	20.86
27	Iseyin	7.980	3.670	14.24
28	Minna	9.600	6.550	19.20
29	Makurdi	7.730	8.530	18.28
30	Efon Alaye	7.670	4.880	14.31
31	Owo	7.190	5.590	15.47
32	Ado	7.670	5.270	15.37
33	Ede	7.730	4.520	14.31
34	Gombe	10.290	11.170	21.02
35	Ilesha	8.920	3.420	17.01
36	Umuahia	5.540	7.480	14.51
37	Ondo	7.090	4.840	14.31
38	Damaturu	11.750	11.960	21.44
39	Jimeta	9.280	12.460	20.60
40	Iwo	7.630	4.180	14.31
41	Ikot ekpene	5.190	7.710	14.51
42	Gusau	12.170	6.660	21.44
43	Mubi	10.270	13.270	20.96
44	Shagamu	6.850	3.640	12.05
45	Ugep	5.810	8.080	15.07
46	Owerri	5.500	7.020	14.51
47	Ijebu ode	6.810	3.920	12.05
48	Ikire	7.340	4.180	14.31
49	Nnewi	6.030	6.920	15.39
50	Ise	7.460	5.420	15.47
51	Gboko	7.330	8.900	18.25
52	Abuja	9.180	7.170	19.89
53	Bida	9.080	6.010	19.70

S/No	City	Latitude ^{o}N	Longitude ^{o}E	Average global solar irradiance calculated from Solar Map (MJ/m^2/day)
54	Ilawe	7.400	5.060	15.47
55	Ikare	7.450	5.600	15.48
56	Sango ota	6.700	3.230	12.05
57	Okpoko	6.530	6.170	15.39
58	Awka	6.220	7.070	16.07
59	Suleja	9.170	7.170	19.89
60	Sapele	5.900	5.670	12.91
61	Ila	8.020	4.900	16.91
62	Shaki	8.660	3.400	17.01
63	Ijero	7.810	5.070	15.47
64	Inisa	7.840	4.330	14.31
65	Otukpo	6.820	8.670	16.64
66	Kishi	9.090	3.850	19.14
67	Ikirun	7.920	4.660	14.31
68	Bugama	4.730	6.870	11.90
69	Okrika	4.740	7.080	12.44
70	Obosi	6.110	6.870	15.39
71	Funtua	11.530	7.310	20.97
72	Abakaliki	6.330	8.110	16.64
73	Gbongan	7.470	4.350	14.31
74	Lafia	8.490	8.520	19.20
75	Ejigbo	7.900	4.320	14.31
76	Igboho	8.830	3.750	17.01
77	Amaigbo	5.780	7.830	14.51
78	Gashua	12.880	11.040	21.86
79	Offa	8.140	4.720	16.91
80	Ifon osun	7.870	4.480	14.31
81	Jalingo	8.890	11.370	19.94
82	Bama	11.520	13.680	21.34
83	Uromi	6.720	6.320	15.39
84	Nsukka	6.860	7.390	16.07
85	Uyo	5.010	7.850	14.51
86	Okigwe	5.850	7.350	14.60
87	Modakeke	7.380	4.270	14.31
88	Hadejia	12.460	10.040	21.81
89	Ilobu	7.840	4.480	14.31
90	Azare	11.680	10.190	21.43
91	Ijebu igbo	6.970	4.000	12.85
92	Nguru	12.880	10.450	21.81
93	Birnin kebbi	12.460	4.190	21.00
94	Nkpor	6.160	6.830	15.39
95	Kontagora	10.400	5.470	20.18
96	Oron	4.810	8.250	12.87
97	Ikere	7.500	5.230	15.47
98	Yola	9.230	12.460	20.60
99	Biu	10.600	12.200	21.01

S/No	City	Latitude ^{o}N	Longitude ^{o}E	Average global solar irradiance calculated from Solar Map (MJ/m^2/day)
100	Ishieke	6.400	8.030	16.64
101	Wukari	7.880	9.770	18.82
102	Epe	6.590	3.980	12.05
103	Ogaminana	7.600	6.230	16.61
104	Effium	6.630	8.070	16.64
105	Ifo	6.820	3.200	12.05
106	Keffi	8.840	7.870	18.75
107	Igbo ora	7.430	3.290	14.24
108	Ihiala	5.860	6.850	14.01
109	Ughelli	5.500	5.980	12.91
110	Kafanchan	9.590	8.280	20.12
111	Ikom	5.970	8.710	15.07
112	Gamboru	12.370	14.220	21.49
113	Kagoro	9.610	8.380	20.12
114	Agulu	6.110	7.050	16.07
115	Daura	11.530	11.450	21.44
116	Asaba	6.200	6.740	15.39
117	Bende	5.570	7.630	14.51
118	Igbo ukwu	6.020	7.010	16.07
119	Oka	7.370	5.720	15.47
120	Numan	9.470	12.030	20.60
121	Ozubulu	5.950	6.850	14.01
122	Aku	6.700	7.330	16.07
123	Kuroro	7.580	6.230	16.61
124	Afikpo	5.900	7.930	14.51
125	Opobo	4.640	7.560	12.44
126	Okitipupa	6.510	4.690	12.85
127	Idah	7.120	6.730	16.61
128	Eha amufu	6.660	7.750	16.07
129	Abonnema	4.690	6.790	11.90
130	Etiti	5.620	7.350	14.51
131	Ohafia	5.620	7.800	14.61
132	Agbor	6.260	6.190	15.39
133	Malumfashi	11.780	7.620	20.97
134	Enugu ukwu	6.170	7.000	16.07
135	Kaura namoda	12.590	6.580	21.44
136	Ezza	6.450	8.080	16.64
137	Auchi	7.080	6.260	16.61
138	Nkwerre	5.750	7.120	14.51
139	Uga	5.930	7.080	14.53
140	Ankpa	7.380	7.620	17.92
141	Lokoja	7.810	6.740	16.61
142	Ekpoma	6.750	6.130	15.39
143	Nembe	4.490	6.360	11.90
144	Lafiagi	8.850	5.420	17.65
145	Enugu ezike	6.990	7.450	16.07
146	Kabba	7.840	6.070	16.61

S/No	City	Latitude ^{o}N	Longitude ^{o}E	Average global solar irradiance calculated from Solar Map (MJ/m^2/day)
147	Potiskum	11.710	11.070	21.44
148	Okija	5.900	6.830	14.01
149	Gembu	6.700	11.270	17.85
150	Ijebu jesa	7.680	4.810	14.31
151	Argungu	12.740	4.510	21.00
152	Itu	5.200	7.980	14.51
153	Paki	11.500	8.150	21.32
154	Kajuru	10.320	7.680	20.37
155	Igbeti	8.750	4.130	16.91
156	Isanlu	8.270	5.820	17.65
157	Kwale	5.550	6.370	14.01
158	Jega	12.210	4.380	21.00
159	Ayangba	7.520	7.160	17.92
160	Yelwa	10.870	4.770	19.94
161	Kujama	10.450	7.630	20.37
162	Dutsan Wai	10.850	8.200	20.75
163	Bori	4.700	7.350	12.44
164	Birnin Gwari	11.010	6.800	20.78
165	Ilaro	6.880	3.010	12.05
166	Rigacikun	10.640	7.470	20.37
167	Fiditi	7.700	3.910	14.24
168	Degema	4.730	6.770	11.90
169	Mgbidi	5.720	6.890	14.01
170	Igabi	10.790	7.780	20.37
171	Kaura	11.300	7.820	20.97
172	Lere	10.390	8.580	20.75
173	Sabon Birnin Gwari	10.660	6.550	20.19
174	Lalupon	7.470	4.060	14.31
175	Ifon	6.920	5.770	14.16
176	Emure	7.450	5.470	15.47
177	New Bussa	9.880	4.520	16.81
178	Enugu Ngwo	6.420	7.430	16.07
179	Ipoti	7.870	5.070	15.47
180	Soba	10.980	8.060	20.75
181	Usoro	5.540	6.210	14.01
182	Erin-Oshogbo	7.810	4.480	14.31
183	Idanre	7.110	5.110	15.47
184	Kumo	10.040	11.210	21.02
185	Ogwashi-Uku	6.250	6.610	15.39
186	Wudil	11.800	8.850	21.32
187	Kumaganum	13.140	10.630	22.20
188	Ikole	7.790	5.470	15.47
189	Aramoko	7.720	5.050	15.50
190	Egume	7.490	7.200	17.92
191	Ete	7.050	7.450	17.82

S/No	City	Latitude ⁰N	Longitude ⁰E	Average global solar irradiance calculated from Solar Map (MJ/m²/day)
192	Oyan	8.050	4.770	16.91
193	Ogoja	6.660	8.790	16.64
194	Iperu	6.920	3.670	12.05
195	Agbara	7.550	3.400	14.24
196	Anchau	10.970	8.400	20.75
197	Kafarati	10.390	11.100	20.77
198	Atijere	6.420	4.520	12.85
199	Ode	7.790	5.710	15.47
200	Okwe	5.020	7.260	14.51
201	Okata	8.220	3.450	17.01
202	Shendam	8.900	9.470	19.78
203	Nafada	11.090	11.340	21.44
204	Olupona	7.600	4.180	14.31
205	Otukpa	7.090	7.660	17.92
206	Yan	10.050	12.170	21.01
207	Orerokpe	5.640	5.900	12.91
208	Apomu	7.330	4.180	14.31
209	Talata Mafara	12.570	6.070	21.44
210	Ilara	7.350	5.120	15.47
211	Titiwa	12.150	12.900	21.80
212	Yelwa	8.840	9.630	19.76
213	Awgu	6.080	7.470	16.07
214	Nike	6.530	7.540	16.22
215	Jikamshi	12.170	7.770	21.60
216	Amassama	5.110	6.240	14.01
217	Gandi	12.970	5.750	21.27
218	Orodo	5.620	7.040	14.51
219	Ochobo	7.190	7.960	17.92
220	Amagunze	6.330	7.650	16.07
221	Sauri	11.730	6.790	20.78
222	Udi	6.320	7.410	16.08
223	Umuduru	5.690	7.250	14.51
224	Oke-mesi	7.830	4.920	14.31
225	Koko	5.980	5.430	12.91
226	Ruma	12.870	7.230	21.60
227	Gumel	12.630	9.400	21.79
228	Giwa	11.300	7.450	20.97
229	Isara	6.980	3.680	12.05
230	Dan Sadau	11.300	6.500	20.78
231	Ihuo	5.570	7.100	14.51
232	Kona	8.810	11.080	19.94
233	Moriki	12.870	6.490	21.44
234	Gwadabawa	13.370	5.240	21.65
235	Oturkpo	7.200	8.130	18.25
236	Agbabu	6.580	4.830	12.85
237	Gummi	12.140	5.110	21.27
238	Igede	7.650	5.120	15.47

S/No	City	Latitude ^{o}N	Longitude ^{o}E	Average global solar irradiance calculated from Solar Map (MJ/m^2/day)
239	Owode	6.950	3.520	12.05
240	Abraka	5.780	6.100	14.01
241	Zungeru	9.810	6.150	19.70
242	Yashikera	9.760	3.400	19.14
243	Ilushi	6.670	6.630	15.39
244	Hunkuyi	11.270	7.650	20.97
245	Shagunnu	10.330	4.470	19.94
246	Ajaokuta	7.470	6.700	16.61
247	Baro	8.600	6.430	18.34
248	Bagudo	11.400	4.230	20.51
249	Gora	11.920	7.660	20.97
250	Dan Gulbi	11.640	6.290	20.78
251	Jemma	11.670	9.930	21.41
252	Kamba	11.860	3.660	20.35
253	Ikem	6.780	7.700	16.07
254	Icheu	7.700	6.770	16.61
255	Loko	8.010	7.830	18.75
256	Tegina	10.070	6.190	20.19
257	Isa	13.230	6.330	21.74
258	Irrua	6.790	6.240	15.39
259	Beli	7.860	10.970	19.02
260	Mando	10.720	6.570	20.19
261	Dekina	7.700	7.020	17.92
262	Obudu	6.670	9.160	17.19
263	Ubiaja	6.650	6.380	15.39
264	Gaya	11.860	9.010	21.41
265	Agenebode	7.110	6.690	16.61
266	Jemaa	9.470	8.380	20.12
267	Tambawel	12.400	4.650	21.00
268	Omoko	5.350	6.650	14.01
269	Bununu Dass	10.000	9.520	20.92
270	Kotorkoshi	12.100	6.850	21.44
271	Ajasse	8.240	4.800	16.91
272	Igarra	7.280	6.100	16.61
273	Geidam	12.890	11.930	21.86
274	Ifaki	7.800	5.240	15.47
275	Oguta	5.700	6.800	14.01
276	Elele	5.100	6.820	14.01
277	Alapa	8.620	4.380	16.91
278	Bara	10.370	10.730	21.01
279	Biliri	9.880	11.230	20.56
280	Chibok	10.880	12.900	21.01
281	Gwarzo	11.920	7.930	20.97
282	Omu-Aran	8.140	5.100	17.65
283	Duku	10.820	10.770	21.01
284	Obolo	6.880	7.630	16.07

S/No	**City**	**Latitude ^oN**	**Longitude ^oE**	**Average global solar irradiance calculated from Solar Map (MJ/m^2/day)**
285	Lapai	9.040	6.570	19.70
286	Faggo	11.390	9.950	21.41
287	Umunede	6.270	6.300	15.39
288	Ago-Are	8.500	3.410	17.01
289	Kusheriki	10.510	6.450	20.19
290	Wurno	13.290	5.420	21.65
291	Gombi	10.160	12.750	21.01
292	Benisheikh	11.800	12.480	21.42
293	Bokkos	9.280	8.990	20.12
294	Garko	10.170	11.170	21.02
295	Badeggi	9.050	6.150	19.70
296	Akamkpa	5.300	8.360	15.07
297	Siluko	6.530	5.170	14.16
298	Babana	10.400	3.820	19.74
299	Misau	11.320	10.470	21.43
300	Yenagoa	4.930	6.250	11.90

Note: Latitude and Longitude values are extracted from Worldwide Index, 2021.

Table 4 shows the differences between experimental irradiance values from literature and calculated values arrived at in the study for various locations in Nigeria. The locations were selected for sites that have experimental irradiance data available. An additional criterion was the spread of the locations across Nigeria. It can be seen from the table that the values are close to map values. The maximum percentage difference was recorded at Ibadan. This could be attributed to the number of data points used in arriving at the average values (Sanusi and Abisoye, 2011). However, the other locations fitted satisfactorily.

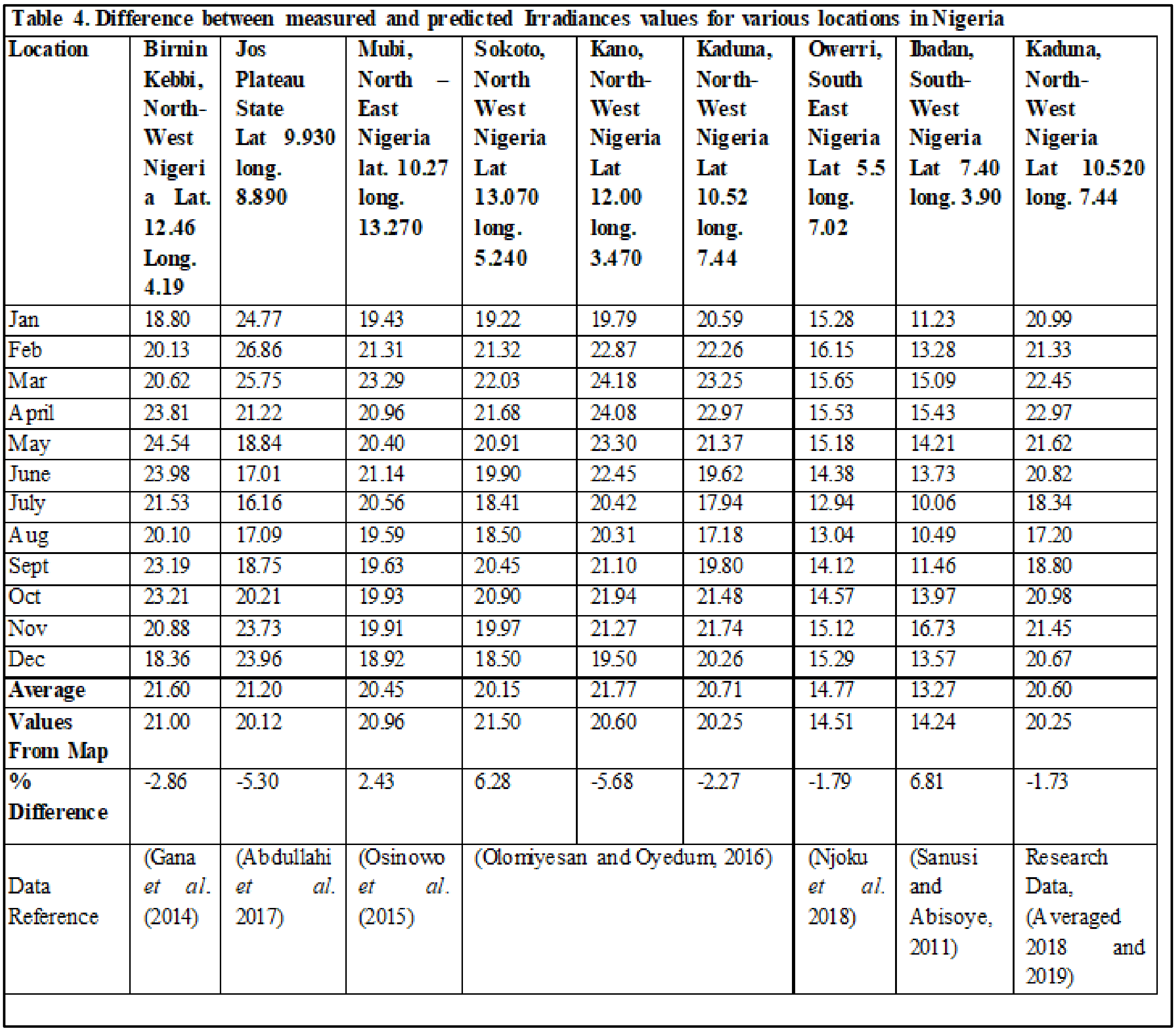

Table 4. Difference between measured and predicted Irradiances values for various locations in Nigeria

Location	**Birnin Kebbi, North-West Nigeria Lat. 12.46 Long. 4.19**	**Jos Plateau State Lat 9.930 long. 8.890**	**Mubi, North – East Nigeria lat. 10.27 long. 13.270**	**Sokoto, North West Nigeria Lat 13.070 long. 5.240**	**Kano, North-West Nigeria Lat 12.00 long. 3.470**	**Kaduna, North-West Nigeria Lat 10.52 long. 7.44**	**Owerri, South East Nigeria Lat 5.5 long. 7.02**	**Ibadan, South-West Nigeria Lat 7.40 long. 3.90**	**Kaduna, North-West Nigeria Lat 10.520 long. 7.44**
Jan	18.80	24.77	19.43	19.22	19.79	20.59	15.28	11.23	20.99
Feb	20.13	26.86	21.31	21.32	22.87	22.26	16.15	13.28	21.33
Mar	20.62	25.75	23.29	22.03	24.18	23.25	15.65	15.09	22.45
April	23.81	21.22	20.96	21.68	24.08	22.97	15.53	15.43	22.97
May	24.54	18.84	20.40	20.91	23.30	21.37	15.18	14.21	21.62
June	23.98	17.01	21.14	19.90	22.45	19.62	14.38	13.73	20.82
July	21.53	16.16	20.56	18.41	20.42	17.94	12.94	10.06	18.34
Aug	20.10	17.09	19.59	18.50	20.31	17.18	13.04	10.49	17.20
Sept	23.19	18.75	19.63	20.45	21.10	19.80	14.12	11.46	18.80
Oct	23.21	20.21	19.93	20.90	21.94	21.48	14.57	13.97	20.98
Nov	20.88	23.73	19.91	19.97	21.27	21.74	15.12	16.73	21.45
Dec	18.36	23.96	18.92	18.50	19.50	20.26	15.29	13.57	20.67
Average	21.60	21.20	20.45	20.15	21.77	20.71	14.77	13.27	20.60
Values From Map	21.00	20.12	20.96	21.50	20.60	20.25	14.51	14.24	20.25
% Difference	-2.86	-5.30	2.43	6.28	-5.68	-2.27	-1.79	6.81	-1.73
Data Reference	(Gana *et al.* (2014)	(Abdullahi *et al.* 2017)	(Osinowo *et al.* (2015)	(Olomiyesan and Oyedum, 2016)			(Njoku *et al.* 2018)	(Sanusi and Abisoye, 2011)	Research Data, (Averaged 2018 and 2019)

4.0 CONCLUSIONS

The design and simulation of solar energy systems usually required solar irradiance data over long periods for that location. With solar irradiance values available for various locations in the country, a solar map can be created. NASA has, however, captured and stored such data in the form of figures for use by solar energy researchers and stakeholders. This information has been used to develop a numerical solar irradiance map for Nigeria. This was achieved by estimating the average daily global solar irradiance for various longitude-latitude nodes in Nigeria from the NASA resources. With these data available, it was then possible by simple interpolation to estimate the average daily global solar irradiance for any location, provided the longitude and latitude of the location are known. Irradiance values for 300 locations in the country were evaluated from values presented by the maps. To validate the accuracy of the method used to calculate the irradiance values presented on the map, calculated values were compared with experimental values. These values agreed closely with calculated values. A maximum percentage deviation of 6.8% was arrived at when calculated values were compared with experimental values. Therefore, the developed solar energy map provided satisfactory solar irradiance values for the various locations and can therefore be used to estimate irradiance values for other locations where such data did not exist. The procedure presented could be applied to other countries and regions.

Acknowledgement

The authors wish to acknowledge the funding provided for this research work by Tertiary Education Trust Fund (TETFund) under the National Research Fund (NRF) Grants. REF: TETF/R&D/CE/NRF/POLY /KADUNA/VOL. 1/B5).

5.0 REFERENCES

Abam, F. I., Nwankwojike, B. N., Ohunakin, O. S. and Ojomu, S. A. (2014). Energy resource structure and on-going sustainable development policy in Nigeria: A review. International *Journal of Energy and Environmental Engineering*, 5(2-3), pp 1 - 16. doi:10.1007/s40095-014-0102-8

Abdullahi, A., Gujahar, R. D. R., Amodu, U. S. and Okeke, C. J. (2017). Investigation of monthly global solar radiation of Plateau State, Nigeria. *International Journal of Development and Sustainability*, 6 (8), pp. 914-923

Awachie, I.R.N. and Okeke, C.E. (1985) Solar radiation patterns during the harmattan season at Enugu, Nigeria; *Energy Conversion and Management*, 25(4), pp 487-490

Boxwell, M. (2012) *Solar Electricity Handbook: A Simple, Practical Guide to Solar Energy,* pp. 41–42

Charles, A. (2014). *How is 100% renewable energy possible for Nigeria? Global Energy Network Institute*. Retrieved July, 2021 from http://geni.org/globalenergy/research/renewable-energy-potential-of-nigeria/100-percent-renewable-energy-Nigeria.pdf

Federal Ministry of Power and Steel (2006). *Renewable electricity policy guidelines.* Retrieved July, 2021 from https://www.iceednigeria.org/resources/dec.-2006.pdf

Forster, P., V. Ramaswamy, P. Artaxo, T. Berntsen, R. Betts, D.W. Fahey, J. Haywood, J. Lean, D.C. Lowe, G. Myhre, J. Nganga, R. Prinn, G. Raga, M. Schulz and R. Van Dorland (2007) Changes in Atmospheric Constituents and in Radiative Forcing. *In: Climate Change 2007: The Physical Science Basis. Contribution of Working Group I to the Fourth Assessment Report of the Intergovernmental Panel on Climate Change* [Solomon, S., D. Qin, M. Manning, Z. Chen, M. Marquis, K.B. Averyt, M.Tignor and H.L. Miller (eds.)]. Cambridge University Press, Cambridge, United Kingdom and New York, NY, USA.

Gana, N. N. , Jitendra K. Rai and Musa Momoh (2014); Estimation of Global and Diffuse Solar; Radiation for Kebbi, North-Western, Nigeria; *International Journal of Scientific & Engineering Research*, 5(1), pp. 1654-1661

Gao, J. (2002) Integration of GPS with Remote Sensing and GIS: Reality and Prospect; *Photogrammetric Engineering & Remote Sensing*; 68(5), pp. 447-453.

Global Solar Atlas (2019) Https://globalsolaratlas.info/ download /Nigeria

NASA Prediction of Worldwide Energy Resources (POWER) (2021). *Prediction of Worldwide Energy Resources (POWER)*. Retrieved August, 21, 2021, from https://power.larc.nasa.gov /common/php/ SSE_ExSummary.php

Newsom, C. (2012) *Renewable Energy Potential in Nigeria; International Institute for Environment and Development*; Retrieved March 2, 2022 from https://pubs.iied.org › sites › files › pdfs

Njoku, M. C., Ofong I, Ogueke N. V. and Anyanwu, E. E. (2018). Characterization of sky conditions at Benin City and Owerri in Nigeria. *Journal of Fundamentals of Renewable Energy and Applications* 8 (5), pp. 1-8.

Olomiyesan, B. M. and Oyedum, O. D. (2016). Comparative study of ground measured satellite-derived, and estimated global solar radiation data in Nigeria. *Journal of Solar Energy*, 2016, 1–7. doi:10.1155/2016/8197389

Osinowo, A. A. , E. C. Okogbue, S. B. Ogungbenro, and O.Fashanu (2015) Analysis of Global Solar Irradiance over Climatic Zones in Nigeria for Solar Energy Applications; Journal of Solar Energy; https://doi.org/10.1155/2015/819307

Sanusi, Yekinni K and Abisoye Segun G (2011) Estimation of Solar Radiation at Ibadan, Nigeria Journal of Emerging Trends in Engineering and Applied Sciences, 2 (4), pp. 701-705.

Solar Resources Glossary (2021) Retrieved August 21, 2021 from https://www.nrel.gov/grid/solar-resource/solar-glossary.html

The World Bank Group (2021). *Global Solar Atlas*. Retrieved July, 2021 from https://olc.worldbank.org/content/global-solar-atlas

Worldwide Index (2021). *Federal Republic of Nigeria (NG)*. Retrieved July, 2021, from http://www.tageo.com/index-e-ni-cities-NG-step-4.htm

DOI:10.51975/22370105.som
Journal of the Nigerian Society of Chemical Engineers, 37(1), 2022

MODELING AND OPTIMIZATION OF PARTICLEBOARDS PRODUCED FROM RICE HUSK WASTE USING R7AD2 ADHESIVE

***Hamidu, L. A. J.[1*], Aroke, U. O.[2], Osha, O. A.[3] and Muhammad, I. M. [2]**

[1]Nigerian Building and Road Research Institute 10, NBRRI Way/ I.T. Igbani Street, off Awolowo Way, Jabi, Abuja, Nigeria
[2] Department of Chemical Engineering, Abubakar Tafawa Balewa University, P.M.B. 0248, Bauchi, Nigeria
[3] Department of Chemical Engineering, University of Calabar, P.M.B. 1115, Calabar, Nigeria
***Email of the Corresponding author: lucadohamidu@yahoo.com**

ABSTRACT

The desired to be among the industrialized nation is very important for a developing country like Nigeria with rapid population growth. Waste is generated due to socio-economic activities from various sources such as agricultural residue, but the potentials of these wastes from different sources are not adequately harnessed for usefulness and thus increase in ecology management and environmental sustainability. This paper seeks to determine the best formulated particleboard produced from rice husk (RH) waste using R7AD2 adhesive via modeling and optimization process. Particleboards was formulated from RH waste using Design-Expert software, Version 6.0.8 which generated eight (8) formulations based on 2 factorial designs with 3 responses. The responses percentage water absorption and density data were modeled and optimized to determine the best fit from the particleboards produced using the statistical tools: analysis of variance (ANOVA) and sequential model sum of squares (SMSS). The analyzed data for percentage water absorption (%WA) at 2hours, 24 hours and density were best described with Cubic models based on the following factors: precision adequacies of 19.347, 19.238 and 3.454; standard deviations of 1.81, 1.47 and 33.78; F values of 25.94, 49.50 and 1..84, Prob > F values of 0.0070, 0.0019 and 0.246 respectively. The numerical model found a solution with the high desirability factor of 0.979 suggesting formulation RHP8 with 0.32A (rice husk) to 0.68B (R7AD2) adhesive as best fitted model from the optimization, with characteristic properties of 2.26 %WA at 2 hours, 21.25%WA at 24 hours and 843.13 kg/m^3. Thus placing the produced particleboard formulation in high density category based on Japanese Industrial Standard A5908 (2003) and American National Standard Institute A208.1 (2009).

Keywords: Modeling, optimization, particleboard, Waste, Adhesive

1. INTRODUCTION

The challenges of waste management have been a subject of interest in the wake of climate change and global warming in the research world, as a result of human activities and socio-economic emancipation due to rural-urban migration. Furthermore; the insecurity in the rural communities had propelled rural dwellers to search for safe and better condition of leaving. The effect of which is increasing to ecosystem management from the municipal solid waste (MSW) generation which was projected to be about 0.56 kg per capita daily in Nigeria (Hamidu et al., 2018). Therefore waste generated from the daily activities when harnessed into usefulness will aid development and can reduce the emission into the environment. The actual total costs of current waste disposal taking into account health and environmental impacts are not known particularly in developing counties, due to lack of interest in waste conversion not minding its contribution to the circular economy. Nevertheless, findings suggested the adoption of ‘waste to wealth’ as a sustainable strategy to reduce the impact of waste disposal (Sridhar and Hammed, 2014).

Agricultural residue such as palm kernel shell (Atoyebi et al., 2018), sugar cane and wheat straw (Halvarson, 2009), fruit bunch, hazelnut shell and husk, peanut shell and Kenaf fibre (Baskaran et al., 2017), coffee husk and rice husk (Da Silva Cesar et al., 2017; Hamidu et al., 2021; Temitope et al., 2015), rice straw and maize husk (Sampathrajan, et al., 1992) are some potential raw materials that can be a source of income from farming in the production of particleboard. Rice which is a major staple food in every home given 10% annual increments in Nigeria was projected to be about 6.72 million tons per annum by 2020 (Osabuohien et al., 2018). Although there are no data available for the amount of rice husk generated, nevertheless, about 3 million tons of rice is produced annually in Nigeria with almost 20% being husks (Chukwudebelu et al., 2015, Ghosal and Moulik, 2015). This amount of waste generated from rice husk has not been optimally harnessed, thereby creating menace in the environment (Ciannamea et al., 2017) and increasing expense of ecology sustainability (Baiyeri et al., 2019; Yu and Wu, 2018). When the rice husks waste is burnt it could be emitting oxides of carbon thereby aiding climate change and contributing to global warming in the wake of green-house-gas consciousness.

Particleboard has found usage in most applications as office furniture, household furniture (kitchen divider), wall and ceiling panels, counter tops amongst others (MacCleery, 1995; Chew et al., 1991). Therefore the responses generated from the produced particleboards from rice husk waste have been desired in this study for process modeling and optimization to obtain the best fit particleboard among several formulations.

In modeling, a conceived idea is developed into mathematical process which employs the essentials that rely best on the responses from the formulation (Li et al., 2015), that can also be experimentally verified in order to determine the best fit or improve on the existing process condition (Olubajo and Makarfi 2019; Roffel and Betlem, 2006) using mathematical model equation as presented in Equation 1 (Silva et al., 2014).

$$Y = \beta_0 + \beta_1 A + \beta_2 B + \beta_3 C \qquad (1)$$

where Y= Predicted response, β_0 = Intercept while β_1, β_2 and β_3 are the model coefficient for the factors A, B and C respectively.

While in optimization, the process based on the parameters from the mathematical model developed select the best fit which satisfy the optimal values either to maximize or minimize within the process boundary conditions.

The design of experiment (DOE) often used in process formulation for selection of the best fit includes: simplex-lattice, axial, simplex-centroid and D-optimal designs. Others are central composite design, Taguchi and Plackett Burman designs (Richard, 2007). While statistical data from the experimental runs are analyzed using different models such as: linear, 2FI, quadratic, cubic (Sarteshnizi et al., 2015) and special cubic (Richard, 2007) in selecting the best fit. Furthermore, other factors such as F-value, coefficient of variation (C.V), the "predicted R-square (Pred. R^2) and adjusted R-square (Adj. R^2), precision adequacy and lack of fit are also used in the analyses (Gryze et al., 2007). Where pred. R^2 value is negative, then mean model is suggested, while lack of fit appear when there are replicates which should be insignificant for p-value > 0.10 being desirable (Miller, 1984). Significant model has real effects on the responses especially if Prob > F is less than 0.05, however; greater than 0.05 is insignificant model (Richard, 2007; Miller, 1984).

In determining the model trend, plots of predicted values versus actual values are often used to enable assessment of the prediction over the range of data. Accordingly, plots from the experiment are used to study the characteristic behaviors between the predicted and actual values, which exhibits random scatter about the line for significance, while cluster points above or below the line indicates problems of over or under prediction of data (Shari, 2018). Hamidu et al. (2021) produced particleboard from rice husk using R7AD2 adhesive as reported; the generated data for responses percentage water absorption and density were used in this research work for the modeling and optimization to determine the best fit amongst eight (8) formulated and produced particleboards using simplex lattice mixture design responses.

2. MATERIALS AND METHODS

The materials used in this research are; Design-Expert Software, Version 6.0.8 model W6XC3475, processed rice husk, R7AD2 adhesive, metal mould, mixer and Universal compressing machine model LM-02 digital type (Hamidu et al., 2021). Particleboard was produced from rice husk and R7AD2 adhesive as presented in Table 1 using Equation 2 (Da Silva Cesar et al., 2017).

$$A + B = RHP \qquad (2)$$

Where A is the rice husk, B is R7AD2 adhesive and RHP is rice husk particleboard.

Boundary condition: $0.30 \leq A \leq 0.40$ and $0.60 \leq B \leq 0.70$

Table 1: Rice Husks Particleboard Design Matrix Using Mixture Composition

Components	Name	Low Actual	High Actual	Low Coded	High Coded
A	Rice Husk	0.30	0.40	0.000	1.000
B	R7AD2 Adhesive	0.60	0.70	0.000	1.000

Produced and characterized particleboards coded RHP1 – RHP8 as presented in Table 2.

Table 2: Rice Husk Particleboards Water Absorption and Density

Rice Husk Particleboards	Percentage Water Absorption		Density (ρ)
	2 hours	24 hours	kg/m^3
RHP1	8.57	25.52	911.27
RHP2	26.08	34.59	814.29
RHP3	11.17	31.43	862.50
RHP4	27.60	43.61	859.38
RHP5	12.17	31.66	830.21
RHP6	28.38	35.87	900
RHP7	8.68	27.05	915.23
RHP8	4.49	23.66	818.75

Mixture design was chosen for modeling due to its compatibility based on the constraints factors using simplex lattice for 2 components evaluated with 3 responses: percentage water absorptions (%WA) at 2 and 24 hours, and density data presented in Tables 2 was based on model Equation 2. Furthermore, Table 3 present the optimization process criteria focusing on produced particleboards to: minimize water absorption and within the density range, that form the basic requirement for particleboard based on JIS A5908 (2003) (Da Silva Cesar et al., 2017).

Table 3: Rice Husks Particleboard Constraints Criteria for Optimization Model

Name	Goal	Lower Limit	Upper Limit
Rice Husks	is in range	0.3	0.4
R7AD2 Adhesive	is in range	0.6	0.7
%WA at 2hours	minimize	10	20
%WA at 24hours	minimize	20	50
Density (kg/m^3)	is in range	800	1200

3. RESULT AND DISCUSSIONS

3.1 Rice Husks Particleboards Responses Analysis of Variance (ANOVA)

Table 4 presents analysis of variance (ANOVA) for responses for water absorptions percentage at 2 and 24 hours and density of the produced rice husks particleboards.

Table 4: Rice Husks Particleboards Analysis of Variance Responses

Source	Sum of Squares	DF	Mean Square	F Value	Prob > F	
2 hours %WA						
Model	655.54	3	218.51	66.90	0.0007	significant
Linear Mixture	528.45	1	528.45	161.80	0.0002	
AB	42.36	1	42.36	12.97	0.0227	
AB(A-B)	84.73	1	84.73	25.94	0.0070	
Residual	13.06	4	3.27			
Lack of Fit	9.91	1	9.91	9.44	0.0545	not significant
Pure Error	3.15	3	1.05			
Cor Total	668.60	7	95.51			
24 hours %WA						

Source	Sum of Squares	DF	Mean Square	F Value	Prob > F	
Model	283.52	3	94.51	43.94	0.0016	significant
Linear Mixture	172.55	1	172.55	80.23	0.0009	
AB	4.50	1	4.50	2.09	0.2215	
AB(A-B)	106.47	1	106.47	49.50	0.0022	
Residual	8.60	4	2.15			
Lack of Fit	6.58	1	6.58	9.79	0.0521	not significant
Pure Error	2.02	3	0.67			
Cor Total	292.12	7				
Density						
Model	7278.79	3	2426.26	2.13	0.2397	not significant
Linear Mixture	1878.64	1	1878.64	1.65	0.2688	
AB	3302.82	1	3302.82	2.89	0.1641	
AB(A-B)	2097.33	1	2097.33	1.84	0.2467	
Residual	4565.29	4	1141.32			
Lack of Fit	362.83	1	362.83	0.26	0.6459	not significant
Pure Error	4202.46	3	1400.82			
Cor Total	11844.08	7				

The %WA at 2 hours response ANOVA for produced rice husks particleboard shows that Model "F value" of 66.90 and "Prob > F" value of 0.0007 implies the model is significance, analyzed based on 3 degrees of freedom (DF). Linear model have "F-value" of 161.80, AB have "F-Value" of 12.97 and AB (A-B) have "F value" of 25.94 and corresponding "Prob > F" values of 0.0002, "Prob > F" value of 0.0227 and 0.0070 respectively, are less than 0.0500 also shows the model terms are significant. However; where there are more existing significant models, the model with highest polynomial is selected, while lack of fit is insignificant (Richard, 2007). Equation 3 was the model equation in terms of pseudo components for 2 hours water absorption generated by the software with the diagnostic case plot (Figure 1) for the predicted versus actual values for the analysis.

%WA at 2 hours = +27.45*A+8.85*B-20.62*A*B+73.64*A*B*(A-B) (3)

where %WA at 2 hours = water absorption at 2 hrs response for rice husks particleboard,
A = Rice husks and B = R7AD2 adhesive

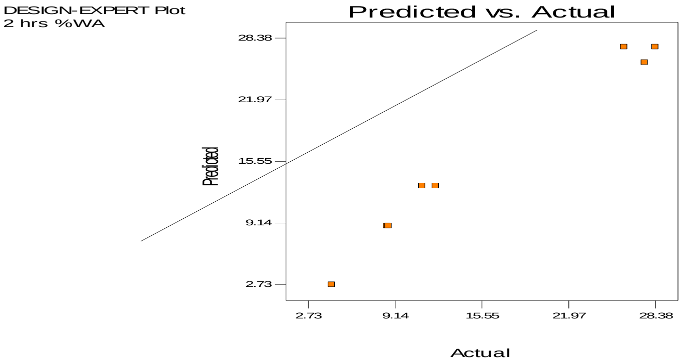

Fig.1: Predicted versus Actual Values for Rice Husks Particleboard Water Absorption at 2 hours

The cluster points observed above in the plot implies that there are some problems with the predicted values for the water absorption at 2 hours which deviated at the middle towards 15.5 and under prediction between 21.97 and 28.38 for actual value.

The percentage water absorption at 24 hours response ANOVA for the produced rice husk particleboard, shows the Model "F value" of 43.94 and "Prob > F" values of 0.0016 which is less than 0.0500 implies that the model terms are significant. Linear Mixture have "F value" of 80.23 and "Prob > F" value of 0.0009 and AB (A-B) have "F value" of 49.50 and "Prob > F" value of 0.0022 are less than 0.0500 indicating model terms are significance. Whereas Model AB "F value" of 2.09 and "Prob > F" value of 0.2215 was not a significant model, as the values are not in agreement with the standard (Richard, 2007). The lack of fit value 9.79 and 0.0521 is insignificant in this model. Equation 4 was the corresponding model equation generated by the software in terms of pseudo component and the diagnostic case plot (Figure 2) for the predicted versus actual values.

$$\%WA\ \text{at}\ 24\ \text{hours} = +35.41*A+26.46*B+6.72*A*B+82.55*A*B*(A-B) \qquad (4)$$

Where %WA at 24 hours = water absorption at 24 hours.

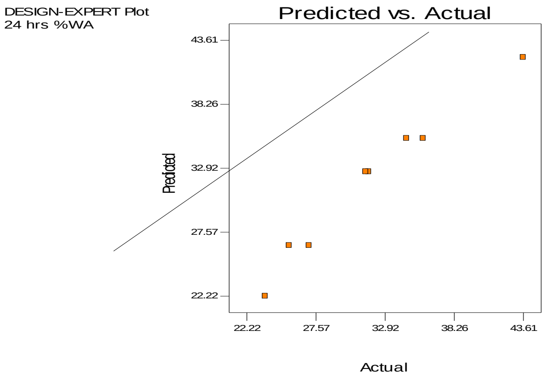

Fig.2: Predicted versus Actual Values for Rice Husks Particleboard Water Absorption at 24 hours

There were neither clusters nor scattered points observed in the plot below/above, which could read over/under prediction of the values. This implies that there were adequate data precision and accuracy for the water absorption at 24 hours. Also, this is an indication of adequate cross linking between the components of the produced particleboard in repelling water penetration.

In the density response for produced rice husks particleboard ANOVA, the "Model F value" of 2.13 implies the model is not significant when compared to the ANOVA standard, because a model that has Prob greater than F value of 0.0500 is not a significant model. Linear Mixture Components AB with F value of 2.89 and P greater than F value of 0.1641 and AB (A-B) with F value of 1.84 and P less than F value of 0.2467 are not significant model terms to suggests the design, a desired model should have F value greater than 1 and Prob greater than F value less than 0.0500 (Gryze et al., 2007). Therefore, the analysis for the density has not met the required standard. Equation 5 was the corresponding model equation generated by the software in terms of pseudo component and the diagnostic case plot (Figure 3) for the predicted versus actual values.

$$\rho = +855.81*A+911.94*B-182.09*A*B+366.37*A*B*(A-B) \qquad (5)$$

where; ρ = density of produced rice husk particleboard (kg/m^3).

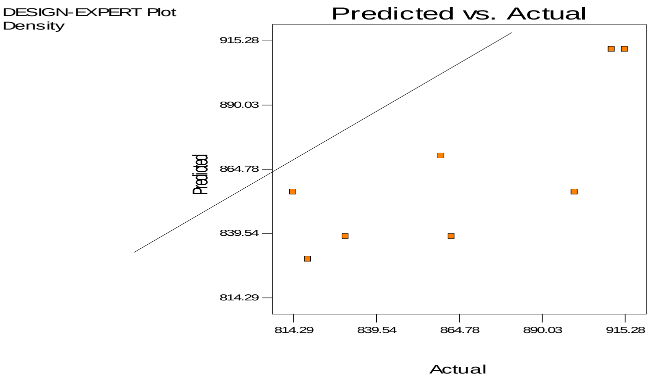

Fig.3: Predicted versus Actual Values for Rice Husks Particleboard Density

There were over prediction of values which exhibits randomly scattered data with clustered points above, indicating occurrence of deviations in some values between the “predicted and actual” in terms of densities; nevertheless, these values are within the standard of high density particleboard (Monteiro et al., 2019). The variation between the predicted and actual were observed, at RHP1 and RHP8 which has residual values of 44.19 and 24.15, implies, the predicted values for densities were less than the actual experimental values, while at RHP2, RHP4, RHP5 and RHP7 has residuals of -8.14, -10.67, - 10.67 and - 41.52 implying that the predicted values were greater than the actual values from the experiment.

3.2 Rice Husks Particleboards Responses Sequential Model Sum of Square (SMSS)

The SMSS using different model statistical tools for responses at 2 and 24 hours water absorption and density are presented in Table 5. Process was analyzed using three models (Linear, Quadratic and Cubic) to suggesting the best fitted model from the optimization.

Table 5: Rice Husks Particleboard Sequential Model Sum of Squares for Water Absorption Percentage at 2 hrs, 24 hrs and Density

2 hrs %WA					
Source	Mean	Linear	Quadratic	Cubic	Total
Sum of Squares	2020.57	528.45	42.36	84.73	2689.18
DF	1	1	1	1	8
Mean Square	2020.57	528.45	42.36	84.73	336.15
F value		22.62	2.17	25.94	
Prob > F		0.0031	0.2011	0.0070	
Std. Dev.		4.83	4.42	1.81	
R^2		0.6610	0.7102	0.9902	
R^2 Adjusted		0.7904	0.8537	0.9805	
R^2 Predicted		0.7554	0.7952	0.9658	
PRESS		226.65	193.79	83.10	
Precision Adeq.	19.347			Suggested	
24 hrs %WA					
Source	Mean	Linear	Quadratic	Cubic	Total
Sum of Squares	8025.18	172.55	4.50	106.47	1.079E+005
DF	1	1	1	1	8
Mean Square	8025.18	172.55	4.50	106.47	13487.18
F value		8.66	0.20	49.50	
Prob > F		0.0259	0.6767	0.0019	
Std. Dev.		4.46	4.80	1.47	
R^2		0.3401	0.2259	0.8103	
R^2 Adjusted		0.5907	0.6061	0.9706	
R^2 Predicted		0.5224	0.4485	0.9485	
PRESS		192.78	226.13	55.43	
Precision Adeq.	19.238			suggested	
Density					
Source	Mean	Linear	Quadratic	Cubic	Total
Sum of Squares	5.971E+006	1878.64	3302.82	2097.33	5.983E+006
DF	1	1	1	1	8
Mean Square	5.971E+006	1878.64	3302.82	2097.33	7.479E+005
F value		1.13	2.48	1.84	
Prob > F		0.3285	0.1762	0.2467	
Std. Dev.		40.75	36.50	33.78	
R^2		-0.6495	-0.5939	-0.5366	
R^2 Adjusted		0.1586	0.4375	0.6146	
R^2 Predicted		0.0184	0.2125	0.3255	
PRESS		19537.32	18878.02	18200.03	
Precision Adeq.	3.454			suggested	

The SMSS analysis for rice husks particleboard water absorption at 2 hours, shows Cubic model had F value of 25.94 and Prob > F value of 0.007 is less than 0.050, implies that the model was significant. Furthermore, Linear model which had F value of 22.62 and Prob > F value of 0.0031 was also a significant model; however, Cubic model having the highest polynomial value that satisfied the model criteria was the suggested model (Gryze et al., 2007). The suggested Cubic model had the least std. dev. of 1.81 values with corresponding adjusted R^2 values of 0.9805 and predicted R^2 value of 0.9658, compared to Linear and Quadratic models which had 4.83 and 4.42 std. devs., and corresponding adjusted R^2 values of 0.7904 for Linear, 0.8537 for Quadratic, and predicted R^2 values of 0.7554 for Linear and 0.7952 for Quadratic models. Furthermore; the PRESS value was low in Cubic model, signifying that the model was adequate without aliases from the modeling, and therefore selected as the best fit model.

The SMSS analyses for rice husks particleboard at 24 hours water absorption were tested with three models; Linear, Quadratic and Cubic. The Linear model had f value of 8.66 and Prob > F value of 0.0359 and Cubic model had F value of 49.50 and Prob > F value 0.0022 are both significant models, while Quadratic model with F value of 0.20 and Prob > F value of 0.6767 was not a significant model. A model is significant when the Prob > F value is less than 0.05 and F value is greater than 1 (Shari, 2018; Gryze et al., 2007). The Cubic model with the highest F value and least Prob > F value which satisfied the modeling criteria was the significant model. Furthermore, other criteria such as std. dev. of 1.47 and PRESS value of 55.43 were less in Cubic model compared to Linear with 4.46 std. dev. and high PRESS value of 192.78. Also the Quadratic model had std. dev. of 4.80 and 226.13 PRESS values considered not fit. The adjusted R^2 and predicted R^2 were in reasonable agreement as compared to Linear and Quadratic models, which suggested the Cubic model to focus on maximizing the model (Gryze et al., 2007).

The SMSS analyses for rice husks particleboard density has negative values for R^2 which could be due to the deviations observed from the predicted and actual values from the ANOVA diagnostic plot. However, Cubic model was suggested, even though the F values and Prob > F values for the models did not meet the standard values of P > F less than 0.0500 for model validity. The overall analyses of density model shows that the model is not significant and was not suggested for navigation in model space.

Finally, the modeling responses for water absorptions (2 and 24 hours soaking period) and density of the produced rice husks particleboard using R7AD2 adhesive as binder, had numerical values obtained by the design expert solution as presented in Table 6 and corresponding Figure 4. The model had a single solution with a high desirability factor of 0.979 suggesting that formulation 0.32 A to 0.68 B as the best fitted model placing the particleboard in high density category (Monteiro et al., 2019).

Table 6: Numerical Solution for Rice Husks Particleboard Modeling

Number	A	B	%WA 2 hours	%WA 24 hours	ρ	Desirability	
1	0.32	0.68	2.25622	21.2459	843.127	0.979	Selected

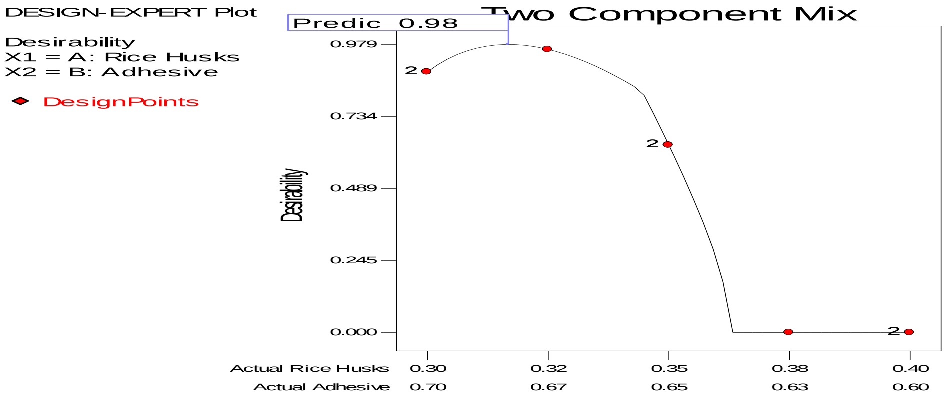

Fig.4: Rice Husks Particleboard Numerical Solution Desirability

The modeling analysis for density, though was not significant due to variations in the values between the predicted by the design expert software and the actual values obtained from the experimental data, the density was within the international standard of high density particleboard which fell between 800 – 1200 kg/m^3 JIS A5908 (2003).

4. CONCLUSION AND RECOMMENDATION

In this study, the produced rice husk particleboards responses %WA and density were modeled and optimized based on eight formulations and data generated by the Design Expert Software, Version 6.0.8. The following specific conclusion was drawn: The modeled responses based on numerical solution of percentages water absorption and density shows that RHP8 was the best fit with the desirability factor of 0.979. The properties of the produced particleboards from rice husks using R7AD2 adhesive has met the international standard of particleboard based on Japanese Industry Standard (JIS 2003) and ANSI A208.1 (2009). The general conclusion is that, production of particleboard from these wastes is feasible and could aid development and industrialization in Nigeria when the available renewable sources are harnessed.

5. CONFLICT OF INTEREST

The Authors declared no conflict of interest in this work.

6. ACKNOWLEDGEMENT

The Authors sincerely appreciate Engr. Prof. Samson Duna the DG/CEO of the Nigerian Building and Road Research Institute, his management team and Engr. Ali Abdullahi (Sarkin Fulani Bauchi) for payment and sponsoring the conference and publication of this research**.**

7. REFERENCES

ANSI (American National Standards Institute). American National Standard for particleboard. ANSI/A208.1," Gaithersburg, Maryland: Composite Panel Association; 2009.

Atoyebi, O. D., Awolusi, T. F. and Davies, I. E. (2018)."Artificial Neural Network Evaluation of Cement Bonded Particle Board Produced from red iron Wood (Lophira alata) Sawdust and Palm Kernel Shell Residues,," *Case Studies in Construction Materials*, 19(2018), 2340-2343.

Baiyeri, K. P., Chukwudi, U. P., Chizaram, C. A. and Aneke, N. (2019). Maximizing Rice Husk Waste for *Daucus Carota* Production International Journal of Recycling of Organic Waste in Agriculture (2019) 8 (Suppl 1):S399–S406https://doi.org/10.1007/s40093-019-00312-9

Baskaran, M,. Azmi, N. A. C. H., Hashim, R.* and Sulaiman, O. (2017). Properties of Binderless Particleboard and Particleboard with Addition of Urea Formaldehyde Made from Oil Palm Trunk Waste. *J. Phys. Sci.*, 28(3), 151–159, https://doi.org/10.21315/jps2017.28.3.10

Chew, L.T., Nurulhuda, M.N., Ong, C. L. and Rahim, S. (1991). Particleboard from Some Plantation Species. In: Abod SA et al. (eds.). Proceedings of a Regional Symposium on Recent Developments in Tree Plantations of Humid/Subhumid Tropics of Asia. 5−9 June 1989. Serdang. Universiti Putra Malaysia, Serdang. 708−724.

Chukwudebelu, J. A., Igwe, C., C., and Madukasi, E. I., (2015), Prospects of Using Whole Rice Husk for the Production of Dense and Hollow Bricks. African Journal of Environmental Science and Technology, 9(5), 493 – 501. Doi: 10.5897/AJEST2013.1631.

Ciannamea, E. M., Marin, D. C., Ruseckaite, R. A., and Stefani, P. M., (2017), Particleboard Based on Rice Husk: Effect of Binder Content on Processing Conditions. Journal of Raw Materials, Doi: 10.7569/JRM.2017.634125.

Da Silva César, A. A., Bufalino, L., Mendes, L. M., De Almeida Mesquita, R. G., De Paula Protásio, T., Mendes, R. F., and Ferreira Andrade, L. M., (2017), Transforming Rice Husk into a High-Added Value Product: Potential for Particleboard Production. Ciência Florestal, Santa Maria, 27(1), 303-313.

Ghosal S, Moulik S (2015) Use of rice husk ash as partial replacement with cement in concrete—a review. Int J Eng Res 4:506–509. https://doi.org/10.17950 /ijer/v4s9/907.

Gryze, D. S., Langhans, I., and Vandebroek, M., (2007), Using the correct intervals for predictions. A tutorial on tolerance intervals of ordinary least regression. Chemometrics and Intelligent Laboratory System, 87(2), 147 – 154.

Halvarson, S., Edlund, H. and Norgen, M. (2009). "Manufacture of non-resin wheat straw fibre boards," *Industrial Crops and Products,* 29(2009), 437-445.

Hamidu, L. A. J., Aroke, U. O., Osha, O. A., and Muhammad, I. M., (2021), Maximizing the Potentials of Rice Husk for Particleboard Production Using R7AD2 Adhesive. 10th International Conference of the Nigerian Building and Road Research Institute: Circular Economy in the Built Environment for Enhanced Performance of the Nigerian Construction Industry (28th April, 2021).

Hamidu, L. A. J., Aroke, U. O., Osha, O. A., and Muhammad, I. M., (2018), A Review of Polystyrene Waste Disposal for Environmental Sustainability; Proceedings of the National Engineering Conference and Annual General Meeting of the Nigerian Society of Engineers, 26th – 30th November, 2018. https://www.nse.org.ng/downloads/summary/9-kada-2018/69-kada-2018-technical-papers.

Japanese Industrial Standard A5908 (2003). Particleboards. Japanese Standard Association. Tokyo, Japan, pp. 1 – 12.

Li, R., Guo, X., Ekevad, M., Marklund, B., and Cao, P., (2015), Investigation of Glue line Shear Strength of Pine Wood Bonded with PVAc by Response Surface Methodology. Journal of BioResources, 10(3), 3831 – 3838.

MacCleery, R. (1995). "Resiliency, the Trade Mark of American Forests". Forest Prod. J. 45:19-28.

Miller, D., (1984), Reducing Transformation Bias in Curve Fitting. The American Statistician, 38(2), 124 – 126.

Monteiro, S., Martins, J., Magalhães, F. D., and Carvalho, L., (2019), Low Density Wood Particleboards Bonded with Starch Foam—Study of Production Process Conditions. Journal of Materials, 12(1975), 1 – 14. Doi: 10.3390/ma12121975.

Olubajo, O. O., Makarfi, I. Y., (2019), Prediction and Optimization of Sulphur Trioxide Yield from Calcination of Aluminium Sulfate Using Central Composite Design. Path of Science, 5(10), 1001 – 1013. doi:10.22178/pos.51 – 2.

Osabuohien, E., Okorie, U., and Osabohien, R., (2018), Rice Production and Processing in Ogun State, Nigeria: Qualitative Insights from Farmers' Association. In Obayelu, E. (Eds). Food Systems Sustainability and Environmental Policies in Modern Economics (pp. 188-215), Hershey, PA: IGI Global. DOI: 10.4018/978-1-5225-3631-4.ch009.

Richard, B., (2007), Mathematical Learning Support Center, Design Expert 7 Tutorial, pp. 1 – 10.

Roffel, B., and Betlem, B., (2006), Process Dynamics and Control Modeling for Control and Prediction. Copyright © 2006 John Wiley & Sons Ltd. The Atrium, Southern Gate, Chichester, West Sussex PO19 8SQ, England Telephone (+44) 1243 779777.

Sampathrajan, A., Vijayaraghavan, N. C. and Swaminathan, K. R. (1992). "Mechanical and thermal properties of particleboards made from farm residues," *Bioresource Technology*, 40(1992), 249–251.

Sarteshnizi, R. A., Hosseini, H., Bondarianzadeh, D., Colmenero, F. J., and Khaksar, R., (2015), Optimization of prebiotic sausage formulation: Effect of using b-glucan and resistant starch by D-optimal mixture design approach, LWT - Food Science and Technology 62(2015) , 704 – 710. http://dx.doi.org/10.1016/j.lwt.2014.05.014.

Shari, K., (2018), How to get started with design expert software. Pages 1 – 53, retrieved on 6/1/2018 at http://www.statease.com/pubs/doe-keys.pdf.

Silva, F. B. M., Vianna, R. F. and Neubert, I., (2014), Study of Adhesion Properties of Natural Rubber - Based Pressure Sensitive Adhesive with Variation of Tackifier Resin and Plasticizers Agents, 19(22), 1 – 8.

Sridhar, M. K. C., and Hammed, T. B., (2014), Turning Waste to Wealth in Nigeria: An Overview. Journal of Human Ecology, 46(2), 195 – 203.

Temitope, A., Onaopemipo, A., Olawale A. and Abayomi, O. (2015). "Recycling of Rice Husk Into A Locally Made Water-Resistant Particleboard," *Industrial Engineering and Management*, 4(3), 1-6.

Yu, J. and Wu, J. (2018). The Sustainability of Agricultural Development in China: The Agriculture–Environment Nexus. Sustainability, 10(6):1776. Https ://Doi.Org/10.3390/Su100 61776

DOI:10.51975/22370106.som
Journal of the Nigerian Society of Chemical Engineers, 37(1), 2022

ECONOMIC STUDY OF CONVENTIONAL AND IMPROVED EXTRACTIVE DISTILLATION SYSTEM USING ASPEN ECONOMIC ANALYSER

***Zubairu, A. A. and Eletta, O. A. A.**
Department of Chemical Engineering, University of Ilorin. Ilorin, Nigeria
*Email of the Corresponding author: zubyrabk@gmail.com

ABSTRACT

Simulation and the economic analysis of a conventional and an improved extractive distillation system has been carried out. Aspen plus and the Aspen Economic Analyser were used to simulate and generate data tables and charts while the non-random two liquid physical property was selected for the process. The case study adopted is the separation of Isopropyl alcohol (IPA) – water (H_2O) azeotrope mixture using dimethyl sulfoxide (DMSO) as the entrainer. Maintaining the optimum parameters, an improved configuration was designed to improve economic efficiency by reducing the amount and cost of utility requirements. The modification involved the addition of heat exchangers to make use of the available sensible heat from the entrainer stream to be recycled. The heat exchangers serve as preheaters for both column feed streams by using the excess sensible heat from the entrainer recovered as heat source. Results showed that the utility cost requirement for the extractive distillation column and the entrainer recovery column decreased from 49.4 \$/hr to 41.9 \$/h and from 57.7 \$/hr to 47.2 \$/h respectively. The total system utility cost requirement also decreased by 167,589 \$/year in the proposed modification.

Keywords: *economic analysis; extractive distillation; heat integration; process simulation.*

1. INTRODUCTION

Distillation is a very common method used in separation processes because of the advantages in operation and control (Lumin et al, 2016; Peizhe et al, 2020). Extractive distillation (ED) is used broadly in the chemical industry; it possesses the advantages of both distillation and extraction (Lumin et al, 2016). ED uses two conventional columns in a sequence; the first column separates an azeotrope using a solvent while the second column produces the pure solvent, each of these columns utilizes an individual reboiler and condenser, involving reasonably high capital and energy cost (Jana & Aurangzeb, 2019; Li et al, 2016). The introduction of an entrainer makes the separation process of azeotropes more expensive due to the regeneration of the entrainer (Yang et al, 2019).

While ED produces very high purity products, it is very attractive to reduce the energy consumption of the processes by introducing distillation-intensification technologies (Qiao et al, 2020; Cui et al, 2020; An et al, 2015; Anokhina & Timoshenko, 2015). The need for energy efficiency and sustainable processes is crucial to societal development, given that the global energy demand is expected to grow rapidly with increase in population and advancement in technology and primary energy consumption is expected to rise by 41% in 2035 (Langè et al, 2015).

Lumin et al, (2016) proposed an industrial separation case, which focused on the separation of benzene/cyclohexane mixture with sulfolane as entrainer, with the process retrofitted to make full use of the entrainer sensible heat. The application of complex extractive distillation column with a side refining section for isopropyl alcohol-water mixture separation was proposed by (Anokhina et al, 2014). Xinqiang et al, (2014) worked with an improved design and efficiency of a homogenous extractive distillation process for acetone-methanol minimum boiling azeotrope with water. Li et al, (2016) proposed three energy saving extractive distillation processes to separate 2-methoxyethanol/toluene mixture. The economic analysis and the simultaneous preheating of the two distillation columns feed streams of an ED system using recycle stream has not been explored previously in heat integrated systems from literature.

From all the literatures consulted so far, it has been discovered that no work has used the Aspen economic analyser to carry out economic evaluations of an extractive distillation for IPA dehydration. Therefore, this work introduced an improved design configuration for the extractive distillation and carried out the economic analysis to show enhancement in the cost and amount of the system's utility requirement.

2. PROCESS DESIGNS

The process design flowsheet for the IPA dehydration with DMSO as the entrainer is shown in Figure 1. The IPA- H_2O azeotrope and the solvent are fed into the ED column (EDC) at different feed plates. The DMSO changes the relative volatility of the azeotrope mixture making IPA to move toward the top part of the column (rectification section) and H_2O to move down to the bottom of the column (stripping section). This bottoms stream consisting of majorly the entrainer and H_2O is fed into the entrainer recovery column (ERC) to extract highly pure water in the distillate and highly pure DMSO in the column bottoms. The entrainer which is a heavy solvent is recycled back to the EDC. IPA and H_2O specifications are set to be exactly the same as in (Arifin & Chien, 2008; Luyben & Chien, 2010) which are 0.999999 mol of IPA in D1 and 0.9999 mol of water in D2. Reflux drums of both columns are operated at atmospheric pressure for ease of operation. Column pressure drops are automatically calculated in the Aspen simulation.

The simulation was carried out using the Aspen plus software V10.0 based on the non-random two liquids (NRTL) physical property model. The optimum parameters (Table 1) were determined following rigorous simulations of the conventional process using the data from (Luyben & Chien, 2010).

Table 1: optimum operating parameters for the ED system

Operating Conditions		EDC	ERC
Feed conditions	Pressure (atm)	1	1
	N_T	41	24
	N_{FF}	35	9
	N_{FE}	7	-
	RR	0.8	0.4
Temperature (^OC)	FF	25	-
	EE	25	-
Flow rate (kmol/h)	FF	100	-
	EE	10	-
	DT	50	50
Feed composition (wt%)	IPA	0.5	-
	H_2O	0.5	-
	DMSO	1	-
Column operating pressure (atm)	DT	1	1

2.1 Conventional Extractive Distillation (CED)

Figure 1 shows the conventional design flowsheet for the IPA-water separation with the azeotrope mixture and the entrainer fed into the EDC at different feed locations. The IPA is extracted as the distillate and the DMSO-H_2O mixture collected from the bottoms serves as the ERC feed stream. Almost pure water is then collected in the ERC distillate and almost pure DMSO is recovered in the column bottoms, the DMSO stream is then recycled back to the EDC.

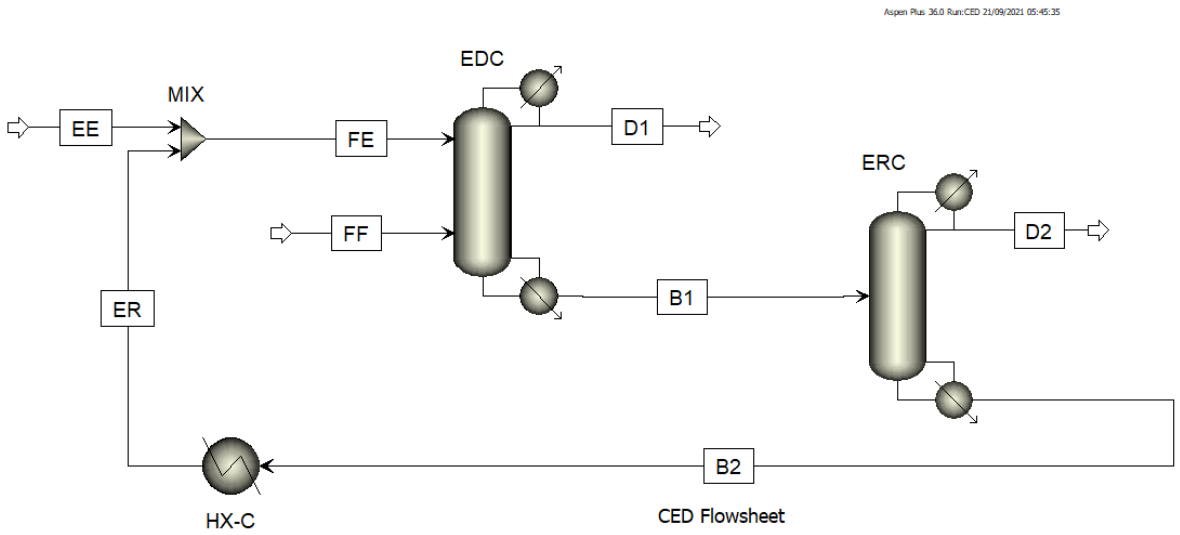

Figure 1: Conventional ED process flowsheet

The process parameters which include the concentrations of the primary and secondary components were generated and tabulated in Table 2. The IPA concentration which is the EDC top product is 99.999% by weight. The entrainer was also recovered from the bottom of the ERC. These high mole concentrations of the column output affirm the effectiveness of optimum parameters adopted from the simulations.

Table 2: Streams data from the CED process

Stream Name	**Units**	**EE**	**FF**	**D1**	**B1**	**D2**	**B2**	**ER**
From				EDC	EDC	ERC	ERC	HX-C
To		MIX	EDC		ERC		HX-C	MIX
Temperature	°C	25	25	82.048	142.257	99.5132	190.743	85
Pressure	atm	1	1	1	1	1	1	1
Mole Flows	kmol/hr	3	100.421	50	148.421	53.421	95	95
IPA	kmol/hr	0	50.2105	50	0.2106	0.2106	1.70E-18	6.32E-19
H2O	kmol/hr	0	50.2105	1.99E-05	50.2105	50.2105	2.75E-06	8.46E-07
DMSO	kmol/hr	3	0	3.24E-06	98	3	95	95
Mole Fractions								
IPA		0	0.5	0,999999	0.001419	0.003941	1.79E-20	6.65E-21
H2O		0	0.5	3.97E-07	0.338298	0.999301	2.89E-08	8.90E-09
DMSO		1	0	6.49E-08	0.660284	0.0561576	0.999999	1

2.2 Improved Extractive Distillation (IED)

It can be seen from Table 2 that the temperature of stream B2 is 190.7°C. Thus, the temperature of the recycled entrainer stream is high enough to provide the heat required in the EDC. Introducing intermediate heating gives an opportunity to further reduce the cost of utilities which would lead to reduction in energy consumption by the system.

The proposed IED was retrofitted from the CED; this stems from the need to make valuable use of the sensible heat from the DMSO stream. Two separate heat exchangers were introduced; one was used to exchange heat between the ERC bottom stream and the ERC feed stream while the other one to transfer heat to the fresh feed containing the azeotrope mixture. The design configuration is shown in Figure 2. The purpose of the heat exchangers is to make use of the excess heat available from the ERC bottom stream while preheating the feed streams to both distillation columns, this will in turn reduce the required energy needed by the columns. The stream data was calculated for the heat integrated system. The data shows that the temperatures of the two feed streams have been increased as a result of the heat exchange. It also shows the significant drop in temperature of the recycle stream which eliminates the use of a cooler; Table 3.

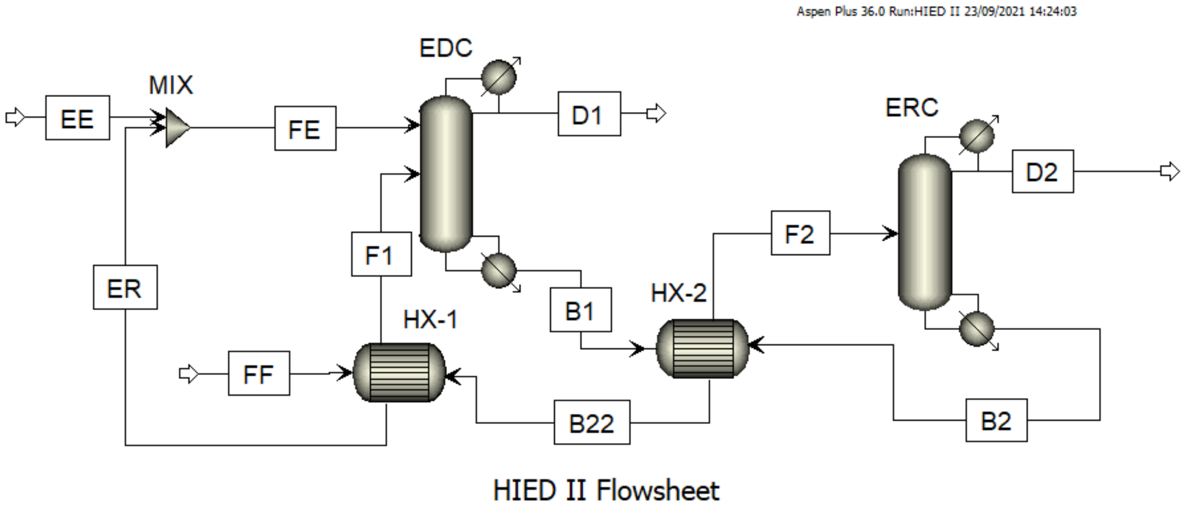

Figure 2: Improved ED process flowsheet

Table 3: Streams data from the IED process

Stream Name	**Units**	**FE**	**F1**	**D1**	**B1**	**D2**	**B2**	**ER**
From		MIX	HX-1	EDC	EDC	ERC	ERC	HX-1
To		EDC	EDC		HX-2		HX-2	MIX
Temperature	^{o}C	83.3	80.5	82.1	142.3	99.5	190.7	85.0
Pressure	atm	1	1	1	1	1	1	1
Mole Flows	kmol/hr	98	100.421	50	148.421	53.421	95	95
IPA	kmol/hr	6.98E-18	50.2105	50	0.2106	0.2106	6.98E-18	6.98E-18
H2O	kmol/hr	2.58E-05	50.2105	3.50E-05	50.2105	50.2105	2.58E-05	2.58E-05
DMSO	kmol/hr	98	0	3.24E-06	98	2.99999	95	95
Mole Fractions								
IPA		7.12E-20	0.5	0.999999	0.001419	0.003942	7.34E-20	7.34E-20
H2O		2.64E-07	0.5	7.00E-07	0.338298	0.999301	2.72E-07	2.72E-07
DMSO		1	0	6.49E-08	0.660283	0.0561575	0.999999	1

3. ECONOMIC EVALUATION

After the simulations of the conventional and improved ED processes for the azeotrope separation, their economic analyses were carried out with the aid of Aspen economic analyser (AEA). The aim of this analysis is to determine the more economical process design between the two systems in terms of energy consumption. The summary of the cost of each proposed configuration is generated from the simulations; to show the implications of the process reconfiguration, some evaluations were carried out.

3.1 Unit Operations

The unit operation costs data includes highlights of the costs of equipment and costs of installations of each unit operations in both processes. These costs data were generated using the Aspen economic analyser v10.0. The cost values for the CED and IED processes are shown in Tables 4 and 5 respectively. The tables also include the equipment weight for each unit as well as the total utility rate required by each unit. It can be seen from the tables that the cost of the EDC and ERC units reduced by 8,300 and 13,200 USD respectively for the

IED. This is because they now perform less work due to the increase in temperature of the feed streams.

Table 4: Cost data for each unit from the CED process

Unit operation				
Name	**Equipment Cost [USD]**	**Installation Cost [USD]**	**Equipment Weight [kg]**	**Utility Cost [$/h]**
HX-C	11100	63000	630	1.096985
ERC	200400	641700	17680	57.672015
EDC	355000	832100	45780	49.438165

Table 5: Cost data for each unit from the IED process

Unit operation				
Name	**Equipment Cost [USD]**	**Installation Cost [USD]**	**Equipment Weight [kg]**	**Utility Cost [$/h]**
HX-2	12500	77300	930	-
ERC	187200	619200	15780	47.188779
HX-1	10300	64600	490	-
EDC	346700	797900	48080	41.90033

3.2 Utility Costs

The utilities required for both the CED and the IED processes are tabulated in Tables 6 and 7. These data includes required rate of the heating and cooling utility and the equivalent costs per time. From the utility cost data, Figure 3 depicts that the proposed modification resulted in a drop in the general utility requirement except for the electricity which remains the same. The cost for the low pressure steam and the high pressure steam which have a negative effect on the environment has been improved in the modification.

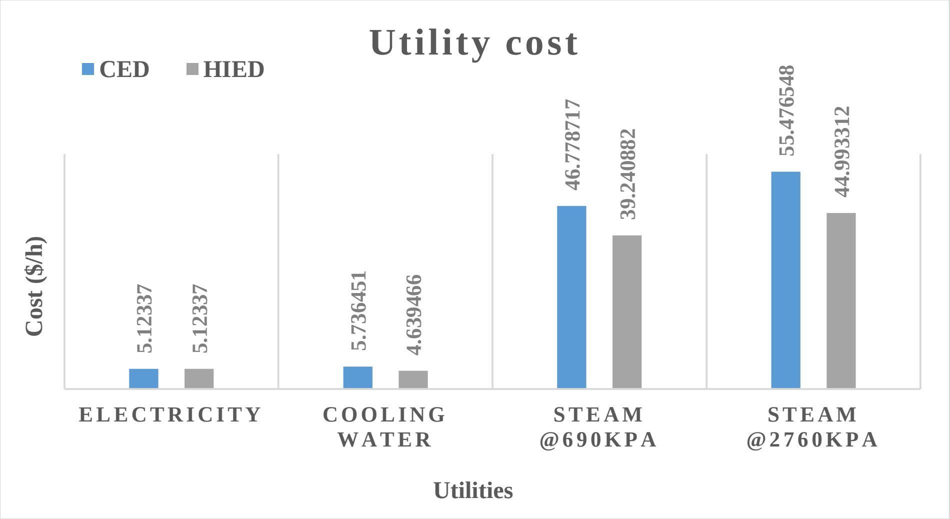

Figure 3: Utility cost for the CED & IED processes

Table 6: Utility costs data for the CED process

Utilities					
Name	**Fluid**	**Rate**	**Rate Units**	**Cost per Hour**	**Cost Units**
Electricity		66.108	kW	5.12337	USD/h
Cooling Water	Water	180.9606	m^3/h	5.736451	USD/h
Steam @690kpa	Steam	2.611877	ton/h	46.778717	USD/h
Steam @2760kpa	Steam	2.152757	ton/h	55.476548	USD/h

Table 7: Utility costs data for the IED process

Utilities					
Name	**Fluid**	**Rate**	**Rate Units**	**Cost per Hour**	**Cost Units**
Electricity		66.108	kW	5.12337	USD/h
Cooling Water	Water	146.3554	m^3/h	4.639466	USD/h
Steam @690kpa	Steam	2.191004	ton/h	39.240882	USD/h
Steam @2760kpa	Steam	1.745957	ton/h	44.993312	USD/h

3.3 Equipment and Installation costs

The breakdown of each unit equipment costs for both designs are shown in Tables 8 and 9. For the distillation columns, the data includes costs for the tower, condenser, reboiler, pumps and any other component attached to the unit. Figure 4 shows the decrease in the cost of each unit equipment in the IED process. This further confirms the significant positive cost effect that this proposed process can offer when adopted. The addition of two heat exchanger cost for the proposed process caused the increase in the total capital cost.

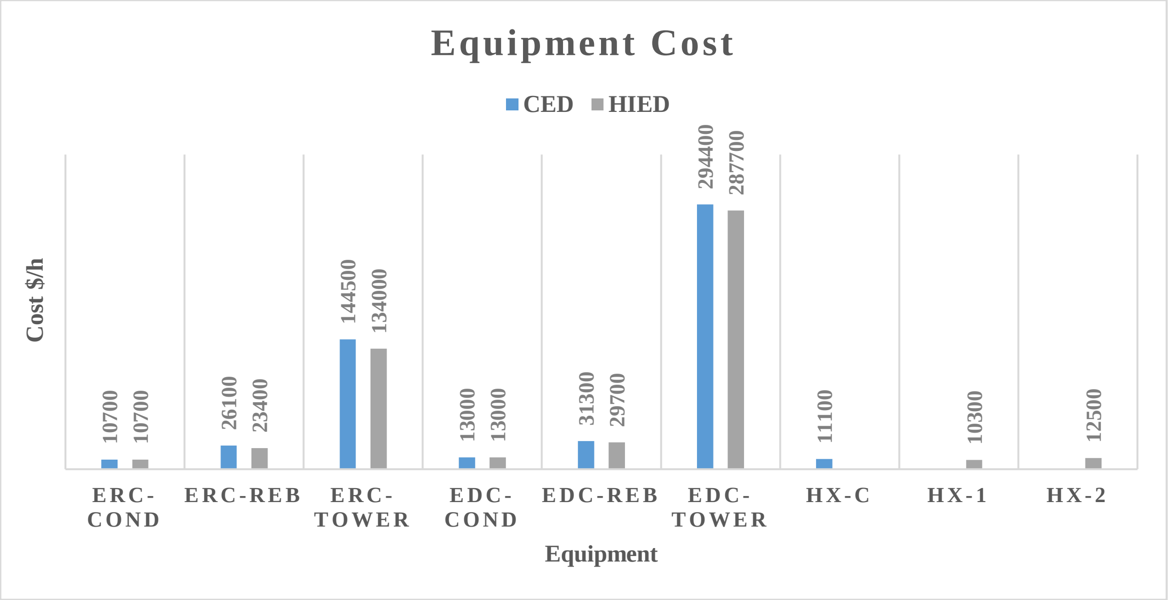

Figure 4: Unit Components cost chart for the CED & IED processes

Table 8: Unit components cost data for the CED process

Equipment				
Name	**Equipment Cost [USD]**	**Installed Cost [USD]**	**Equipment Weight [kg]**	**Installed Weight [kg]**
HX-C	11100	63000	630	3454
ERC-cond	10700	61800	570	3214
ERC-cond acc	14500	105400	1200	5677
ERC-reb	26100	92100	2600	6371
ERC-reflux pump	4600	28700	110	1127
ERC-tower	144500	353700	13200	27396
EDC-cond	13000	71100	1100	4668
EDC-cond acc	11600	79400	750	3571
EDC-reb	31300	106000	3500	8358
EDC-reflux pump	4700	32200	130	1455
EDC-tower	294400	543400	40300	57021

Table 9: Unit components cost data for the IED process

Equipment				
Name	**Equipment Cost [USD]**	**Installed Cost [USD]**	**Equipment Weight [kg]**	**Installed Weight [kg]**
HX-2	12500	77300	930	6060
ERC-cond	10700	61800	570	3214
ERC-cond acc	14500	105400	1200	5677
ERC-reb	23400	87500	2200	5707
ERC-reflux pump	4600	28700	110	1127
ERC-tower	134000	335800	11700	24853
HX-1	10300	64600	490	3790
EDC-cond	13000	71100	1100	4668
EDC-cond acc	11600	79400	750	3571
EDC-reb	29700	97800	3200	7139
EDC-reflux pump	4700	32200	130	1455
EDC-tower	287700	517400	42900	57484

Following the economic evaluations, the total utility cost which includes annualized heating and cooling costs, the total annual cost (TAC) which includes annualized capital costs and operating costs were evaluated. The TAC was calculated using the formula in equation (1).

$$TAC\ (\$/year) = operating\ cost + \frac{capital\ cost}{payback\ period} \qquad (1)$$

The capital costs include column shell, trays, reboiler, and condenser. The operating costs include the steam and cooling water for the operation of reboiler and condenser. The data summary in Table 10 clearly shows that, the total utility requirement for the whole system has decreased from 991,567 to 823,978 USD/year when heat integration was introduced, this is as a result of the decrease in energy consumption by the EDC reboiler and the absence of the cooler. The total operating cost also reduced by 184,010 USD/year and the total cost of equipment also decreased by 9,800 USD. However, the total capital cost increased by 194,150 USD majorly due to the increase in the cost of acquiring and installing the heat exchangers, this is negligible because the reduction in energy consumption is of higher priority due to its advantage to the environment. Calculating the total annual cost for both processes shows that there is an improved cost disparity as the total annual cost has decreased from 14,272,432 to 14,093,230 USD.

Table 10: Cost summary of the CED and IED processes

Property	**CED**	**IED**
Total Capital Cost [USD]	8,091,060	8,285,210
Total Operating Cost [USD/Year]	7,184,300	7,000,290
Total Raw Materials Cost [USD/Year]	4,109,530	4,109,530
Total Product Sales [USD/Year]	26,339,400	26,339,400
Total Utilities Cost [USD/Year]	991,567	823,978
Desired Rate of Return [Percent/'Year]	20	20
P.O. Period [Year]	1.16225	1.20528
Equipment Cost [USD]	628,500	618,700
Total Installed Cost [USD]	1,698,200	1,720,400
Total Annual Cost [USD]	14,272,432	14,093,230

4. CONCLUSION

In extractive distillation process systems, the heavy entrainer with high boiling point is always introduced to alter the relative volatility of the azeotrope mixture in order to achieve efficient separations. Consequently, the heavy entrainer usually with a very high temperature needs to be cooled before recycling. In this work, a modified configuration was proposed to make use of the heat of the entrainer stream in the form of heat integration to preheat the EDC and the ERC feed streams. The case study adopted is the separation of Isopropyl alcohol (IPA) – water (H_2O) azeotrope mixture using dimethyl sulfoxide (DMSO) as the entrainer. The improved configuration designed maintained the optimum parameters of the conventional system. Economic evaluations were carried out with the aid of the Aspen Economic Analyser (AEA) tool to determine the more economical one between the two process designs in terms of energy consumption. Relatively high decrease in annual utility cost and total annual cost was achieved in the modified process. Results showed that the utility cost requirement for the EDC and the ERC decreased by 15.25 and 18.18 % respectively, the total system utility cost requirement decreased by 16.9% in the proposed modification. The total operating cost also reduced by 184,010 USD/year, the total cost of equipment also decreased by 9,800 USD and the total annual cost decreased from 14,272,432 to 14,093,230 USD. The total capital cost increased by 194,150 USD majorly due to the increase in the cost of acquiring and installing the heat exchangers, this is negligible because the reduction in energy consumption is of higher priority due to environmental advantage.

NOMENCLATUREB – Bottoms
CED – Conventional extractive distillation
D – Distillate
DMSO – Dimethyl sulfoxide
D_T – Distillate
ED – Extractive distillation
EDC – Extractive distillation column
EE - Entrainer
ERC – Entrainer regeneration column
FF – Fresh feed
IED – Improved extractive distillation
IPA – Isopropyl alcohol
N_{FE} – Entrainer feed stage
N_{FF} – Fresh feed stage
N_T – Number of stages
RR – Reflux ratio
USD – United state dollars

REFERENCES

Anokhina, E. A., Rudakov, D. G. & Bogdanova, A. A., 2014. *Isopropyl Alcohol Dehydration in the Complex Column with Refining Side Section.* Moscow, Russia., Research Gate, p. 77.

Anokhina, E. & Timoshenko, A., 2015.. Criterion of the energy effectiveness of extractive distillation in the partially thermally coupled columns.. *Chem. Eng. Res,* pp. 165-175.

An, Y. et al., 2015. Design/optimization of energy-saving extractive distillation process by combining preconcentration column and extractive distillation column.. *Chem. Eng. Sci.,* pp. 166-178.

Arifin, S. & Chien, I.-L., 2008. Design and Control of an Isopropyl Alcohol Dehydration Process via Extractive Distillation Using Dimethyl Sulfoxide as an Entrainer. *Industrial Engineering Chemical Resources,* Issue 47, pp. 790-803.

Cui, P. et al., 2020. Energy-saving exploration of mixed solvent extractive distillation combined with thermal coupling or heat pump technology for the separation of an azeotrope containing low-carbon alcohol..

Jana, A. K. & Aurangzeb, M., 2019. A Novel Heat Integrated Extractive Dividing Wall Column for Ethanol Dehydration. *Ind. Eng. Chem. Res.,* p. 9109−9117.

Langè, S., Pellegrini, L. A., Vergani, P. & Savio, M. L., 2015. Energy and Economic Analysis of a New Low-Temperature Distillation Process for the Upgrading of High-CO2 Content Natural Gas Streams. *Industrial & Engineering Chemistry Research.*

Li, L. et al., 2016. Comparison of different extractive distillation processes for 2-methoxyethanol/toluene separation: design and control. *Computers and Chemical Engineering.*

Lumin, L. et al., 2016. Enhanced Efficient Extractive Distillation by Combining Heat-Integrated Technology and Intermediate Heating. *Industrial and Engineerinr Chemistry Research.*

Luyben, W. L. & Chien, I.-L., 2010. *Design and Control of Distillation Systems for Separating Azeotropes.* s.l.:John Wiley & Sons, Inc..

Peizhe, C. et al., 2020. Energy-Saving Exploration of Mixed Solvent Extractive Distillation Combined with Thermal Coupling or Heat

Pump Technology for the Separation of an Azeotrope Containing Low-Carbon Alcohol. *Industrial and Engineering Chemistry Research.*

Qiao, L., Feng, Z., Rangaiah, G. P. & Dong, L., 2020. Process Optimization of Heat-Integrated Extractive Dividing-Wall Columns for Energy-Saving Separation of CO2 and Hydrocarbons. *Industrial & Engineering Chemistry Research.*

Xinqiang, Y., Ivonne, R.-D. & Vincent, G., 2014. Improved Design and Efficiency of the Extractive Distillation Process for Acetone-Methanol with Water. *Industrial & Engineering Chemistry Research.*

Yang, A. et al., 2019. Design and control of pressure-swing distillation for separating ternary systems with three binary minimum azeotropes. *AIChEJournal, Wiley.*, pp. 1281-1293.

DOI:10.51975/22370107.som
Journal of the Nigerian Society of Chemical Engineers, 37(1), 2022

EVALUATION OF THE SUGAR CONTENT OF SELECTED COKE DRINKS

***Offurum, J. C.[1]; Ibeto, T. M.[2] and Nwakaudu, A. A.[3]**
[1,2]*Department of Chemical Engineering, Imo State Polytechnic, Umuagwo-Ohaji.*
[3]*Department of Food Science Technology, Federal University of Technology, Owerri.*
*Email of the Corresponding author: jullyengine@yahoo.com

ABSTRACT
This research work is aimed at the Evaluation of sugar contents of Selected Coke Drinks. The study was motivated by the increasing global concern of reported cases of sugar-related ill health. Three different Coke drinks namely; RC, Pepsi and Coca-cola were tested to determine the amount of sugar present in the drinks. The selection of these three products was justified by the fact that they are the most commonly consumed coke drinks (amongst others), as reviewed. The soft drink bottles were purchased from "Everyday" supermarket in Owerri, Imo State; analysis was conducted on the samples at the New Concept Laboratory, Obinze Owerri. The parameters tested include pH, Total soluble sugar, Reducing sugar, Total reducing sugar, Sucrose, Glucose and Fructose. The results of the analysis showed that the pH of the three samples were 2.19, 2.21 and 2.27 for RC, Pepsi and Coca-Cola respectively. The Total Soluble Sugar was 8.50%, 10.20% and 7.20% for RC, Pepsi and Coca-cola products respectively. Also in that order, the Reducing sugar was gotten as 8.22%, 11.75%, and 10.18% respectively, while the Total reducing sugar was found to be 18.27%, 17.97% and 15.16% respectively. The sucrose content was 154.56% for RC, 148.53% for Pepsi and 125.06% for Coca-Cola. The glucose and fructose were 1.13%, 0.82%, 1.03% and 7.09%, 10.93% and 9.15% both for RC, Pepsi and Coca-Cola products respectively. Generally, RC was found to have the highest percentage of sugar content amongst the three samples examined. It is, thus, recommended that there should be prudent check in the rate of soft drink consumption, especially those that contain high sugar and phosphoric acids value (as are obtainable in our locality); also drinking plenty of water, instead of sugary drinks like soft drink, is better due to its high sugar and acidic contents.

Keywords: *Coke, Drinks, Evaluation, Sugar Content.*

1. INTRODUCTION

Sugar is a white crystalline carbohydrate used as a sweetener and preservative. Sugars are used extensively in food industries and at home as sweeteners, as well as sources of energy especially in non-alcoholic beverages (Achard, 2009). Sugars are the most abundant and widely distributed food component in the form of carbohydrate. Carbohydrates provide most of the energy in almost all human diets, especially for average income earners. Green plants can synthesize carbohydrates from water and carbon dioxide under the influence of sunlight (through photosynthesis), which gives Glucose-D ($C_6H_{12}O_6$) as a major product (Bosma, 2013).

Chemically, sugar belongs to the class of food "carbohydrates", and it is an energy source in the human diet. Sucrose or table sugar contains the chemical formula: $C_{12}H_{22}O_{11}$, and it is a disaccharide of fructose and glucose (Blanding, 2010). Sugars have a white crystalline appearance, and are found or obtained from various sources. Today, however, sugar is available commercially in mainly two plants; sugar cane (56%) and beet sugar (44%) (Bosma, 2013).

On the other hand, soft drinks are complex mixtures containing different substances such as colour combinations, flavouring agents, acidifiers, sweeteners, preservatives and caffeine. Eschner (2015) and Richard (2012) reported that soft drinks are usually mixed with water plus 1-3% liquid carbon dioxide, 3-5% liquid sugar, acidified to a pH of about 2.4 - 4.0, emulsifiers, colours, flavours and/or spices, herbs and extracts of roots, leaves, seed and flower or bark. According to the reports, soft drinks belong to the category of non-alcoholic beverages, which is usually (but not very necessarily) carbonated, containing natural or synthetic sweetening agents, edible acids, natural or artificial flavours, and sugars (or sugary substances) form major requirements for soft drinks production.

In spite of their numerous benefits (such as providing pleasant flavor and minerals, easy absorption, antioxidant roles and fibres, which are important vehicles for hydration), natural acids and sugars have all the acidogenic and cariogenic potentials that can lead to dental caries and enamel erosion (Eschner, 2015). The public health profile is strongly influenced by its dietary status and health style. Nigeria is one of the developing countries of the world where the aforementioned problem is common. Healthcare providers have raised concerns about the importance of soft drinks since they were included in human diets abinitio, and in western and developing countries, there is high tendency of consumption of soft drinks after meals or snacks/confectionaries. There are three main areas for the nutritional significance for soft drinks (Edwards, 2015). The first is energy provision; the second area is the roll of isotonic drinks to body fluids, and finally, its low calorie content (for those who wish to minimize their caloric intake).

There are different types of soft drinks within Nigeria from various manufacturers, which many believe some of them have high sugar content, and can increase the blood sugar level. It is therefore important to determine the sugar content of soft drinks found in our locality. It is important to ensure that sugar content does not exceed recommended dietary consumption. If the assertion of people concerning some of these drinks believed to contain lesser quantity of sugar is true, to establish the fact that the sugar content of some of these drinks have exceeded the stipulated dietary allowance, and if the sugar content in these selected soft drinks is higher than recommended dietary allowance, people may need to reconsider the amount of commercial soft drinks they consume on daily basis. In addition, excessive sugar consumption is an ongoing global concern, and it is therefore vital to assess the quantity of sugar added to soft drinks in Nigeria, to ensure appropriate food security. The choice of the samples is traceable to the high rate of consumption of the products globally, especially in Nigeria (Eze, 2017).

2. MATERIALS AND METHODS

The methods used for the analysis of the products were as developed by AOAC (1997). Plastic containers of the three soft drink brands and flavours (Coca-Cola, RC and Pepsi) were purchased from Everyday Supermarket in Owerri, Imo State of Nigeria during the month of January 2021. Sugar analysis was carried out with the samples at the New Concept Laboratory, Obinze Owerri within the same month, alongside with the determination of parameters like pH, total soluble sugar, reducing sugar, sucrose and fructose.

2.1 Determination of Fehling's Factor

Principle:

Invert sugar reduces the copper in Fehling-A solution to a brick-red insoluble cuprous oxide.

Use of the Reagents:

Fehling A: 69.3 g copper sulphate ($CuSO_4.5H_2O$) was dissolved in distilled water, and diluted to 1000 ml. It was filtered and stored in amber-coloured bottle.

Fehling B: 34.6 g Rochelle salt (potassium sodium tartrate) and 100 g of sodium hydroxide were dissolved in distilled water. The solution was diluted to 1000ml mark. It was filtered and store in amber coloured bottle. The Fehling factor is given by equation 1:

$$Fehling\ Factor = \frac{\text{Titre X Weight of Sucrose (in g)}}{5000} \qquad (1)$$

Neutral Lead Acetate: 20% neutral lead acetate solution was prepared. This reagent was used to clarify sugar solutions.

Potassium Oxalate Solution: 10% Potassium oxalate ($K_2C_2O_4.H_2O$) solution was prepared. This reagent was used to remove the excess lead used during clarification.

2.2 Determination of Reducing Sugars:

25 g of sample was weighed into 250 ml volumetric flask. 10 ml of neutral lead acetate solution was added and diluted to volume with water and filter. An aliquot of 25 ml of the clarified filtrate was transferred to 500 ml volumetric flask, containing 100 ml water. Potassium oxalate was added in small amounts until there is no further precipitation. It was made up to volume. The solution was mixed well and filtered using 'whatman' filter paper (No. 1). The filtrate was then transferred to a 50 ml burette, and the percentage volume evaluated using the following relationship in equation 2:

$$Reducing\ Sugar\ \%\ (as\ invert\ Sugar) = \frac{\text{Diltions X factor of Fehling (in g)}}{\text{Weight of Sample X Titre}}\ \text{X}\ 100 \qquad (2)$$

2.3 Determination of Total Reducing Sugars:

An aliquot of 50 ml of the clarified leaded filtrate was pipetted into a 100 ml volumetric flask, containing 25 g of sample. 5 ml of concentrated HCl was added, and allowed to stand at room temperature for 24 hours. It was then neutralized with concentrated sodium hydroxide solution, followed by 0.1N of the sodium hydroxide. It was made up to 100 ml volume, and transferred to a burette having an offset tip. The sodium was titrated against Fehling's solution using starch indicator, and reducing sugars was determined using the relationship in equation (3):

$$Total\ Reducing\ Sugar\ \%\ (as\ invert\ Sugar = \frac{\text{Diltions X factor of Fehling (in g)}}{\text{Weight of Sample X Titre}}\ \text{X}\ 100 \tag{3}$$

2.4 Determination of Sucrose, Glucose and Fructose: Glucose ratio Principle:

Glucose % is determined eudiometrically using a weak alkaline medium and the value is subtracted from reducing sugars percentage, to arrive at fructose percentage; and fructose equals glucose ratio.

Reagents:

0.1N Iodine: 13g iodine and 20 g potassium iodide were weighed together and dissolved in water, to make up to 1litre. It was stored in amber coloured bottle.

0.2N Sodium bi-carbonate: 3.5 g sodium bicarbonate was dissolved in 200 ml of distilled water.

0.2N Sodium Carbonate: 4.25 g sodium carbonate was dissolved in 200 ml of distilled water.

0.1N Sodium Thiosulphate: 25 g sodium thiosulphate was dissolved in boiling distilled water. It was cooled and made up to 1litre. It was filtered, stored in amber-coloured bottle and standardized against potassium dichromate.

Procedure:

2 g of sample was weighed to 250 ml volumetric flask, and made up to volume with distilled water. It was mixed well, and an aliquot of 25 ml was transferred to a 250 ml of iodine flask. 50 ml of the 0.1N iodine was pipetted into the flask, and 50 ml of the 0.2N sodium carbonate was added, as well as 50 ml of the 0.2N sodium bicarbonate solution. It was allowed to stand in dark for 2hours, after which it was acidified with 12 ml of 25%H_2SO_4, and titrated with the standardized sodium thiosulphate, using starch as indicator. The Sucrose, Glucose and Fructose percentage were evaluated, using the provisions of equations 4, 5 and 6 respectively.

$$\text{Sucrose \%} = (\text{Total Reducing Sugar \% of Invert Sugar \%})\ \text{X}\ 0.95 \tag{4}$$

$$\text{Glucose \%} = \frac{\text{Normality of Thiosuphate X Dilution X }(B - S)\text{ X }0.009005}{0.1\text{N X Weight of Sample}}\ \text{X}\ 100 \tag{5}$$

Where B = Standard of the Blank (21.0), S = Titre value

$$\text{Fructose \%} = \text{Reducing Sugar \%} - \text{Glucose \%} \tag{6}$$

2.5 Determination of Potential Hydrogen (pH) Value

25 g of the sample was poured into a clean dry 25 ml beaker, and 13 ml of hot distilled water was added to it and stirred slowly. It was then cooled in a cold water bath to 25°C. Then the pH electrode was standardized with buffer solution, and the electrode immersed into the sample; the pH value was read and recorded accordingly.

3. RESULTS AND DISCUSSION

The results of analysis of the three coke samples are presented in table 1.

Table 1: Results of Analysis of Study Samples

Parameters Tested	Result obtained		
	RC	PEPSI	COCA-COLA
pH	2.19	2.21	2.27
Total Soluble Sugar	8.50	10.20	7.20
Reducing Sugar	8.22%	11.75%	10.18%
Total reducing sugar	18.27%	17.97%	15.16%
Sucrose	154.56%	148.53%	125.06%
Glucose	1.13%	0.82%	1.03%
Fructose	7.09%	10.93%	9.15%

From the result of analysis of the study samples, the three samples showed high acid levels, with 2.19 for RC, 2.21 for Pepsi and 2.27 for Coca-Cola. The high acid level of the products could be traceable to the level of phosphoric acid added to the drinks (mostly to give them tangy/sharper flavours, and prevent the growth of moulds/bacteria); this has the tendency of increasing the ulceric nature of the stomach. (Joshi and Agte, 2001). Dorota (2015) reviewed that high level of phosphoric acid can lead to organ damage, most notably the kidneys. And poor kidney functions can raise levels of phosphorous in the blood, which in turn lowers the calcium levels, increasing the risk of brittle-bone disease (Martin and Gonzalez, 2011; Calvo and Tucker, 2013; Calvo and Uribarri, 2013). However, the acid level of Coca-Cola was found to be higher than that of Pepsi and then RC.

Also the reducing sugars, as well as total soluble sugars were higher in Pepsi products than its other counterparts. Reducing sugar reduces the body calories, and thus increases the body fats (Bosma, 2013). So, high consumption of Pepsi would be a great disadvantage to weighty individuals (Edwards, 2015). Again, soluble sugar would regularly lead to increase in the blood sugar level, which exposes the body to diabetes *mellitus* (Blanding, 2010). Non-reducing sugars are commonly found in fungi, bacteria, yeast, insects and plants; their significant levels act as protectors of the body against various abiotic stresses, including heat drought, high salinity and ultra-violet rays (Blanding, 2010).

On the other hand, reducing sugars react easily with the free amino groups in amino acids, to form unique compounds for desirable flavors and aroma; they cause food browning in baked foods (Edwards, 2015). The levels of glucose fall between 0.82% and 1.13%, and that of fructose (mainly of natural sources) fall between 7.09% and 10.93%, and they both are simple sugars that are easily controlled by body metabolism (Achard, 2009).

4. CONCLUSION

The study samples were, generally, found to have high acid and sugar contents, with RC coke topping the chart for both parameters amongst other samples. This raises a great deal of global concern. The national health authorities and regulatory agencies, especially in developing countries (such as Nigeria) must, as a matter of urgency, sit up to their functions in this regard. The European partners of Coca-cola, for instance, use very small amount of phosphoric acid the products (like coca-cola classic, diet cokes and coca-cola zero sugar), and this has been found to give better tartness; our local companies in this business should imbibe the same culture. A nnumber of alternative flavouring and microbial growth-controlling drink additives such as *Acefulfame* (E950) and *Aspartame* (E951), whose health and safety status have been certified by the World Health Organization (WHO), as well as by the Scientific Committee on Food (SCF) and the European Union for food and beverages, are recommended, in replacement of phosphoric acids for the production of these drinks by our local manufacturers.

5. REFERENCES

Achard A.E., (2009), Process for Extracting Sugar from Beets, Annales de Chimie, 3(1), 163-168.

Association of Official Analytical Chemist (AOAC), (1997), Official Method of Analysis, Alpha Books Inc., Washington D.C.

Blanding, M., (2010). The Coke Machine: The Dirty Truth Behind the World's Favorite Soft Drink, Avery Publishers, New York.

Bosma, U., (2013), The Sugar Plantation in India and Indonesia: Industrial Production Studies in Comparative World History, Cambridge University Press, London.

Cavo, M.S. and Tucker K.L., (2013), Is Phosphorous Intake that Exceeds Dietary Reqirement a Risk Factor in Bone Health?, Annals of the New York Academy of Sciences, 1301(1), 29-35.

Cavo, M.S. and Uribarri J., (2013). Contributions to Total Phosphorous Intake: All Sources Considered, Seminars in Dialysis, 26(1), 54-61.

Dorota, K., (2015), Health Safety of Soft Drinks: Contents, Containers and Microorganisms, International Journal of Biomedical Research, 11(2), 170–177.

Edwards, W.P. (2015), The Science of Sugar Confectionery, Royal Society of Chemistry, pp. 120.

Eze, J.A., (2017), Consumption Rate of Soft Drinks in Nigerian States, Premium Times Quarterly, April 18.

Eschner, K., (2017), Coca-Cola's Creator Said the Drink Would Make You Smart, Smithsonian, Archived from the original on August 14, 2019.

Joshi, S and Agte, V., (2001), Digestibility of Dietary Fiber Components in Vegetarian Men: Plant Foods for Human Nutrition, Dordrecht, 48 (1), 39–44.

Martin, K.J. and Gonzalek E.A., (2011), Prevention and Control of Phosphate Retention/Hyperphosphatemia in CKD-MBO: What is Normal, When to Start and How to Treat, Clinical Journal of American Society of Nephrology, 6(2), 440-446.

Richard, G., (2012), The Civil War Origin of Coca-Cola in Columbus, Georgia, Muscogiana, Journal of the Muscogee Genealogical Society, 23(2), 21–24.

DOI:10.51975/22370108.som
Journal of the Nigerian Society of Chemical Engineers, 37(1), 2022

JUSTIFICATION OF ORDER OF CORROSION INHIBITION KINETICS FOR ESTERS OF CASTOR AND RUBBER SEED OILS

***Offurum, J. C.[1], Chukwu, M.M.[2], Mbadike, C. A.[3], Nwaneri, T. U.[4] and Nwakaudu, A. A.[5].**
[1,2,3,4]Department of Chemical Engineering, Imo State Polytechnic, Umuagwo-Ohaji.
[5]Department of Food Science Technology, Federal University of Technology, Owerri.
*Email of the Corresponding author: jullyengine@yahoo.com

ABSTRACT

The present study centres on the justification of order of corrosion inhibition kinetics for esters of castor and rubber seed oils. Inhibition of mildsteel corrosion was studied in the presence of sulphuric acid medium. The study was justified by the regular misprediction of order of chemical reactions (especially corrosion reaction), due to varying individual perceptions in this regard. While many researchers assume that corrosion reaction kinetics is of first order in most cases, others resolve that it is of zero or even second order. Experimental (gravimetric) data from the mildsteel corrosion inhibition process was used to generate the kinetic data at different experimental conditions of 10g/l (concentration), 40^{o}C (temperature) and 50% stroke (pressure), at different times of 4, 8, 16, 24 and 32hours. Equations of the lines were generated, and coefficient of determination, R^2 values for the different (derived) kinetic equations (zero, first and second orders) were obtained. While R^2 values for zero order curves fall between 0.9250 – 0.9790, those of first order fall between 0.9740 – 0.9880, and those of second order fall between 0.7820 – 0.9520, which indicates that the R^2 values of first order kinetics tend more towards unity than those of zero and second orders. This implies that the corrosion reaction, generally, is governed by the postulations of first order kinetics, followed by the zero order and, then, second order. The results, therefore, justify that kinetics of corrosion reactions is (always) of first order.

Keywords: *Corrosion inhibition, Justification, Kinetics, Order of reaction*.

1. INTRODUCTION

The order of a (chemical) reaction refers to the relationship between the rate of the reaction and the concentration of the species (reagents) taking part in the reaction. In order to obtain the reaction order, the rate expression (or the rate equation) of the given reaction must be obtained. This would enable a good understanding of the mixture of all the species in the reaction. More specifically, the order of a reaction is the exponent to which the concentration of the reactant specie(s) is raised (Patil and Sharma, 2011). It indicates to what extent the concentration of the specie(s) affect(s) the reaction rate, as well as which specie has the greatest effect (Libre Texts, 2020). Corrosion reactions of metallic materials are electrochemical in nature, that is, the reaction can be divided into oxidation (anodic) and reduction (cathodic) reactions. In corrosion, the anodic and cathodic reactions can either take place statistically distributed all over the surface, leading to uniform corrosion, or be separated at cathodic and anodic sites of the surface, leading to localized corrosion (Viranen, 2009; Refat and Ishaq, 2013)). Corrosion reaction proceeds more rapidly as temperature increases and with increasing oxygen concentration. **(**Khadom, 2012**)**. In theory, Faraday's law of electrolysis ($m = Izt$) could serve as a tool for predicting the possibility of corrosion reaction, as well as how fast the reaction could proceed (the kinetics).

Corrosion reactions, generally, usually involves the effect of one component (medium) on one material (the element, which is, in most cases, a metal). And severally, it becomes taskful to predict the right order for the reaction kinetics. While many researchers assume first order in most cases, others insist on zero or second order kinetics. Whichever prevails amongst these options, the choice may not be far from the truth, which is that corrosion kinetics revolves around the first order concepts.

2. THEORETICAL PRINCIPLES

For a given corrosion reaction as presented in equation 1:

$$A \xrightarrow{k} B \qquad (1)$$

The rate of disappearance of specie, '**A**' is given by equation 2.

$$-r_{A} = \mathrm{K(A)}^{n} \qquad (2)$$

Where 'n' is the order of the reaction.

So, for zero order, - r_A = $K(A)^0$, in agreement with equation (2).

$$-\frac{\mathrm{d(A)}}{\mathrm{dt}} = \mathrm{K} \qquad (3)$$

$$-\mathrm{d(A)} = \mathrm{Kdt} \qquad (3a)$$

By integration, we have:

$$-(A)\,{}_{0}^{\mathrm{t}} = (Kdt)\,{}_{0}^{\mathrm{t}} \qquad (3b)$$

$$-(A)_{\mathrm{t}} - [-(A)_{0}] = \mathrm{Kt} \qquad (3c)$$

Equation (3c) is the kinetic representation of zero order system.

For first order, - r_A = $K(A)^1$, in agreement with equation (2).

$$\text{Then} \quad -\frac{\mathrm{d(A)}}{\mathrm{dt}} = \mathrm{K(A)} \qquad (4)$$

Separating the variables, we have:

$$-\frac{\mathrm{d(A)}}{\mathrm{dA}} = \mathrm{Kdt} \qquad (4a)$$

By integration, we have:

$$-1n(A)\,{}_{0}^{\mathrm{t}} = (Kdt)\,{}_{0}^{\mathrm{t}} \qquad (4b)$$

$$-1n(A)_{\mathrm{t}} - [-1n(A)_{0}] = \mathrm{Kt} \qquad (4c)$$

$$-1n(A)_{\mathrm{t}} + 1n(A)_{0} = \mathrm{Kt} \qquad (4d)$$

But, 1nA = 2.303logA

So, this implies that:

$$-2.303log(A)_{\mathrm{t}} + 2.303log(A)_{0} = \mathrm{Kt} \qquad (4e)$$

$$log(A)_{\mathrm{t}} + log(A)_{0} = \frac{\mathrm{Kt}}{2.303} \qquad (4f)$$

Equation (4f) is the kinetic representation of first order system.

Similarly, for second order system, - r_A = $K(A)^2$, in agreement with equation (2).

$$\text{Then,} -\frac{\mathrm{d(A)}}{\mathrm{dt}} = \mathrm{K(A)}^{2} \qquad (5)$$

Separating the variables, we have

$$-\frac{\mathrm{d(A)}}{\mathrm{(A)}^{2}} = \mathrm{Kdt} \qquad (5a)$$

By integration, we have:

$$[\frac{1}{\mathrm{(A)}^{2}}]\,{}_{0}^{\mathrm{t}} = \mathrm{K}(dt)\,{}_{0}^{\mathrm{t}} \qquad (5b)$$

$$\text{Then,} \quad \frac{1}{[A_t]} - \frac{1}{[A_0]} = \mathrm{Kt} \qquad (5c)$$

Equation (5c) is the kinetic representation of second order system.

3. MATERIALS AND METHODS

Corrosion inhibition experiments were performed to access the inhibitive properties of esters of castor and rubber seed oils on mildsteel, in the presence of sulphuric acid medium. This was done at different times of 4, 8, 16, 24 and 32 hours, and different experimental conditions of concentration (10g/l), temperature (40°C) and pressure (50% stroke) in the presence and absence of each of the samples (Esters of castor seed oil-ECSO and Esters of rubber seed oil-ERSO), using weight loss method, and as postulated by the Association of Official Analytical Chemists, AOAC (1997). The temperature and pressure conditions (40°C and 50% stroke) used represent the minimum conditions obtainable in flow lines (Bai and Bai, 2019). Results of the experiments were duly generated, and subjected to kinetics study, in which the kinetic data were generated, as explained below:

In terms of weight loss, equation (3c) becomes:

$$-(W)_{\mathrm{t}} + (W)_{0} = \mathrm{Kt} \qquad (6)$$

At 't' = 0, W = 0

So, equation (6) becomes:

$$-(W)_{\mathrm{t}} = \mathrm{Kt} \qquad (6a)$$

Similarly, equation (4f) implies:

$$-log(W)_{\mathrm{t}} + log(W)_{0} = \frac{\mathrm{Kt}}{2.303} \qquad (7)$$

But at 't' = 0, W_o = 0, and log W_o is undefined.

$$\text{So,} \quad -log(W)_{\mathrm{t}} = \frac{\mathrm{Kt}}{2.303} \qquad (7a)$$

In the same vein, equation (5c) implies:

$$\frac{1}{[W]} - \frac{1}{[W_0]} = Kt \qquad (8)$$

But at 't' = 0, $W_o = 0$, and $\frac{1}{W} = \frac{1}{0}$ is indeterminate.

So, $$\frac{1}{W_t} = Kt \qquad (8a)$$

By plotting the weight parameters against time of equations 6a, 7a and 8a (as contained in appendix 1), the kinetic constants, 'K' were duly evaluated, equations of the lines were generated and values of coefficient of determination were noted.

4. RESULTS AND DISCUSSION

The results of the kinetic study for ECSO (sample A) are presented in figure 1, while those of ERSO are presented in figure 2.

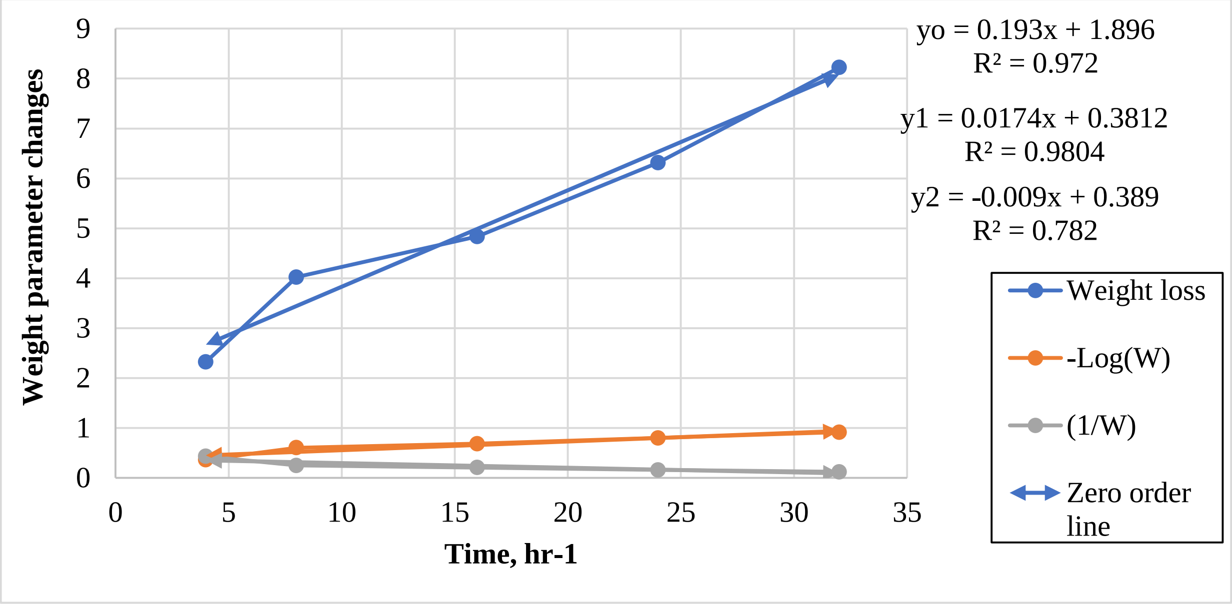

Figure 1(a): Kinetic plot of corrosion reaction in the presence ECSO

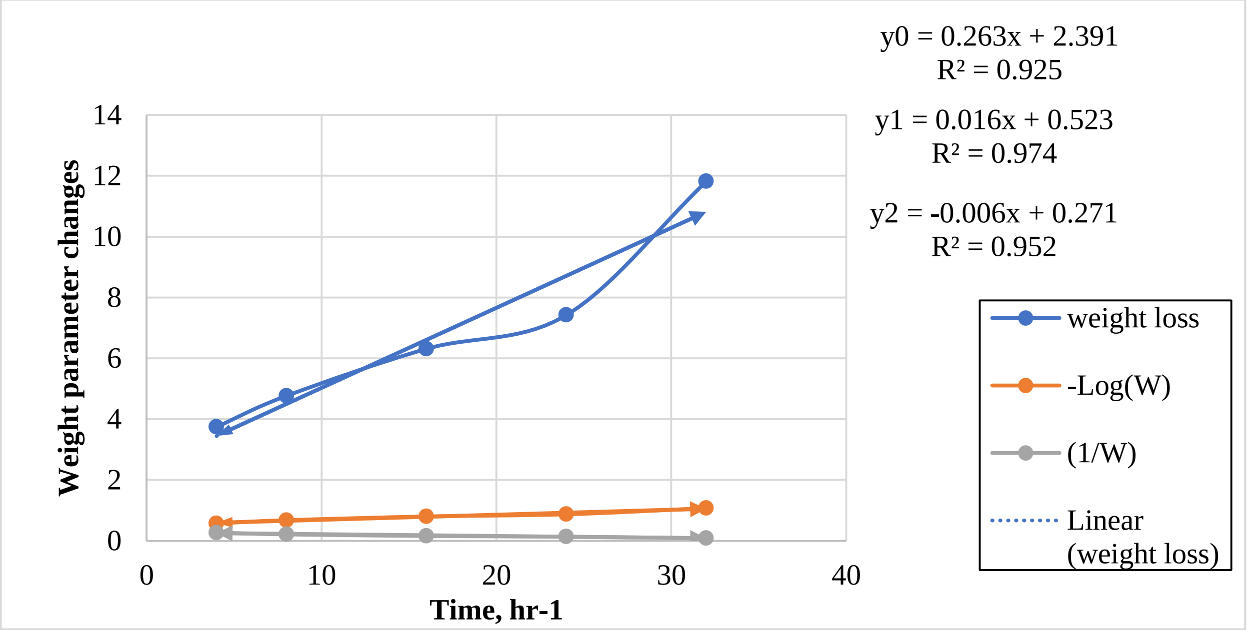

Figure 1(b): Kinetic plot of corrosion reaction in the absence ECSO

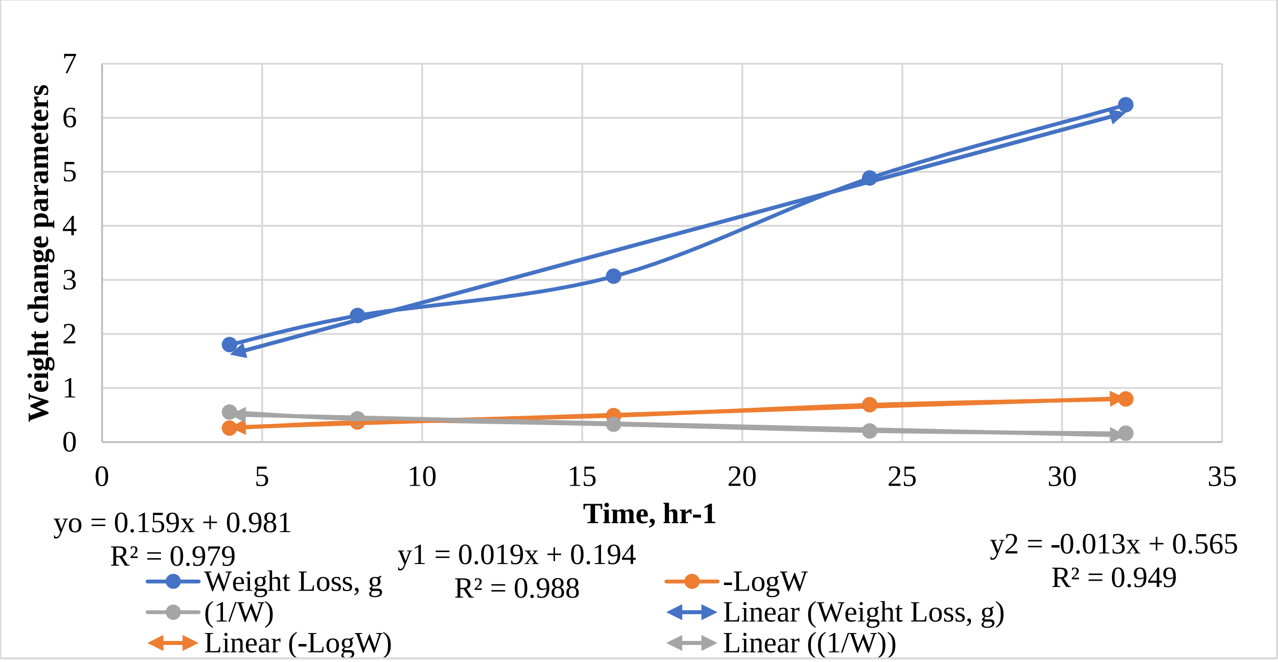

Figure 2(a): Kinetic plot of corrosion reaction in the presence ERSO

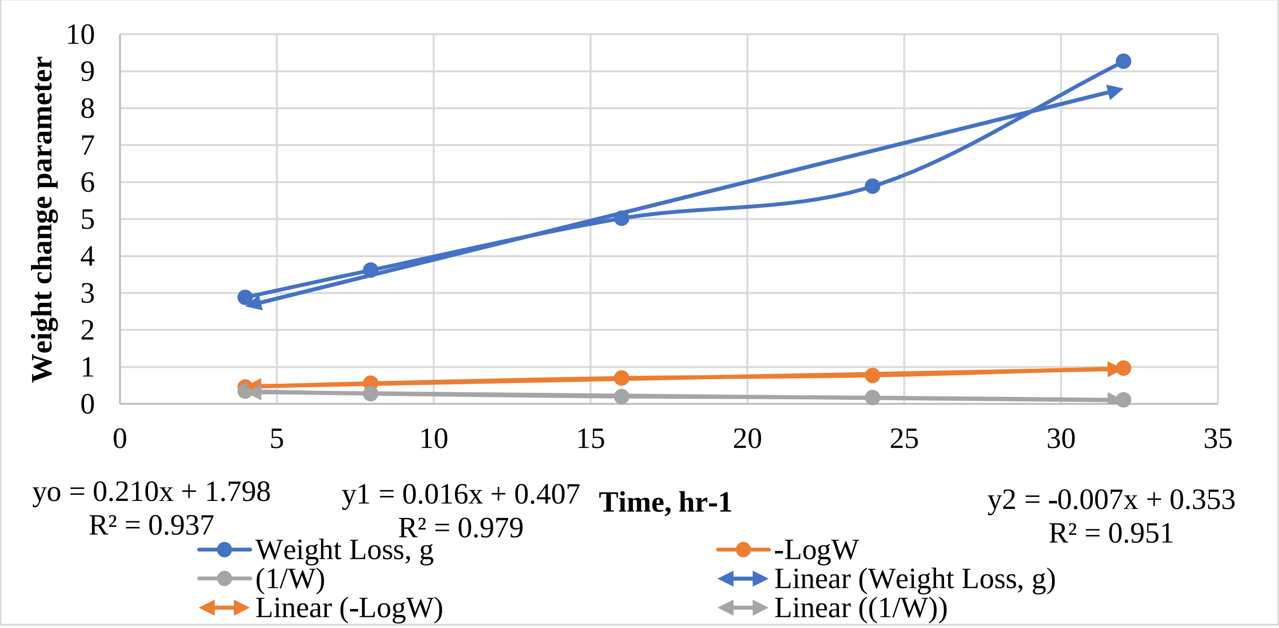

Figure 2(b): Kinetic plot of corrosion reaction in the absence ERSO

From the kinetic plots presented in figures 1 and 2, it could be observed that the coefficient of determination, R^2 values for zero order curves fall between 0.9250 – 0.9790, those of first order fall between 0.9740 – 0.9880, while those of second order fall between 0.7820 – 0.9520, which indicates that the R^2 values of first order kinetics tend more towards unity than those of zero order and then second order. This implies that the corrosion reaction, generally, is governed by the postulations of first order kinetics, followed by the zero order and, then, second order. This explains why most corrosion reactions usually fit monolayer coating (Langmuir) model, that is one inhibitor-to-one specimen coating concept (Offurum *et al*, 2011; Ahmad *et al*, 2014; Okewale and Adesina, 2020). The rate of first order reaction is largely dependent on the concentration of one specie in the reaction.

The values of the coefficient of determination, therefore, justifies that kinetics of corrosion reactions is (always) of first order concept.

5. CONCLUSION

The reaction order of chemical reactions is always defined by the help of reactant(s) concentration(s), and not the product concentrations(s) as usually misconstrued by some scholars. Corrosion reaction is electrochemical in nature, and in almost all cases, obeys first order kinetics. For the two inhibitors studied, the kinetic performance of sample B (ERSO) was found to be better than that of sample A (ECSO), comparing the coefficient of determination (R^2) values.

6. REFERENCES

Ahmad M.A., Nabeel A.J., Nuhu D.M. and Rihan O.R., (2014), Thermodynamics and Kinetics of Corrosion Inhibition of Aluminum in Hydrochloric Acid by Date Paim Leave Extract, International Journal of Chemistry Sciences, 57(2), 1011-1020.

Association of Official Analytical Chemist (AOAC), (1997), Official Method of Analysis, Alpha Books Inc., Washington D.C.

Bai, Young and Bai, Qiang, (2019), Subsea Engineering Handbook, 2nd edition, www.sciencedirect.com.

Khadom A.A., (2012), Generalization of Corrosion Reaction Kinetic Models for Steels in Inhibited Acidic Media, Journal of Applied Sciences, 7(1), 429-437.

Libre Texts Updates, (2020), Chemistry: Reaction Order, Available: https://chem.liretexts.org .

Offurum J.C., Iheme C. and Chikaire A.J., (2011), Isotherm and thermodynamics Studies for Adsorption of Dissolved Solid Particles on Cow Bone Granule, Continental Journal of Engineering Science, 6(1), 31-36.

Okewale A.O. and Adesina O.A., (2020), Kinetics and Thermodynamics Study of Corrosion Inhibition of Mildsteel in 1.5MHCl Medium, using Cocoa Leaf Extract as Inhibitor, Journal of Applied Science, Environment and Management, 24(1), 37-47.

Patil D.B. and Sharma A.R., (2011), Study on the Corrosion Kinetics of Iron in Acid and Base Medium, Journal of Chemistry, 8(1), 358-362.

Refat M.H. and Ishaq A.Z., (2013), Kinetics of Corrosion Inhibition of Aluminum in Acidic Media by Water-soluble Natural Polymeric Pectates as Anionic Polyelectrolyte Inhibitors, International Journal of Material Sciences, 6(2), 2436-2451.

Viranen S. (2009), Electrochemical Theory of Corrosion, Encyclopedia of Electrochemical Power Sources (4th edition), www.sciencedirect.com.

APPENDIX 1

Weight Loss and Kinetic Data for the Study:

Table 1: Castor Oil (Sample A), 10g/*l* at 40°C and 50% Stroke

S/N	**Time, *hr***	WITH INHIBITOR				WITHOUT INHIBITOR	
		Weight Loss, *g*	**-LogW**	**(1/W)**	**Weight Loss, *g***	**-LogW**	**(1/W)**
1	4	2.3246	0.3645	0.4302	3.7453	0.5735	0.2670
2	8	4.0219	0.6044	0.2486	4.7664	0.6782	0.2098
3	16	4.8346	0.6844	0.2068	6.3128	0.8002	0.1584
4	24	6.3172	0.8005	0.1583	7.4217	0.8705	0.1347
5	32	8.2214	0.9149	0.1216	11.8161	1.0725	0.0846

Table 2: Rubber Seed Oil (Sample B), 10g/l at 40oC and 50% Stroke

S/N		WITH INHIBITOR			WITHOUT INHIBITOR		
	Time, hr	Weight Loss, g	-LogW	(1/W)	Weight Loss, g	-LogW	(1/W)
1	4	1.8024	0.256	0.5548	2.8841	0.4600	0.3467
2	8	2.3412	0.369	0.4271	3.6182	0.5585	0.2764
3	16	3.0681	0.487	0.3259	5.0213	0.7008	0.1992
4	24	4.8853	0.689	0.2047	5.8898	0.7701	0.1698
5	32	6.2418	0.795	0.1602	9.2673	0.9670	0.1079

DOI:10.51975/22370109.som
Journal of the Nigerian Society of Chemical Engineers, 37(1), 2022

PERFORMANCE EVALUATION OF TETRABUTYLAMMONIUM BROMIDE-BASED DEEP EUTECTIC SOLVENTS IN ENHANCED OIL RECOVERY OF NIGERIAN HEAVY OIL

***Abdurrahman, A. [1], Shuwa, S.M.[1], Dabai, F. N.[2], Orodu, O. D.[3], Ogunkunle, F. T.[3], Adamu, S.Y.[1] and El-Yakubu, B.J.[1]**
[1]Department of Chemical Engineering, Ahmadu Bello University, Zaria
[2]Department of Chemical Engineering, University of Abuja
[3]Department of Petroleum Engineering, Covenant University, Ota.
Corresponding: Email: acl645035@gmail.com, Tel: 07036088332

ABSTRACT

Deep eutectic solvent (DES) is used as a green solvent in science due to its benefits over ionic liquids, such as biocompatibility and biodegradability, chemical stability with water, ease of preparation, and non-toxicity.DES 1 was successfully synthesized in a 1:2 molar ratio of Tetrabutylammonium bromide (TBAB) and polyethylene glycol 400 (PEG 400), while the novel DES 2 and DES 3 were synthesized in a 1:6 molar ratio of TBAB/ dimethyl sulfoxide (DMSO), and TBAB/N,N-dimethyl formamide (DMF) respectively. The performance(s) of the three DESs in the enhancement of heavy Nigerian crude oil recovery at ambient temperature was investigated. DES 1 recovered additional 16.07 % oil from core flooding using Berea sandstone core sample, resulting in an overall recovery of 53.44 %. DES 1 also resulted in an incremental recovery of 35.94 % from Niger-Delta sandstone, with a high ultimate recovery of 85.94 %. The presence of DES 2 and DES 3 were also shown to result in additional oil recovery. A drastic IFT reduction from 5.19 to 2.46mN/m was observed between the oil and the DES2 phase. Thus the study confirms that the presence of TBAB-based DES promotes reduction in the viscosity of the heavy oil and results in more oil recovery.

Keywords: *Deep eutectic solvents (DES), enhanced oil recovery, interfacial tension, tetrabutylammoniumbromide (TBAB)*

1. INTRODUCTION

As environmental awareness increases around the world, there has been a surge of interest in green solvents to supplement or substitute the existing non-green chemicals(Merchan-Arenas &Villabona-Delgado, 2019).Rapid biodegradability, low toxicity, non-flammability, low volatility, widespread availability and recyclability are the main characteristics of green solvents (Tarczykowska, 2017). Examples of green solvents used in oil recovery are water, supercritical fluids, non-toxic liquid polymers and their varied combinations, alkalis, biopolymers and bio-surfactants (Tackie-Otoo et al., 2020), nanoparticles (Orodu et al., 2019; Zargar et al., 2020), switchable hydrophilic solvent (SHS) like tertiary amines (Wang et al., 2019) and ionic liquids (Manshad et al., 2017). Poor biodegradability, high cost of synthesis and significant toxicology (El-hoshoudy et al., 2019) are the set back of ionic liquids (ILs), which has led to interest in another class of Ionic Liquid (IL-analogue) called Deep Eutectic Solvent (DES).

DES is a liquid that is usually made up of two or more elements that can self-associate, often by hydrogen bond interactions, to form an eutectic mixture with a melting point lower than the melting point of each individual component (Mohsenzadeh et al., 2015). It is used as a green solvent in science and industry due to its benefits over ionic liquids, such as biocompatibility and biodegradability, chemical stability with water, ease of preparation, and non-toxicity. They are often applied in the oil sector, specifically in EOR applications because of their polarity, high viscosity, and high thermal stability (El-hoshoudy et al., 2019; Mohsenzadeh et al., 2017). DESs have only recently gained interest, so studies on their use in the oil sector are limited. It was used as a novel chemical for heavy oil recovery by Mohsenzadeh et al. (2015), and later modified by dissolving Molybdenum oxide catalyst in DES (Choline Chloride/Urea) in the catalytic upgrading reaction of heavy crude oil. Mohsenzadeh et al. (2017), proposed and experimentally investigated concurrent DES and steam flooding as a new setting for heavy oil recovery enhancement, with potential for in-situ heavy oil upgrade using interfacial tension (IFT) and contact angle monitoring. The DESs were reported to be prominent and promising in altering rock wettability, decreasing the IFT between oil and water, lowering capillary pressure, and increasing injected solution viscosity, thereby improving heavy oil recovery and upgrading. Hadj-Kali et al. (2015) used separate amounts of the DESs (ChCl/glycerol and ChCl/urea) and their individual constituents as surfactants to reduce the IFT between crude oil and brine at ambient pressure and temperatures. It was determined that when the water content is less than 25 vol%, the interactions of the DES components become small, and the addition of 50 vol% water breaks the hydrogen bonding, resulting in no interactions between the hydrogen bond donor (HBD) and the salt. Hanamertani et al. (2017) used the Langmuir-Freundlich isotherm model to reduce surfactant adsorption on Berea sandstone during chemically enhanced oil recovery by using an imidazolium-based ionic liquid and a deep eutectic solvent as adsorbate material. Choline chloride-based DES with urea, thiourea, ethylene glycol and glycerol were experimentally and theoretically carried out by El-hoshoudy et al. (2019). An oil recovery of 77.4% was obtained at the laboratory scale, which is similar to that of a field scale, using Computer Modelling Group (CMG) software on a three- dimensional reservoir model. Sanati et al. (2021) compared an acidic DES (choline chloride:citric acid (1:1)) and an IL (1-dodecyl-3-methylimidazolium chloride) as chemical agents for enhanced oil recovery via experimental and theoretical investigations. The work showed that the core flooding of IL and DES-cetyltrimethylammoniumbromide (CTAB) mixtures obtained63.1% and 54.7 % recovery of the initial oil in place, respectively, and the adsorption of IL and DES was significantly lower than CTAB, with DES showing the least adsorption on dolomite surface.

Choline chloride-based-DES is the most widely used DES for EOR, as evident by some of the works mentioned above. However, choline-based-DESs are highly viscous solvents and are less effective in forming aqueous biphasic systems (Ijardar, 2020) required for the IFT reduction of heavy oil–water interface. High DES concentration or use of co-surfactant at low DES concentration have also been the demerits of the aforementioned DESs and these reduce the economic feasibility of employing DES at the industrial level. Thus, a rigorous analysis is needed to assess the efficiency of new tertiary ammonium salts. One of such salts is Tetrabutylammonium bromide (TBAB). TBAB is a quaternary ammonium salt, which may be explored as a potential substitute to other salts like chloline chloride. It is recyclable, simple to operate, non-corrosive, environmentally friendly with greater selectivity, and often known as a phase-transfer catalyst in different organic modifications (Yusof et al., 2014).

This research is focused on the synthesis of different DES, using tetrabutylammonium bromide (TBAB) as salt and polyethylene glycol (PEG) 400, dimethyl sulfoxide (DMSO), and N,N-dimethyl formamide (DMF as hydrogen bond donors (HBD), and the investigation of their performance(s) on enhanced oil recovery and IFT reduction, using Niger-Delta and Berea core samples**.**

2.0MATERIALS AND METHODS

2.1 Materials

A Nigerian heavy crude oil sample was obtained and characterized. Tetrabutylammonium bromide was purchased from Shangai Mackline Biochemical Co. Ltd., Shangai China, Polyethylene glycol 400 from BHD Laboratory Supplies Pooles, BH 15 1 TD, England, Dimethyl sulfoxide from Merck KGaA 64271 Darmstadt, Germany, and N,N-dimethyl formamide from Riedel-de Haen Ag Seelze-Hannover, Germany. All the chemicals had 98% purity and were used in the synthesis of DESs without any prior purification or drying.

2.2 Preparation of the DESs

DESs samples were synthesized as reported in literature(Ijardar, 2020).Tetrabutylammonium bromide (TBAB) was used as salts, while polyethylene glycol 400 (PEG 400), dimethyl sulfoxide (DMSO) and N,N-dimethyl formamide (DMF) as hydrogen bond donors (HBD), in the molar ratio of1:2 for DES 1, and ratio of 1:6 for DES 2 and DES 3, following a preliminary study, which showed that a molar ratio of 1:2 was not feasible for the synthesis of the novel DES 2 and DES 3. To combine the salt and the hydrogen bond donor, a magnetic stirrer (Stuart, Scientific Model US152) was used. Each DES mixture was stirred for 1 hour at 1000 rpm and 80 °C before a homogeneous transparent colorless liquid was obtained. DES samples were synthesized at atmospheric pressure.TBAB/PEG 400 was named DES 1, TBAB/DMSO as DES 2, and TBAB/DMF as DES 3.

2.3 **Determination of physical properties of oil and core samples**

Kinematic viscosity and specific gravity of the crude oil were determined at 27^{o}C using a digital viscometer (modelNTV-E1) and Attension tensiometer (Sigma 703D) respectively. API gravity was calculated from the specific gravity obtained. While the length and diameter of core samples (made from Berea and Niger-Delta sandstone) were measured with a vernier caliper.

2.4 **Core flooding test**

The experiment was carried out at the Department of Petroleum Engineering, Covenant University Ota, using Ofite - Reservoir Permeability Tester (RPT), 2015 as shown in Plate 1.The three accumulators in the RPT unit were loaded; the first accumulator was loaded with crude oil, the second was loaded with brine, and the third was loaded with a 25 vol % concentration of the prepared DES. Crude oil was pumped into the core flooding machine at ambient temperature(Orodu et al., 2019) at a rate of 1mL/min until there was no further water flowing from the effluent. The amount of oil stored in the column was measured volumetrically, and the core sample was left in equilibrium at room temperature for 48 hours. After 48 hours of ageing, the core was flooded with brine to simulate real recovery process and achieve residual oil saturation (Sor). The crude oil was extracted until no further oil was observed in the outlet, and the quantity of oil retrieved over time was recorded.

As part of the tertiary recovery operation, a 25 vol % concentration of the DES in the third accumulator was used to flood the core plug in the core holder, the effluent was extracted, and the 'incremental' oil recovered with time was measured.

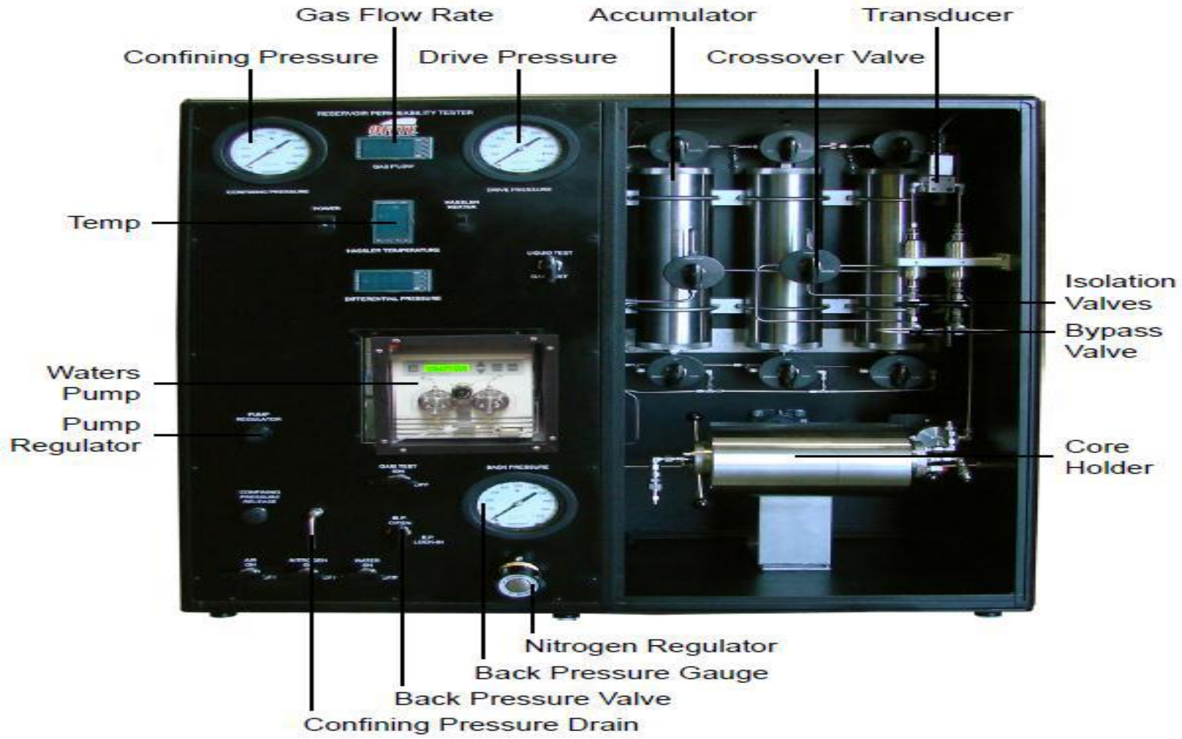

Plate 1: Ofite - Reservoir Permeability Tester, 2015 (Source – Covenant University, Ota)

3. RESULTS AND DISCUSSION

3.1Synthesis and characterization of the DES

DES 1 was successfully synthesized in a 1:2 molar ratio of TBAB and polyethylene glycol 400 (PEG 400), while DES 2 and DES 3 were synthesized in a 1:6 molar ratio of TBAB:DMSO and TBAB:DMF respectively.

The applicability of DES in interfacial processes involving mass transport is mostly determined by viscosity, density and surface tension(Makoś et al., 2020), while moisture content and refractive index is used to assess the purity of the DES or the concentration of that DES in a matrix (Naser et al., 2013). Table 1 shows the properties of the synthesized DESs (DES 1, DES 2 and DES 3), as well as some of the properties of synthesized DESs in literature (Ijardar, 2020; Xu et al., 2020). Some of the values, such as the viscosity and density of DES 1, are found to be similar to the literature values, which suggest that the produced DES 1 may be similar to some other synthesized DES in literature. Also, Table 1 shows that DES 3 has the lowest density (1.0079g/cm^3) followed by DES 2 (1.0809g/cm^3), which confirms that the density of DESs depends on the components of DES as well as their molar ratio (Sanati et al., 2021). The table also shows that DES 1, which is a mixture of TBAB and PEG 400, has the highest viscosity (198.0mm^2/s) compared to DES 2 and DES 3.This is attributed to the availability of extra hydroxyl groups from PEG 400, which creates more hydrogen bonds and in turn increases the attractive forces between molecules, making DES 1 more viscous than DES 2 and DES 3. As a result, DES 1 may be less efficient in reducing the interfacial tension (IFT) between water and heavy oil, which can reduce residual oil saturation trapped in porous medium after water flooding. Therefore, Wettability alteration as a result of its higher viscosity will be the primary mechanism for oil recovery in DES 1.

Table 1. Physical Properties of DES

Physical property	DES 1	DES 2	DES 3	Literature
Viscosity @ 28.7℃ (mm^2/s)	198.0	17.30	44.3	198.77(Ijardar, 2020)
Density @ 28.7℃ (g/cm^3)	1.1052	1.0809	1.0079	1.1054(Ijardar, 2020)
Surface tension (mN/m)	42.98	35.06	35.86	
Moisture content	0.0242	0.0409	0.0716	0.0618 (Xu et al., 2020)
Refractive index @ 28.7℃	1.4740	1.4845	1.4570	

3.2 FT-IR characterization of the DES

Aside the formation of transparent homogeneous liquids and the physical properties of the synthesized DESs displayed in Table 1, FT-IR spectra were also used to study intermolecular interactions of various tetrabutylammonium bromide based-DESs and 25 v/v % DESs in the brine. In Figure 1, for bromide (TBAB), absorption band at 738cm^{-1} depicts C-Br stretching vibrations, 1472.3 cm^{-1}depicts C-H stretching vibrations of methyl group, 2873.8 cm^{-1}depicts C–H stretching vibrations of sp^3 hybridized, while the absence of a peak at 3634.2 cm^{-1}shows the absence of O-H stretching vibrations. In Figure 1 (a), 2862.6 cm^{-1}depicts C–H stretching vibrations of sp^3 hybridized, 3447.8 cm^{-1}O-H stretching vibrations in polyethylene glycol 400 (PEG 400). While Figure 1 (b) shows1043.7 cm^{-1}S=O stretching vibrations of sulfoxide group in dimethyl sulfoxide (DMSO), and Figure 1 (c) shows 1658.7 cm^{-1} C=O stretching vibrations of amide group, and 3313.6 cm^{-1}, which depicts N-H stretching vibrations of amide group in N,N-dimethyl formamide (DMF).

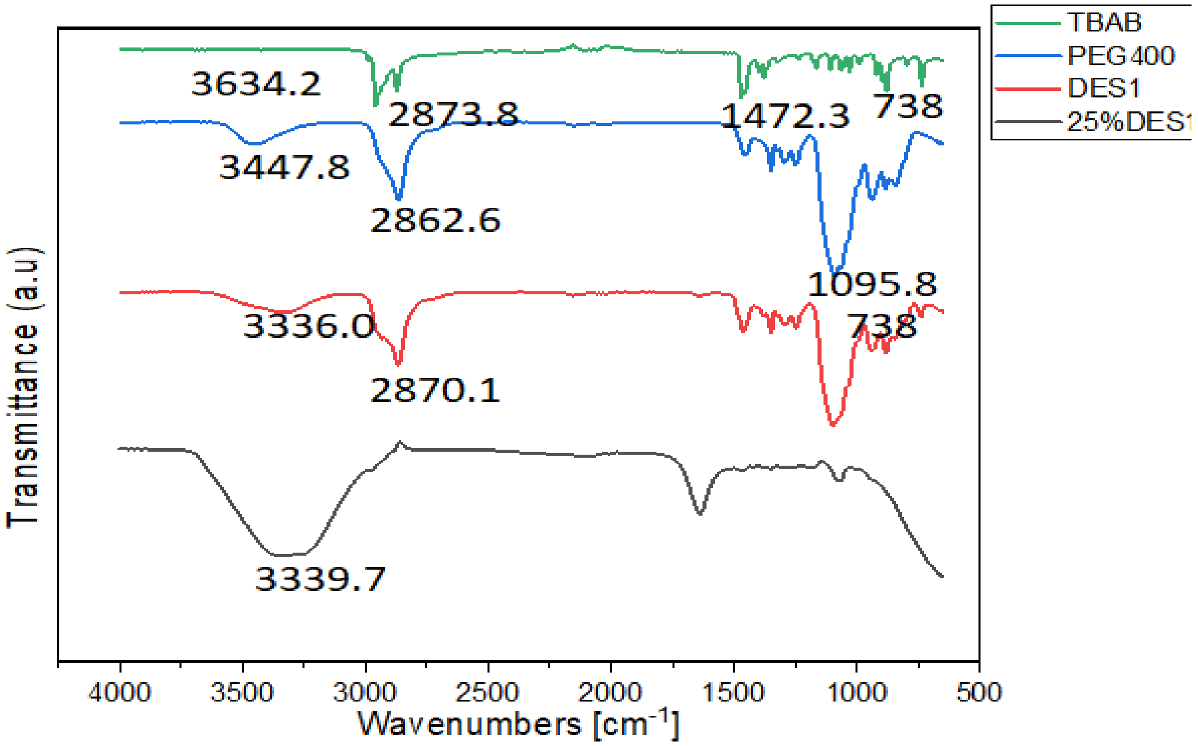

a

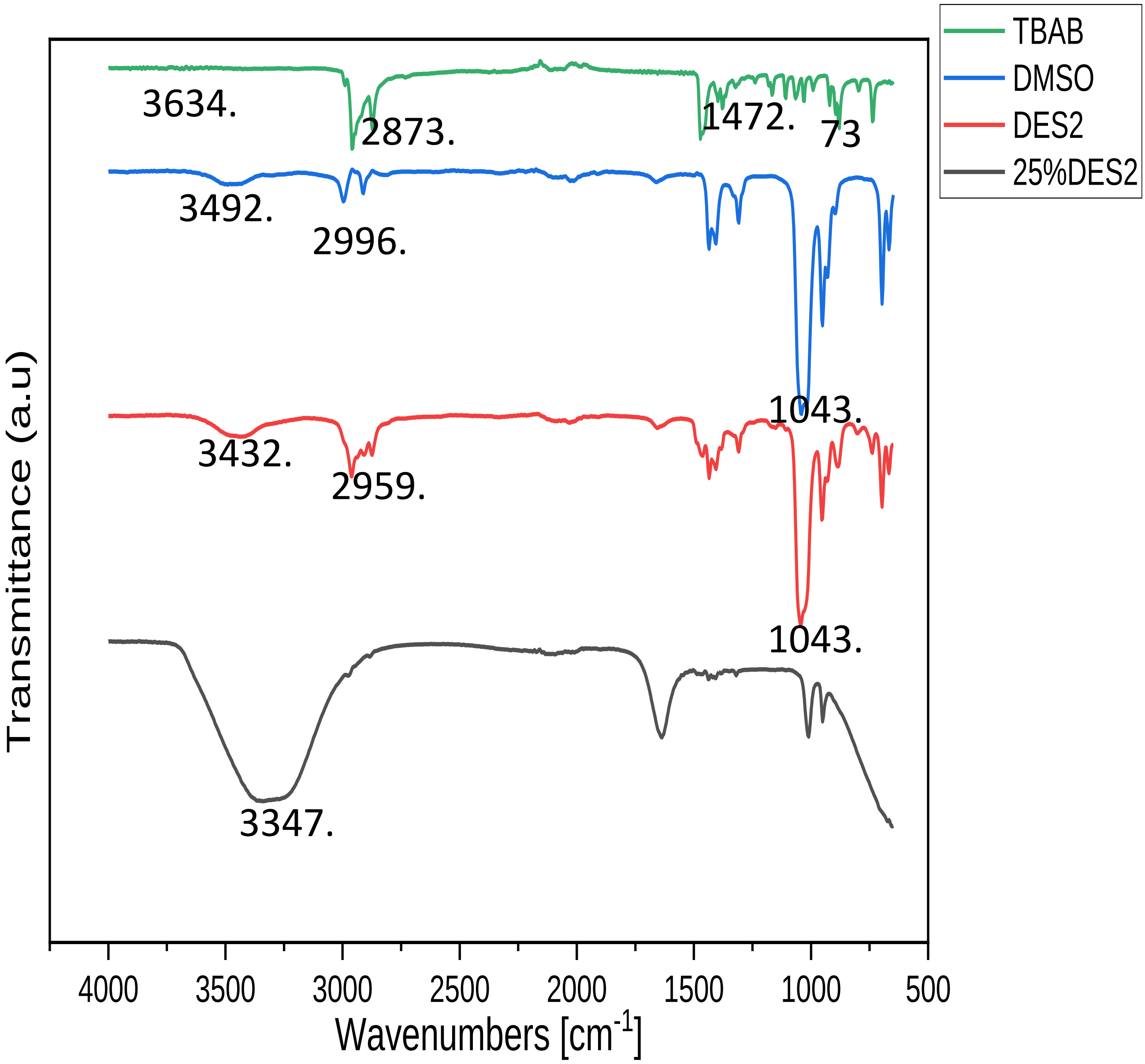
TBAB
DMSO
DES2
25%DES2
3634.
2873.
1472.
73
3492.
2996.
1043.
3432.
2959.
1043.
3347.
Transmittance (a.u)
4000
3500
3000
2500
2000
1500
1000
500
Wavenumbers [cm-1]

b

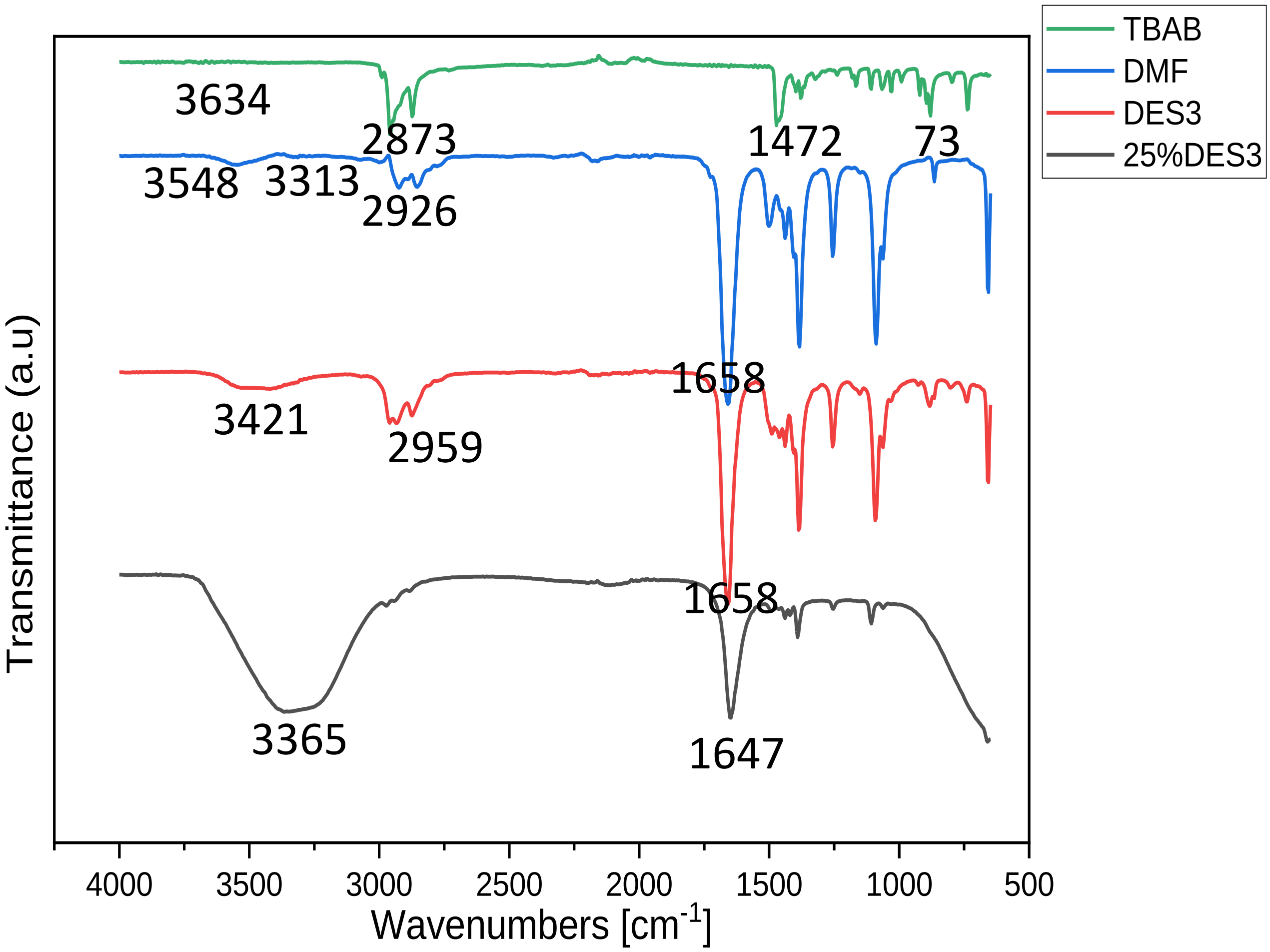

c

Figure 1. FT-IR of (a) TBAB, PEG400, DES 1 and dilute DES 1, (b) TBAB, DMF, DES 2 and dilute DES 2, (c) TBAB, DSO, DES 3 and dilute DES 3.

As indicated in Figure 1(a, b and c), DES1 displays absorption band at 3336.0 $cm^{-1}$and DES2 exhibits a peak at 3432.9 cm^{-1} and DES3 depicts a peak at 3421.7 cm^{-1}which indicate O-H stretching vibrations. These show that there are interactions between the components of the DES, which confirm the formation of hydrogen bonding and DES formation, as reported in the literature (El-hoshoudy et al., 2019; Majidi&Hadjmohammadi, 2020; van Osch et al., 2015; Xu et al., 2020). In the three DES formed, there were no new peaks displayed, confirming that formation of DES is a physical process and no chemical reaction takes place. To also confirm the presence of hydrogen bond interaction in 25 v/v % DESs in the brine, FT-IR was carried out. Although there were distortions in peaks of the three DESs, the presence of 3339.7 cm^{-1}, 3347.1 $cm^{-1}$and 3365.8 cm^{-1} in the 25 v/v % DES 1, DES 2 and DES 3 respectively confirm the existence of hydrogen bond interaction and the DES system. However, the hydrogen bond interaction is weakened by the addition of the brine to DES, as stated in literature (Hadj-Kali et al., 2015).

3.3 Core Flooding Test

Core samples were obtained from Berea and Niger-Delta sandstone, and the core flooding test was carried out at ambient temperature. The performance(s) of the three DES on Niger-Delta and the Berea sandstones are shown in Table 2. Core with DES 1has a length of 0.024 m and a diameter of 0.0340 m, with a porosity of 32.11 % and a permeability of 208.5 mD, resulting in an incremental oil recovery of 35.94 % and a very high ultimate recovery of 85.94 %.There was also an incremental oil recovery of 17.14 % using DES 2 from core flooding using Niger-Delta sandstone, while the presence of DES 3 improved the recovery by 19.56% for the Berea sandstones. This demonstrates the potency of DES as a solvent for improved oil recovery.

Table 2.Core flooding experiment

Core sample		Niger-Delta **Core with DES 1**	Niger-Delta **Core with DES 2**	Berea **Core with DES 3**
Core properties	Length (m)	0.0240	0.062	0.024
	Diameter (m)	0.0340	0.032	0.035
	Pore Volume x 10^{-6} (m^3)	7.00	8.0	6.0
	Porosity (%)	32.11	16.04	25.97
	Permeability (mD)	208.5	315.12	211.89
Initial conditions	Initial oil in place, IOIP x10^{-6} (m^3)	6.40	7.0	4.6
	Initial oil saturation S_{oi} (%)	91.43	87.5	76.67
	Initial water saturation S_{wi} (%)	8.57	12.5	23.33
Oil recovery factor based on IOIP (%)	Brine flooding	50.0	44.29	30.43
	25 vol % DES 1 flooding	35.94	17.14	19.56
	Total recovery factor	85.94	61.43	49.99

3.4 Characterization of the crude oil

After flooding with DES, the effluent was taken and the crude oil was separated from the DES using a separating funnel. In order to see the interaction between the heavy oil and the crude oil, FT-IR analysis was carried out. As depicted in Figure 2, there was no formation of new peak, which implies there was only an infinitesimal amount or trace of DES in the oil. Hence, DES is a good solvent for oil recovery as it does not react with oil and it has the potential of upgrading heavy oil, e.g. by decreasing the viscosity of the oil, as shown in Table 3.

Table 3. Physical Properties of crude oil before and after flooding

Physical property	**Crude oil before injection**	**Crude oil after DES 1 injection**	**Crude oil after DES 2 injection**	**Crude oil after DES 3 injection**
Viscosity @ 28.7°C(mm^2/s)	374.5	366.8	314.6	290.0
Relative Density	0.96	0.94	0.95	0.95
API˚@ 15 ^{o}C	15.25	18.27	16.75	16.75
Moisture content (%)	0.0505	0.0348	0.0227	0.0510

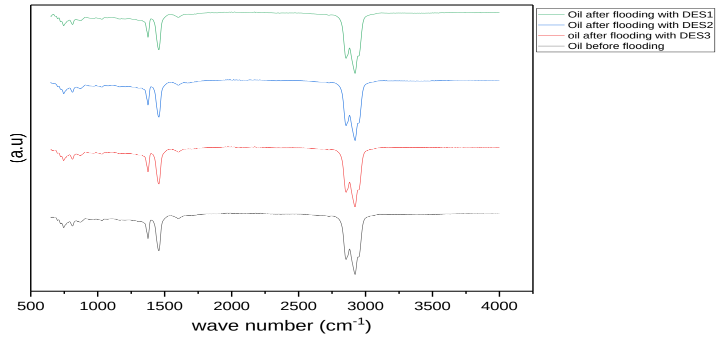

Figure 2. FT-IR of oil before and after flooding with DES

3.5 Interfacial tension reduction test

Figure 3 shows that 25 vol % DES 2 substantially reduces the IFT from 5.19 to 2.46 mN/m, while 25 vol

% DES 3 moderately reduces the IFT from 5.19 to 4.29 mN/m. Alternatively, there was an increase in IFT from 5.19 to 6.61 mN/m between the oil/25 v/v% DES 1. It was only after the concentration of DES 1 was increased from 25 v/v% to 27 v/v % that a decrease to 4.34 mN/m was observed. The increase in IFT at 25 and 26 v/v% of DES could be as a result of insufficient DES available to effectively increase the capillary number (Sanati et al., 2021), and/or the higher viscosity of DES 1, as shown in Table 1. Nevertheless, the study confirms that DES has a significant effect on IFT.

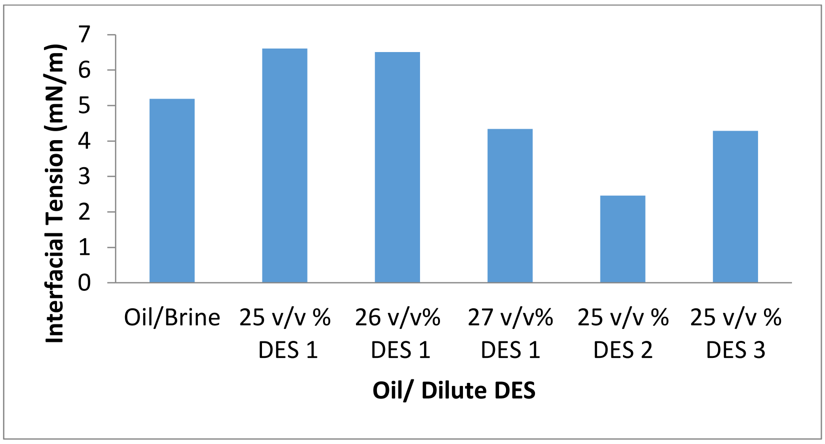

Figure3. Interfacial (IFT) reduction test

4. CONCLUSION

In this study, DES 1 was successfully synthesized in a 1:2 molar ratio of tetrabutylammonium bromide (TBAB) and polyethylene glycol 400 (PEG 400), while DES 2 and DES 3 were successfully synthesized in a 1:6 molar ratio of TBAB/dimethyl sulfoxide (DMS) and TBAB/N,N-dimethyl formamide (DMF) respectively. FT-IR results confirmed the existence of hydrogen bond interaction, and the DES system in 25 v/v % DESs in the brine. The presence of 25 vol % DES 1 led to the recovery of additional35.94%, resulting in a high overall oil recovery of 85.94 %. While an additional recovery of 17.14 % was obtained using DES 2 from core flooding using Niger-Delta sandstone. Similarly, the presence of DES 3 improved the recovery by up to 19.56% for the Berea sandstones. For the recovered oil, FT-IR confirmed that there was no trace of DES in the oil. This study highlights that it was possible to reduce the Interfacial (IFT) between the oil and the DES phase from 5.19 to 2.46 mN/m, showing that DES can significantly reduce IFT. Thus the study confirms that the presence of DES promotes reduction in the viscosity of the heavy Nigerian oil, increase in API gravity, decrease in IFT, and results in enhanced oil recovery.

Acknowledgement

The authors would like to express their gratitude to the Tertiary Education Trust Fund (TETFund) for their financial assistance, as well as the administrations of Covenant University and Ahmadu Bello University for their collaborative efforts and permission to publish this work.

5. REFERENCES

El-hoshoudy, A. N., Soliman, F. S., Mansour, E. M., Zaki, T., & Desouky, S. M. (2019). Experimental and theoretical investigation of quaternary ammonium-based deep eutectic solvent for secondary water flooding. *Journal of Molecular Liquids*, *294*, 111621. https://doi.org/10.1016/j.molliq.2019.111621

Hadj-Kali, M. K., Al-khidir, K. E., Wazeer, I., El-blidi, L., Mulyono, S., & AlNashef, I. M. (2015). Application of deep eutectic solvents and their individual constituents as surfactants for enhanced oil recovery. *Colloids and Surfaces A: Physicochemical and Engineering Aspects*, *487*, 221–231. https://doi.org/10.1016/j.colsurfa.2015.10.005

Hanamertani, A. S., Pilus, R. M., & Irawan, S. (2017). A Review on the Application of Ionic Liquids for Enhanced Oil Recovery. In M. Awang, B. M. Negash, N. A. Md Akhir, L. A. Lubis, & A. G. Md. Rafek (Eds.), *ICIPEG 2016* (pp. 133–147). Springer Singapore. https://doi.org/10.1007/978-981-10-3650-7_11

Ijardar, S. P. (2020). Deep eutectic solvents composed of tetrabutylammonium bromide and PEG: Density, speed of sound and viscosity as a function of temperature. *The Journal of Chemical Thermodynamics*, *140*, 105897. https://doi.org/10.1016/j.jct.2019.105897

Majidi, S. M., & Hadjmohammadi, M. R. (2020). Hydrophobic borneol-based natural deep eutectic solvents as a green extraction media for air-assisted liquid-liquid micro-extraction of warfarin in biological samples. *Journal of Chromatography A*, *1621*, 461030. https://doi.org/10.1016/j.chroma.2020.461030

Makoś, P., Słupek, E., & Gębicki, J. (2020). Hydrophobic deep eutectic solvents in microextraction techniques–A review. *Microchemical Journal*, *152*, 104384. https://doi.org/10.1016/j.microc.2019.104384

Manshad, A. K., Rezaei, M., Moradi, S., Nowrouzi, I., & Mohammadi, A. H. (2017). Wettability alteration and interfacial tension (IFT) reduction in enhanced oil recovery (EOR) process by ionic liquid flooding. *Journal of Molecular Liquids*, *248*, 153–162. https://doi.org/10.1016/j.molliq.2017.10.009

Merchan-Arenas, D. R., & Villabona-Delgado, C. C. (2019). Chemical-Enhanced Oil Recovery Using *N* , *N* - Dimethylcyclohexylamine on a Colombian Crude Oil. *International Journal of Chemical Engineering*, *2019*, 1–10. https://doi.org/10.1155/2019/5241419

Mohsenzadeh, A., Al-Wahaibi, Y., Al-Hajri, R., Jibril, B., & Mosavat, N. (2017). Sequential deep eutectic solvent and steam injection for enhanced heavy oil recovery and in-situ upgrading. *Fuel*, *187*, 417–428. https://doi.org/10.1016/j.fuel.2016.09.077

Mohsenzadeh, A., Al-Wahaibi, Y., Jibril, A., Al-Hajri, R., & Shuwa, S. (2015). The novel use of Deep Eutectic Solvents for enhancing heavy oil recovery. *Journal of Petroleum Science and Engineering*, *130*, 6–15. https://doi.org/10.1016/j.petrol.2015.03.018

Naser, J., Mjalli, F., Jibril, B., Al-Hatmi, S., & Gano, Z. (2013). Potassium Carbonate as a Salt for Deep Eutectic Solvents. *International Journal of Chemical Engineering and Applications*, 114–118. https://doi.org/10.7763/IJCEA.2013.V4.275

Orodu, K. B., Afolabi, R. O., Oluwasijuwomi, T. D., & Orodu, O. D. (2019). Effect of aluminum oxide nanoparticles on the rheology and stability of a biopolymer for enhanced oil recovery. *Journal of Molecular Liquids*, *288*, 110864. https://doi.org/10.1016/j.molliq.2019.04.141

Sanati, A., Rahmani, S., Nikoo, A. H., Malayeri, M. R., Busse, O., & Weigand, J. J. (2021). Comparative study of an acidic deep eutectic solvent and an ionic liquid as chemical agents for enhanced oil recovery. *Journal of Molecular Liquids*, *329*, 115527. https://doi.org/10.1016/j.molliq.2021.115527

Tackie-Otoo, B. N., Ayoub Mohammed, M. A., Yekeen, N., & Negash, B. M. (2020). Alternative chemical agents for alkalis, surfactants and polymers for enhanced oil recovery: Research trend and prospects. *Journal of Petroleum Science and Engineering*, *187*, 106828. https://doi.org/10.1016/j.petrol.2019.106828

Tarczykowska, A. (2017). *Green Solvents*. https://doi.org/10.5281/ZENODO.893346

van Osch, D. J. G. P., Zubeir, L. F., van den Bruinhorst, A., Rocha, M. A. A., & Kroon, M. C. (2015). Hydrophobic deep eutectic solvents as water-immiscible extractants. *Green Chemistry*, *17*(9), 4518–4521. https://doi.org/10.1039/C5GC01451D

Wang, J., Du, Y., Du, C., Xu, A., Yao, G., Zhao, H., Zhu, X., & Guo, X. (2019). Physicochemical properties of switchable-hydrophilicity solvent systems: N,N-Dimethylcyclohexylamine, water and carbon dioxide. *The Journal of Chemical Thermodynamics*, *133*, 1–9. https://doi.org/10.1016/j.jct.2019.01.030

Xu, K., Xu, P., & Wang, Y. (2020). Aqueous biphasic systems formed by hydrophilic and hydrophobic deep eutectic solvents for the partitioning of dyes. *Talanta*, *213*, 120839. https://doi.org/10.1016/j.talanta.2020.120839

Yusof, R., Abdulmalek, E., Sirat, K., & Rahman, M. (2014). Tetrabutylammonium Bromide (TBABr)-Based Deep Eutectic Solvents (DESs) and Their Physical Properties. *Molecules*, *19*(6), 8011–8026. https://doi.org/10.3390/molecules19068011

Zargar, G., Arabpour, T., Khaksar Manshad, A., Ali, J. A., Mohammad Sajadi, S., Keshavarz, A., & Mohammadi, A. H. (2020). Experimental investigation of the effect of green TiO2/Quartz nanocomposite on interfacial tension reduction, wettability alteration, and oil recovery improvement. *Fuel*, *263*, 116599. https://doi.org/10.1016/j.fuel.2019.116599

DOI:10.51975/22370110.som
Journal of the Nigerian Society of Chemical Engineers, 37(1), 2022

EFFICIENCY OF ACTIVATED PERIWINKLE CHAR IN THE RECOVERY OF LEAD (II) ION FROM INDUSTRIAL WASTEWATER USING FIXED BED ADSORPTION PROCESS

***Babalola, R.[1] and Aniedìong, U. [2]**
[1,2]Department of Chemical/Petrochemical engineering, Faculty of Engineering, Akwaibom state university, Akwa Ibom State, Nigeria.
rasheedbabalola@aksu.edu.ng, *+234 803 159 2001.*

ABSTRACT

The discharge of untreated industrial wastewater containing lead and the indiscriminate disposal of periwinkle shell causes lead poisoning and blockage of drainage. The cost of industrial wastewater treatment is demanding; thus the research is focused on creating wealth from waste periwinkle shell as a cheap adsorbent material to reduce the cost of lead removal from industrial wastewater. Therefore, activated periwinkle shell char (APSC) in removal of lead Pb (II) ion from industry wastewater was investigated using fixed-bed adsorption column. APSC was prepared by treating the periwinkle Char with 1M H_2SO_4 *solution. Characterization of the adsorbent before and after continuous adsorption was performed using Fourier transform infrared spectroscopy (FTIR) and Scanning electron microscopy (SEM) to show modifications in the surface and chemical structure of APSC after adsorption process. The effect of design variables such as bed height, Influent concentration and withdrawal flowrate were studied.The breakthrough profiles were obtained by an analysis of the column experimental data and the relationship between operating parameters using the Thomas, Clark, Yoon-Nelson and Adams-Bohart models. The equilibrium data was best represented by the Yoon and Nelson model having the highest correlation coefficient* (R^2) *of 0.9751. This suggest that Activated periwinkle shell char is a potential adsorbent for heavy metals removal from industrial wastewater.*

Keywords: *activated, adsorption, char, periwinkle.*

1. INTRODUCTION

Communities in industrial areas are facing the challenge of save and healthy drinking water due to the discharge of untreated industrial wastewater into the environment. To contend with these challenges, regulatory bodies have come up with standard for treatment of industrial wastewater and stiff punishment for violators because of the adverse effect of these pollutants, evidence are established in the National Environmental Regulations(National Environmental Standard and Regulations Enforcement Agency, 2009; Ministry of Environment , 1999). Lead is a priority pollutant; it finds its way into the receiving water body majorly through industrial wastewater, they bio-accumulate in the tissues of the marine lives and translocates to humans through food chains. Consequently, Lead poisoning occur leading to mental retardations, kidney malfunctioning and anaemia (Mohsen, Sara, & Masoud, 2015; Uzoije & Uche, 2016).

Aimikhe & Lekia(2021) related that in coastal communities' periwinkle is a major source of proteins in most delicacies. It shells contribute to environmental degradation because of the indiscriminate disposal blocking drainages. They reviewed the various ways by which periwinkle shell can be processed and utilized, including its use as an adsorbent material. The studies of Fe^{3+} ion removal from aqueous solutions using periwinkle shell activated carbon was investigated by Akpa & Ndukam (2018). The thermodynamic parameters results showed that adsorption process was endothermic with Enthalpy change (ΔH°): 222.91 kJ/mol; a positive Entropy change (ΔS°) of 19.19 kJ/mol, indicating an increase in the degree of freedom (or disorder) of the adsorbed species and a negative Gibb's free energy (ΔG°) at all temperature indicating that the adsorption process was spontaneous and favourable at high temperature.

Mohsen, Sara &Masoud (2015) reviewed various methods for lead removal from industrial wastewater including chemical precipitation, electrochemical reduction, ion exchange, reverse osmosis, membrane separation, and adsorption. Based on technical applicability, plant simplicity and cost-effectiveness, they concluded that adsorption is the most effective method. Uzoije & Uche (2016) investigated the dynamic adsorption process of Pb(II) ion onto fixed-beds plantain peel activated carbon (PPAC) and bamboo activated carbon (BAC) materials to treat vegetable oil polluted wastewater. The capacity of these materials to adsorb Pb(II) ion increased with increase in initial concentration and bed height but decreased as inflow rate increase, decrease in initial concentration and bed height. Their data were fitted into Thomas, Adams Bohart, Yoons and Nelson dynamic adsorption models to determine the extent of compatibility. Thomas model was most complied followed by Yoon-Nelson model whereas the least complied model was Adams-Bohart.

This research is focused on creating wealth from waste periwinkle shell as a cheap adsorbent material to reduce the cost of lead removal from industrial wastewater. Therefore, the objective of the paper is to characterize APSC adsorbent before and after the adsorption of lead to investigate the effect of design variables such as bed height, influent concentration and withdrawal flowrate by analysis of the column experimental data and the relationship between operating parameters using the Thomas, Clark, Yoon-Nelson and Adams-Bohart models.

2. MATERIALS ANDMETHODS

2.1. Materials.

Periwinkle shells were obtained from Ukam market. The chemicals used in the experiment were of analytical reagent grade. Sulphuric acid (98%, Aldrich), Lead nitrate (99%, Aldrich), Hydrochloric acid (99.5%, Lab Tech Chemicals) and sodium hydroxide (99.5%, Phillip Harris). A stock solution of 1000 mg/l was prepared through dissolution of appropriate amount of $Pb(NO_3)_2$ salt in deionized water. The stock solution was diluted to obtain the required concentrations used in the experiment.

2.2. Preparation of Adsorbent.

The adsorbent was prepared by first washing the periwinkle shells with distilled water to remove dirt and soil debris. The clean shells were sun-dried for 2 days and oven dried for 3 hours. It was carbonized in a tubular muffle furnace for 1 hr 30 min at 800 ^oC. Then, the materials were crushed into smaller particle sizes with the aid of a mortar and a pestle. Next, the material was chemically impregnated with a ratio of 2:1 using a 1M solution of sulphuric acid. It was allowed to stay for 48 h and was further heated in furnace at 900^oC for 1 hr 30 min using the muffle furnace. 0.1M sodium hydroxide (NaOH) and 0.1M Hydrochloric acid (HCl) were used to stabilize the pH. The prepared adsorbent is presented in Figure 1.

Figure 1.Activated Periwinkle Shell Char

2.3 Analysis and Characterization.

The granulometric curve of the APSC and the simple percentages (%) of each granular fraction were established using a vibrating sieve shaker (RETSCH AS 200). The concentrations of the lead ion in the solutions were determined by using atomic absorption spectrophotometer (Perkin Elmer

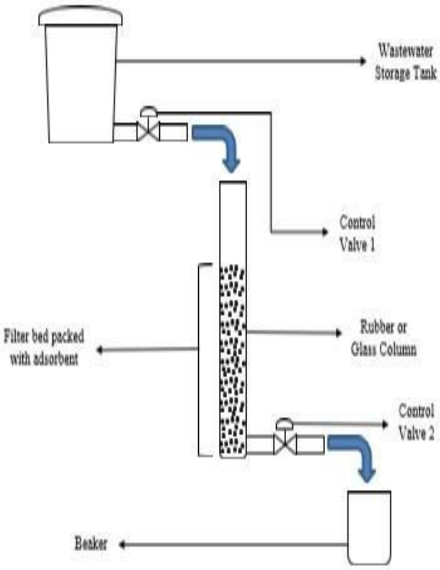

Model AAS 700). The pH meter (Hach) was used to determine the pH of the sample, while Functional groups of the adsorbent were identified by the Fourier transform infrared spectroscopy (FTIR) (Bruker 3000 Hyperion, Germany). Morphological analysis of the adsorbent was done by using the scanning electron microscope (SEM) (JELO JSM7600F), (Oxford Aztec energy system).

2.4. **Process Description**.

Dynamic column studies were carried out in a rubber column of 6.80 cm internal diameter and 35 cm height. The adsorbent bed were packed into the column and wetted with distilled water to release the trapped air between the particles. Industrial wastewater was continuously supplied through the column using the influence of gravity; installed valves were used to maintain the desired influent and effluent flow rate. Experiments were carried out at room temperature 28 ± 1 °C. Effects of process parameter like withdrawal flowrates (5, 7, and 10 mL/min), bed depth (3, 5, and 7 cm) and concentration (10, 50, and 100 mg/L) were investigated. Samples were collected at predefined time intervals from the bottom of the column and were tested to know the lead concentration. Figure 2represents a basic design of adsorption column.

Figure 2: Basic design of column adsorption

3. RESULTS ANDDISCUSSION

3.1 Adsorbent Granulometry Result.

The descriptive percentages of the granulometric analysis are illustrated in Figure 3. The graph shows the allocation of 6 fractions for the granulometric distribution of APSC, and the preponderant size which predominates is 1 mm with a percentage of 49.1%. This size is greater than 0.5 mm but less than 2mm, which gives it a medium class.

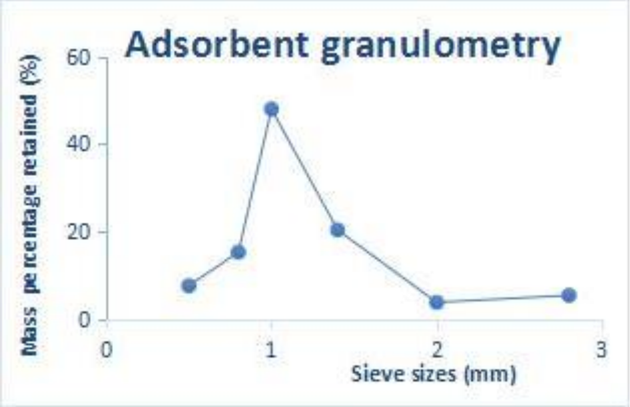

Figure 3: Granulometric curve of prepared Adsorbent

3.2. Fourier Transform Infrared Spectroscopy (FTIR) Result.

The spectra of the adsorbents were measured in the wave number range of 1000-3500 cm^{-1}as shown in Figure 4. The FTIR spectrum of APC implies the presence of predominant peaks at 3052.8 cm^{-1} (–OH and – NH stretching), 2516.0 cm^{-1} (–OH stretching), 2107.0 cm^{-1} (-C≡C- stretching), 1756.5 cm^{-1} (– C=O Stretching). Other notable peaks are summarized in Table1.

It is visible from the Table 1 that all functional groups present are readily available for interaction with heavy metals. The observation proves that functional groups such as NH and OH are involved in binding heavy metal ions to APSC. After the adsorption process the shifting of the peaks was observed which further affirms that the adsorption process actual took place Figure 5. The major shifts in peaks found were from 3052.8 to 2508.5 cm-1(for –OH and –NH stretch), 2516.0 to 2105.9 cm-1 (for –OH stretch), 2107.0 to 1871.1 cm-1 (for $-C \equiv C -$), 1156.6 to 1095.8cm-1 (for C-H bend).

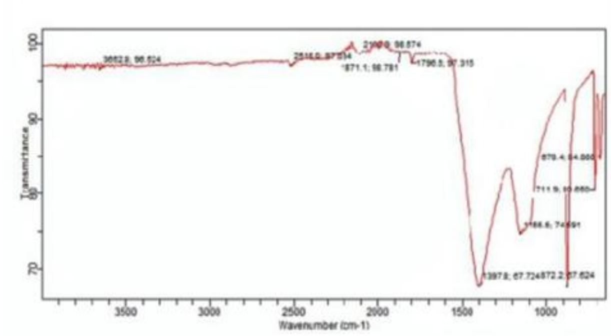

Figure 4: FTIR spectra of the adsorbent before adsorptionexperiment

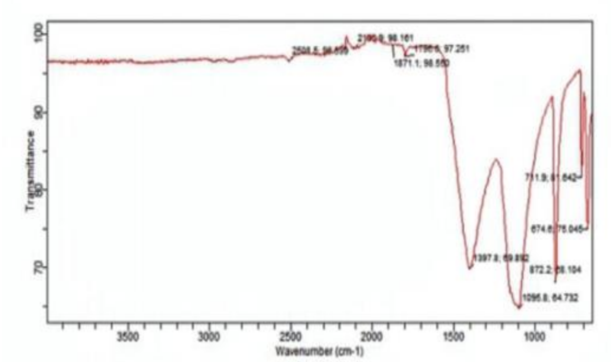

Figure 5: FTIR spectra of the adsorbent after adsorptionexperiment

Table 1: Summary of FTIR spectra bond, frequency and functional group

Frequency, cm^{-1}	Bond	Functional group
3052.8 (s, m)	O-H Stretch and N-H Stretch	Alcohol/Phenols, Amine/Amides
2516 (m)	O-H Stretch	Carboxylic acids
2107.0 (w)	- C ≡ C -	Alkynes
1756.5 (s)	- C = O Stretch	Carbonyls
1397.8 (w, m)	N-H bend	Amines
1156.6	C-H	Alkanes

m = medium, w = weak, s = strong

3.3 Scanning Electron Microscopy (SEM) Result.

The internal microstructure of unused adsorbent shows a rough, irregular, and proportionally porous and cracked appearance with the presence of some luminous and relatively ordered fragments which allows the interchanges of substances with adjacent cells and thus makes the adsorption mechanism possible (Figure 6). Microstructural analysis reveals significant changes in the surface morphology of the adsorbent after the adsorption of lead. A dense and compact matrix with a decrease in the degree of porosity and luminosity was noticed, and this can be explained by the adsorption of the molecules contained in the treated solute on the adsorbent cracks and pores (Figure7).

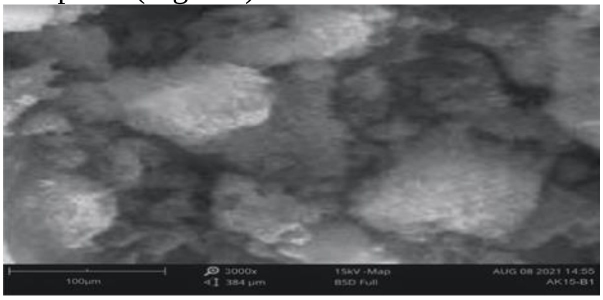

Figure 6: SEM photograph of prepared adsorbent at 3000x

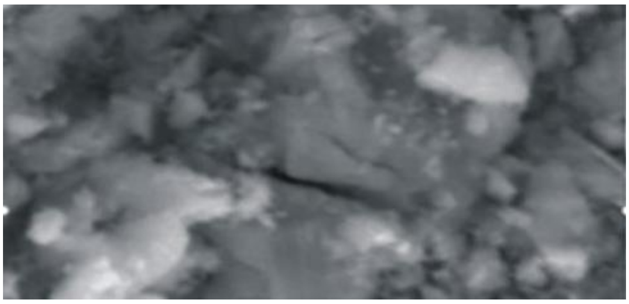

Figure 7: SEM photograph of the adsorbent after adsorption at 3000x

3.4. Absorption Spectroscopy (Lead Analysis)Result

From the results of the elemental analysis of the treated wastewater samples, the Table2 was created.

Table2: Parameters in fixed bed column for lead adsorption by Activated periwinkleshell

Co (mg/l)	Qw (ml/min)	Z (cm)	MA (g)	C @5mins (mg/l)	C@30mins (mg/l)	C@60mins (mg/l)	C@180mins (mg/l)	C@300mins (mg/l)
10	5	5	168.5	2.085	2.934	3.371	4.868	6.248
50	5	5	167.9	14.947	18.684	25.590	31.769	39.613
100	5	5	168.2	46.891	59.747	71.392	80.671	95.955
1.426	5	5	169.0	0.384	0.414	0.498	0.572	0.775
1.426	7	5	168.4	0.423	0.456	0.523	0.727	0.895
1.426	10	5	168.0	0.492	0.536	0.632	0.802	1.007
1.426	5	3	101.8	0.517	0.545	0.692	0.937	1.122
1.426	5	5	168.6	0.405	0.433	0.509	0.688	0.915
1.426	5	7	227.2	0.373	0.395	0.452	0.521	0.704

3.5. Column Experiment Result

3.5.1 Effect of Bed Height on Lead Adsorption

Breakthrough curves obtained at different bed depth (3, 5, and 7 cm) with a constant influent concentration of 1.426 mg/L and withdrawal flow rate of 5 mL/min are shown in Figure 8. From the Figure 8, it is observed that time of breakthrough and time of exhaustion increases with increasing bed depth. At the lowest bed depth there is no sufficient time for lead ions to diffuse into the holes of APSC. A similar tendency is also reported in the work of Mondal Mondal (2009) who also attested to the fact that at smaller bed depths there is little interaction between the adsorbent and wastewater to be remedied.

3.5.2 Effect of Withdrawal Flowrate on Lead Adsorption

Breakthrough curves obtained at different withdrawal flowrate (5, 7, and 10ml/min) with a constant influent concentration of 1.426 mg/L and adsorbent bed height of 5cm are shown in Figure 9. From the plot it is observed that time of breakthrough and time of exhaustion increases with the decreasing withdrawal flowrate, which is expected since the increase in withdrawal flowrate causes a rapid saturation of the adsorption bed due to the increase in exchange speed

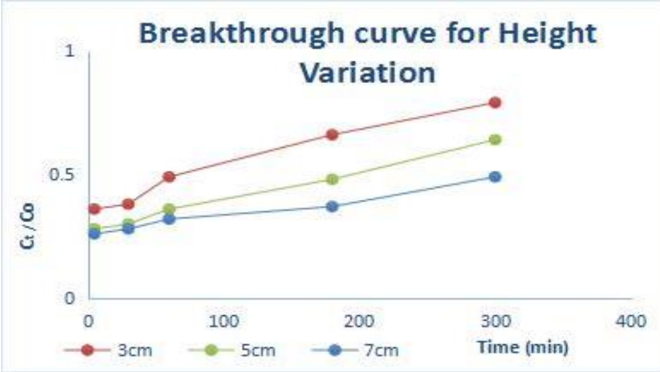

Figure 8: Breakthrough curve under varying bed heights

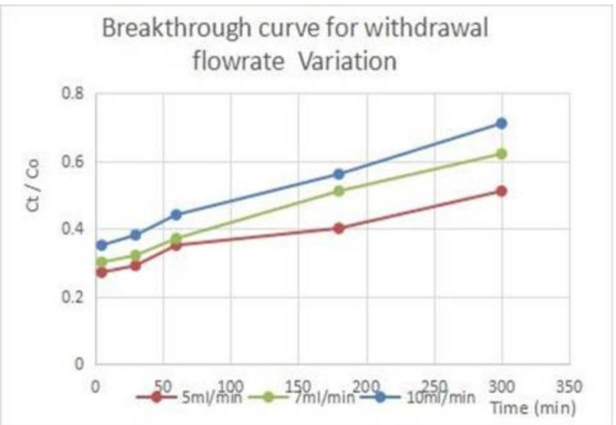

Figure 9: Breakthrough curve under varying withdrawal flowrates

3.5.3 Effect of Concentration dosage on lead adsorption on lead adsorption

Breakthrough curves obtained at different concentration dosages (10, 50, and 100mg/l) with a constant adsorbent bed height of 5cm and withdrawal flow rate of 5 mL/min are shown in Figure 10. From the plot it is observed that time of breakthrough and time of exhaustion increases with decreasing concentration dosages, and this makes sense since a higher concentration dosage would fill up the available active sites for adsorption faster. The findings of this study agree with the work of Cruz-Olivares, et al. (2013) who had a similar result in their work.

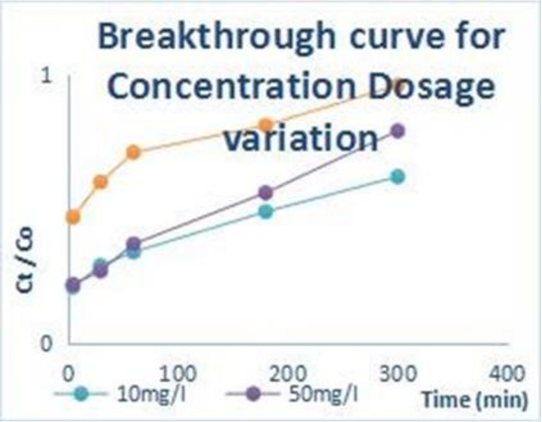

Figure 10: Breakthrough curve under varying Concentration dosages

3.6 Continuous Adsorption Isotherm Modeling

The isotherm models used in correlating the equilibrium data obtained from this experiment includes the Thomas model, Bohart-Adams model, Yoon and Nelson model and the Clark model. After computing the values of the parameters for each model, the average R^2 value obtained from each of the models will be compared to determine the isotherm model that best fits this adsorption process.

3.6.1 Bohart-AdamsModel

The experimental data Table 3 was fitted to Bohart-Adams model Eq. (1) to investigate its compliance with lead (II) ions adsorption process on Activated periwinkle shell char

$$ln\left[\frac{C_t}{C_0}\right] = K_{BA}C_0 t - K_{BA}N_0\frac{Z}{Q} \qquad (1)$$

Were C_0 and C_t are the influent and effluent concentration, t is time, K_{BA} is the mass transfer coefficient, N_0 is the saturation concentration, Z is the bed height and Q is the influent flowrate. The constant in the model were estimated by plotting $ln\left[\frac{C_t}{C_0}\right]$ against t the mass transfer coefficient was obtained from the slope of the graph while the saturation concentration (N_0) was obtained from the intercept. It was observed from the result, Table 3 that the mass transfer coefficient increases with the increase in bed height and influent flowrate, while the saturation concentration increased as the influent concentration, flowrate and bed height increases.

This agrees with the experiment on the sorption of Mn(II) ions by using mangostana garcinia peel-based granular-activated carbon (Chowdhurt, et al., 2012) and the experiments on adsorption of Pb (II) ion using activated carbon of plantain peels and bamboo (Uzoije & Uche, 2016). Bohart-Adams has a lower correlation coefficient compared to other models and this agrees with the observation of previous research.

3.6.2 Yoon and NelsonModel

The experimental data Table 4 was fitted to Yoon and Nelson model Eq. (2) to investigate its compliance with lead (II) ions adsorption processon APSC.

$$ln\left[\frac{C_t}{C_0 - C_t}\right] = K_{YN}t - \tau K_{YN} \qquad (2)$$

Where K_{YN} is the rate constant and τ is the time required for 50% adsorbent break through. The constant in the model were estimated by plotting $ln\left[\frac{C_t}{C_0 - C_t}\right]$ against t, $K_{YN}$was obtained from the slope of the graph while τ was obtained from the intercept. It was observed in Table 4 that with the increase in influent concentration and flowrate, theK_{YN} value increased while the value of τ decreased. This agrees with the results of the experiment carried out by Lopamudra et al.(2021). This is due to the fact that increase in influent concentration increases the competition between adsorbate molecules for the adsorption site resulting in increased uptake rate (Nwabanne, Okoye, & Lebele-Alawa, 2011). This model had the highest correlation coefficient compared to other models.

3.6.3 Thomas Model

The experimental data Table 5 was fitted to Thomas model Eq. (3) to investigate its compliance with lead (II) ions adsorption process on APSC.

$$ln\left[\frac{C_0}{C_t}-1\right]=\frac{K_{th}q_{th}M}{Q}-K_{th}C_0t \qquad (3)$$

Where $K_{th}, q_{th}, MandQ$ represent Thomas adsorption constant, maximum adsorption capacity, and the influent flowrate respectively.

The $K_{th}\, and\, q_{th}$ were estimated from the slope and intercept of $ln\left[\frac{C_0}{C_t}-1\right]$ against *t.*

it was observed from Table 5 that the increase in the packed bed height resulted in an increased in the maximum adsorption capacity of the system. Uzoije and Uche (2016) attributed this tobroadening of mass transfer zone as a result of increasing the bed height.

Table 3: Parameters of Bohart Adams model under column adsorption process

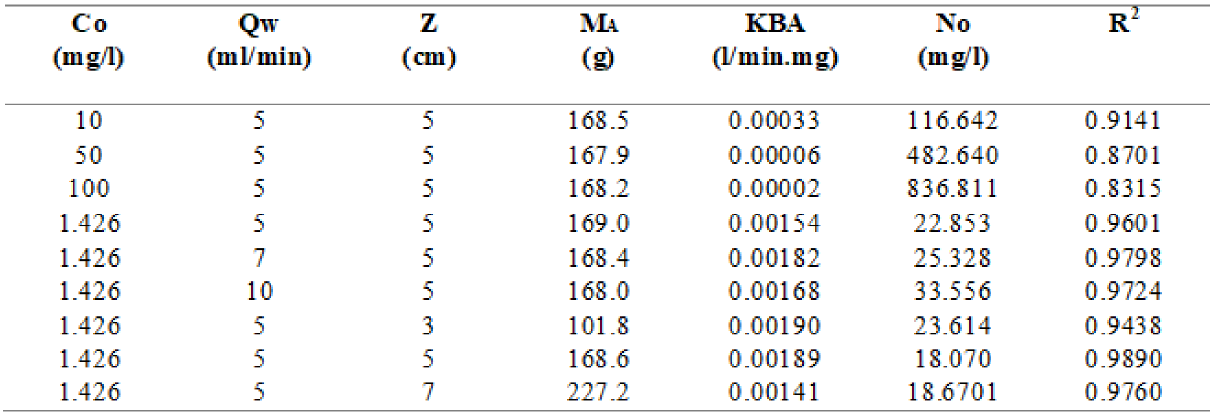

Co (mg/l)	Qw (ml/min)	Z (cm)	MA (g)	KBA (l/min.mg)	No (mg/l)	R^2
10	5	5	168.5	0.00033	116.642	0.9141
50	5	5	167.9	0.00006	482.640	0.8701
100	5	5	168.2	0.00002	836.811	0.8315
1.426	5	5	169.0	0.00154	22.853	0.9601
1.426	7	5	168.4	0.00182	25.328	0.9798
1.426	10	5	168.0	0.00168	33.556	0.9724
1.426	5	3	101.8	0.00190	23.614	0.9438
1.426	5	5	168.6	0.00189	18.070	0.9890
1.426	5	7	227.2	0.00141	18.6701	0.9760

Table 4: Parameters of Yoon and Nelsonmodel under column adsorption process

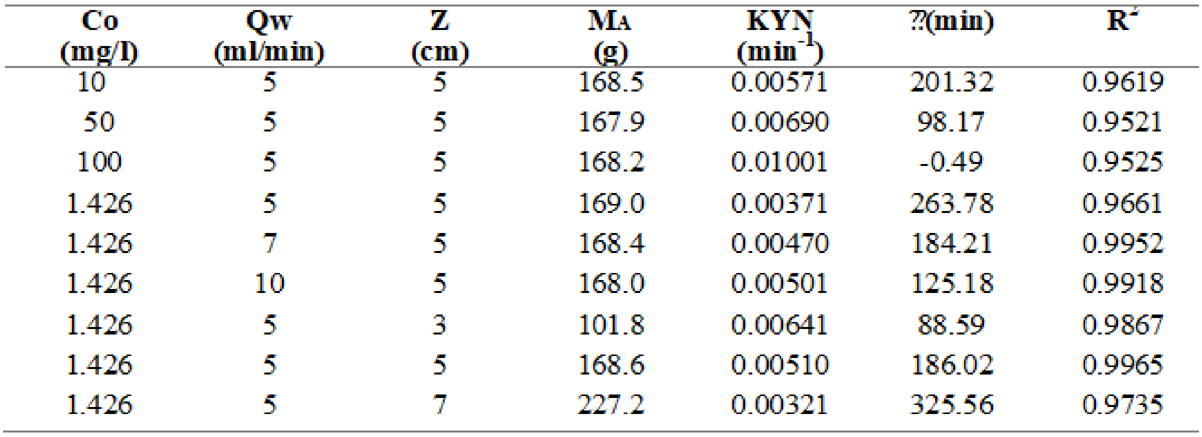

Co (mg/l)	Qw (ml/min)	Z (cm)	MA (g)	KYN (min^{-1})	??(min)	R^2
10	5	5	168.5	0.00571	201.32	0.9619
50	5	5	167.9	0.00690	98.17	0.9521
100	5	5	168.2	0.01001	-0.49	0.9525
1.426	5	5	169.0	0.00371	263.78	0.9661
1.426	7	5	168.4	0.00470	184.21	0.9952
1.426	10	5	168.0	0.00501	125.18	0.9918
1.426	5	3	101.8	0.00641	88.59	0.9867
1.426	5	5	168.6	0.00510	186.02	0.9965
1.426	5	7	227.2	0.00321	325.56	0.9735

Table5: Parameters of Thomas model under column adsorption process

Co (mg/l)	Qw (ml/min)	Z (cm)	M_A (g)	K_{Th} (l/mg.min)	q_{Th} (mg.ml/g.l)	R^2
10	5	5	168.5	0.00057	59.741	0.9619
50	5	5	167.9	0.00014	145.680	0.9521
100	5	5	168.2	0.00011	-1.454	0.9526
1.426	5	5	169.0	0.00260	11.160	0.9658
1.426	7	5	168.4	0.00331	10.902	0.9953
1.426	10	5	168.0	0.00351	10.583	0.9918
1.426	5	3	101.8	0.00451	6.189	0.9867
1.426	5	5	168.6	0.00372	7.936	0.9921
1.426	5	7	227.2	0.00224	10.217	0.9736

Table 6: Parameters of Clarkmodel under column adsorption process

Co (mg/l)	Qw (ml/min)	Z (cm)	M_A (g)	r (min^{-1})	A	R^2
10	5	5	168.5	0.00690	7.3681	0.9521
50	5	5	167.9	0.00781	4.0597	0.9423
100	5	5	168.2	0.01062	1.7704	0.9518
1.426	5	5	169.0	0.00452	5.9390	0.9654
1.426	7	5	168.4	0.00560	5.1542	0.9931
1.426	10	5	168.0	0.00581	3.8183	0.9901
1.426	5	3	101.8	0.00720	3.5282	0.9826
1.426	5	5	168.6	0.00601	5.7001	0.9961
1.426	5	7	227.2	0.00402	6.4661	0.9746

3.6.4Clark Model

The Thomas Clark model is expressed in Eq. (4)

$$ln\left[\left(\frac{C_0}{C_t}\right)^{n-1}-1\right]=lnA-rt \qquad (4)$$

Where the values of A and r are obtained from the slope and intercept of $ln\left[\left(\frac{C_0}{C_t}\right)^{n-1}-1\right]$ vs t. The experimental data was fitted to the Clark model, the results Table 6 indicated that an increase in the influent concentration increased the values of *A* and decreased the value of *r*. while influent flowrate has a reverse effect. The prediction of effluent concentration by the Clark model has a good correlation coefficient.

4.0 Conclusion

The study concluded that removal of lead ion in a fixed bed system using APSC is an effective and feasible method.

The FTIR spectrum of APSC indicated the presence of predominant peaks and after the adsorption process the shifting of the peaks was observed which further affirms that the adsorption process actual took place. Additionally, the *SEM*microstructural analysis reveals significant changes in the surface morphology of the adsorbent after the adsorption of lead.

The behaviour of breakthrough curves and lead removal efficiency were strongly influenced by withdrawal flowrate, bed depth and influent concentration. The prediction of breakthrough curves was obtained by using Adams-Bohart, Thomas, Clark and Yoon-Nelson model. However, the entire breakthrough curve was best predicted by Yoon and Nelson model with an average R^2value of 0.9751.

Conflict of Interests

The authors hereby declare no conflict of interests.

Acknowledgment

The authors are thankful to the Almighty God for his grace, mercy and love upon them and their different families.

REFERENCES

Aimikhe, V., & Lekia, G. (2021). An Overview of the Applications of Periwinkle (Tympanotonus fuscatus) Shells. *British Journal of Applied Science & Technology, 40*(18), 31-58.

Akpa, J. G., & Nduka, C. (2018). Kinetics, Equilibrium and Thermodynamics Studies of Fe3+ Ion Removal from Aqueous Solutions Using Periwinkle Shell Activated Carbon. *Advances in Chemical Engineering and Science, 8*, 49-66.

Chowdhurt, Z., Zain, S., Rashid, A., Rafique, R., & Khalid, K. (2012). Breakthrough Curve Analysis for Column Dynamics Sorption of Mn(II) Ions from Wastewater by Using Mangostana garcinia Peel-Based Granular-Activated Carbon. *Journal of Chemistry*.

Cruz-Olivares, J., Perez-Alonso, C., Barrera-Diaz, C., i. Urena- Nunez, C., Chaparro-Mercado, C., & Bilyeu, B. (2013). Modeling of Lead (II) Biosorption by Residue of Allspice in a Fixed-bed Column. *Chemical Engineering Journa, 228*, 21-27.

Lopamudra, D., Saptarshi, S., Papita, D., Avijit, B., & Chiranjib, B. (2021). Experimental and Numerical modeling on dye adsorption using pyrolyzed mesoporous biochar in Batch and fixed-bed column reactor: Isotherm, Thermodynamics, Mass transfer, Kinetic analysis. *Surface and Interfaces, 23*.

Ministry of Environment . (1999). *National Environment (Standards for Discharge of Effluent.* Government of Ughanda.

Mohsen, A., Sara, H., & Masoud, A. (2015). Removal of Lead ions from Industrial Wastewater: A Review of Removal Methods. *International Journal of Epidemiologic Research, 2*(2), 105-109.

Mondal, M. (2009). Removal of Pb (II) ions from Aqueous Solution using Activated Tea Waste: Adsorption on a Fixed-Bed Column. *Journal of Environmental Manegement, 90*(11), 3266-3271.

National Environmental Standard and Regulations Enforcement Agency. (2009). *National Environmental Regulations.* Abuja: The Federal Government Printer.

Nwabanne, J., Okoye, A., & Lebele-Alawa, B. (2011). Packed Bed Column Studies for the Removal of Lead (II) using Oil Palm Empty Fruit Bunch. *European Journal of Scientific Research, 63*(2), 296-305.

Uzoije, A., & Uche, C. (2016). Studying and Modeling Dynamic Adsorption of Lead (II) ion onto Fixed Bed Column of Activated Carbon of Plantain Peels and Bamboo. *Science Journal of Environmental Engineering Research*.

INSTRUCTION TO AUTHORS

1. TYPES OF PUBLICATION

The Journal of the Nigerian Society of Chemical Engineers will publish articles on the original research on the science and technology of Chemical Engineering. Preference will be given to articles on new processes or innovative adaptation of existing processes. Critical reviews on current topics of Chemical Engineering are encouraged and may be solicited by the Editorial Board. The following types of articles will be considered for publication:

a. Full length **articles or review papers**.
b. **Communication** – a preliminary report on research findings.
c. **Note** – a short paper describing a research finding not sufficiently completed to warrant a full article.
d. **Letter to the Editor** – comments or remarks by readers and/or authors on previously published materials.

The authors are entirely responsible for the accuracy of data and statements. It is also the responsibility of authors to seek ethical clearance and written permission from persons or agencies concerned, whenever copyrighted material is used.
For now the journal is published twice in a year, March/April and September/October.

2. MANUSCRIPT REQUIREMENTS

a. The **Manuscript** should be written in clear and concise English and typed (single column) in Microsoft Word using double spacing on A4-size paper, Times New Romans font and 12 point. A full length article or review should not exceed 15 pages. Margin should be Normal (i.e. 2.54cm for Top, Bottom, Left & Right margins).
b. The **Manuscript** should be prepared in the following format: Abstract, Introduction, Materials and Methods, Results, Discussion, Conclusion, Acknowledgements, and References..
c. The **Manuscript** must contain the full names, address and emails of the authors. In the case of multiple authorship, the person to whom correspondence should be addressed must be indicated with functional email address. As an examples, authors' names should be in this format:
Momoh, S. O., Adisa, A. A. and **Abubakar, A. S.**
If the addresses of authors are different, use the following format:
***Momoh, S. O.[1], Adisa, A. A.[2]** and **Abubakar, A. S.[3]**
Use star * to indicate the corresponding author.
d. **Symbols** should conform to America Standard Association. An abridged set of acceptable symbols is available in the fourth edition of Perry's Chemical Engineering Handbook. Greek letters, subscripts and superscripts should be carefully typed. A list of all symbols used in the paper should be included after the main text as **Nomenclature**.
e. All **Units** must be in the SI units (kg, m, s, N, etc).
f. The **Abstract** should be in English and should not be more than 200 words. The Abstract should state briefly the purpose of the research, methodology, results, major findings and major conclusions. Abstracts are not required for Communications, Notes or Letters.
g. **Citation** must be in the Harvard Format i.e. (Author, Date). Examples are (Smith, 1990) or (Jones et al, 2011). (Kemp, 2000) demonstrated that …..; (Mbuk, 1985; Boma, 1999; Sani, 2000) if more than two authors. (Telma, 2001a), (Telma, 2001b); etc if the citation have the same author and year of publication.
For more information on Harvard Referencing:
Guide visit http://www.citethisforme.com/harvard-referencing
h. **References** must also be in the Harvard Format i.e. (Author, Date, Title, Publication Information). References are listed in alphabetical order. Examples are shown below:
Haghi, A. K. and Ghanadzadeh, H. (2005). A Study of Thermal Drying Process. *Indian Journal of Chemical Technology*, Vol. 12, November 2005, pp. 654-663
Kemp, I.C., Fyhr, C. B., Laurent, S., Roques, M. A., Groenewold, C. E., Tsotsas, E., Sereno, A. A., Bonazzi, C. B., Bimbernet, J. J. and Kind M.(2001). Methods for Processing Experimental Drying Kinetic Data. *Drying Technology,* 19: 15-34.
i. **Tables** should contain a minimum of descriptive materials. Tables should be numbered serially throughout the manuscript in Arabic numerals (1, 2, 3, etc), and should be placed at the referenced point with captions (centralised) placed at the top of the table.
j. **Figures**, charts, graphs and all illustrations should be placed at the referenced point, numbered serially throughout the manuscript in Arabic numerals (1, 2, 3, etc) and incorporated in the text. Caption for Figures should be placed at the bottom of the Figure (centralised). Lettering set or symbols should be used for all labels on the figures, graphs, charts, photographs even when drawn in colours. (Note that figures drawn in colours may be unreadable if printed in black and white).
k. **Equations** should be typed using MS Word Equation Editor and should be centred and numbered serially throughout the manuscript (in Arabic numeral) at the right margin.

l. Wherever possible, **Fractions** should be shown using the oblique slash. E.g. x/y
m. **Footnotes** should not be incorporated in the text.
n. **Acknowledgements** should appear at the end of the paper, before the list of references.

3. SUBMISSION OF MANUSCRIPTS

Manuscripts should be submitted by sending a Microsoft Word document (taking into account the Manuscript Requirements described in section 2 above) to the following email address: nschejournal@yahoo.com and copy stevmomoh@yahoo.com**.**
All correspondences are directed to the Editor-in-Chief using the submission emails addresses: nschejournal@yahoo.com and copy stevmomoh@yahoo.com. Meanwhile the online submission of articles on the journal website will soon be ready.

Authors should note that:

a. All authors listed in the manuscript have significantly contributed to the research.
b. All authors are obliged to provide retractions or corrections of mistakes.
c. All references cited are listed and financial support acknowledged.
d. It is forbidden to publish same research in more than one journal.

The fee charged for paper review and publication will be borne by the authors as follows:
a. Manuscript Review charges = N6,500 payable by both Members and Non-Member. Overseas is $30.00.
b. Publication Charges = N10,000 payable by Non-Members and Members who are not financially up-to-date. Overseas is $40.00.
c. Members would only get one (1) Journal free and buy the other if they so wish.
d. Corresponding Author whose paper is published on a particular edition would get one (1) free copy on behalf of all the co-authors. Other co-authors will buy if they so wish.
All fees are paid after the paper had been accepted for publication. These charges may be reviewed from time to time by the Governing Board of Directors of the Society.

4. ACCEPTED PAPERS

On acceptance, authors will be required to submit a copy of their manuscripts using Microsoft Word by emails to nschejournal@yahoo.com and copy stevmomoh@yahoo.com.

The following additional information should be observed for accepted papers: (i) Typed in Microsoft Word using 1.15 spacing on A4-size paper, Times New Romans font and 10 point; (ii) Margin should be 2.54cm for Top & Bottom; 2.20cm for Left & Right margins; (iii) The abstract should be one column document while the body of the manuscript should be double columns with 0.5cm gutter spacing except some tables and figures that may have to go in for one column document.

5. PUBLICATION

Full NSChE Journal edition in hard copy will be published twice annually – March/April Edition and September/October Edition.

6. REPRINT

Reprints are available on request at a moderate fee per page. Orders must be placed before the paper appears in Print.

7. READER’S INFORMATION

The papers are wholly the view of their author(s) and therefore the publisher and the editors bear no responsibility for such views.

8. SUBSCRIPTION INFORMATION

The subscription price per volume is as follows:

a.	Individual Reader -	N3,000.00
b.	Institutions, Libraries, etc.-	N5,000.00
c.	Overseas Subscription -	$100.00

Request for information or subscription should be sent to the Editor-in-Chief through the following emails addresses: nschejournal@yahoo.com and copy stevmomoh@yahoo.com.

9. COPYRIGHT NOTICE

By submitting your manuscript to the Journal, you have agreed that the copyright of the published material belongs to the journal.

10. PRIVACY STATEMENT

The names and email addresses entered in this journal site will be used exclusively for the stated purposes of this journal and will not be made available for any other purpose or to any other party.

RE: MEMO FROM COUNCIL ON CHARGES FOR PUBLICATION IN NSChE JOURNAL

You would recall that the above subject matter has been announced on the different platforms of the Society including our Journal Editions since then. It actually came into effect in the March/April Edition 2020.

The summary of the charges is as follows:

1, Payment of ₦6,500 for Review of manuscripts;

2. Payment of ₦10,000 as Publication Charge for manuscript that has been accepted for publication:

3. These payments (totaled N16,500) shall be payable to the following account.

Name of account: Nigerian Society of Chemical Engineers

UBA account No:1001730178
or
GTB account No 0139519728

4. The narration on the slip should be “**Journal Publication Charges**”

5. Make your payments and send a proof to the email of the Chairman/Editor-in-Chief, stevmomoh@yahoo.com. Until these payments are made, your manuscript will not be published.

Thank you sir.